Modelling and simulation of thermo-hydro-mechanical processes in fractured porous media

Ivar Stefansson

Thesis for the degree of Philosophiae Doctor (PhD)
University of Bergen, Norway
2021

UNIVERSITY OF BERGEN

Modelling and simulation of thermo-hydro-mechanical processes in fractured porous media

Ivar Stefansson

Thesis for the degree of Philosophiae Doctor (PhD)
at the University of Bergen

Date of defense: 26.02.2021

Year: 2021

Title: Modelling and simulation of thermo-hydro-mechanical processes in fractured porous media

Name: Ivar Stefansson

Print: Skipnes Kommunikasjon / University of Bergen

Preface

This thesis is submitted as a partial fulfillment of the requirements for the degree of Philosophiae Doctor (Ph.D.) at the University of Bergen. The advisory committee has consisted of Inga Berre (University of Bergen) and Eirik Keilegavlen (University of Bergen).

The Ph.D. project has been financially supported by the Research Council of Norway, ERiS project, grant number 267908.

Acknowledgments

As a candidate undertaking my PhD, I have found myself in a most privileged position. Four years on, I am more grateful than ever to all those who have contributed to making the project interesting, rewarding and highly enjoyable:

Inga Berre and Eirik Keilegavlen have advised me with academic excellence and integrity. Their considerate and generous treatment made me feel both a peer and in the safest possible quartet of hands. Thank you.

The rest of the porous media group at UiB has also been an extraordinary college, both academically and socially. I am particularly thankful to Runar Berge who reliably made sure we arrived at the correct destination, both in scientific discussions and skiing between mountain cabins.

My thanks also go to Adriana Paluszny and Rainer Helmig for generously hosting my research visits to Imperial College, London and Universität Stuttgart, respectively.

It goes without saying that non-academical support has also been indispensable. I thank my parents, siblings and friends from the bottom of my heart.

Ivar Stefansson
Bergen, December 2020

Abstract

Understanding and predicting processes in fractured porous media is of wide interest, with applications such as geothermal energy extraction, water management and storage of CO_2 and energy. Characterisation and monitoring are inherently challenging, and can be supplemented by modelling and simulation studies.

Strong interaction between structural features and physical processes calls for advanced models. The strong impact posed by fractures requires that they be explicitly represented in the model alongside the surrounding porous medium. Their high aspect ratio motivates a dimension reduction approach leading to a mixed-dimensional discrete fracture-matrix model. In this thesis, we consider the physical processes of fluid and heat flow and deformation of both fractures and the surrounding medium, including propagation of the former.

The model and its open-source implementation is tested in the papers constituting Part II, including benchmark studies for the flow problem and convergence studies for various parts of the model. The papers also contain simulations investigating various process-structure interaction mechanisms. Studies of fracture deformation in different regimes of thermal and hydraulic driving forces and with perturbations of various rock properties highlight the strongly coupled nature of the problem. Applications include stimulation of geothermal reservoirs and fracture propagation caused by forced and natural convection. The results demonstrate physics-based modelling's potential of advancing our understanding of complicated coupled processes.

List of papers

Part II consists of the following eight papers:

A **Finite-Volume Discretisations for Flow in Fractured Porous Media**
Ivar Stefansson, Inga Berre, Eirik Keilegavlen
Transport in Porous Media, 2018 Vol. 124, pp. 439-462
DOI: 10.1007/s11242-018-1077-3

B **Benchmarks for single-phase flow in fractured porous media**
Bernd Flemisch, Inga Berre, Wietse Boon, Alessio Fumagalli, Nicolas Schwenck, Anna Scotti, Ivar Stefansson, Alexandru Tatomir
Advances in Water Resources, 2018, Vol. 111, pp. 239-258
DOI: 10.1016/j.advwatres.2017.10.036

C **Verification benchmarks for single-phase flow in three-dimensional fractured porous media**
Bernd Flemisch, Inga Berre, Wietse Boon, Alessio Fumagalli,Dennis Gläser, Eirik Keilegavlen, Anna Scotti, Ivar Stefansson, Alexandru Tatomir, Konstantin Brenner, Samuel Burbulla, Philippe Devloo, Omar Duran, Marco Favino, Julian Hennicker, I-Hsien Lee, Konstantin Lipnikov, Roland Masson, Klaus Mosthaf, Maria Giuseppina Chiara Nestola, Chuen-Fa Ni, K. Nikitin, Philipp Schaedle, Daniil Svyatskiy, Ruslan Yanbarisov, Patrick Zulian
Advances in Water Resources, 2021, Vol. 147, pp. 239-258
DOI: doi.org/10.1016/j.advwatres.2020.103759

D: **PorePy: an open-source software for simulation of multiphysics processes in fractured porous media**
Eirik Keilegavlen, Runar L. Berge, Alessio Fumagalli, Michele Starnoni, Ivar Stefansson, Jhabriel Varela, Inga Berre
Computational Geosciences, 2020, pp. 1–23
DOI: 10.1007/s10596-020-10002-5

E: **A fully coupled numerical model of thermo-hydro-mechanical processes and fracture contact mechanics in porous media**
Ivar Stefansson, Inga Berre, Eirik Keilegavlen
Submitted to Computer Methods in Applied Mechanics and Engineering
Preprint: arXiv:2008.06289 [math.NA]

F: **Fault slip in hydraulic stimulation of geothermal reservoirs: Governing mechanisms and process-structure interaction**
Inga Berre, Ivar Stefansson, Eirik Keilegavlen
The Leading Edge, 2020, Vol. 39, pp. 893–900
DOI: 10.1190/tle39120893.1

G: **Numerical modelling of convection-driven cooling, deformation and fracturing of thermo-poroelastic media**
Ivar Stefansson, Eirik Keilegavlen, Sæunn Halldórsdóttir, Inga Berre
In preparation for Transport in Porous Media
Preprint: arXiv:2012.06493 [math.NA]

H: **Hydro-mechanical simulation and analysis of induced seismicity for a hydraulic stimulation test at the Reykjanes geothermal field, Iceland**
Eirik Keilegavlen, Laure Duboeuf, Anna Maria Dichiarante, Sæunn Halldórsdóttir, Ivar Stefansson, Marcel Naumann, Egill Árni Guðnason, Kristján Ágústsson, Guðjón Helgi Eggertsson, Volker Oye, Inga Berre
Submitted to Journal of Geophysical Research – Solid Earth
Preprint: arxiv.org/abs/2011.03370

During the PhD period, the author also contributed significantly to four papers not included in Part II:

Implementation of mixed-dimensional models for flow in fractured porous media
Eirik Keilegavlen, Alessio Fumagalli, Runar Berge, Ivar Stefansson
Numerical Mathematics and Advanced Applications ENUMATH 2017, 2019, pp 573-580
DOI: 10.1007/978-3-319-96415-7_52

Finite Volume Discretisation of Fracture Deformation in Thermo-poroelastic Media
Ivar Stefansson, Eirik Keilegavlen, Inga Berre
International Conference on Finite Volumes for Complex Applications, 2020, pp 519–526
DOI: 10.1007/978-3-030-43651-3_48

Call for participation: Verification benchmarks for single-phase flow in threedimensional fractured porous media

Inga Berre, Wietse Boon, Bernd Flemisch, Alessio Fumagalli, Dennis Gläser, Eirik Keilegavlen, Anna Scotti, Ivar Stefansson, Alexandru Tatomir
arXiv:1809.06926 [math.NA]

Modelling of Thermally Induced Fracture Slip Caused by Fluid Injection During Geothermal Production
Ivar Stefansson, Runar Berge, Eirik Keilegavlen, Inga Berre
Accepted for World Geothermal Congress 2020, postponed to 2021

Contents

Part I

Background

Chapter 1

Introduction

This thesis concerns thermo-hydro-mechanical (THM) processes in fractured porous media. The term porous medium refers to a solid allowing fluid flow through a network of connected pores. The fractures are inclusions with a high aspect ratio and properties strongly deviating from those of the porous medium. They significantly impact the THM processes in a range of applications both in natural and engineered systems. Focusing on subsurface processes, prominent examples include groundwater management, extraction of hydrocarbons and geothermal energy and storage of nuclear waste, CO_2 and energy.

While the relative importance of the individual physical processes varies, the above applications can be reasonably modelled as a combination of flow and heat transfer through and deformation of both porous rock and fractures. For some applications, a subset of the processes is sufficient. Other applications may require consideration of even more processes, notably chemical ones, which are not pursued in this thesis. In geothermal systems, which receive particular attention in Part II, thermal effects play a major role and the fractures are typically crucial for fluid circulation.

Inherent inaccessibility makes the subsurface difficult to monitor and characterise. This can be partly alleviated by mathematical modelling and computer simulations, which both extend understanding in a qualitative sense and provide quantitative predictions. The current thesis offers modelling and simulation of THM processes in fractured porous media and of the associated process-structure interactions.

Coupled physical processes naturally yield elaborate mathematical models, typically formulated as a system of possibly nonlinear partial differential equations. Tightly coupled systems pose severe challenges to numer-

ical discretisation and simulation, including stiff linear equation systems and time step restrictions. To partly circumvent such issues, a common approach is to couple the processes weakly, i.e. solve the partial differential equations sequentially, facilitating combination of different simulation tools for different physical processes [88, 74, 96]. However, since the additional modelling error thus introduced may be considerable, a monolithic approach where all processes are solved fully coupled is preferred in this thesis.

The above applications are all characterised by strong coupling between physical processes and fractures. One classical example of fractures' strong impact on physical processes is as conduits for fluid flow: Especially in low-permeable media, the fracture network often carries a substantial part of the flow. On the other hand, fractures deform and propagate in response to changes in fluid pressure and rock temperature, in turn altering fracture characteristics such as permeability [53]. Thus, the system is characterised by strong two-way process-structure interaction.

Incorporation of the fractures and their impact on the THM processes requires a model which accurately represents the fractures and permits fracture deformation. Furthermore, consistent coupling between porous medium and fractures is requisite. These requirements are met in discrete fracture-matrix (DFM) models through explicit representation of both porous medium and fractures.

DFM models can be computationally costly, especially for networks containing many fractures. Moreover, resolving the minute fracture thickness in the model introduces severe restrictions, particularly for spatial discretisation and meshing. Therefore, the fractures are commonly represented as lowerdimensional objects, yielding mixeddimensional discrete fracture-matrix methods as used throughout this thesis.

Mixed-dimensional DFM models are reasonably widespread for flow in fractured media. They are used in combination with a variety of discretisation approaches [59, 71, 86], and mathematical analysis has been developed [20]. The number of available methods motivated the benchmarking efforts presented in Papers B and C, which also demonstrate that many existing models, included those considered in the thesis, handle quite complex fracture networks.

Mixed-dimensional models for coupled problems is a significantly less mature research topic. The last two decades have seen a development of increasingly complex multiphysics models, progressing from coupled TH, HM and TM processes to recent THM contributions such as [90, 82, 43].

Modelling how structures evolve, i.e. how fractures propagate, adds

another dimension of complexity. In mixed-dimensional models, fracture propagation is evaluated on the basis of a stress solution for the current geometry, rather than solved together with the rest of the governing equations. Thus, the main difficulty lies in how to handle and represent the evolving geometry in the model [81]. The choice of representation must be compatible with the other requirements of a multiphysics DFM model.

To summarise, three key challenges to the construction of a multiphysics mixed-dimensional DFM model are: i) Tight coupling between processes and between structures and processes, requiring careful modelling. ii) Different governing mechanisms and processes in matrix and fractures, which does not fit in traditional modelling approaches. iii) The mere number and complexity of processes involved.

Given this context, a mixed-dimensional framework introduced for flow methods in [20] is developed and extended to multiphysics problems herein. This is key to the presented formulation of a mixed-dimensional DFM model for fully coupled thermo-hydromechanical processes, as the framework allows breaking complicated problems into manageable parts by considering individual subdomains separately, and thus facilitates structured, transparent and consistent modelling and coupling between physical processes and different parts of the domain.

The difference in maturity between single- and multiphysics methods is also evident in the applied numerical discretisations and their implementation. Mixed-dimensional discretisation schemes for the individual subprocesses have been around for some time; the central schemes used herein were proposed the last two decades. Combination of the discretisations started with the more recent [77, 99, 11]. The main focus herein is on extending and integrating these combinations, again utilising the mixed-dimensional framework.

1.1 Main contributions

A mathematical and numerical model for coupled thermo-poro-elasticity, contact mechanics and fracture propagation. A poro-elasticity model with contact mechanics [11] is extended to cover thermal effects and propagation of pre-existing fractures in Paper E. The model accounts for THM processes in matrix, fractures and intersection and provides consistent coupling between both physical processes and subdomains, including a novel formulation of fracture shear dilation capturing stress redistribution in the surrounding medium. Paper G extends the model even further to include tensile fracture propagation along existing faces of the

mesh.

Simulation applications and studies of coupling mechanisms. Applications of the model to various scenarios demonstrate numerical modelling's potential to improve understanding of processes-structure interaction and identify processes and couplings at play. Prominent examples are the Paper E identification of how cooling-induced fracture deformation preferentially occurs where fluid transitions between matrix and fractures, the Paper F demonstration of how small parameter perturbations result in significantly altered fracture deformation and the Paper G investigations of fracture propagation due to changes in pressure and temperature.

Benchmarking of numerical methods for flow in fractured porous media. Papers B and C are based on a wide, international collaborative effort and compare a range of numerical methods for flow in fractured porous media applied to a suite of test cases. The benchmarks facilitate discrimination between the methods and establishes benchmarks for new methods in the field. The finite volume schemes used in the rest of the thesis are among the tested schemes; the two-point scheme shows some inconsistency for unstructured grids, while the multi-point scheme is among the best performers, albeit at a rather high computational cost.

Open-source simulation tool for fractured porous media. Excepting part of the benchmark studies, the above contributions are implemented in the open-source software PorePy, and run scripts for most of the presented simulations are publicly available in online repositories. This both ensures reproducibility and renders the effort available for future application and extension. The contributions to the toolbox include:

- Design and implementation of fracture propagation.
- Design and implementation of structures for data management and storage, including a framework for fully coupled mixed-dimensional simulations.
- Improvements and extensions of discretisations for contact mechanics and terms coupling between dimensions and different physical processes.
- Design of high-level code architecture and general maintenance.

1.2 Outline

The remainder of Part I is organised as follows:

Chapter 2 presents conceptual models for fractured porous media, in particular the discrete fracture-matrix model and mixed-dimensional geometry representation used in this thesis.

Chapter 3 details the mathematical model, including governing equations for each of the thermo-hydro-mechanical processes and their coupling. The governing equations consist of balance equations for entropy, mass and momentum complemented by constitutive relations.

Chapter 4 describes conversion from mathematical to numerical model through temporal and spatial discretisation, including some aspects pertaining to implementation.

Chapter 5 summarises each of the eight papers constituting Part II.

Chapter 6 concludes Part I summing up the central contributions of the thesis.

Chapter 2

Conceptual representations of fractured porous media

A key choice in construction of a conceptual model is how to represent the spatial domain of interest. The decision must be made bearing in mind the application(s) and which physical processes the model must accommodate, since the domain representation may restrict the range of resolvable physical processes. Another consideration is that the system of equations ensuing from the combination of conceptual model and physical processes is to be solved, in the current context through computer simulation. Hence, the chosen model should lend itself to discretisation and not be prohibitively computationally expensive, while the modelling error remains acceptable.

2.1 Characteristics of fractured porous media

The studied systems contain two types of structures, namely a porous medium and fractures, as illustrated in Fig. 2.1. The former consists in general of a solid containing a large number of pores, the interconnected part of which permits fluid flow, see Fig. 2.2a. While porous media can take such different forms as live tissue and engineered industrial materials, the subsurface rocks considered herein are comparatively homogeneous in important aspects. The pores are several orders of magnitude smaller than the domains of interest, and the amount of available pore space is fairly limited. The rock permits flow of both fluid and heat, albeit at moderate rates. Moreover, while the solid grains are quite rigid in themselves, the medium as a whole is somewhat deformable due to the presence of pores.

Figure 2.1: Rock exposure with fairly regularly oriented fractures of varying size.

The distinguishing feature of a fracture is its high aspect ratio: While the lateral extension is on the scale of metres or even kilometres, the thickness is on the order of millimetres [2]. Characteristics of multi-fracture networks include size and shape distribution and spatial density, which combine into network geometry and connectivity. All these properties are of high consequence to the network's impact on the THM processes, which often is substantial: High permeability contrast to the surrounding medium directly affects the fluid flow. Similarly, a fracture will typically be a local material weakness allowing more deformation than the intact rock. The effect on heat is primarily indirect through advection along the fluid flow.

Given the focus on geothermal energy extraction in some of the papers of Part II, some additional detail on the characteristics of the considered reservoirs is appropriate. The permeability of the intact rock is very low [83]. While extensive fracture networks may be present, their situation at depths of several kilometres implies high normal loads and small apertures. Thus, the overall effective permeability is low, motivating stimulation operations to increase fluid circulation. In hard rocks, an important mechanism achieving this is shear stimulation, whereby tangential fracture displacement incurs normal displacements [84].

The main driving force for stimulation is commonly assumed to be pressure increase, but temperature effects may be equally important [10]. Shear displacement has been linked to induced seismicity [36, 29], resulting in a twofold interest in the phenomenon - both to evaluate stimulation and to control seismicity. Mechanisms related to shear displacement are among

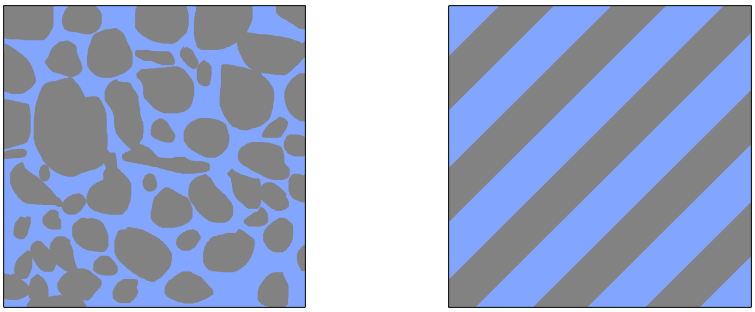

(a) (b)

Figure 2.2: (a) Porous medium consisting of solid grains and fluid. (b) In the corresponding upscaled representation, the solid and fluid phase coexist within the representative volume and the geometry of individual pores and grains is disregarded.

the phenomena studied in Papers D through H.

2.2 Continuum and discrete models

Classical representations of porous media (e.g. [9]) rely on the identification of a solid phase and an interconnected pore space, see Fig. 2.2. The individual pores being far too small and numerous to resolve individually on the scale of interest, a continuum model is constructed based on the concept of a representative elementary volume (REV). Representing properties of the medium by upscaled parameters is possible if a length scale can be identified which both gives adequate spatial resolution of the domain and is such that fluctuations of the medium properties are moderate. Taking the distinction between solid and pores as an example, the second scale restriction implies that there should be enough pores and grains within the REV to make their distribution homogeneous. Averaging the volume fraction of (interconnected) pore space over the REV now leads to the fundamental porous medium property of porosity. The upscaled rock and pore space will be referred to as the matrix.

Several conceptual models for incorporation of fractures' impact on physical processes exist, see [15] for a review in the context of fluid flow. In some cases, it is possible to treat the fractures by an upscaling approach. The simplest model treats them in the exact same way as pores, i.e. the

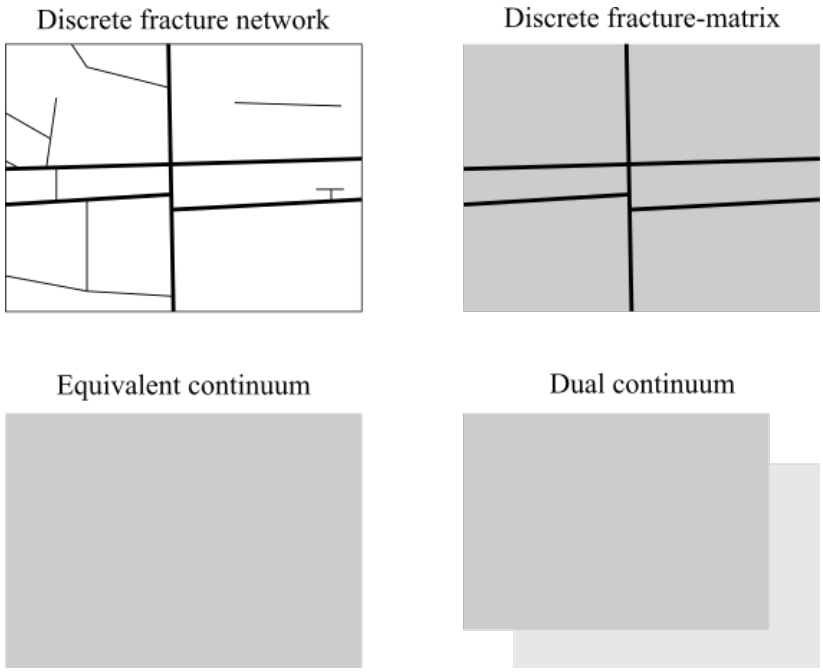

Figure 2.3: Representations of the fractured rock mass of Fig. 2.1 using four different conceptual models.

upscaled properties of the continuum model incorporate the fractures as well (Fig. 2.3). If the matrix and fracture processes are to some extent decoupled or independent, the fractures can be upscaled separately from the matrix, leading to a dual-continuum model [8]. If multiple classes of fractures are identified, e.g. based on length scale, the natural extension yields multi-continuum models. While these models apply to stronger heterogeneity between fractures and matrix than does the single continuum model, they require some means of coupling the continua, which can be quite complicated for multiple coupled physical processes.

If the fracture impact is sufficiently complex and dominant, upscaling is not feasible and faithful representation requires explicit representation of fractures, leading to discrete fracture models [33]. In the extreme of strong fracture dominance, the matrix may be left out altogether in a discrete fracture network model. Thus focusing on only a small volume fraction of the domain makes resolution of geometrically complex fracture

networks possible.

When explicit modelling of both matrix and fractures is required, discrete fracture models can be combined with continuum models for the matrix producing a discrete fracture-matrix (DFM) model. The strengths and weaknesses of a DFM model are both those inherited from its "parents" and those resulting from their combination: On the one hand, a DFM model can represent both fractures and matrix faithfully and additionally allows for accurate modelling of interaction between the two. On the other hand, it must tackle both the geometrical complexity of the network and the cost of representing the whole domain and additional restrictions such as small discrete matrix cells arise from the combination.

With the above strengths and weaknesses, DFM models rather favour accuracy over efficiency. However, the relative sophistication also enables adaptation in order to restrain computational cost. For example, one may choose to include a subset of the fracture network, while the rest of the fractures are upscaled in the matrix parameters. However, the assumed identification of which fractures require explicit representation is not necessarily trivial.

2.3 Mixed-dimensional models

The fracture aspect ratio challenges any model with explicit fracture representation. In particular, resolving the fracture thickness in a spatial discretisation of the domain leads to either a prohibitively high number of small cells or cells having high aspect ratio and correspondingly low quality. This motivates the common choice of averaging along the thickness of the fracture, whereby its dimension can be reduced [71, 86]. Thus, the spatial grid representing a fracture can be twodimensional, with no shape regularity constraints imposed by the minute thickness. The approach extends to intersections of multiple fractures as detailed in Section 2.4.

Spatial discretisation of mixed-dimensional DFM models can be classified as either conforming or non-conforming. In the former, the lowerdimensional subdomains act as gridding constraints to which faces of neighbouring higherdimensional subdomains must adhere. As illustrated in Paper B, these restrictions significantly impact mesh quality and size for networks containing challenging geometrical features such as barely or almost intersecting fractures.

In non-conforming methods, this restriction is circumvented and matrix and fractures are gridded independently. The most prominent nonconforming discretisations are embedded DFMs going back to [66], where

matrix-fracture coupling is handled by geometry dependent transfer terms, and extended finite elements, where the spaces of the basis functions in cells cut by a lowerdimensional inclusion are enriched to capture the pressure discontinuity at the fractures [95]. While the simplified grid construction is a significant advantage, no systematic approach exists for transfer term construction for coupled processes and basis function enrichment is both geometry and process dependent.

Conforming meshes are used throughout this thesis, with transparent matrix-fracture coupling at the price of complex grids possibly containing a high number of small grid cells. The severity of this drawback is lessened by the location of these small cells typically coinciding with regions where high solution accuracy is required.

2.4 Geometry framework

This section introduces a partitioning of the D-dimensional domain into subdomains of different dimensions and assosiated notation. The approach borrows from domain decomposition and mortar element approaches as put forth in [13, 71, 39]. The framework was introduced by Boon et al. [20] and generalised in the context of flow in fractured porous media in [79] and to the coupled poromechanical problem in [99, 11]. Paper D combines these developments and expands on implementational aspects. The resulting mixed-dimensional representation of the domain serves as an overarching framework for modelling, discretisation and implementation, thereby enabling the model extensions in Papers E and G.

The equidimensional domain Ω consists of the matrix, the fractures, fracture intersections and (for $D = 3$) intersection points of fracture intersections. After reducing the dimension of all parts but the matrix, Ω is partitioned into subdomains Ω_i^d, with the dimension d ranging from 0 through D. $\partial\Omega_i$ denotes the boundary of Ω_i and $\partial_j\Omega_i$ the internal part corresponding to an interface Γ_j. Γ_j has dimension $d-1$ and coincides geometrically with the lowerdimensional neighbour subdomain. Thus, an interface connects a subdomain pair exactly one dimension apart, see Fig. 2.4.

Subscript indices also identify the subdomain or interface where variables and parameters are defined, but are suppressed where context removes ambiguity, as is the dimension index d. Where convenient, indices h and l denote the higher- and lower-diensional neighbour of an interface. Conversely, the higher- and lowerdimensional interfaces of Ω_i constitute the sets $\hat{S}_i$ and $\check{S}_i$. Entities are transferred from Γ_j to Ω_i by the projection operator Ξ_j^i and from the part of Ω_i geometrically coinciding with Γ_j to

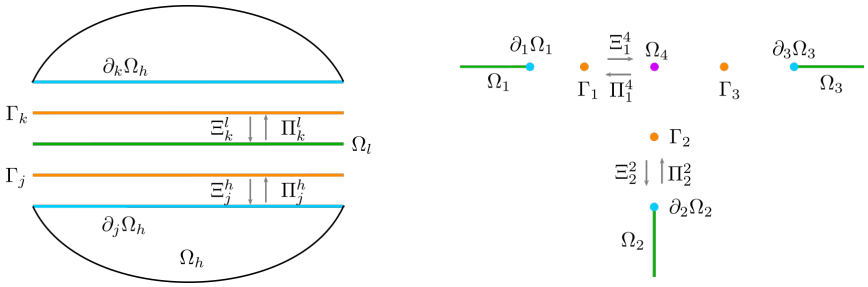

Figure 2.4: A fracture surrounded by a twodimensional medium (left) and three fractures meeting at an intersection (right). The subdomains are connected through the interfaces Γ by projection operators Ξ and Π. While expanded for visualisation here, all internal boundaries coincide geometrically with interfaces and lowerdimensional subdomains in the model. The figure is reproduced from Paper E.

Γ_j by Π_j^i as illustrated in Fig. 2.4. In the particular case of a fracture subomain, the two members Γ_j and Γ_k of $\hat{S}_i$ correspond to the fracture's surfaces or walls.

The geometry of a fracture is described using a basis with normal (n) and tangential (τ) components. To accommodate description relative to the tip of a propagating fracture, the basis is defined locally, see Fig. 2.5. The normal basis vector equals the higherdimensional outward normal vector on the j side:

$$\boldsymbol{e}_n = \Xi_j^l \Pi_j^h \boldsymbol{n}_h. \tag{2.1}$$

For $D = 3$, the tangential (τ) directions are further specified at the fracture tips by the components $\boldsymbol{e}_\perp$ and $\boldsymbol{e}_\parallel$, which are perpendicular and parallel to the fracture tip, respectively. For $D = 2$, only the former is needed, while $\boldsymbol{e}_\parallel$ is undefined.

Finally, some concepts and notation are needed for the dimension reduction producing the lowerdimensional equations in Section 3.2. The fracture thickness is characterised by the aperture a [m]. For intersections, the aperture is the average of the intersecting higherdimensional neighbours:

$$a_l = \frac{1}{|\hat{S}_l|} \sum_{j \in \hat{S}_l} \Xi_j^l \Pi_j^h a_h. \tag{2.2}$$

For the particular geometry shown to the right in Fig. 2.4, $\hat{S}_l = \{\Gamma_1, \Gamma_2, \Gamma_3\}$ and $l = 4$.

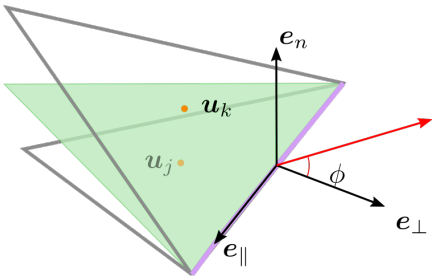

Figure 2.5: The local coordinate system at the tip of a fracture. The red propagation vector lies in the plane spanned by $\boldsymbol{e}_\perp$ and $\boldsymbol{e}_n$ and strikes an angle ϕ with $\boldsymbol{e}_\perp$. The separation of the interfaces (grey outlines) from the fracture surface (green) is for visualisation purposes only. The figure is reproduced from Paper G.

Averaging along the $D-d$ "small" dimensions transforms a deforming equidimensional domain Ω to its spatially fixed and dimensionally reduced counterpart Ω_i^d. For a scalar quantity ζ and a vector quantity $\boldsymbol{\iota}$, averaging produces the dimension reduction

$$\begin{aligned} &\frac{d}{dt}\int_{\Omega}\zeta dx = \int_{\Omega_i}\frac{\partial}{\partial t}(\mathcal{V}_i\zeta_i)dx, \\ &\int_{\partial\Omega}\boldsymbol{\iota}\cdot d\boldsymbol{x} = \mathcal{V}_i\int_{\partial\Omega_i}\boldsymbol{\iota}_i\cdot d\boldsymbol{x} - \sum_{j\in\hat{S}_i}\Xi_j^l\left(\Pi_j^h\mathcal{V}_h\int_{\Gamma_j}\iota_j dx\right). \end{aligned} \tag{2.3}$$

The specific volume is assumed to satisfy $\mathcal{V} = a^{D-d}$ and $\iota_j = \Pi_j^h\boldsymbol{\iota}_h\cdot\boldsymbol{n}_h$ denotes the interface flux into Ω_i. Differentials dx are relative to the domain of integration, with the volume integral reducing to point evaluation for $d=0$. $d\boldsymbol{x} = \boldsymbol{n}_i dx$, with $\boldsymbol{n}_i$ denoting the outwards normal at $\partial\Omega_i$ lying in the tangent plane of Ω_i. For $d=1$, the boundary integral equals evaluation of the integrand at the boundary points, while it is empty for $d=0$. For completeness, ι_j is void and $\mathcal{V}=1$ for $d=D$.

Chapter 3

Mathematical model

The last couple of decades have seen a steady development from single- to multiphysics DFM models for fractured porous media. While Kiraly suggested mixed-dimensional modelling of flow in the late 1970s [62], the approach gained traction in flow modelling at the beginning of the millennium [3, 59]. Extension to coupled fluid flow and heat transport introduces a nonlinearity due to advective heat transport [41]. Incorporation of thermal density dependence (e.g. [48]) yields a considerably more challenging, tightly coupled system. The nonlinearity is particularly pronounced for high flow rates in conductive fractures, demonstrating how processes and structures combine into strong couplings.

Matrix and fracture deformation is usually modelled in qualitatively different ways, e.g. with linear elastic and contact mechanics approaches, respectively, considerably adding to overall model complexity. The last decade has seen the emergence of tightly coupled hydromechanical, also termed poromechanical, models [56, 44, 98, 42, 11]. In the purely thermomechanical problem, models disregarding or simplifying heat flow along (and even across) fractures are widespread, but full mixed-dimensional approaches also exist [34]. Models incorporating a large subset of the THM and contact mechanics processes considered in this chapter include [46, 90, 82, 43]. For a broad review in the context of geothermal reservoirs, refer to [83].

Fracture propagation models based on energy minimisation have been used to model coupled problems [21, 31, 73, 72]. However, these models are not mixed-dimensional and lack a clear definition of the fracture aperture, complicating incorporation of flow and thermal transport and constraining feasible fracture network geometries. Fracture propagation can also

be incorporated in mixed-dimensional models, where propagation usually occurs either along existing faces of the spatial mesh [42], using remeshing to accommodate the predicted propagation path [69, 89] or using numerical discretisations (e.g. extended finite elements) which do not require the mesh to conform to the fractures [34].

This thesis extends the model for poromechanics and fracture contact mechanics presented in [11] to account for thermal effects, shear dilation and fracture propagation. The description of the thermo-poroelasticity model closely follows [30], which relates to the poromechanics equations derived by Biot [18]. While certain modelling choices are made here, it is worth mentioning that the mixed-dimensional framework introduced in Section 2.4 provides considerable flexibility in model adjustment: Constitutive laws can easily be replaced in individual subdomains, e.g. for non-laminar (Forchheimer [40]) fracture flow in highly conductive fractures, and whole equations may be dropped altogether, e.g. producing a DFN type model for flow while keeping the momentum balance of the matrix.

First, equations of state and constitutive relations are specified. The constitutive equations are chosen in accordance with the applications outlined in Chapter 1, in particular geothermal energy extraction. Then, balance laws are stated for individual subdomains using the mixed-dimensional framework. Finally, the equation system is formed by collecting the conservation equations, inserting the constitutive laws and connecting the subdomains through interface conditions.

3.1 Constitutive relations

The primary variables are pressure and temperature in all subdomains, matrix displacement and fracture contact traction, denoted by p, T, $\boldsymbol{u}$ and $\boldsymbol{\lambda}$, respectively. Additionally, flux variables are defined on all interfaces and displacements on the twodimensional interfaces between matrix and fractures.

3.1.1 Fluxes

Given the applications considered herein, Darcy's law is assumed within all subdomains satisfying $d \geq 1$, yielding a relationship between the fluid flux and the pressure gradient and gravity acceleration $\boldsymbol{g}$ through the permeability tensor $\mathcal{K}$ and the fluid viscosity η:

$$\boldsymbol{v} = -\frac{\mathcal{K}}{\eta}(\nabla p - \rho \boldsymbol{g}). \tag{3.1}$$

For open fractures, the idealisation of planar parallel surfaces is invoked, yielding [22]

$$\mathcal{K} = \frac{a^2}{12}. \tag{3.2}$$

The heat flux consists of a conductive and an advective term, the former accounting for dispersion due to tortuous flow in the porous medium and modelled using Fourier's law:

$$\boldsymbol{J} = \boldsymbol{q} + \boldsymbol{w} = -\Lambda_e \nabla T + \rho_f C_f T \boldsymbol{v}, \tag{3.3}$$

where ρ and C denote density and specific heat capacity and the effective thermal conductivity, Λ_e, arises from the assumption of local thermal equilibrium, i.e. $T_f = T_s$, with subscripts f and s denoting fluid and solid, respectively. Also introducing effective heat capacity $(\rho C)_e$ and volumetric thermal expansion β_e, the three effective parameters are computed as [60, 27]

$$\begin{aligned} \Lambda_e &= \phi\Lambda_f + (1-\phi)\Lambda_s, \\ (\rho C)_e &= \phi\rho_f C_f + (1-\phi)\rho_s C_s, \\ \beta_e &= \phi\beta_f + (\alpha - \phi)\beta_s. \end{aligned} \tag{3.4}$$

Here, ϕ and α denote porosity and the Biot coefficient, respectively.

The constitutive laws for interface fluxes are interdimensional extensions of Eqs. (3.1) and (3.3). With $\mathcal{K}_j$ and Λ_j denoting the normal permeability and conductivity at Γ_j, the diffusive fluxes are

$$\begin{aligned} v_j &= -\frac{\mathcal{K}_j}{\Pi_j^l \eta_l}\left[\frac{2}{\Pi_j^l a_l}\left(\Pi_j^l p_l - \Pi_j^h p_h\right) - \Pi_j^l \rho_l \boldsymbol{g}\cdot\Pi_j^h \boldsymbol{n}_h\right], \\ q_j &= -\Lambda_j \frac{2}{\Pi_j^l a_l}\left(\Pi_j^l T_l - \Pi_j^h T_h\right) \end{aligned} \tag{3.5}$$

as suggested by Martin et al. [71] for fluid flow. The factor $2/\Pi_j^l a_l$ may be interpreted as the distance component of the normal gradient on Γ_j. Interdimensional upstream weighting [55] is applied to the interdimensional advective heat flux according to the direction of v_j, i.e.

$$w_j = \begin{cases} v_j \Pi_j^h \rho_h C_h T_h & \text{if } v_j > 0 \\ v_j \Pi_j^l \rho_l C_l T_l & \text{if } v_j \leq 0, \end{cases} \tag{3.6}$$

with subscript f suppressed for ρ and C.

3.1.2 Stress and contact mechanics

In Ω^D, the thermo-poroelastic stress is modelled using the extended isotropic Hooke's law

$$\begin{aligned}\sigma - \sigma_0 = \mu(\nabla \boldsymbol{u} + \nabla \boldsymbol{u}^T) + K\mathrm{tr}(\nabla \boldsymbol{u})\mathbf{I} \\ -\alpha(p - p_0)\mathbf{I} - \beta_s K(T - T_0)\mathbf{I}.\end{aligned} \tag{3.7}$$

Here, μ and K denote the shear modulus and bulk modulus of the solid, α the Biot coefficient and $\mathrm{tr}(\cdot)$ the trace of a tensor.

The relative movement of the two fracture surfaces is governed by contact mechanics relations as described in [51, 54]. The gap function g is the normal distance between the interfaces when there is mechanical contact, and the displacement jump over a fracture is defined as

$$[\![\boldsymbol{u}]\!] = [\![\boldsymbol{u}]\!]_l = \Xi_k^l \boldsymbol{u}_k - \Xi_j^l \boldsymbol{u}_j. \tag{3.8}$$

Whenever $g = [\![\boldsymbol{u}]\!]_n$, the tangential components of the displacement increment and the contact traction follow the Coulomb fraction law:

$$\begin{aligned}||\boldsymbol{\lambda}_\tau|| &\leq -F\lambda_n, \\ ||\boldsymbol{\lambda}_\tau|| &< -F\lambda_n \rightarrow [\![\dot{\boldsymbol{u}}]\!]_\tau = 0, \\ ||\boldsymbol{\lambda}_\tau|| &= -F\lambda_n \rightarrow \exists\, \zeta \in \mathbb{R}^+ : [\![\dot{\boldsymbol{u}}]\!]_\tau = \zeta \boldsymbol{\lambda}_\tau,\end{aligned} \tag{3.9}$$

with F denoting the friction coefficient. Further, the surfaces are prevented from interpenetrating and the non-positive normal traction is zero when there is no mechanical contact:

$$\begin{aligned}[\![\boldsymbol{u}]\!]_n - g &\geq 0, \\ \lambda_n([\![\boldsymbol{u}]\!]_n - g) &= 0, \\ \lambda_n &\leq 0.\end{aligned} \tag{3.10}$$

The shear dilation mechanism described in Section 2.1 is illustrated in Fig. 3.1, showing how tangential displacement induces normal displacement due to roughness of the fracture surfaces. The mechanism is modelled by setting

$$g = \tan(\psi)||[\![\boldsymbol{u}]\!]_\tau||, \tag{3.11}$$

with ψ denoting the dilation angle (see Paper E). Equation (3.10) ensures the gap increase is transferred to $[\![\boldsymbol{u}]\!]_n$, which in turn is related to the aperture by

$$a = a_0 + [\![\boldsymbol{u}]\!]_n, \tag{3.12}$$

with a_0 denoting the residual aperture in the undeformed state.

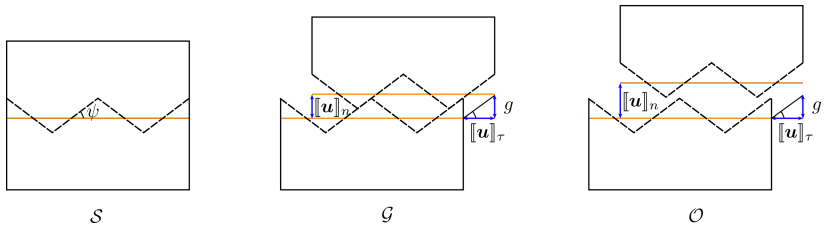

Figure 3.1: Schematic representations of fracture contact mechanics and shear dilation. The sawtooth pattern represents idealised fracture surface roughness, with the inclination of the teeth equalling the dilation angle ψ. Fracture states gliding and open have indicators of displacement jumps and fracture gap - these are zero in the sticking state to the left. The figure is reproduced from Paper E.

3.1.3 Fracture propagation criteria

The classical theory of fracture propagation goes back to Griffith [49] and is based on energy considerations: Fracture occurs when the potential energy released by its growth exceeds the energy required to break the material, in such a way that the global energy of the system is minimised. The "microscope principle" modelling assumption that propagation may be evaluated based on the local stress state [28] and linear elastic fracture mechanics is adopted herein, see e.g. [4].

The stress state in the vicinity of the fracture tips is described by the mode I, II and III stress intensity factors (SIFs). Assuming plane strain in the vicinity of the fracture tip, the SIFs are computed from the interface displacement as follows [25, 76]:

$$\begin{aligned} K_I &= \sqrt{\frac{2\pi}{R_d}}\left(\frac{\mu}{\kappa+1}[\![\boldsymbol{u}]\!]_n\right), \\ K_{II} &= \sqrt{\frac{2\pi}{R_d}}\left(\frac{\mu}{\kappa+1}[\![\boldsymbol{u}]\!]_\perp\right), \\ K_{III} &= \sqrt{\frac{2\pi}{R_d}}\left(\frac{\mu}{4}[\![\boldsymbol{u}]\!]_\parallel\right). \end{aligned} \tag{3.13}$$

Here, R_d is the distance from the fracture tip to the point at which $[\![\boldsymbol{u}]\!]$ is evaluated. $\kappa = 3-4\nu$ is the Kolosov constant, with ν denoting the Poisson ratio.

Two criteria described in [87] and computed from the SIFs are used in the fracture propagation model. Indicating the solid's critical SIFs by

subscript c, the onset criterion for propagation is

$$K_{eq} := \frac{K_I}{2} + \frac{1}{2}\sqrt{K_1^2 + 4\left(\frac{K_{Ic}K_{II}}{K_{IIc}}\right)^2 + 4\left(\frac{K_{Ic}K_{III}}{K_{IIIc}}\right)^2} \geq K_{Ic}. \quad (3.14)$$

The propagation angle relative to the fracture plane ϕ (see Fig. 2.5) is given by

$$\phi = -\text{sgn}(K_{II})\left[140^\circ \frac{|K_{II}|}{K_I + |K_{II}| + |K_{III}|} - 70^\circ \left(\frac{K_{II}}{K_I + |K_{II}| + |K_{III}|}\right)^2\right]. \quad (3.15)$$

In Paper G, a purely tensile propagation model is applied, i.e. K_{II} and K_{III} are assumed to be zero. In turn, Eqs. (3.14) and (3.15) reduce to

$$\begin{aligned} K_I &\geq K_{Ic}, \\ \phi &= 0. \end{aligned} \quad (3.16)$$

3.2 Balance laws

The fundamental physical laws at the heart of the model are three linearised balance statements - for mass and entropy within all subdomains and balance of momentum in the matrix and across the fractures, respectively. We assume local thermal equilibrium between the two phases and neglect viscous fluid dissipation.

Following [30], the matrix equations are the mass balance

$$\int_{\Omega^D} \left(\phi c + \frac{\alpha - \phi}{K}\right)\frac{\partial p}{\partial t} + \alpha \frac{\partial(\nabla \cdot \boldsymbol{u})}{\partial t} - \beta_e \frac{\partial T}{\partial t} dx + \int_{\partial\Omega} \boldsymbol{v} \cdot d\boldsymbol{x} = \int_{\Omega^D} q_p, \quad (3.17)$$

the entropy balance

$$\int_{\Omega^D} \frac{(C\rho)_e}{T_0}\frac{\partial T}{\partial t} + \beta_s K \frac{\partial(\nabla \cdot \boldsymbol{u})}{\partial t} - \beta_e \frac{\partial p}{\partial t} dx + \int_{\partial\Omega} \frac{\boldsymbol{J}}{T_0} \cdot d\boldsymbol{x} = \int_{\Omega^D} q_T dx \quad (3.18)$$

and, neglecting inertia terms, the momentum balance

$$\int_{\partial\Omega} \sigma \cdot d\boldsymbol{x} = \int_{\Omega^D} q_{\boldsymbol{u}} d\boldsymbol{x}. \quad (3.19)$$

Here, c denotes fluid compressibility and q denotes source and sink terms.

Referring to the dimension reduction concepts in Section 2.4 and Paper E, the $d < D$ linearised mass and entropy balance laws with constitutive relations inserted are respectively

$$\begin{aligned}&\int_{\Omega_i^d} \mathcal{V}_i \left(c \frac{\partial p_i}{\partial t} - \beta_e \frac{\partial T_i}{\partial t} \right) + \frac{\partial \mathcal{V}_i}{\partial t} dx - \int_{\partial \Omega_i} \mathcal{V}_i \frac{\mathcal{K}}{\eta} (\nabla p_i - \rho \boldsymbol{g}) \cdot d\boldsymbol{x} \\ &= \sum_{j \in \hat{S}_i} \Xi_j^i \Pi_j^h \mathcal{V}_h \int_{\Gamma_j} v_j dx + \int_{\Omega_i^d} \mathcal{V}_i q_p dx\end{aligned} \tag{3.20}$$

and

$$\begin{aligned}&\int_{\Omega_i^d} \frac{C_f \rho_f}{T_0} (T_i - T_0) \frac{\partial \mathcal{V}_i}{\partial t} + \frac{C_f \rho_f}{T_0} \mathcal{V}_i \frac{\partial T}{\partial t} - \beta \mathcal{V}_i \frac{\partial p_i}{\partial t} dx \\ &+ \int_{\partial \Omega_i} \mathcal{V}_i \left[\frac{C_f \rho_f}{T_0} (T_i - T_0) \boldsymbol{v}_i - \frac{\Lambda_f}{T_0} \nabla T_i \right] \cdot d\boldsymbol{x} \\ &= \sum_{j \in \hat{S}_i} \Xi_j^i \Pi_j^h \mathcal{V}_h \int_{\Gamma_j} \frac{q_j}{T_0} + \frac{w_j}{T_0} dx + \int_{\Omega_i^d} \mathcal{V}_i q_T dx.\end{aligned} \tag{3.21}$$

The first right hand side terms containing interface fluxes is the additional source term shown in Eq. (2.3). Note that the effective quantities of Eqs. (3.17) and (3.18) are replaced by fluid properties on the assumption that there is no porous medium in the fractures.

Newton's third law requires balance of the contact traction between the fracture surfaces:

$$\begin{aligned}\Pi_j^l \boldsymbol{\lambda}_l - p_l \mathbf{I} \cdot \boldsymbol{n}_l &= \Pi_j^h \sigma_h \cdot \boldsymbol{n}_h, \\ \Pi_k^l \boldsymbol{\lambda}_l - p_l \mathbf{I} \cdot \boldsymbol{n}_l &= -\Pi_k^h \sigma_h \cdot \boldsymbol{n}_h.\end{aligned} \tag{3.22}$$

To complete the interdimensional coupling, internal Neumann boundary conditions

$$\begin{aligned}\boldsymbol{v}_i \cdot \boldsymbol{n}_i &= \Xi_j^i v_j, \\ \boldsymbol{q}_i \cdot \boldsymbol{n}_i &= \Xi_j^i q_j, \\ \boldsymbol{w}_i \cdot \boldsymbol{n}_i &= \Xi_j^i w_j\end{aligned} \tag{3.23}$$

are imposed on $\partial_j \Omega_i$ for $d > 0$. On $\partial_j \Omega_h^D$, the Dirichlet condition

$$\boldsymbol{u}_h = \Pi_j^h \boldsymbol{u}_j \tag{3.24}$$

is also enforced. From a mathematical point of view, there is no difference between the conditions on the internal and external boundary of Ω_i.

The mass balance source term q_p accounts for any fluid volume added or extracted, typically representing an injection or production well. In analogy with Eq. (3.3), entropy sources are assumed to be on the form $q_T = q_p C_f \rho_f (T - T_0)/T_0 + q_H$. The latter term accounts for direct heating and is typically void in the applications considered herein. The momentum balance source term accounts for gravity, i.e. $q_{\boldsymbol{u}} = \rho_s \boldsymbol{g}$.

The system of governing equations is obtained by combination of the above balance laws and constitutive relations in the appropriate subdomains and on the interfaces. The equation system is complemented by conditions on the external boundary and initial conditions in the entire domain. The full model is invoked in Papers E and F without propagation and Paper G with propagation. Depending on the application, a subset of the model may also be considered, as done in Papers A through C for flow, Paper D for various models and Paper H for poroelasticity and contact mechanics.

Chapter 4

Numerical model

Since the system of partial differential equations of the previous chapter is far too complicated to solve analytically, an approximated solution is sought through numerical simulation. This requires both spatial and temporal discretisation of the equations, which are described in this chapter along with a solution strategy for fracture propagation and some implementational aspects.

In analogue to the model in Chapter 3, the mixed-dimensional framework allows spatial discretisation on individual subdomains and interfaces. Each such discretisation produces a local discretisation matrix to be assembled in the global matrix A. A further dissection of the local matrices based on primary variables reveals an inner structure with coupling terms between different variables on the off-diagonals. This two-level block structure is illustrated for a one-fracture domain in Fig. 4.1, and the block in row i and column j of A is denoted by $A_{(i,j)}$.

4.1 Temporal discretisation

Temporal discretisation follows the Implicit Euler scheme, i.e. the system $\frac{\partial \mathbb{X}}{\partial t} = \mathbb{F}(\mathbb{X})$ is advanced over the time step $\Delta t = t^{n+1} - t^n$ by solving

$$\mathbb{X}^{n+1} + \Delta t \mathbb{F}\big(\mathbb{X}^{n+1}\big) = \mathbb{X}^n, \tag{4.1}$$

with $\mathbb{X}$ denoting the vector of unknowns. The nonlinearity of $\mathbb{F}$ is handled by a Newton-Raphson scheme, each iteration of which is solved monolithically. The contact mechanics part of $\mathbb{F}$ is also discontinuous, requiring a semi-smooth extension described in Section 4.5.

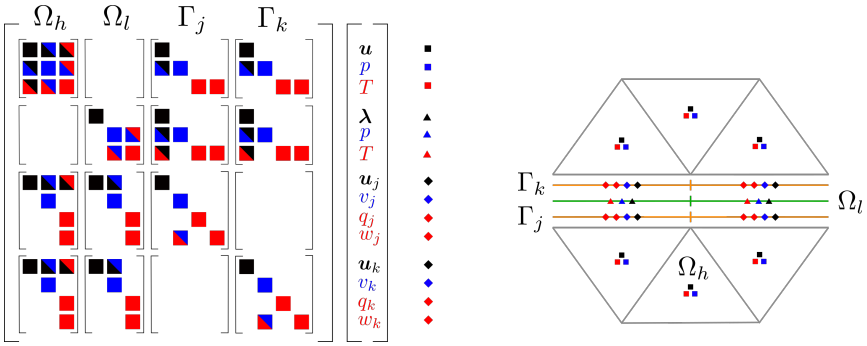

(a) (b)

Figure 4.1: (a) The two-level block structure arising from discretisation of the governing equations for a fracture, matrix and two interfaces, with variable markers identified to the right. (b) The corresponding grids and degrees of freedom, expanded at the fracture for visualisation purposes. The interface grids match faces in Ω_h and cells in Ω_l. The figure is adapted from Paper E.

4.2 Spatial grids

The spatial grid of subdomain Ω_i^d consists of non-overlapping d-dimensional polygonal cells ω covering Ω_i^d. ω is defined by its vertices v located at the points x_v, and $\gamma_{k,l}$ denotes the face shared by ω_k and ω_l. As discussed in Section 2.3, the grids conform in the sense that any immersed co-dimension one object coincides geometrically with faces of the higherdimensional neighbour.

The interfaces are gridded likewise. The mortar technique and resulting freedom in choice of projection operators allows non-matching grids [13], in which there is not a one-to-one correspondence between interface cells ω_j and higherdimensional faces γ_h nor between interface cells and lowerdimensional cells ω_l [79]. For this option, projection operator construction involves computation of the spatial overlap of ω_j with γ_h and with ω_l. Non-matching grids relieves the gridding restrictions and are explored for flow and transport in Paper D. However, the extension to the contact mechanics discretisation of Section 4.5 is not immediate, and matching grids are applied in the rest of the thesis.

4.3 Scalar conservation equations

The mass and entropy balance laws on individual subdomains consist of accumulation type terms and flux terms at the boundaries. They are usually discretised using either finite element or finite volume methods in the context of porous media [68]. These can also be generalised to mimetic methods, i.e. methods constructed with the explicit aim of mimicking central properties of the governing equations such as conservation, symmetry and monotonicity [101], with mixed-dimensional methods including [57].

For finite elements, preservation of the balance property locally requires the subclass of mixed methods, where a system consisting of the balance equation and the corresponding flux Eq. (3.1) or (3.3) is solved by assigning degrees of freedom for fluxes as well as pressures [37]. Mixed-dimensional finite element methods include [61, 26, 32] and the methods used in parts of Papers A and D, which are described in [19, 20] and [100].

Herein, the finite volume method is used to approximate all accumulation or mass terms and the three fluxes. Assuming the cell unknown ζ_ω to be constant on each cell, the former are

$$\begin{aligned} \int_\omega \frac{\partial \zeta_\omega}{\partial t} &\approx V_\omega \frac{\zeta_\omega^{n+1} - \zeta_\omega^n}{\Delta t}, \\ \int_\omega \zeta_\omega &\approx V_\omega \zeta_\omega, \end{aligned} \tag{4.2}$$

with V_ω denoting the d-dimensional volume of the cell.

Flux terms are collected for ω according to

$$\int_{\partial\omega} \boldsymbol{\iota} \cdot d\boldsymbol{x} = -\sum_\gamma \int_\gamma \boldsymbol{\iota} \cdot d\boldsymbol{x} \approx -\sum_\gamma \iota_\gamma, \tag{4.3}$$

with summation over the faces of ω and ι_γ denoting the approximated flux, or more precisely discharge, over γ. Adding contributions from all accumulation and flux types yields one equation for each balance equation and cell. These are collected in $A_{(2,2)}$, $A_{(2,3)}$, $A_{(3,2)}$ and $A_{(3,3)}$ for Ω_h and $A_{(5,5)}$, $A_{(6,5)}$, $A_{(6,5)}$ and $A_{(6,6)}$ for Ω_l.

4.3.1 Flux approximations

The appropriate approximation of the flux depends on the nature of the term. Diffusive terms are usually assumed to depend linearly on nearby

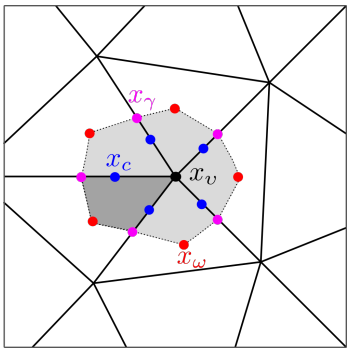

Figure 4.2: Interaction region for computation of weights in the multi-point approximations. The interaction region formed by connecting face centres x_γ and cell centres x_ω surrounds a vertex v located at x_v. Continuity points are shown as blue dots, whereas the dark shaded area indicates one subcell.

cell potentials:

$$\iota_\gamma \approx \sum_\omega t_{\gamma,\omega}\zeta_\omega. \tag{4.4}$$

In analogy with Eqs. (3.1) and (3.3), the weights t represent the discrete gradient and the tensor $\mathcal{K}$ or Λ.

Finite volume schemes are defined by the number of nonzero weights and how these are computed. Herein, we use the two-point flux approximation [7] and the multi-point flux approximation [1, 35], which were extended to DFM methods by Karimi-Fard et al. [59] and Sandve et al. [91], respectively. In the former, the flux depends on the potential in the two immediate neighbour cells of γ only. In the latter, a subgrid is constructed as shown in Fig. 4.2. The weights are computed by solving local problems in interaction regions surrounding each vertex of the primal grid. These systems are constructed by representing the gradient of the potential as constant on each subcell and enforcing flux continuity over subfaces and potential continuity at the continuity points x_c.

The advective term is discretised by a first-order upstream scheme, i.e.

$$\left(\rho_f C_f T\boldsymbol{v}\right)_{k,l} = \begin{cases} C_f \boldsymbol{v}_{k,l} T_k \rho_{f,k} & \text{if } \boldsymbol{v}_{k,l} > 0 \\ C_f \boldsymbol{v}_{k,l} T_l \rho_{f,l} & \text{if } \boldsymbol{v}_{k,l} \leq 0, \end{cases} \tag{4.5}$$

4.3.2 Interface conditions

Discretisation of the diffusive interface fluxes amounts to assembling contributions according to Eqs. (3.5). The pressure or temperature at $\partial_j\Omega_h$ is taken as the cell centre value for the adjacent ω_h when a two-point approximation is used for Ω_h. For the multi-point scheme, the value in the continuity point x_c, which is set to coincide geometrically with the centre of ω_j, is reconstructed using the discrete gradients. The advective flux is discretised according to Eq. (3.6) with cell centre values for all variables. The internal boundary conditions of Eqs. (3.23) and (3.24) are imposed in the standard way, i.e. just as for external boundaries.

4.4 Momentum balance

The finite element method is the dominating discretisation for mechanical problem [106], also in fractured media [93]. However, naive coupling to scalar conservation problems yields unstable schemes [102]. While stabilisation approaches have been suggested [75], this deficiency motivates the choice of the multi-point stress approximation proposed by Nordbotten [78]. Its extension to the coupled scalar-vector problem is stable without addition of regularisation terms [77].

Computation of stress approximation weights is done by constructing discrete gradients for each subcell and solving local systems in each interaction region to obtain the gradient expressed in terms of cell-centre displacements. This may be viewed as the vector generalisation of the multi-point flux approximation described above, and assembly of the entries of $A_{(1,1)}$ follows the same finite volume principle.

Coupling to T and p is accomplished by considering a discrete version of Eq. (3.7) in the stress approximation and adding a discrete divergence of $\boldsymbol{u}$ to the scalar balance equations, see [80] for details. These coupling terms are indicated by entries $A_{(1,2)}$, $A_{(1,3)}$, $A_{(2,1)}$ and $A_{(3,1)}$ in Fig. 4.1.

4.5 Contact mechanics

The contact mechanics discretisation rests on the approach described in [52] and [104]. It produces $A_{(4,4)}$, $A_{(4,7)}$ and $A_{(4,11)}$, thus relating $\boldsymbol{\lambda}$ to $[\![\boldsymbol{u}]\!]$ according to Eqs. (3.9) and (3.10), which are formulated as two complementary functions $\mathcal{C}$. The generalised Jacobians $\mathcal{D}$ of $\mathcal{C}$ are the convex hull of the regular Jacobians wherever $\mathcal{C}$ are differentiable. Denoting the increment of a function f between successive iterations k and $k+1$ by

$\delta f(\mathbb{X}^k) = f(\mathbb{X}^{k+1}) - f(\mathbb{X}^k)$, imposing the constraints amounts to solving $\mathcal{C} = 0$ by the semi-smooth Newton method

$$\mathcal{D}(\mathbb{X}^k)(\delta\mathbb{X}^k) = -\mathcal{C}(\mathbb{X}^k). \tag{4.6}$$

The deformation state of a fracture (or a fracture cell) is characterised as open, sticking or gliding corresponding to the sets

$$\begin{aligned} \mathcal{O} &= \{b \leq 0\}, \\ \mathcal{S} &= \{||\boldsymbol{\lambda}_\tau + \tilde{c}[\![\dot{\boldsymbol{u}}]\!]_\tau|| < b\}, \\ \mathcal{G} &= \{||\boldsymbol{\lambda}_\tau + \tilde{c}[\![\dot{\boldsymbol{u}}]\!]_\tau|| \geq b > 0\}. \end{aligned} \tag{4.7}$$

$\tilde{c}$ denoties a numerical parameter and $[\![\dot{\boldsymbol{u}}]\!]_\tau$ the increment $[\![\boldsymbol{u}]\!]_\tau^{k+1} - [\![\boldsymbol{u}]\!]_\tau^k$. $b = -F[\lambda_n + \tilde{c}([\![\boldsymbol{u}]\!]_n - g)]$ is the friction bound, with g depending on $[\![\boldsymbol{u}]\!]_\tau$ according to Eq. (3.11).

For the normal and tangential direction, the complementary functions are

$$\mathcal{C}_n([\![\boldsymbol{u}]\!]_n, \lambda_n) = -\lambda_n - \frac{1}{F}\max(0, b) \tag{4.8}$$

and

$$\begin{aligned} \mathcal{C}_\tau([\![\delta\boldsymbol{u}]\!]_\tau, [\![\boldsymbol{u}]\!]_\tau, \boldsymbol{\lambda}\tau) =& \max(b, ||\boldsymbol{\lambda}_\tau + \tilde{c}[\![\boldsymbol{u}]\!]_\tau||)(-\boldsymbol{\lambda}_\tau) \\ &+ \max(0, b)(\boldsymbol{\lambda}_\tau + \tilde{c}[\![\dot{\boldsymbol{u}}]\!]_\tau). \end{aligned} \tag{4.9}$$

As detailed in Paper E, these produce the following cellwise active set constraints

$$\begin{aligned} \boldsymbol{\lambda}^{\omega,k+1} &= \mathbf{0} && \omega \in \mathcal{O}, \\ [\![\boldsymbol{u}^{\omega,k+1}]\!]_n - g_{\boldsymbol{u}}^{\omega,k}[\![\dot{\boldsymbol{u}}^{\omega,k+1}]\!]_\tau &= g^{\omega,k} - g_{\boldsymbol{u}}^{\omega,k}[\![\dot{\boldsymbol{u}}^{\omega,k}]\!]_\tau && \omega \in \mathcal{G} \cup \mathcal{S}, \\ [\![\dot{\boldsymbol{u}}^{\omega,k+1}]\!]_\tau - \frac{F[\![\dot{\boldsymbol{u}}^{\omega,k}]\!]_\tau}{b^{\omega,k}}\lambda_n^{\omega,k+1} &= [\![\dot{\boldsymbol{u}}^{\omega,k}]\!]_\tau && \omega \in \mathcal{S}, \\ \boldsymbol{\lambda}_\tau^{\omega,k+1} - L^{\omega,k}[\![\dot{\boldsymbol{u}}^{\omega,k+1}]\!]_\tau + F\boldsymbol{\nu}^{\omega,k}\lambda_n^{\omega,k+1} &= \boldsymbol{r}^{\omega,k} + b^{\omega,k}\boldsymbol{\nu}^{\omega,k} && \omega \in \mathcal{G}. \end{aligned} \tag{4.10}$$

In addition to the modification of g and consequently b, the shear dilation extension introduces $g_{\boldsymbol{u}}$, denoting the derivative of g with respect to $[\![\boldsymbol{u}]\!]_\tau$, into the second of these equations. The coefficients L, $\boldsymbol{r}$ and $\boldsymbol{\nu}$ are computed from $[\![\boldsymbol{u}]\!]_\tau^k$ and $\boldsymbol{\lambda}^k$, and are regularised to ensure convergence as described in [11] and [104].

The traction balance Eq. (3.22) is imposed by constructing the higher-dimensional stress on $\partial_j\Omega_i$ using the discretisation matrices pertaining to the stress discretisation and equating with $\boldsymbol{\lambda}_l$ and p_l, cf. rows 7 and 11 in Fig. 4.1.

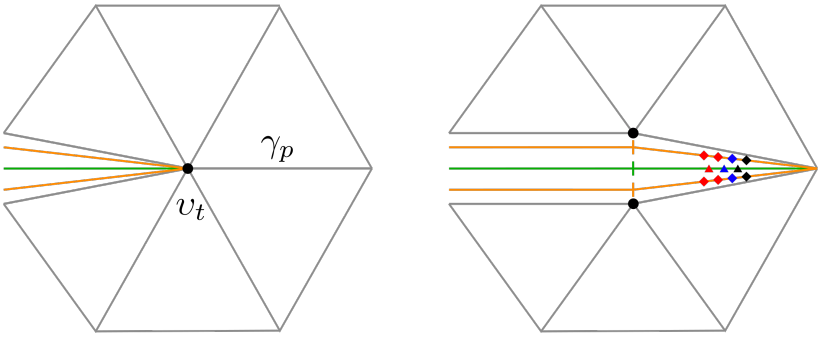

Figure 4.3: Updates to geometry and variables for the propagation along a face γ_p. The new geometric entities are the duplicates of γ_p and the tip vertex υ_t, a new face in Ω_l and two new interface cells. The new fracture and interface variables which arise are indicated using the Fig. 4.1b markers.

4.6 Fracture propagation

Motivated by Griffith's theory of fracture outlined in Section 3.1.3, numerical methods minimising the global energy to predict fracture propagation first emerged from fracture mechanics modelling and include phase-field [38] and peridynamics [94] approaches. In discrete fracture growth modelling, propagation is evaluated based on the stress solution for the current fracture geometry [97]. Such approaches may therefore also be applied to complex and coupled processes by considering e.g. the poroelastic [67], thermo-viscoelastic [50] or thermo-poroelastic [90] stress.

Adhering to the latter approach, propagation is evaluated from the converged solution at the end of a time step in this thesis and Paper G in particular. Stress intensity factors are computed according to Eq. (3.13) at all fracture tips, with $[\![\boldsymbol{u}]\!]$ evaluated at the centre of the fracture cell next to the tip, see Fig. 2.5. The SIFs are inserted into Eqs. (3.14) and (3.15) to determine which matrix faces γ_p to extend the fractures along. As illustrated in Fig. 4.3, the geometry update consists of duplicating γ_p and tip vertices υ_t. For the fracture, new cells and faces are added, as are cells at the interfaces. The geometry update is completed by updating connectivity maps for all subdomains and projection operators. All variables are mapped to the new geometries and values for the newly arisen degrees of freedom are initialised for new fracture and interface cells, see Fig. 4.3.

Before proceeding to the next time step, the discretisations are updated for affected subdomains. For the computationally expensive discretisations, the update can be done locally to the geometrically changed regions.

The strategy may be considered an explicit temporal discretisation of fracture propagation: The propagation criteria are evaluated given a converged solution of the rest of the problem and the updated geometry is used for the subsequent time step. This procedure is designed for stable propagation, in which the fracture arrests after propagating a limited distance [16]. Unstable growth calls for more elaborate propagation algorithms, e.g. involving multiple propagation evaluations within the same time step and more advanced criteria for propagation length [97].

4.7 Implementation

Many simulation toolboxes exist for porous media, providing the functionality needed for advanced simulation. Their relative strengths and weaknesses differ along axes including userfriendliness, applicability to large-scale simulations and supercomputers, range of physical problems and models and choice of numerical discretisation schemes. Referring to Bilke et al. [17] for an extensive review, some open-source toolboxes include DuMux [63], OPM [85], OpenGeoSys [64], MOOSE [45] and MRST [68]. The particular constraints posed by simulations with explicit fracture representation motivates and characterises the simulation toolbox PorePy, which is used and extended in this thesis. PorePy is developed by the Porous Media Group at the University of Bergen, written in Python and available at www.github.com/pmgbergen/porepy. As detailed in Paper D, the core code architecture implemented in PorePy relies heavily on the mixed-dimensional framework.

The code includes construction of unstructured simplex grids for subdomains and functionality for collecting these in a `GridBucket` representing a mixed-dimensional domain. The `GridBucket` is a graph, with one node for each subdomain and edges corresponding to interfaces.

Discretisation of each term on individual subdomains and interfaces is performed by `Discretization` objects, i.e. implementations of the schemes described in Sections 4.3 through 4.5. A global degree-of-freedom manager, the `Assembler`, invokes individual discretisations and collects the ensuing discretisation matrices to form the mixed-dimensional discrete system illustrated in Fig. 4.1a. The division of labour between `Assembler` and `Discretization` objects allows for bespoke mixed-

dimensional models: Adding, removing or changing a term from a governing equation in a given subdomain simply amounts to adjusting the corresponding discretisation when setting up the simulation.

The remainder of this section discusses four topics related to the model extensions and implemented as part of this thesis. The two former topics pertain to structures for data managing and simulation setup for mixed-dimensional multi-process simulations. These become increasingly intricate with model complexity, and the goal is to both facilitate model development and provide a certain userfriendliness. The two latter are the core functionalities added, both of which rely heavily on the former structures to resolve their respective challenges. For details on PorePy in general and implementation of the rest of the model, refer to Paper D and [11, 12].

A multiphysics mixed-dimensional simulation requires defining and passing considerable amounts of data such as physical and numerical parameters around the code. In particular, each Discretization needs access to the correct set of parameters at run time. Thus, ensuring simulation practicability requires a tailored design for data assignment and management. The implemented structure takes care of transfer between different parts of the code, provides default values for common problems and is highly flexible in accommodating non-standard parameter specification.

Setting up a simulation using a large subset of PorePy's capability from scratch is a daunting task for most users. It involves discretisation and parameter specification, time stepping and solving nonlinearities, all done for multiple subdomains, variables and equations. Therefore, Model objects were implemented for the most common models. Again, a balance between practicality and flexibility is attempted: The Model has default methods for all operations required for a simulation. The implementation utilises inheritance from simpler to more complex models, e.g. from the model for HM and contact mechanics to its THM extension, also facilitating user adjustment of the Model by overwriting individual methods.

The new discretisations added in this thesis centre around coupling of different variables at matrix-fracture interfaces, i.e. the off-diagonal minor blocks of the off-diagonal major blocks of A. These pose the greatest challenge to book-keeping and the Assembler and require great care from the developer, since they involve three sets of geometry objects (Ω_h, Ω_l and Γ_j), parameters and variables. Conceptually, this is solved by allowing interface discretisations access to all three sets, while the subdomain discretisations provide entities pertaining to Ω_h or Ω_l only.

The geometry update part of the fracture propagation implementation builds on PorePy's functionality for grid construction and splitting of the

matrix grid along immersed fractures, including updates to connectivity lists and projection operators. Keeping track of all geometry changes for a given time step is required for the considerable book-keeping operation of transferring variables and parameters from old to new geometries, which is performed using the data structure described above. The propagation implementation is partly integrated with the Model classes, providing methods for all operations described in Section 4.6.

Chapter 5

Paper summaries

This chapter describes each of the eight papers constituting Part II. Since the papers are collaborations, some of which have numerous authors, a short description of the thesis author's contributions concludes each description.

Paper A

Title:	Finite-Volume Discretisations for Flow in Fractured Porous Media
Authors:	Ivar Stefansson, Inga Berre, Eirik Keilegavlen
Journal:	Transport in Porous Media
DOI:	10.1007/s11242-018-1077-3

Paper A discusses interdimensional coupling and fracture intersections for the flow problem and transport of a passive tracer. Subdomain coupling is treated with a simple two-point stencil involving cell-centre pressures of Ω_h and Ω_l. We demonstrate the coupling's independence of the internal subdomain discretisation, which implies that it may be combined with a broad range of existing monodimensional discretisations yielding mixed-dimensional methods. An example of such an extension is the non-linear TPFA presented in [105], which also justifies the use of linear TPFA for the coupling by citing the Paper A numerical investigation of the coupling's performance for anisotropic matrix permeability.

Further, we propose a Schur complement approach to elimination of intersection cells to alleviate time step restrictions and the high condition number caused by these minute cells, and demonstrate its superiority

over the established approach [59] in cases involving both conducting and blocking fractures, a topic which was later investigated for two-phase flow in [103].

The numerical examples demonstrate that the pressure error may in some cases be considerably more forgiving than the tracer error, e.g. in revealing whether the correct fracture network connectivity is captured. The observation is unsurprising given the elliptic and hyperbolic nature of the pressure and tracer equations. However, the insight is of consequence since the advected quantity often is of primary interest.

Contributions: The candidate designed and ran all simulations, wrote most of the paper and implemented the extensions for the interface discretisation and Schur complement elimination in PorePy.

Paper B

Title:	Benchmarks for single-phase flow in fractured porous media
Authors:	Bernd Flemisch, Inga Berre, Wietse Boon, Alessio Fumagalli, Nicolas Schwenck, Anna Scotti, Ivar Stefansson, Alexandru Tatomir
Journal:	Advances in Water Resources
DOI:	10.1016/j.advwatres.2017.10.036

Motivated by the substantial growth in the field of DFM methods for flow over the last decades, we propose benchmarks to evaluate and compare such methods. The four cases are designed to address different challenges facing DFM methods, including conducting and blocking fractures, fractures extending to the boundary, fully immersed fractures and various intersection configurations and angles. The final test case is based on an outcrop of a real fracture network and contains 64 fractures.

The eight methods participating in the study were compared in terms of measures of computational cost, and errors were computed relative to an equidimensional reference solution. The benchmarks have seen extensive use as a reference for other methods, including [5, 6, 24, 47, 65, 92].

Contributions: The candidate provided scripts for error computation and ran the simulations for the three methods identified as "TPFA", "MPFA" and "Flux-Mortar" in the paper. Further, he wrote the method description for the two first of these methods and took part in the general design of the study and test cases.

Paper C

Title:	Verification benchmarks for single-phase flow in three-dimensional fractured porous media
Authors:	Bernd Flemisch, Inga Berre, Wietse Boon, Alessio Fumagalli, Dennis Gläser, Eirik Keilegavlen, Anna Scotti, Ivar Stefansson, Alexandru Tatomir, Konstantin Brenner, Samuel Burbulla, Philippe Devloo, Omar Duran, Marco Favino, Julian Hennicker, I-Hsien Lee, Konstantin Lipnikov, Roland Masson, Klaus Mosthaf, Maria Giuseppina Chiara Nestola, Chuen-Fa Ni, K. Nikitin, Philipp Schaedle, Daniil Svyatskiy, Ruslan Yanbarisov, Patrick Zulian
Journal:	Advances in Water Resources
DOI:	10.1016/j.advwatres.2020.103759

Building on the experience gained in the Paper B effort, a second benchmark study was announced in an open call for participation published on arXiv [14]. The proposed test cases are threedimensional and cover conducting and blocking fractures, intersection lines and points, the geometric challenges of small distances and acute angles and one outcrop-based case with a total of 52 fractures. Eight research groups answered the call and joined the authors of [14] to report results for a total of 17 DFM methods in Paper C.

Inspired by Paper A, the comparison was based on a tracer solution as well as the pressure. Unlike Paper B, the reference solution was computed using one of the well established participating mixed-dimensional methods on a significantly refined grid. Comparison to this solution was done through line plots and integration of quantities of interest in different subdomains and, for tracer, over time. Indicators of computational cost were also reported.

The main distinction revealed is between those methods reporting results for all cases and those not able to handle the more complicated cases. The agreement in the reported results is quite good for most points of comparison, but about a third of the methods fail on a number of points. The inconsistency of the two-point method for unstructured grids is reflected in some results, while no discrepancies are revealed for the multi-point method.

The considerable number of participating methods supports the authors' belief that 3d simulation on non-trivial geometries is a reasonable expectation from DFM methods, given the field's maturity. Despite the

recent publication of the paper, the benchmarks have already been used in other works [23, 58, 107].

Contributions: As one of the nine core authors who proposed the study, the candidate took active part in organising, planning and writing the paper, in particular designing test cases 2 and 3 and coordinating data collection and analysis for test case 3. He was also involved in setting up the simulations for the four methods having the prefix "UiB" in their identifying acronym.

Paper D

Title:	PorePy: an open-source software for simulation of multiphysics processes in fractured porous media
Authors:	Eirik Keilegavlen, Runar L. Berge, Alessio Fumagalli, Michele Starnoni, Ivar Stefansson, Jhabriel Varela, Inga Berre
Journal:	Computational Geosciences
DOI:	10.1007/s10596-020-10002-5

The mixed-dimensional framework used throughout this thesis is useful for various aspects of modelling, software implementation and simulation of fractured porous media, including grids, discretisation and data structures. It also facilitates flexible coupling between physical processes within and between subdomains of different dimension. Paper D both discusses these issues in the context of general DFM simulator design and presents the open-source PorePy simulation toolbox. We describe the core components of the code and their relation to the underlaying framework.

The simulations contain validation examples for flow, poroelasticity and fracture deformation. Moreover, we provide simulations of coupled processes showcasing the code's capability and flexibility.

Contributions: In addition to taking part in general writing, the candidate was responsible for designing the last of the simulation examples, which demonstrates shear deformation and poroelasticity, as well as contributing to general development and maintenance of PorePy, cf. the end of Chapter 1 and Section 4.7.

Paper E

Title:	A fully coupled numerical model of thermo-hydro-mechanical processes and fracture contact mechanics in porous media

Authors:	Ivar Stefansson, Inga Berre, Eirik Keilegavlen
Journal:	Submitted to Computer Methods in Applied Mechanics and Engineering
Preprint:	arXiv:2008.06289 [math.NA]

Paper E presents a mixed-dimensional model for the THM problem with contact mechanics on which the Chapter 3 model is based. We pay particular attention to coupling between fracture deformation and dilation and the latter's impact on the conservation equations. We propose a novel model for shear dilation fully capturing the stress redistribution in the matrix.

In the numerical results, we first validate the model and its PorePy implementation through a convergence study. Then, we investigate process-structure interaction effects, both demonstrating the effect of the proposed dilation model and identifying a cooling mechanism by which fractures preferentially dilate in regions where fluid transitions between fracture and matrix. Finally, we simulate a threedimensional reservoir-scale scenario demonstrating shear dilation caused by both hydraulic stimulation and long-term cooling, and study differences between these inducing mechanisms leading to dilation in different regions of the fracture network.

Contributions: The candidate was responsible for extensions of the model and corresponding PorePy implementation and designed, ran and visualised simulations. He assisted in writing the Introduction section and wrote the rest of the paper with the co-authors' assistance.

Paper F

Title:	Fault slip in hydraulic stimulation of geothermal reservoirs: governing mechanisms and process-structure interaction
Authors:	Inga Berre, Ivar Stefansson, Eirik Keilegavlen
Journal:	The Leading Edge
DOI:	10.1190/tle39120893.1

Paper F presents the state of the art of fractured porous media modelling of coupled processes to a broad readership within the applied geophysics community. We apply the model as presented in Paper E. Simulations demonstrate qualitative investigation of processes leading to fracture deformation and the impact of individual regimes for the parameters $\mathcal{K}_h$, $\mathcal{K}_l$ and α.

Contributions: The candidate designed and ran all simulations, visualised the results and took part in interpreting them.

Paper G

Title:	Numerical modelling of convection-driven cooling, deformation and fracturing of thermo-poroelastic media
Authors:	Ivar Stefansson Eirik Keilegavlen, Sæunn Halldórsdóttir, Inga Berre,
Journal:	In preparation for Transport in Porous Media
Preprint:	arXiv:2012.06493 [math.NA]

The model and PorePy implementation is extended to tensile fracture propagation in Paper G. Using the Paper E model, propagation is evaluated based on stress intensity factors computed from displacement jumps at the fracture tips. Propagation is restricted to be purely tensile and to follow existing faces of the matrix mesh. The paper can be seen as a step towards bridging the gap between modelling of fracture mechanics and coupled processes in fractured porous media.

Simulations demonstrate convergence for the SIFs and self-convergence of the propagation velocity subject to time step restrictions. Furthermore, applications show the relevance of thermo-hydraulically driven propagation in both forced and natural convection. The latter represents the first fully coupled THM simulation of convective downward fracture migration, which has been suggested as a mechanism for heat transport into geothermal systems [70]. The simulations epitomise the highly complex two-way coupling between evolving structures and THM processes central to this thesis.

Contributions: The candidate wrote the bulk of sections 2 through 4 and parts of the remaining sections. He designed and implemented most of the fracture propagation model extension, designed and ran all test cases, produced all figures and contributed to result interpretation.

Paper H

Title:	Hydro-mechanical simulation and analysis of induced seismicity for a hydraulic stimulation test at the Reykjanes geothermal field, Iceland

Authors: Eirik Keilegavlen, Laure Duboeuf, Anna Maria Dichiarante, Sæunn Halldórsdóttir, Ivar Stefansson, Marcel Naumann, Egill Árni Guðnason, Kristján Ágústsson, Guðjón Helgi Eggertsson, Volker Oye, Inga Berre
Journal: Submitted to Journal of Geophysical Research – Solid Earth
Preprint: arxiv.org/abs/2011.03370

This interdisciplinary paper integrates seismic analysis and simulations for hydraulic stimulation at a geothermal field. Seismic interpretations are combined with existing field data to determine model parameters and network geometry. Results from different simulation scenarios are compared to the seismicity analysis to discriminate slip along closely located and similarly oriented fractures, thereby improving the seismic analysis. While data scarcity prevents definite conclusions, the workflow demonstrates how combination of methods may further the understanding of complex subsurface processes.

Contributions: In addition to taking part in general discussions and writing, the candidate mainly contributed to the simulation related sections 4 through 6 by assisting with design of the simulation cases and result description and interpretation, as well as integrating simulations results and seismic analysis.

Chapter 6

Conclusion and outlook

Collecting the contributions described in the previous chapter, this section provides a unified résumé of the thesis, before some possible extensions and future possibilities are suggested. The paper topics range from fluid flow to THM processes and emphasis varies between modelling, implementation, testing and application. This covers a large portion of the efforts required to construct and apply a simulation tool. Indeed, all papers contribute to the development and application of what may be considered the end product - a mixed-dimensional THM model for porous media with fracture contact mechanics and propagation. Since modelling, discretisation and implementation is elaborated in Chapters 2 through 4, the main focus below is on application and its final prerequisite - model testing.

Recapitulating the modelling, Papers A and D employ and elaborate on a mixed-dimensional framework that allows for extension to coupled problems in the other papers, especially construction of the THM model in Paper E and fracture propagation in Paper G. Similarly, the discretisation contributions consist in coupling discretisation schemes for the subprocesses, including the coupling between matrix and fractures, as well as extension of contact mechanics and fracture propagation. Crucially, all developments are implemented in PorePy, facilitating their use in other works, and general code development and maintenance is also a significant part of the thesis. PorePy has been used to generate (parts of) the numerical results for numerous papers listed at github.com/pmgbergen/porepy/blob/develop/Papers.md.

Testing the model and its implementation is paramount to reveal mistakes and inconsistencies. As mentioned in Chapter 1, the complexity of the problem is a key part of the motivation for constructing a numerical

model. This very complexity also challenges validation through comparison to the real world, experiments and analytical solutions, typically requiring simplifications.

Comparison between numerical models is possible for relatively mature research topics and models. This approach is taken for flow in fractured media in Papers A, B and C. In the first two, the modelling error of dimension reduction is also assessed through comparison to more complete models, i.e. equidimensional ones.

In the earlier stages of model development, simplification options include comparison to idealised problems for which analytical solutions exist and testing of selected parts of the model, as done in Papers D and G. Since the PorePy implementation is dynamically changed by multiple developers, regularly running simplified tests on the code base is crucial to reveal bugs introduced by adjustments or new features.

One can also verify model consistency and implementation through mesh refinement and convergence studies (Papers A, B, C, E and G). At later stages, comparison to experiments, which may be designed to limit process complexity in the interest of transparent validation, and field cases, ideally reasonably well characterised and monitored, provides invaluable validation. This final step may be computationally demanding and requires thorough deliberation in the design of simulation model and identification of parameters and fracture network geometry.

The above combination can provide a reasonable validation of even highly complex models, at which point simulation applications are warranted. The goal of such simulations can be to quantify and predict the outcome of specific processes or operations at a specific site. Paper H exemplifies this, with emphasis on the advantages of combining simulation studies and data analysis to interpret, explain and complement reservoir characterisation. The results suggest how this combination can be used to discriminate between different scenarios or data interpretations related to both permeability and location of the fractures. Running this type of simulation involves parameter selection and computational cost challenges similar to field case validation.

The goal of performing simulations may also be to increase our understanding in a qualitative sense. That is the main concern of this thesis, with particular focus on the tight coupling between fractures and physical processes. Again reflecting that the individual subprocesses have been considerably better studied than their combination, the insights gained centre around the THM problem.

cooling-induced deformation in regions where fluid leaves or enters a

fracture is identified in both Paper E and Paper G, thus revealing a characteristic phenomenon of fracture deformation in porous media. A phenomenon may also be postulated and investigated through simulation, e.g. corroborating hypotheses about which mechanisms govern it. This is done in Paper G, where simulation demonstrates the interplay between convection in fractures, cooling of the surrounding matrix and downward fracture migration. Finally, the parameter sensitivity of a quantity of interest is investigated in Paper F, which demonstrates the strong impact of both matrix and fracture parameters ($\mathcal{K}$, α) on fracture displacement.

In their different ways, all these simulation studies contribute to increasing our understanding of coupled processes in fractured porous media. However, they do not span the range of application possibilities offered by the presented model. In addition to studies at larger scale and involving real data, a plethora of phenomena remain to be studied, especially if the scope is widened beyond the subsurface.

However, model extensions and their implementation may also tempt the adventurous scientist. Emphasising the first half of process-structure interaction, introduction of chemical processes would unlock a well of possibilities (and certainly challenges), including the study of structure interaction such as precipitation and fracture clogging.

On the structure side, fracture deformation extensions can expand the current contact mechanics approach or possibly consider lowerdimensional linear elastic inclusions. The fracture propagation would benefit hugely if the restriction of propagation along existing faces were overcome. While this has been done for other models and implementations e.g. by remeshing the matrix domain, the task is far from a trivial one. A key conceptual choice of great consequence to the implementation is how to represent the evolving fracture geometry.

While adding new model components is exciting, it also adds to computational cost. Even harnessing the steady gains in available computational power, solving the equation system naively at some point becomes infeasible. This urgently calls for more sophisticated solution strategies dealing with nonlinearities and preconditioners and iterative solvers for the linear equation system. These tasks require and include rigorous mathematical analysis of the model, a topic not addressed by the current thesis.

The open-source availability of the PorePy implementation accommodates both novel application and model extension. Hopefully, such efforts remain true to the spirit of reproducible science by releasing both source code and run scripts.

Bibliography

[1] I. Aavatsmark. "An Introduction to Multipoint Flux Approximations for Quadrilateral Grids". English. In: *Computational Geosciences* 6 (3-4 2002), pp. 405–432. DOI: 10.1023/A:1021291114475.

[2] P. M. Adler, J.-F. Thovert, and V. V. Mourzenko. *Fractured porous media*. Oxford University Press, 2013.

[3] C. Alboin, J. Jaffré, J. E. Roberts, X. Wang, and C. Serres. "Domain decomposition for some transmission problems in flow in porous media". In: *Numerical treatment of multiphase flows in porous media (Beijing, 1999)*. Ed. by Z. Chen, R. E. Ewing, and Z.-C. Shi. Vol. 552. Lecture Notes in Phys. Berlin: Springer, 2000, pp. 22–34. DOI: 10.1007/3-540-45467-5_2.

[4] T. L. Anderson. *Fracture mechanics: fundamentals and applications*. CRC press, 2017.

[5] N. Andrianov and H. M. Nick. "Machine Learning of Dual Porosity Model Closures From Discrete Fracture Simulations". In: *Advances in Water Resources* (2020), p. 103810.

[6] A. Arrarás, F. J. Gaspar, L. Portero, and C. Rodrigo. "Mixed-Dimensional Geometric Multigrid Methods for Single-Phase Flow in Fractured Porous Media". In: *SIAM Journal on Scientific Computing* 41.5 (2019), B1082–B1114. DOI: 10.1137/18M1224751.

[7] K. Aziz and A. Settari. *Petroleum Reservoir Simulation*. Springer Netherlands, 1979.

[8] G. I. Barenblatt, I. P. Zheltov, and I. Kochina. "Basic concepts in the theory of seepage of homogeneous liquids in fissured rocks [strata]". In: *Journal of applied mathematics and mechanics* 24.5 (1960), pp. 1286–1303.

[9] J. Bear. *Dynamics of Fluids in Porous Media*. American Elsevier, 1972.

[10] S. Benson. "Analysis of thermally induced permeability enhancement in geothermal injection wells". In: *PROCEEDINGS. Twelfth Workshop on Geothermal Reservoir Engineering*. 1987.

[11] R. L. Berge, I. Berre, E. Keilegavlen, J. M. Nordbotten, and B. Wohlmuth. "Finite volume discretization for poroelastic media with fractures modeled by contact mechanics". In: *International Journal for Numerical Methods in Engineering* 121.4 (2020), pp. 644–663. doi: 10.1002/nme.6238.

[12] R. L. Berge. "Numerical methods for coupled processes in fractured porous media". PhD thesis. The University of Bergen, 2019.

[13] C. Bernardi, Y. Maday, and A. T. Patera. "Domain decomposition by the mortar element method". In: *Asymptotic and numerical methods for partial differential equations with critical parameters*. Springer, 1993, pp. 269–286.

[14] I. Berre, W. Boon, B. Flemisch, A. Fumagalli, D. Gläser, E. Keilegavlen, A. Scotti, I. Stefansson, and A. Tatomir. "Call for participation: Verification benchmarks for single-phase flow in three-dimensional fractured porous media". In: *arXiv preprint arXiv:1809.06926* (2018).

[15] I. Berre, F. Doster, and E. Keilegavlen. "Flow in fractured porous media: A review of conceptual models and discretization approaches". In: *Transport in Porous Media* (2018), pp. 1–22.

[16] Z. Bieniawski. "Stability concept of brittle fracture propagation in rock". In: *Engineering Geology* 2.3 (1967), pp. 149–162.

[17] L. Bilke, B. Flemisch, T. Kalbacher, O. Kolditz, R. Helmig, and T. Nagel. "Development of open-source porous media simulators: principles and experiences". In: *Transport in Porous Media* 130.1 (2019), pp. 337–361.

[18] M. A. Biot. "General theory of three-dimensional consolidation". In: *Journal of applied physics* 12.2 (1941), pp. 155–164.

[19] D. Boffi, F. Brezzi, M. Fortin, et al. *Mixed finite element methods and applications*. Vol. 44. Springer, 2013.

[20] W. M. Boon, J. M. Nordbotten, and I. Yotov. "Robust discretization of flow in fractured porous media". In: *SIAM Journal on Numerical Analysis* 56.4 (2018), pp. 2203–2233.

[21] B. Bourdin, J.-J. Marigo, C. Maurini, and P. Sicsic. "Morphogenesis and propagation of complex cracks induced by thermal shocks". In: *Physical Review Letters* 112 (1 2014), p. 014301. doi: 10.1103/PhysRevLett.112.014301.

[22] J. Boussinesq. "Mémoire sur l'influence des frottements dans les mouvements réguliers des fluids". In: *Journal de mathématiques pures et appliquées* 13.2 (1868), pp. 377–424.

[23] K. Brenner, R. Masson, and E. Quenjel. "Vertex Approximate Gradient Discretization preserving positivity for two-phase Darcy flows in heterogeneous porous media". In: *Journal of Computational Physics* 409 (2020), p. 109357.

[24] A. Budisa and X. Hu. "Block Preconditioners for Mixed-dimensional Discretization of Flow in Fractured Porous Media". In: *arXiv e-prints*, 1905.13513 (2019), p. 1905.13513.

[25] S. Chan, I. Tuba, and W. Wilson. "On the finite element method in linear fracture mechanics". In: *Engineering Fracture Mechanics* 2.1 (1970), pp. 1–17. doi: 10.1016/0013-7944(70)90026-3.

[26] H. Chen, A. Salama, and S. Sun. "Adaptive mixed finite element methods for Darcy flow in fractured porous media". In: *Water Resources Research* 52.10 (2016), pp. 7851–7868. doi: 10.1002/2015WR018450.

[27] A. H.-D. Cheng. *Poroelasticity*. Vol. 27. Springer, 2016.

[28] G. P. Cherepanov. "Crack propagation in a continuum". In: *Prikl. Mat. Mekh.; (USSR)* 31.3 (1967).

[29] T. Cladouhos, S. Petty, G. Foulger, B. Julian, and M. Fehler. "Injection induced seismicity and geothermal energy". In: *GRC Transactions* 34 (2010), pp. 1213–1220.

[30] O. Coussy. *Poromechanics*. John Wiley & Sons, 2004.

[31] P. D'Antuono and M. Morandini. "Thermal shock response via weakly coupled peridynamic thermo-mechanics". In: *International Journal of Solids and Structures* 129 (2017), pp. 74–89. doi: 10.1016/j.ijsolstr.2017.09.010.

[32] D´Angelo, Carlo and Scotti, Anna. "A mixed finite element method for Darcy flow in fractured porous media with non-matching grids". In: *ESAIM: M2AN* 46.2 (2012), pp. 465–489. doi: 10.1051/m2an/2011148.

[33] P. Dietrich, R. Helmig, H. Hötzl, M. Sauter, J. Köngeter, and G. Teutsch. *Flow and transport in fractured porous media*. Springer Science & Business Media, 2005.

[34] M. Duflot. "The extended finite element method in thermoelastic fracture mechanics". In: *International Journal for Numerical Methods in Engineering* 74.5 (2008), pp. 827–847. doi: 10.1002/nme.2197.

[35] M. G. Edwards and C. F. Rogers. "Finite volume discretization with imposed flux continuity for the general tensor pressure equation". In: *Computational geosciences* 2.4 (1998), pp. 259–290.

[36] K. F. Evans, A. Zappone, T. Kraft, N. Deichmann, and F. Moia. "A survey of the induced seismic responses to fluid injection in geothermal and CO2 reservoirs in Europe". In: *Geothermics* 41 (2012), pp. 30–54. doi: 10.1016/j.geothermics.2011.08.002.

[37] M. Fortin and F. Brezzi. *Mixed and hybrid finite element methods*. New York: Springer-Verlag, 1991.

[38] G. A. Francfort and J.-J. Marigo. "Revisiting brittle fracture as an energy minimization problem". In: *Journal of the Mechanics and Physics of Solids* 46.8 (1998), pp. 1319–1342.

[39] N. Frih, V. Martin, J. E. Roberts, and A. Saâda. "Modeling fractures as interfaces with nonmatching grids". In: *Computational Geosciences* 16.4 (2012), pp. 1043–1060.

[40] N. Frih, J. E. Roberts, and A. Saada. "Modeling fractures as interfaces: a model for Forchheimer fractures". In: *Computational Geosciences* 12.1 (2008), pp. 91–104.

[41] A. Fumagalli and A. Scotti. "A Reduced Model for Flow and Transport in Fractured Porous Media with Non-matching Grids". In: *Numerical Mathematics and Advanced Applications 2011*. Ed. by A. Cangiani, R. L. Davidchack, E. Georgoulis, A. N. Gorban, J. Levesley, and M. V. Tretyakov. Berlin, Heidelberg: Springer Berlin Heidelberg, 2013, pp. 499–507.

[42] E. Gallyamov, T. Garipov, D. Voskov, and P. Van den Hoek. "Discrete fracture model for simulating waterflooding processes under fracturing conditions". In: *International Journal for Numerical and Analytical Methods in Geomechanics* 42.13 (2018), pp. 1445–1470.

[43] T. Garipov and M. Hui. "Discrete Fracture Modeling approach for simulating coupled thermo-hydro-mechanical effects in fractured reservoirs". In: *International Journal of Rock Mechanics and Mining Sciences* 122 (2019), p. 104075. doi: 10.1016/j.ijrmms.2019.104075.

[44] T. Garipov, M. Karimi-Fard, and H. Tchelepi. "Discrete fracture model for coupled flow and geomechanics". In: *Computational Geosciences* 20.1 (2016), pp. 149–160.

[45] D. Gaston, C. Newman, G. Hansen, and D. Lebrun-Grandie. "MOOSE: A parallel computational framework for coupled systems of nonlinear equations". In: *Nuclear Engineering and Design* 239.10 (2009), pp. 1768–1778.

[46] A. Ghassemi and X. Zhou. "A three-dimensional thermo-poroelastic model for fracture response to injection/extraction in enhanced geothermal systems". In: *Geothermics* 40.1 (2011), pp. 39–49.

[47] D. Gläser. "Discrete fracture modeling of multi-phase flow and deformation in fractured poroelastic media". PhD thesis. DOI: 10.18419/opus-11040: University of Stuttgart, 2020.

[48] D. Gläser, B. Flemisch, R. Helmig, and H. Class. "A hybrid-dimensional discrete fracture model for non-isothermal two-phase flow in fractured porous media". In: *GEM-International Journal on Geomathematics* 10.1 (2019), p. 5.

[49] A. A. Griffith. "VI. The phenomena of rupture and flow in solids". In: *Philosophical transactions of the Royal Society of London. Series A, containing papers of a mathematical or physical character* 221.582-593 (1921), pp. 163–198.

[50] S. E. Hamdi, R. M. Pitti, and F. Dubois. "Temperature variation effect on crack growth in orthotropic medium: Finite element formulation for the viscoelastic behavior in thermal cracked wood-based materials". In: *International Journal of Solids and Structures* 115-116 (2017), pp. 1–13. doi: https://doi.org/10.1016/j.ijsolstr.2016.09.019.

[51] S. Hüeber. "Discretization techniques and efficient algorithms for contact problems". PhD thesis. DOI: 10.18419/opus-4837: University of Stuttgart, 2008.

[52] S. Hüeber, G. Stadler, and B. I. Wohlmuth. "A primal-dual active set algorithm for three-dimensional contact problems with Coulomb friction". In: *SIAM Journal on Scientific Computing* 30.2 (2008), pp. 572–596.

[53] E. Huenges. "Enhanced geothermal systems: Review and status of research and development". In: *Geothermal Power Generation*. Elsevier, 2016, pp. 743–761.

[54] J. C. Jaeger, N. G. Cook, and R. Zimmerman. *Fundamentals of rock mechanics*. John Wiley & Sons, 2009.

[55] J. Jaffré, M. Mnejja, and J. Roberts. "A discrete fracture model for two-phase flow with matrix-fracture interaction". In: *Procedia Computer Science* 4 (2011). Proceedings of the International Conference on Computational Science, ICCS 2011, pp. 967–973. doi: 10.1016/j.procs.2011.04.102.

[56] B. Jha and R. Juanes. "Coupled multiphase flow and poromechanics: A computational model of pore pressure effects on fault slip and earthquake triggering". In: *Water Resources Research* 50.5 (2014), pp. 3776–3808.

[57] J. Jiang and R. M. Younis. "Numerical study of complex fracture geometries for unconventional gas reservoirs using a discrete fracture-matrix model". In: *Journal of Natural Gas Science and Engineering* 26 (2015), pp. 1174–1186. doi: 10.1016/j.jngse.2015.08.013.

[58] T. Kadeethum, H. Nick, S. Lee, and F. Ballarin. "Flow in porous media with low dimensional fractures by employing enriched Galerkin method". In: *Advances in Water Resources* 142 (2020), p. 103620.

[59] M. Karimi-Fard, L. J. Durlofsky, and K. Aziz. "An Efficient Discrete-Fracture Model Applicable for General-Purpose Reservoir Simulators". In: *SPE Journal* 9.2 (2003), pp. 227–236.

[60] A. Karrech, O. Beltaief, R. Vincec, T. Poulet, and K. Regenauer-Lieb. "Coupling of thermal-hydraulic-mechanical processes for geothermal reservoir modelling". In: *Journal of Earth Science* 26.1 (2015), pp. 47–52.

[61] L. Király. "Large scale 3-D groundwater flow modelling in highly heterogeneous geologic medium". In: *Groundwater flow and quality modelling*. Springer, 1988, pp. 761–775.

[62] L. Király. "Remarques sur la simulation des failles et du réseau karstique par éléments finis dans les modèles d'écoulement". In: *Bulletin du Centre d'hydrogéologie* 3 (1979), pp. 155–167.

[63] T. Koch et al. "DuMu^x 3 – an open-source simulator for solving flow and transport problems in porous media with a focus on model coupling". In: *Computers & Mathematics with Applications* (2020). doi: 10.1016/j.camwa.2020.02.012.

[64] O. Kolditz et al. "OpenGeoSys: an open-source initiative for numerical simulation of thermo-hydro-mechanical/chemical (THM/C) processes in porous media". In: *Environmental Earth Sciences* 67.2 (2012), pp. 589–599.

[65] M. Köppel, V. Martin, and J. E. Roberts. "A stabilized Lagrange multiplier finite-element method for flow in porous media with fractures". In: *GEM - International Journal on Geomathematics* 10.1 (2019), p. 7. doi: 10.1007/s13137-019-0117-7.

[66] L. Li, S. H. Lee, et al. "Efficient field-scale simulation of black oil in a naturally fractured reservoir through discrete fracture networks and homogenized media". In: *SPE Reservoir Evaluation & Engineering* 11.04 (2008), pp. 750–758.

[67] S. Li, A. Firoozabadi, and D. Zhang. "Hydromechanical Modeling of Nonplanar Three-Dimensional Fracture Propagation Using an Iteratively Coupled Approach". In: *Journal of Geophysical Research: Solid Earth* 125.8 (2020). e2020JB020115 2020JB020115, e2020JB020115. doi: https://doi.org/10.1029/2020JB020115.

[68] K.-A. Lie. *An introduction to reservoir simulation using MATLAB/GNU Octave: User guide for the MATLAB Reservoir Simulation Toolbox (MRST)*. Cambridge University Press, 2019.

[69] X. Lin and R. Smith. "Finite element modelling of fatigue crack growth of surface cracked plates: Part I: The numerical technique". In: *Engineering Fracture Mechanics* 63.5 (1999), pp. 503–522.

[70] C. Lister. "On the penetration of water into hot rock". In: *Geophys J Int* 39.3 (1974), pp. 465–509.

[71] V. Martin, J. Jaffré, and J. E. Roberts. "Modeling Fractures and Barriers as Interfaces for Flow in Porous Media". In: *SIAM J. Sci. Comput.* 26.5 (2005), pp. 1667–1691. doi: 10.1137/S1064827503429363.

[72] C. Miehe, M. Hofacker, L.-M. Schänzel, and F. Aldakheel. "Phase field modeling of fracture in multi-physics problems. Part II. Coupled brittle-to-ductile failure criteria and crack propagation in thermo-elastic–plastic solids". In: *Computer Methods in Applied Mechanics and Engineering* 294 (2015), pp. 486–522.

[73] A. Mikelić, M. F. Wheeler, and T. Wick. "Phase-field modeling of a fluid-driven fracture in a poroelastic medium". In: *Computational Geosciences* 19.6 (2015), pp. 1171–1195.

[74] S. E. Minkoff, C. M. Stone, S. Bryant, M. Peszynska, and M. F. Wheeler. "Coupled fluid flow and geomechanical deformation modeling". In: *Journal of Petroleum Science and Engineering* 38.1-2 (2003), pp. 37–56.

[75] M. A. Murad and A. F. Loula. "On stability and convergence of finite element approximations of Biot's consolidation problem". In: *International Journal for Numerical Methods in Engineering* 37.4 (1994), pp. 645–667.

[76] M. Nejati, A. Paluszny, and R. W. Zimmerman. "On the use of quarter-point tetrahedral finite elements in linear elastic fracture mechanics". In: *Engineering Fracture Mechanics* 144 (2015), pp. 194–221. doi: 10.1016/j.engfracmech.2015.06.055.

[77] J. Nordbotten. "Stable Cell-Centered Finite Volume Discretization for Biot Equations". In: *SIAM Journal on Numerical Analysis* 54 (2016), pp. 942–968. doi: 10.1137/15M1014280.

[78] J. M. Nordbotten. "Cell-centered finite volume discretizations for deformable porous media". In: *International Journal for Numerical Methods in Engineering* 100.6 (2014), pp. 399–418. doi: 10.1002/nme.4734.

[79] J. M. Nordbotten, W. M. Boon, A. Fumagalli, and E. Keilegavlen. "Unified approach to discretization of flow in fractured porous media". In: *Computational Geosciences* 23.2 (2019), pp. 225–237.

[80] J. Nordbotten and E. Keilegavlen. "An Introduction to Multi-Point Flux (MPFA) and Stress (MPSA) Finite Volume Methods for Thermo-Poroelasticity". In: *arXiv preprint arXiv:2001.01990* (2020).

[81] A. Paluszny and R. W. Zimmerman. "Numerical simulation of multiple 3D fracture propagation using arbitrary meshes". In: *Computer Methods in Applied Mechanics and Engineering* 200.9-12 (2011), pp. 953–966.

[82] S. Pandey, A. Chaudhuri, and S. Kelkar. "A coupled thermo-hydro-mechanical modeling of fracture aperture alteration and reservoir deformation during heat extraction from a geothermal reservoir". In: *Geothermics* 65 (2017), pp. 17–31.

[83] S. Pandey, V. Vishal, and A. Chaudhuri. "Geothermal reservoir modeling in a coupled thermo-hydro-mechanical-chemical approach: A review". In: *Earth-Science Reviews* 185 (2018), pp. 1157–1169.

[84] M. Rahman, M. Hossain, and S. Rahman. "A shear-dilation-based model for evaluation of hydraulically stimulated naturally fractured reservoirs". In: *International Journal for Numerical and Analytical Methods in Geomechanics* 26.5 (2002), pp. 469–497.

[85] A. F. Rasmussen et al. "The Open Porous Media Flow Reservoir Simulator". In: *Computers & Mathematics with Applications* (2020).

[86] V. Reichenberger, H. Jakobs, P. Bastian, and R. Helmig. "A mixed-dimensional finite volume method for two-phase flow in fractured porous media". In: *Advances in Water Resources* 29.7 (2006), pp. 1020–1036.

[87] H. A. Richard, M. Fulland, and M. Sander. "Theoretical crack path prediction". In: *Fatigue* 28.1-2 (2005), pp. 3–12. doi: 10.1111/j.1460-2695.2004.00855.x.

[88] J. Rutqvist, Y.-S. Wu, C.-F. Tsang, and G. Bodvarsson. "A modeling approach for analysis of coupled multiphase fluid flow, heat transfer, and deformation in fractured porous rock". In: *International Journal of Rock Mechanics and Mining Sciences* 39.4 (2002), pp. 429–442.

[89] S. Salimzadeh, R. A. Paluszny, and R. Zimmerman. "Effect of cold CO2 injection on fracture apertures and growth". In: *International Journal of Greenhouse Gas Control* 74 (2018), pp. 130–141. doi: 10.1016/j.ijggc.2018.04.013.

[90] S. Salimzadeh, A. Paluszny, H. M. Nick, and R. W. Zimmerman. "A three-dimensional coupled thermo-hydro-mechanical model for deformable fractured geothermal systems". In: *Geothermics* 71 (2018), pp. 212–224. doi: 10.1016/j.geothermics.2017.09.012.

[91] T. H. Sandve, I. Berre, and J. M. Nordbotten. "An efficient multi-point flux approximation method for Discrete Fracture-Matrix simulations". In: *Journal of Computational Physics* 231.9 (2012), pp. 3784–3800. doi: 10.1016/j.jcp.2012.01.023.

[92] P. Schädle, P. Zulian, D. Vogler, S. R. Bhopalam, M. G. Nestola, A. Ebigbo, R. Krause, and M. O. Saar. "3D non-conforming mesh model for flow in fractured porous media using Lagrange multipliers". In: *Computers & Geosciences* 132 (2019), pp. 42–55. doi: 10.1016/j.cageo.2019.06.014.

[93] A. Sedmak. "Computational fracture mechanics: An overview from early efforts to recent achievements". In: *Fatigue & Fracture of Engineering Materials & Structures* 41.12 (2018), pp. 2438–2474.

[94] S. Silling. "Reformulation of elasticity theory for discontinuities and long-range forces". In: *Journal of the Mechanics and Physics of Solids* 48.1 (2000), pp. 175–209. doi: 10.1016/S0022-5096(99)00029-0.

[95] N. Sukumar, N. Moës, B. Moran, and T. Belytschko. "Extended finite element method for three-dimensional crack modelling". In: *International Journal for Numerical Methods in Engineering* 48.11 (2000), pp. 1549–1570. doi: 10.1002/1097-0207(20000820)48:11<1549::AID-NME955>3.0.CO;2-A.

[96] J. Taron, D. Elsworth, and K.-B. Min. "Numerical simulation of thermal-hydrologic-mechanical-chemical processes in deformable, fractured porous media". In: *International Journal of Rock Mechanics and Mining Sciences* 46.5 (2009), pp. 842–854.

[97] R. N. Thomas, A. Paluszny, and R. W. Zimmerman. "Growth of three-dimensional fractures, arrays, and networks in brittle rocks under tension and compression". In: *Computers and Geotechnics* 121 (2020), p. 103447. doi: 10.1016/j.compgeo.2020.103447.

[98] E. Ucar, I. Berre, and E. Keilegavlen. "Postinjection normal closure of fractures as a mechanism for induced seismicity". In: *Geophysical Research Letters* 44.19 (2017), pp. 9598–9606.

[99] E. Ucar, E. Keilegavlen, I. Berre, and J. M. Nordbotten. "A finite-volume discretization for deformation of fractured media". In: *Computational Geosciences* 22.4 (2018), pp. 993–1007.

[100] L. B. da Veiga, F. Brezzi, L. D. Marini, and A. Russo. "Mixed virtual element methods for general second order elliptic problems on polygonal meshes". In: *ESAIM: Mathematical Modelling and Numerical Analysis* 50.3 (2016), pp. 727–747.

[101] L. B. da Veiga, K. Lipnikov, and G. Manzini. *The mimetic finite difference method for elliptic problems*. Vol. 11. Springer, 2014.

[102] P. Vermeer and A. Verruijt. "An accuracy condition for consolidation by finite elements". In: *International Journal for numerical and analytical methods in geomechanics* 5.1 (1981), pp. 1–14.

[103] K. M. Walton, A. J. A. Unger, M. A. Ioannidis, and B. L. Parker. "Benchmarking NAPL Redirection and Matrix Entry at Fracture Intersections Below the Water Table". In: *Water Resources Research* 55.4 (2019), pp. 2672–2689. doi: 10.1029/2018WR023435.

[104] B. Wohlmuth. "Variationally consistent discretization schemes and numerical algorithms for contact problems". In: *Acta Numerica* 20 (2011), pp. 569–734. doi: 10.1017/S0962492911000079.

[105] W. Zhang, M. Al Kobaisi, et al. "Nonlinear Finite Volume Method for 3D Discrete Fracture-Matrix Simulations". In: *SPE Journal* (2020).

[106] O. C. Zienkiewicz, R. L. Taylor, and J. Z. Zhu. *The finite element method: its basis and fundamentals*. Elsevier, 2005.

[107] P. Zulian, P. Schädle, L. Karagyaur, and M. Nestola. "Comparison and Application of non-Conforming Mesh Models for Flow in Fractured Porous Media using dual Lagrange multipliers". In: *arXiv preprint arXiv:2008.06360* (2020).

Part II

Scientific results

Paper A

Finite-Volume Discretisations for Flow in Fractured Porous Media

Ivar Stefansson, Inga Berre, Eirik Keilegavlen

Transport in Porous Media
DOI: 10.1007/s11242-018-1077-3

B

Paper B

Benchmarks for single-phase flow in fractured porous media

Bernd Flemisch, Inga Berre, Wietse Boon, Alessio Fumagalli, Nicolas Schwenck, Anna Scotti, Ivar Stefansson, Alexandru Tatomir

Advances in Water Resources
DOI: 10.1016/j.advwatres.2017.10.036

Advances in Water Resources 111 (2018) 239–258

Contents lists available at ScienceDirect

Advances in Water Resources

journal homepage: www.elsevier.com/locate/advwatres

Benchmarks for single-phase flow in fractured porous media

Bernd Flemisch[*,a], Inga Berre[b], Wietse Boon[b], Alessio Fumagalli[b], Nicolas Schwenck[a], Anna Scotti[c], Ivar Stefansson[b], Alexandru Tatomir[d]

[a] Department of Hydromechanics and Modelling of Hydrosystems, University of Stuttgart, Pfaffenwaldring 61, Stuttgart 70569, Germany
[b] Department of Mathematics, University of Bergen, Allégaten 41, Bergen 5007, Norway
[c] Laboratory for Modeling and Scientific Computing MOX, Politecnico di Milano, p.za Leonardo da Vinci 32, Milano 20133, Italy
[d] Department of Applied Geology, Geosciences Center, University of Göttingen, Goldschmidtstrasse 3, Göttingen 37077, Germany

ARTICLE INFO

Keywords:
Fractured porous media
Discretization methods
Benchmark

ABSTRACT

This paper presents several test cases intended to be benchmarks for numerical schemes for single-phase fluid flow in fractured porous media. A number of solution strategies are compared, including a vertex and two cell-centred finite volume methods, a non-conforming embedded discrete fracture model, a primal and a dual extended finite element formulation, and a mortar discrete fracture model. The proposed benchmarks test the schemes by increasing the difficulties in terms of network geometry, e.g. intersecting fractures, and physical parameters, e.g. low and high fracture-matrix permeability ratio as well as heterogeneous fracture permeabilities. For each problem, the results presented are the number of unknowns, the approximation errors in the porous matrix and in the fractures with respect to a reference solution, and the sparsity and condition number of the discretized linear system. All data and meshes used in this study are publicly available for further comparisons.

1. Introduction

In porous-media flow applications, the domains of interest often contain geometrically anisotropic inclusions and strongly discontinuous material coefficients that can span several orders of magnitude. If the size of these heterogeneities is small in normal direction compared to the tangential directions, these features are called fractures. Fractures can act both as conduits and barriers and affect flow patterns severely. Target applications concerning fractured porous-media systems in earth sciences include groundwater resource management, renewable energy storage, recovery of petroleum resources, radioactive waste reposition, coal bed methane migration in mines, and geothermal energy production.

The analysis and prediction of flow in fractured porous media systems are important for all the aforementioned applications. Many different conceptual and numerical models of flow in fractured porous-media systems can be found in the literature. Even though fractured porous-media systems have been of interest to modelers for a long time, they still present challenges for simulators. During the last 70 years, different modeling approaches have been developed and gradually improved. Comprehensive reviews can be found in Berkowitz (2002), Dietrich et al. (2005), Hoteit and Firoozabadi (2008), Neumann (2005), Sahimi (2011) and Singhal and Gupta (2010). Roughly, the fractured porous media systems are classified in two broad categories: discrete fracture-matrix (DFM) models and continuum fracture models. Within this paper, we will only consider DFM models.

The DFM models consider flow occurring in both the fracture network and the surrounding rock matrix. They account explicitly for the effects of individual fractures on the fluid flow. An efficient way to represent fractures in DFMs is the hybrid-dimensional approach, see e.g. Helmig (1997), Flauraud et al. (2003), Bogdanov et al. (2003), Firoozabadi and Monteagudo (2004), Karimi-Fard et al. (2004), Martin et al. (2005) and Reichenberger et al. (2006). Fractures in the geometrical domain are then discretized with elements of co-dimension one with respect to the dimension of the surrounding matrix, such as one-dimensional elements in two-dimensional settings. Due to the similarities in these models, the gradient scheme framework (Brenner et al., 2016; 2017) allows for a unified analysis of a number of DFM models. The aforementioned classical DFM approaches all rely on matching fracture and matrix grids in the sense that a fracture element coincides geometrically with co-dimension-one mesh entities, i.e. faces of matrix grid elements. In addition to the classical models, several so-called non-conforming DFM models have been developed in recent years, such as EDFM (Hajibeygi et al., 2011; Moinfar et al., 2014), XFEM-based approaches (D'Angelo and Scotti, 2012; Huang et al., 2011; Schwenck et al., 2015), or mortar-type methods (Frih et al., 2012).

* Corresponding author.
E-mail address: bernd.flemisch@iws.uni-stuttgart.de (B. Flemisch).

https://doi.org/10.1016/j.advwatres.2017.10.036
Received 5 January 2017; Received in revised form 27 October 2017; Accepted 30 October 2017
Available online 31 October 2017
0309-1708/

Benchmarking represents a methodology for verifying, testing and comparing the modeling tools. Various codes have been developed by academic institutions or companies based on different conceptual, mathematical, and numerical models. Even though benchmarking studies are increasing in all fields of engineering and workshops have been organized around specific problems (e.g. Class et al., 2009), there are still only a limited number of studies. Some are related to a specific application and are flexible as to how the problem is modeled in terms of assumptions regarding the physics and the selection of the domain, see Class et al. (2009), Nordbotten et al. (2012), Caers (2013) and Kolditz et al. (2015). Others De Dreuzy et al. (2013) and Caers (2013), like ours, focus on the comparison of numerical schemes.

One of the common requirements when selecting the test problems for comparing numerical schemes is that they allow the examination of the capabilities of each of the compared methods. Therefore, our benchmark study proposes a set of problems starting from simple geometries and then gradually increasing the geometrical complexity. The test problems are specifically selected to make clear distinctions between the different methods. They consist of existing and new computational benchmarks for fluid flow in fractured porous media and allow for comparison of several DFM-based numerical schemes in a systematic way.

We would like to invite the scientific community to follow up on this study and evaluate further methods by means of the proposed benchmarks. In order to facilitate this, the paper is accompanied by grid and result files in the form of a Git repository at https://git.iws.uni-stuttgart.de/benchmarks/fracture-flow.

The remainder of this paper is organized as follows. In Section 2, we formulate the model problem in terms of the partial differential equation to be solved. The participating DFM models are described in Section 3. The central Section 4 proposes the benchmarks and compares the results of the different methods. Finally, Section 5 concludes with a summary and outlook.

2. The model problem

We consider an incompressible single-phase flow through a porous medium, assumed to be described by Darcy's law, resulting in the governing system of equations

$$\mathbf{u} = -\mathbb{K}\,\mathbf{grad}\,p, \tag{1a}$$

$$div\,\mathbf{u} = q, \tag{1b}$$

in an open bounded domain $\mathscr{D} \subset \mathbb{R}^N$, subject to boundary conditions

$$p = p_D \quad \text{on } \partial\mathscr{D}_D, \tag{1c}$$

$$\mathbf{u}\cdot\mathbf{n} = q_N \quad \text{on } \partial\mathscr{D}_N, \tag{1d}$$

with $\partial\mathscr{D} = \overline{\partial\mathscr{D}_D \cup \partial\mathscr{D}_N}$ and $\partial\mathscr{D}_D \cap \partial\mathscr{D}_N = \emptyset$. In Eq. (1) $\mathbf{u}$ denotes the macroscopic fluid velocity whereas $\mathbb{K}$ and p stand for absolute permeability and pressure.

Let us assume that $\mathscr{D}$ contains several fractures, that all together constitute a single domain Γ of spatial dimension N such that $\Gamma \subset \mathscr{D}$, which is a possibly unconnected, open subset of $\mathscr{D}$. The surrounding porous rock, namely, the remaining part of $\mathscr{D}$, is called $\Omega = \mathscr{D}\backslash\bar{\Gamma}$. Assuming that the fracture aperture ε at each point of Γ is small compared to other characteristic dimensions of the fractures, the full-dimensional domain Γ can be reduced to the $(N-1)$-dimensional fracture network γ. This reduction involves modeling choices resulting in different hybrid-dimensional problem formulations that form the basis for the methods presented in the following section.

3. Participating discretization methods

Within this section, the discretization methods participating in this benchmark study are described. The purpose of this article is the comparison of well-known, established and/or at least published methods. Therefore, only the most significant aspects of each method are summarized. We do not show a comparison against analytical solutions here. The analysis of the methods and theoretical results such as proofs of optimal convergence can be found in the corresponding references. A summary of all participating methods is provided in Table 1. In the sequel, we will denote with *d.o.f.* the degrees of freedom associated to a specific method. We indicate also the type of conformity required to the computational grid with respect to the fractures and the assumption that the pressure is considered continuous across the fractures. With the exception of P-XFEM, all considered methods are locally conservative by construction.

Table 1
Participating discretization methods.

Method	d.o.f.	frac-dim	conforming	*p*-cont
Box	p (vert)	dim-1	yes	yes
TPFA	p (elem)	dim-1	yes	no
MPFA	p (elem)	dim-1	yes	no
EDFM	p (elem)	dim-1	no	yes
Flux-Mortar	p (elem), $\boldsymbol{u}$ (faces)	dim-1	geometrically	no
P-XFEM	p (vert)	dim-1	no	no
D-XFEM	p (elem), $\boldsymbol{u}$ (faces)	dim-1	no	no
MFD	p (faces)	dim	geometrically	no

The lower-dimensional representation of fractures allows for easier mesh generation for both conforming and non-conforming methods in comparison to the equi-dimensional approach, as it circumvents the appearance of very small elements when discretizing the interior of the fracture (i.e., within the fracture width). Conform meshing implies that the fractures are discretized with a set of line elements (in a 2D domain) that are also the edges of the triangular finite elements.

3.1. Vertex-centred, continuous-pressure, conforming lower-dimensional DFM (Box)

The Box method is a vertex-centred finite-volume method proposed in e.g. Helmig (1997) which combines the advantages of finite element and finite volume grids, allowing unstructured grids and guaranteeing a locally conservative scheme (Reichenberger et al., 2006). Fig. 1 illustrates a two-dimensional representation of the dual-grid with two finite elements E_1 and E_5 sharing the same edge (ij_1) that represents a lower-dimensional fracture with the aperture ε_{ij_1}. The main characteristic in terms of the fractured system is that the pressure is required to be continuous, in particular in those vertices whose control volumes overlap both fracture and matrix regions.

The Box method used for this paper is implemented in the open-source numerical simulator DuMu^x. A detailed description of the conceptual, mathematical and numerical model and code implementation is published in Tatomir (2012). The simulation code used for the benchmark studies is publicly available under https://git.iws.uni-stuttgart.de/dumux-pub/Flemisch2016a.git.

3.2. Cell-centred, discontinuous-pressure, conforming DFM (TPFA)

The control volume finite difference method uses a two-point flux approximation (TPFA) based on the cell-centre pressure values for the evaluation of the face fluxes. The method is a widely applied and standard method for simulation of flow in porous media. The domain is partitioned with fractures coinciding with the interior faces between matrix cells just as described at the beginning of Section 3. The flux over the face between matrix cells i and j is approximated by

$$\mathbf{u}_{ij} = T_{ij}(p_i - p_j), \tag{2}$$

where p_i and p_j are the pressures in the neighbouring cells and T_{ij} is the face transmissibility, computed as the harmonic average of the two half

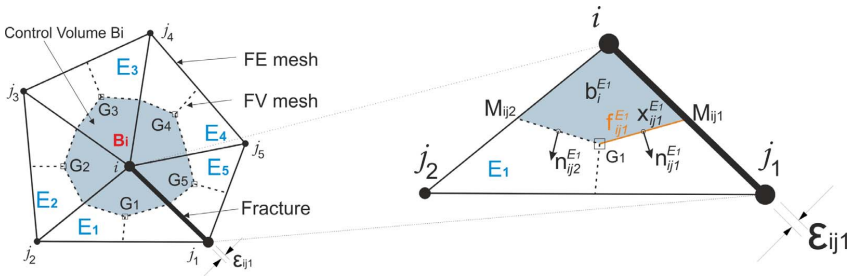

Fig. 1. Conceptual representation of the Box method: (left-hand side) The dual finite element and finite volume mesh from which the control volume B_i around node i is created. Node i is surrounded by nodes $\{j_1, j_2, j_3, j_4, j_5\}$, where segment ij_1 represents both a fracture and a shared FE edge; (right-hand side) Sub-control volume (SCV) $b_i^{E_1}$ in element E_1 has barycentre G_1 and the mid-points of the edges ij_1 and ij_2 are M_{ij1}, respectively M_{ij2}. The SCV face $f_{ij1}^{E_1}$ is the segment $\overline{G_1 M_{ij1}}$ which contains the integration point $x_{ij1}^{E_1}$ where the normal vector $\mathbf{n}_{ij1}^{E_1}$ is applied.

transmissibilities corresponding to the face and the two cells. The half transmissibility of cell-face pair i is in turn given as

$$\alpha_i = \frac{A_i \mathbf{n}_i^\top \mathbb{K}_i}{\mathbf{d}_i^\top \mathbf{d}_i} \cdot \mathbf{d}_i, \tag{3}$$

where A_i and $\mathbf{n}_i$ are the area and unit normal vector of the face, $\mathbb{K}_i$ is the permeability assigned to the cell and $\mathbf{d}_i$ is the distance vector from cell centre to face centroid.

In addition to the unknowns given at the centroids of the matrix cells, unknowns are associated to the centroids of the fracture cells. The fracture cells are associated with apertures, which multiplied with the length give the volume of these cells. The aperture is also used to construct hybrid faces for the matrix-fracture interfaces. These faces, parallel to the fracture but displaced half an aperture to either side, enable us to compute the half transmissibilities between the fracture cell and the matrix cells on the two sides. These faces are indicated by the dashed blue lines in Fig. 2, where the computational domain is superimposed on the geometrical grid. The result is a hybrid grid with fractures which are lower dimensional in the grid, but equi-dimensional in the computational domain at the cost of a small matrix volume error corresponding to the overlap of the matrix cells with the fracture cells.

Following the method proposed by Karimi-Fard et al. (2004), the intermediate fracture intersection cell drawn with dashed red lines in Fig. 2 is removed, leading to direct coupling of the fracture cells neighbour to the intersection. The purpose of this is both to obtain a smaller condition number and to avoid severe time-step restrictions associated with small cells in transport simulations. To each new face between cell i and j, face transmissibilities are assigned, calculated using the star delta transformation as described in Karimi-Fard et al. (2004):

$$T_{ij} = \frac{\alpha_i \alpha_j}{\sum_{k=1}^{n} \alpha_k}, \tag{4}$$

with n denoting the number of fracture cells meeting at the intersection.

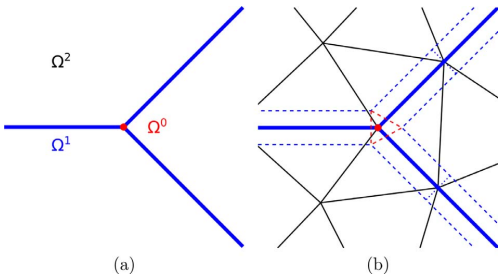

Fig. 2. (a) Conceptual decomposition of the domain according to element dimension with the matrix depicted in black, fractures in blue and their intersections in red. (b) The computational domain of the TPFA method. Dashed lines are faces of the fracture cells. (For interpretation of the references to colour in this figure legend, the reader is referred to the web version of this article.)

As this elimination disregards all information on the permeability of the intersection, it should be used with caution in cases of crossing fractures of different permeability. We encounter this feature in Section 4.3, and include results both with and without the elimination for one of the test cases presented in that section.

3.3. Cell-centred, discontinuous-pressure, conforming DFM (MPFA)

Inspired by the TPFA method presented above, a method based on the multi-point flux approximation has been developed (Sandve et al., 2012), see also e.g. Ahmed et al. (2015). The MPFA variant of the method reduces errors associated with the TPFA approach for grids that are not close to K-orthogonal, and avoids errors related to the splitting of the fluxes in the star-delta transformation. The method is constructed letting each face flux depend on the pressures of several of the neighbouring cells. Specifically, an interaction region defined by cell centroids and continuity points at the faces around each node is constructed (see Fig. 3) and the pressure is assumed to be linear within each cell of the region. Intermediate pressure unknowns are introduced at the continuity points and express the flux over each half face in terms of the weighted pressures of all cell centre and continuity point pressures of the region. Continuity of the flux over each face allows for elimination of the continuity point pressures and a relationship between flux and pressure of the form

$$\mathbf{u}_i = \mathbb{T}_i \mathbf{p} \tag{5}$$

for each half face i is obtained. Here, $\mathbf{p}$ denotes the pressures at the cell centres of the interaction region and $\mathbb{T}_i$ accounts for the effect of geometry and permeability of those same cells. For a detailed description of the method, see, e.g., Aavatsmark (2002).

The handling of the fractures is similar to the one described for the TPFA. For the fracture intersections, the pressure is assumed to be

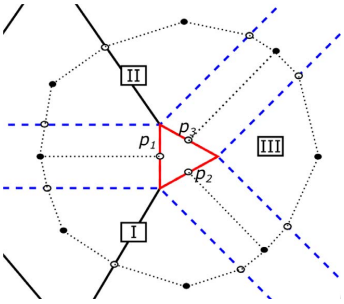

Fig. 3. The three interaction regions (dotted lines) around one fracture intersection for the MPFA consisting of four (I and II) and three (III) sub cells each. The continuity points are marked by circles and the cell centres by black dots. Fracture-matrix faces are depicted by blue dashed lines and the intermediate intersection cell in red. Figure adapted from Sandve et al. (2012). (For interpretation of the references to colour in this figure legend, the reader is referred to the web version of this article.)

constant within the intersection and continuous over the hybrid faces. After elimination of the intermediate pressures (p_1, p_2 and p_3 in Fig. 3), there are no unknowns directly associated to the intersection cells and these are removed from the computational grid. The Eq. (5) type equations are assembled for each cell and the resulting linear system solved for the cell centre pressures.

We refer to Sandve et al. (2012) for a thorough comparison of the TPFA and MPFA approaches. The implementations of both methods are available in the open-source Matlab Reservoir Simulation Toolbox, http://www.sintef.no/projectweb/mrst/ (Lie et al., 2012). An extension of control volume methods to non-matching grids across fractures may be found in Tunc et al. (2012).

3.4. Continuous-pressure, non-conforming embedded DFM (EDFM)

Recently, non-conforming methods for the treatment of lower-dimensional fractures have been developed, for example in Moinfar et al. (2011); 2014) and Hajibeygi et al. (2011), to avoid the time-consuming construction of complex matrix grids which explicitly represent the fractures. They are mostly used in the context of single and multi-phase flow simulations for petroleum engineering applications and require the normal fracture permeability to be orders of magnitude higher than the matrix permeability, as in the case of fractured petroleum reservoirs. In this field of applications corner-point grids are normally employed to describe the geological layers, e.g. different rock type, of the reservoir. An adaptation of such computational grids to the fractures could be unaffordable for real cases. The numerical method belongs to the family of two-point schemes, where a one-to-one connection between the degrees of freedom is considered through the transmissibility concept (Eymard et al., 2000). References on the embedded discrete fracture method (EDFM) can be found, for example, in Li and Lee (2008), Panfili et al. (2013), Moinfar et al. (2014), Panfili and Cominelli (2014), de Araujo Cavalcante Filho et al. (2015) and Fumagalli et al. (2016).

In practice, the mesh of the fractures is generated on top of the rock grid so that each rock cell cut by fractures contains exactly one fracture cell per fracture. Intersections between fractures are computed without affecting the creation of the grids of fractures and rock and used to compute approximate transmissibilities between different fracture cells. See Fig. 4 as an example. A degree of freedom that represents a pressure or a saturation value is assigned to each matrix cell and to each fracture cell. This means that transmissibilities between matrix and fracture cells, as well as those between different fracture cells, need to be computed. We compute the transmissibility between a fracture cell and a matrix cell T_{fm} and the half-transmissibility T_i between two intersecting fracture cells (related to the fracture i) through the following approximate expressions:

$$T_{fm} = A\frac{\mathbf{n}_f^T[\mathbf{K}\cdot\mathbf{n}_f}{d_{f,m}} \quad \text{and} \quad T_i = s\frac{k_i\varepsilon_i}{d_{i,s}}.$$

Here A is the measure of the fracture cell in the current rock cell, $\mathbf{n}_f$ is the normal of the fracture cell and $d_{f,m}$ is an average distance between the fracture cell and the matrix cell, see Li and Lee (2008). For the fracture-fracture transmissibility, s indicates the measure of the intersecting segment, k_i the scalar permeability of the fracture, ε_i the aperture and $d_{i,s}$ is the average distance between the fracture cell and the intersecting segment. The standard harmonic average is considered to compute the transmissibility between the two fracture cells. Standard formulae for fracture-fracture as well as matrix-matrix transmissibilities are computed by means of a two-point flux approximation. It is worth to notice that the recent extension of EDFM called Projection-based EDFM (pEDFM), proposed in Tene et al. (2017), is also able to handle low permeable fractures. Finally, even if the proposed benchmark cases are two-dimensional the method can be extended to three dimensions without any additional constraints.

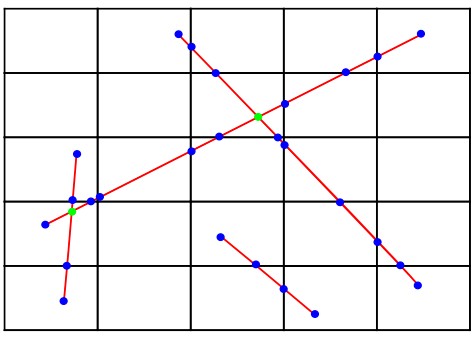

Fig. 4. Example of meshes, for both fractures and rock matrix, suited for EDFM. The rock matrix is considered as a background mesh. Each fracture cell is represented by two blue dots and the green dots are the non-matching intersection among fractures. (For interpretation of the references to colour in this figure legend, the reader is referred to the web version of this article.)

3.5. Cell-centred, discontinuous-pressure, geometrically-conforming mortar DFM (Flux-Mortar)

The key concept behind the Flux-Mortar, as described more thoroughly in Boon et al. (2016), is the idea that fractures can be considered as interfaces between different sub-domains. This has been explored previously by Martin et al. (2005) and Frih et al. (2012), among others. In this context, we consider the domain decomposition technique known as the mortar method to model flow through the fractured porous medium.

The mortar method is generally used to couple equations in different sub-domains by introducing a so-called mortar variable, defined on the interface. In case of modeling fracture flow, a well-explored choice of the mortar variable is the fracture pressure (Martin et al., 2005). The method considered here, however, uses the flux between matrix and fracture domains as the mortar variable, which leads to a stronger imposition of mass conservation. One of the main advantages of the close relationship to mortar methods is the capability to handle non-matching grids. In particular, two sub-domains bordering a fracture can be meshed independently on both sides, as illustrated in Fig. 5. The difficulty in mesh generation is then relieved significantly since only the geometry of the fractures needs to be respected.

By construction, the Flux-Mortar is applicable to problems in arbitrary dimensions. The governing equations in the matrix and the fractures (as well as fracture intersections in 3D) are identical and thus all fractures, intersections and tips are handled in a unified manner. Consequently, although only two-dimensional problems are considered in this study, the discretization scheme also applies to problems in three dimensions.

Due to a slightly different derivation of the reduced model, the scheme handles spatially varying apertures. Moreover, the apertures may be arbitrarily close, or even equal to zero which naturally eliminates the possibility of flow in the tangential direction.

With the use of mixed finite elements, mass is conserved locally in the matrix, fractures, and fracture intersections. The flux $\mathbf{u}$ in the matrix and fractures are modeled using the lowest-order Raviart–Thomas elements and linear Lagrange elements, respectively. The pressure p is then given by piecewise constants in the matrix, as well as the fractures and intersection points. Additionally, the mortar variable is given by piecewise constants on a separately generated, lower-dimensional, mortar grid on the matrix-fracture interface. This grid matches with the surrounding grids in case of matching grids and is coarser otherwise.

The resulting mixed finite element formulation is a saddle-point problem, which may be challenging to solve numerically. To relieve

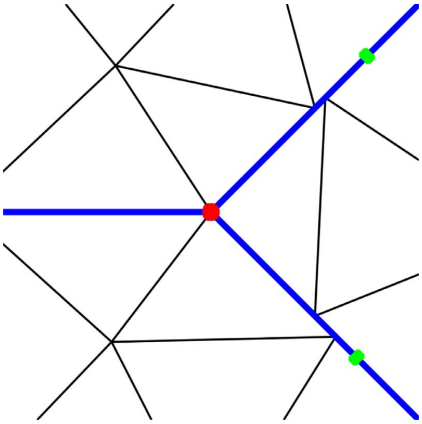

Fig. 5. The Flux-Mortar method allows for non-matching grids along fracture interfaces. Fracture and matrix flows are coupled using a mortar variable, defined on a coarser grid (green dots). (For interpretation of the references to colour in this figure legend, the reader is referred to the web version of this article.)

this, the flux variables may be eliminated through hybridization, which leads to a less computationally expensive scheme containing solely the cell-centre pressures.

Two implementations of the method have been developed, both of which are used in this benchmark study. The first version, implemented in MATLAB, is suited for simpler geometries in 2D, containing relatively few fractures, such as those considered in Benchmarks 1–3. The second version has been implemented for 3D problems and higher-order spaces on matching grids using the open-source finite element library FEniCS (Logg et al., 2012). This code is more efficient for complex cases such as Benchmark 4.

3.6. Discontinuous-pressure, non-conforming primal XFEM (P-XFEM)

The primal XFEM method participating in this benchmarking study is described in detail in Schwenck (2015), see also Flemisch et al. (2016) and Schwenck et al. (2015). The method is based on the hybrid-dimensional problem formulation investigated in Martin et al. (2005), where conditions for the coupling between fracture and matrix are derived:

$$\{\mathbf{u}_\mathrm{m}\cdot\mathbf{n}\}_\gamma = k_\mathrm{f,n}/\varepsilon[[p_\mathrm{m}]]_\gamma \tag{6a}$$

$$\xi_0[[\mathbf{u}_\mathrm{m}\cdot\mathbf{n}]]_\gamma = k_\mathrm{f,n}/\varepsilon\left(\{p_\mathrm{m}\}_\gamma - p_\mathrm{f}\right) \tag{6b}$$

Here, the subscripts “m” and “f” indicate matrix and fracture quantities, while $\{\{\cdot\}\}_\gamma$ and $[[\cdot]]_\gamma$ denote the average and the jump of a matrix quantity over the fracture γ, respectively.

The coupling conditions (6) can be used to define a source term for the fracture flow problem, while they yield an interface problem for the matrix domain. For the discretization of this interface problem, the methodology presented in Hansbo and Hansbo (2002) is used, which amounts to applying the eXtended Finite Element Method (XFEM). Together with an independent standard discretization of the lower-dimensional fracture problem, this yields a hybrid-dimensional, non-conforming primal XFEM-based method. The XFEM space is built enriching the standard Lagrangian $\mathbb{P}_1$ (or $\mathbb{Q}_1$ for quads) finite-element spaces, whose degrees of freedom are located at the vertices of the full-dimensional grid of the matrix Ω and the lower-dimensional grid of the fracture γ. A representative example of matrix and fracture grids is illustrated in Fig. 6. Unlike the EDFM method, see Fig. 4, the fracture grid

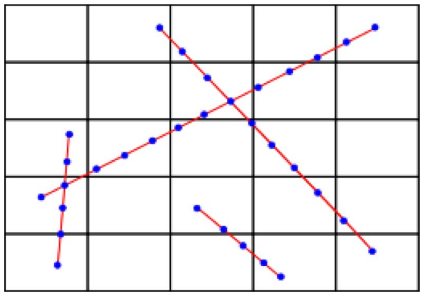

Fig. 6. Example of meshes, for both fractures and rock matrix, suited for P-XFEM. The fracture grid vertices are indicated by the blue dots. (For interpretation of the references to colour in this figure legend, the reader is referred to the web version of this article.)

vertices can be placed arbitrarily without taking into account the matrix grid. On the other hand, the method requires matching fracture branch grids in the form of vertices placed at the fracture intersections. In particular, special care has to be taken of intersecting and immersed fractures (Schwenck et al., 2015).

The method is implemented on top of the DUNE framework (Bastian et al., 2008) and the discretization module DUNe-PDELab (Bastian et al., 2010). For the enrichment of the finite-element spaces in the context of XFEM, the modules DUNe-Multidomain and DUNe-Multidomaingrid are employed (Müthing, 2015). The simulation code for the XFEM approach and for the benchmarks studied here is publicly available under https://git.iws.uni-stuttgart.de/dumux-pub/Flemisch2016a.git. Currently, the method is only implemented in 2D. Conceptually, no difficulties arise for extending it to 3D. However, the possibly multiple enrichment of the function spaces for matrix elements intersected by fracture elements can become a very tedious task for complex fracture networks.

3.7. Discontinuous-pressure, non-conforming dual XFEM (D-XFEM)

The dual XFEM method participating in his benchmark is based on D’Angelo and Scotti (2012). The method, originally derived for a domain cut by one fracture, was further developed in Formaggia et al. (2014) and Fumagalli and Scotti (2014) to account for intersecting fractures with different permeabilities. The same equations and coupling conditions as for the primal XFEM are used, but in a dual formulation where Darcy law and mass conservation give rise to a saddle-point problem for the fluid mean velocity and pressure, both in the fracture and in the surrounding medium. Moreover, unlike the previous method, this method employs triangular/tetrahedral grids. The usual lowest order $\mathbb{RT}_0 - \mathbb{P}_0$ pair for velocity and pressure is enriched following (Hansbo and Hansbo, 2002) in the elements of the porous medium cut by a fracture, or in the elements of a fracture at the intersection with other fractures. Indeed, triangular/tetrahedral grids are arbitrarily cut by triangulated lines/surfaces in 2D and 3D respectively. These surfaces can, in turn, intersect each other in a non-conforming way, as shown in Fig. 7.

In the current implementation of the method no special enrichment is added in the bulk elements containing the fracture tips. Instead, fractures are artificially extended up to the boundary of the domain, and in the extension we prescribe the same permeability of the surrounding porous medium to obtain a “virtual” fracture with no effects on the flow.

The method has been implemented on the basis of the Getfem++ library, http://download.gna.org/getfem/html/homepage/ , which provides support for the computation of the intersections and the quadrature on sub-elements thanks to an interface with QHull, http://www.qhull.org/.

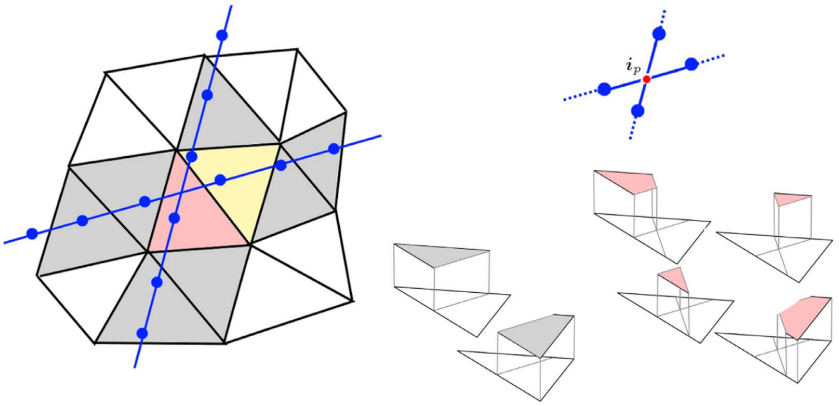

Fig. 7. A portion of the grid cut by two fractures: in the two dimensional case they can split the elements in two (grey), three (yellow), or four (red) independent parts, where the restrictions of the basis functions are defined. The fracture grids are irrespective of the bulk grid and of each other, i.e. the intersection point i_p is not a point of the grid. (For interpretation of the references to colour in this figure legend, the reader is referred to the web version of this article.)

3.8. Reference solutions calculated with mimetic finite differences (MFD)

The reference solutions are computed on very fine grids that discretize both matrix and fractures by full-dimensional triangular or quadrilateral elements. A mimetic finite difference method, see Brezzi et al. (2005) and Flemisch and Helmig (2008), is used to discretize problem (1). The method is employed as it is implemented in DuMu^{x} 2.7 (Flemisch et al., 2011). In particular, a mixed-hybrid approach is used to transform the discrete saddle point problem in terms of cell pressures and face fluxes into a symmetric positive definite formulation with face-pressure degrees of freedom.

4. Benchmark problems

This is the main section, which compares the methods described above by means of four benchmark cases. The first benchmark case, considered in Section 4.1, is based on Geiger et al. (2013) and shows a regular fracture network. Second, in Section 4.2, we present a well established benchmark for groundwater flow from Swedish Nuclear Power Inspectorate (SKI) (1987) that contains two crossing, highly permeable fractures and a non-straight top surface. After that, a small but complex fracture network exhibiting immersed fractures and intersections at different angles is investigated in Section 4.3. Finally, a case synthesized from a real application is considered in Section 4.4.

For each benchmark case, a description of the computational domain is provided, including boundary conditions, the geometrical information about the corresponding fracture network and the associated material parameters such as aperture and permeability. For some of the cases, the reference solution on the complete domain is visualized. This is followed by illustrations of the grids used by the participating methods. Since the methods pose different grid requirements, the grid could be chosen arbitrarily for each method, provided that the number of grid cells or vertices is roughly the same. If a reference solution is available (Benchmarks 1–3), the results of the different methods are compared by evaluating the errors with respect to the reference in the matrix domain as well as in the fracture network, indicated by err_m and err_f, respectively. The errors are calculated according to the formulas

$$err_m^2 = \frac{1}{|\Omega|(\Delta p_{ref})^2} \sum_{f=K_{f,m}\cap K_m} |f| \left(p_m|_{K_m} - p_{ref}|_{K_{ref,m}} \right)^2, \tag{7a}$$

$$err_f^2 = \frac{1}{|\gamma|(\Delta p_{ref})^2} \sum_{e=K_{f,f}\cap K_f} |e| \left(p_f|_{K_f} - p_{ref}|_{K_{ref,f}} \right)^2, \tag{7b}$$

where $|\Omega|$ and $|\gamma|$ indicate the size of the full-dimensional matrix and the lower-dimensional fracture domain, respectively, and $\Delta p_{ref} = \max_{\mathscr{D}} p_{ref} - \min_{\mathscr{D}} p_{ref}$. The sum is taken over all intersections of (full-dimensional) elements $K_{ref,\,m}$ and $K_{ref,\,f}$ of the grid employed for the reference solution with full-dimensional matrix elements K_m in case of err_m and lower-dimensional fracture elements K_f in case of err_f. The quantities $|f|$ and $|e|$ indicate the area of a full-dimensional intersection f and a lower-dimensional intersection e, respectively. We stress the fact that for the calculation of the matrix error err_m, only elements $K_{ref,\,m}$ in the matrix part of the equi-dimensional grid are considered. In other words, the full-dimensional fracture domain Γ is excluded from this calculation. In addition to errors in matrix and fracture, the densities and condition numbers of the resulting linear system matrices are provided. Moreover, a comparison is performed by means of plots along specific lines through the domain for some benchmark cases. Each case is concluded by a short discussion of the results.

4.1. Benchmark 1: regular fracture network

This test case is based on an article presenting a new dual continuum model, Geiger et al. (2013), with slightly modified boundary conditions and material properties. The computational domain including the fracture network and boundary conditions is shown in Fig. 8. The matrix permeability is set to $\mathbb{K}_m = \mathbb{I}$, all fractures have a uniform aperture $\varepsilon = 10^{-4}$. For the fracture permeability we consider two cases: a highly conductive network with $k_{f,n} = k_{f,t} = 10^4$, as worked out in Section 4.1.1, and a case with blocking fractures by setting $k_{f,n} = k_{f,t} = 10^{-4}$, as described in Section 4.1.2. The reference solutions are computed on a grid which resolves every fracture with 10

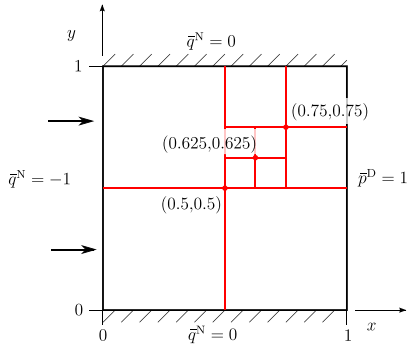

Fig. 8. Benchmark 1: Domain and boundary conditions.

Table 2
Grids for Benchmark 1.

Method	d.o.f.	♯-matr	♯-frac
Box	577	1078 triangles	74
TPFA	1481	1386 triangles	95
MPFA	1439	1348 triangles	91
EDFM	1501	1369 quads	132
Flux-Mortar	3366	1280 triangles	75
P-XFEM	1650	961 quads	164
D-XFEM	4474	1250 triangles	126
MFD	2,352,280	1,136,456 quads	38,600

elements in its normal direction and becomes coarser away from the fractures. It has a total of 1,175,056 elements.

The first distinction between the different schemes are given in Table 2, where the number of degrees of freedom, matrix elements (♯-matr) and fracture elements (♯-frac) for all the participating methods are listed. The corresponding grids are visualized in Fig. 9.

4.1.1. Conductive fracture network

First, we consider a highly conductive network by setting $k_{f,n} = k_{f,t} = 10^4$. The pressure distribution of the corresponding reference solution is shown in Fig. 10. The pressure distributions given by the different methods are first compared along two lines, one horizontal at $y = 0.7$ and one vertical at $x = 0.5$. As shown in Fig. 11, all results are relatively close to the reference solution. Qualitatively, we observe that P-XFEM produces a more diffuse pressure profile in the vertical fracture.

Table 3 lists the errors with respect to the equi-dimensional reference solution for the different methods; particularly, the error for the matrix domain and the one along the two fractures. Moreover, it provides the density of the associated matrix and its condition number for each method. The performance of the methods is comparable as shown by both the matrix and the fracture errors. In fact, since the degree of sparsity does not differ significantly either, the only notable differences between the methods are the number of degrees of freedom and the condition numbers, as shown in the last column of Table 3. In that context, the Flux-Mortar and D-XFEM are clear outliers, containing a large number of degrees of freedom due to the incorporated flux variable and resulting in high condition numbers. Nevertheless, the P-XFEM scheme exhibits the highest condition number, although it has significantly fewer degrees of freedom than Flux-Mortar and D-XFEM.

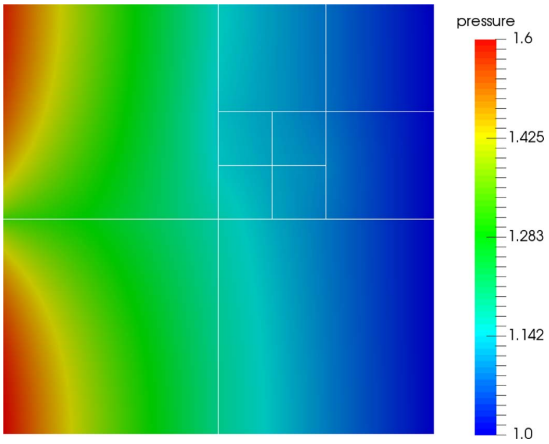

Fig. 10. Benchmark 1 with conductive fractures: pressure reference solution.

In addition to evaluating each method on a single grid, we perform a convergence study by choosing the grids above as initial ones and refining them twice. The results are shown in Fig. 12, detailed numbers are provided in Appendix A. For each method, the matrix error err_m and fracture error err_f is plotted against the square root of the number of matrix cells and against the number of fracture cells, respectively. As suggested by the numbers for the initial grids from Table 3, all methods exhibit a similar behaviour. For the matrix error in particular, the methods are very close to each other and all of them show a linear error decay. Concerning the fracture error, the XFEM methods perform a bit worse than the other ones in terms of absolute numbers. An obvious positive outlier is the fracture error for Box, which stagnates at a level much lower than all other methods. An explanation for this behaviour is still lacking. All other methods exhibit a linear error decay also for the fracture error.

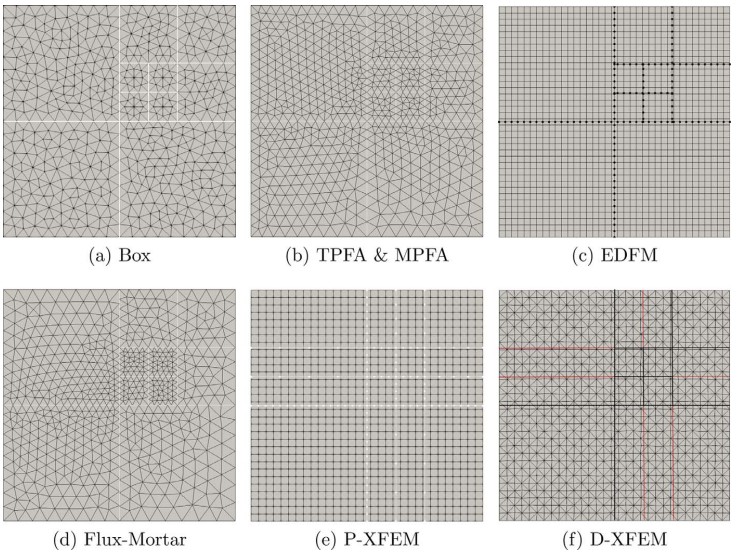

Fig. 9. Benchmark 1: the grids used by the different methods. In the D-XFEM grid the red lines indicate the virtual extension of the fractures up to the boundary. The fracture network has also been virtually extended for the application of P-XFEM. (For interpretation of the references to colour in this figure legend, the reader is referred to the web version of this article.)

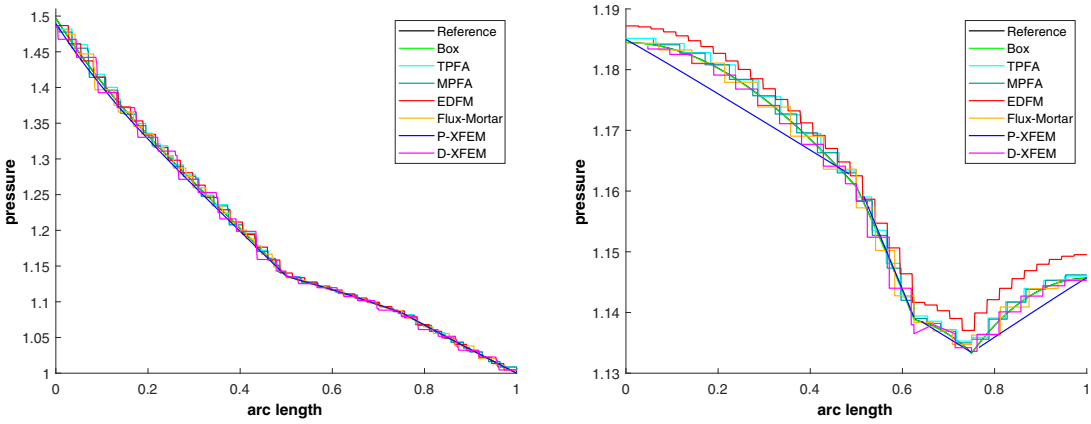

(a) Horizontal line at $y = 0.7$. (b) Longest vertical fracture at $x = 0.5$.

Fig. 11. Benchmark 1 with conductive fractures: comparison of values along two lines. The reference solution is hidden by the Box solution.

Table 3
Errors and matrix characteristics for Benchmark 1 with conductive fractures.

Method	err_m	err_f	nnz/size^2	$\|\cdot\|_2$-cond
Box	1.1e−2	1.9e−4	1.1e−2	2.2e3
TPFA	1.1e−2	4.4e−3	2.7e−3	4.8e4
MPFA	1.1e−2	4.5e−3	8.0e−3	5.8e4
EDFM	6.5e−3	4.0e−3	3.3e−3	5.6e4
Flux-Mortar	1.0e−2	6.9e−3	1.8e−3	2.4e6
P-XFEM	9.3e−3	7.3e−3	8.0e−3	9.3e9
D-XFEM	9.6e−3	8.9e−3	1.3e−3	1.2e6

4.1.2. Blocking fracture network

We now assume a blocking fracture network by setting $k_{f,n} = k_{f,t} = 10^{-4}$. The pressure distribution of the corresponding reference solution is shown in Fig. 13. The results clearly show the pressure discontinuities reminiscent of the low fracture permeability.

Fig. 14 compares the results of the different methods along a diagonal line crossing the whole domain from (0.0, 0.1) to (0.9, 1.0). The errors, sparsity densities, and condition numbers for the different methods are given in Table 4.

In the case of blocking fractures, the distinction between the

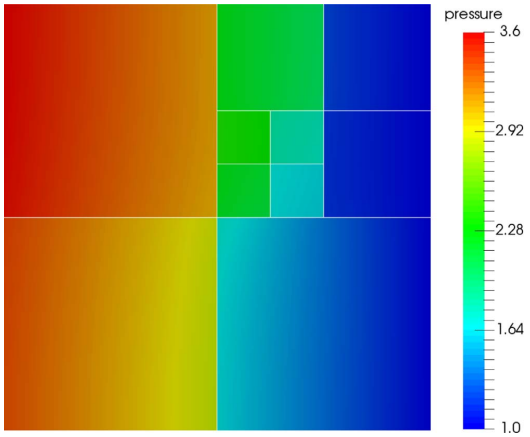

Fig. 13. Benchmark 1 with blocking fractures: pressure reference solution.

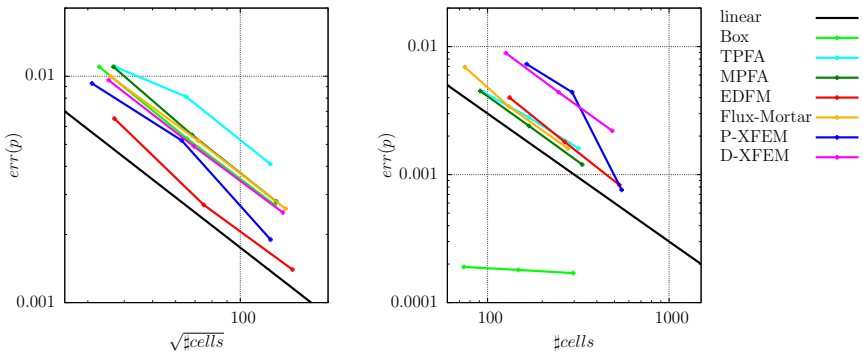

(a) Matrix error err_m. (b) Fracture error err_f.

Fig. 12. Benchmark 1 with conductive fractures: evolution of the matrix and fracture errors over grid refinement.

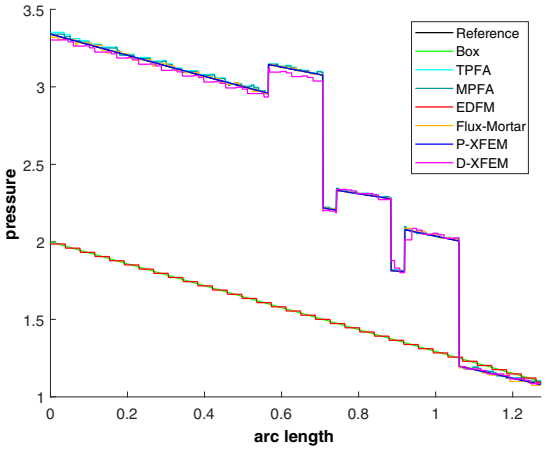

Fig. 14. Benchmark 1 with blocking fractures: values along the line (0.0, 0.1) − (0.9, 1.0). The reference solution is hidden by the P-XFEM solution.

Table 4
Errors and matrix characteristics for Benchmark 1 with blocking fractures.

Method	err_m	err_f	nnz/size^2	$\|\cdot\|_2$-cond
Box	4.1e−1	3.2e−1	1.1e−2	1.3e3
TPFA	5.6e−3	4.4e−3	2.7e−3	2.6e4
MPFA	4.4e−3	3.6e−3	2.7e−3	6.3e4
EDFM	2.9e−1	3.2e−1	3.3e−3	9.2e3
Flux-Mortar	4.3e−3	4.6e−3	1.6e−3	9.0e2
P-XFEM	2.7e−3	2.0e−2	6.9e−3	1.3e7
D-XFEM	1.0e−2	1.8e−2	1.3e−3	2.2e6

different methods is more apparent. As mentioned above, the Box and EDFM schemes are unable to capture the resulting pressure discontinuities. As a result, these methods show large errors in both the matrix and the fracture domains. The remaining methods, which are capable of handling discontinuities, differ a bit more among each other in terms of fracture and matrix errors. The condition numbers have improved significantly for the Flux-Mortar and P-XFEM schemes. Conversely, for TPFA, MPFA and D-XFEM, condition numbers for the blocking fractures case are similar to those obtained for the permeable fractures case.

We investigate the error decays also for the variant of blocking fractures. The decays are illustrated in Fig. 15. The spread between the different methods becomes very explicit here. As to be expected, the errors for Box and EDFM do not improve with grid refinement. Concerning the matrix error, TPFA, MPFA, Flux-Mortar and P-XFEM exhibit a linear decay, while D-XFEM appears to converge with an inferior order. This is due to the fact that in this method fractures are artificially extended to the boundary with a permeability that is the same of the surrounding matrix: the “T” type intersections become “X” intersections with severe permeability jumps between the two branches of the same fractures, causing numerical problems that affect convergence. Although P-XFEM shows the best numbers for the matrix error, both XFEM methods result in considerably higher fracture errors than TPFA, MPFA and Flux-Mortar. For the convergent methods, the rate of convergence for the fracture error between the second and third refinement stage is measured between 0.45 and 0.64.

4.2. Benchmark 2: Hydrocoin

Within the international Hydrocoin project, (Swedish Nuclear Power Inspectorate (SKI), 1987), a benchmark for heterogeneous groundwater flow problems was presented. The domain setup is shown in Fig. 16. We point out that we have slightly modified the original domain such that equi-dimensional and hybrid-dimensional models can be run on exactly the same domain. This allows for an easier comparison of the solution values over the whole domain. The exact modifications are described in Appendix B.

For this case, we keep the original formulation in terms of the piezometric head and the hydraulic conductivity instead of pressure and permeability. In particular, the boundary conditions are Dirichlet piezometric head on the top boundary and Neumann no flow on the other three boundaries. The permeability is 10^{-6} m/s in the fracture zones and 10^{-8} m/s in the rock matrix respectively.

Table 5 lists the number of degrees of freedom, matrix elements and fracture elements for all the participating methods.

The corresponding grids are visualized in Fig. 17.

The original benchmark shows the piezometric head distribution along five horizontal lines through the modeled domain. Here, we first show in Fig. 18 the plot at a depth of 200 m, as indicated by the dashed line in Fig. 16. All participating methods show a good agreement with the reference solution. Only the EDFM method is a bit off. We remark that the plots for the methods employing cell-wise constant solution values exhibit staircase-like patterns corresponding to these values.

Table 6 lists the errors for the different methods. The uniform behaviour exhibited in Fig. 18 is reflected by the error values. Especially the errors in the matrix domain are within very narrow bounds, while the fracture errors show a larger variation. Just like for Benchmark 1,

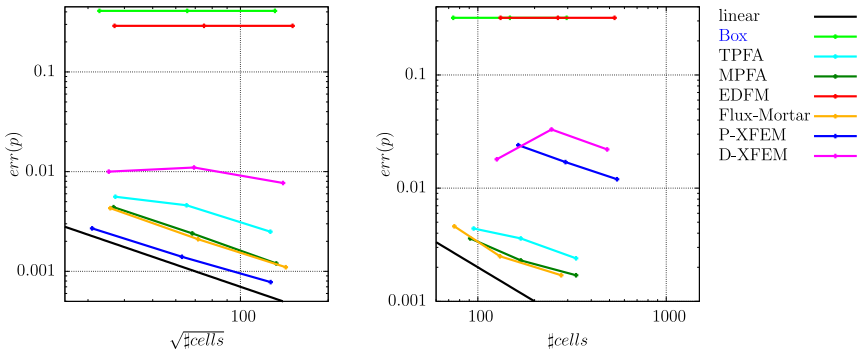

(a) Matrix error err_m. (b) Fracture error err_f.

Fig. 15. Benchmark 1 with blocking fractures: evolution of the matrix and fracture errors over grid refinement.

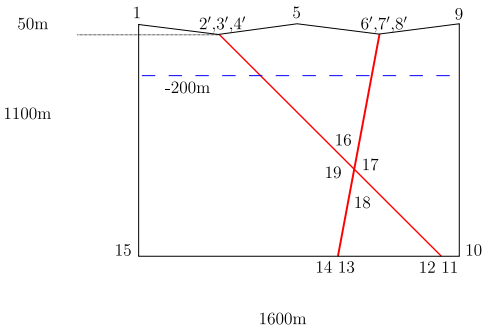

Fig. 16. Geometry of the modeled domain of the Hydrocoin test case 2, Swedish Nuclear Power Inspectorate (SKI) (1987). Modified node locations are indicated by numbers superscripted with ′. Boundary conditions are hydraulic head on top and Neumann no-flow on the other three sides of the domain.

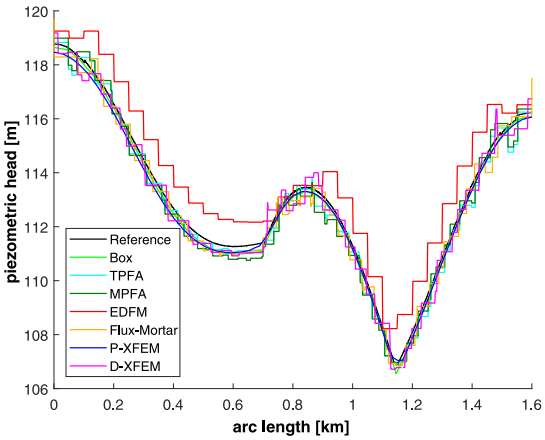

Fig. 18. Benchmark 2: head values along a horizontal line at a depth of 200 m.

Table 5
Grids for Benchmark 2.

Method	d.o.f.	♯-matr	♯-frac
Box	1496	2863 triangles	74
TPFA	1459	1416 triangles	43
MPFA	1532	1416 triangles	43
EDFM	1044	960 quads	84
Flux-Mortar	3647	1384 triangles	63
P-XFEM	1667	1320 quads	68
D-XFEM	3514	1132 triangles	160
MFD	889,233	424,921 mixed	19,287

Table 6
Errors and matrix characteristics for Benchmark 2.

method	err_m	err_f	nnz/size^2	$\|\cdot\|_2$-cond
Box	9.2e−3	3.3e−3	4.5e−3	5.4e3
TPFA	1.1e−2	1.1e−2	2.7e−3	3.5e4
MPFA	9.3e−3	6.8e−3	8.2e−3	6.6e4
EDFM	1.5e−2	8.3e−3	4.7e−3	3.9e4
Flux-Mortar	1.0e−2	7.2e−3	1.5e−3	9.0e12
P-XFEM	1.2e−2	3.2e−3	6.5e−3	2.7e9
D-XFEM	1.2e−2	6.9e−3	1.7e−3	6.2e12

remarkably high differences can be observed for the matrix condition numbers. While the ones for Box, TPFA, MPFA and EDFM are on the order of 10^4, the one for P-XFEM is five orders and the ones for Flux-Mortar and D-XFEM are even seven orders of magnitude larger, due to their saddle-point nature.

We remark that the fracture apertures are, with around 10m, rather high in relation to the dimensions of the computational domain (~ 1000 m) and the element sizes (~ 50 m) employed in the calculations above. Therefore, the assumption of a negligible aperture that justifies the usage of hybrid-dimensional methods is questionable. This is confirmed by the fact that no convergence can be observed for the considered methods when refining the grids depicted in Fig. 17. The total error is already dominated by the modeling error rather than the discretization error. Since our focus is on comparing different DFM methods that all rely on this assumption, we refrain from performing a more detailed analysis in this direction.

We would like to point out that an aperture of 10 m and more is often encountered in real field problems. The original intention of the Hydrocoin groups was to have a representation of a highly conductive fault zone: “The problem is an idealisation of the hydrogeological conditions encountered at a potential site for a deep repository in bedrock” (Swedish Nuclear Power Inspectorate (SKI), 1987). Some examples on modeling the impact of hydraulic fracturing on groundwater where the fault widths range between 10 and 30 m are provided in

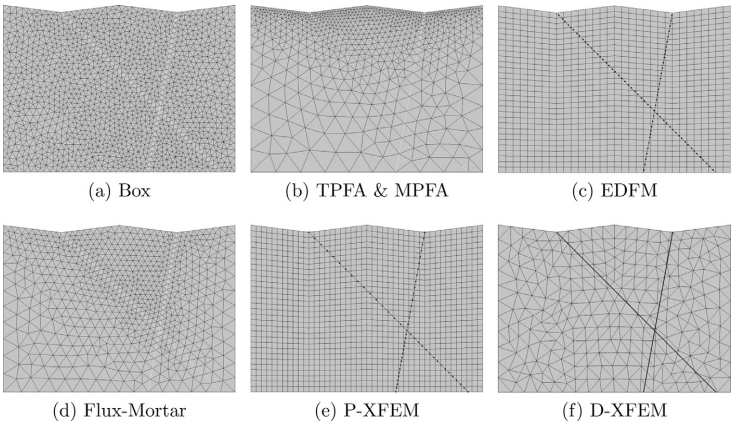

Fig. 17. Benchmark 2: the grids used by the different methods.

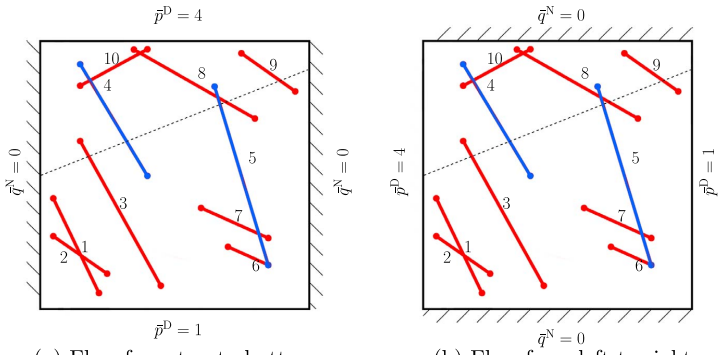

(a) Flow from top to bottom. (b) Flow from left to right.

Fig. 19. Benchmark 3: Domain and boundary conditions for cases (a) and (b). The red fractures are conductive, the blue ones are blocking. The dashed line is chosen to compare pressure profiles across both blocking and permeable fractures. (For interpretation of the references to colour in this figure legend, the reader is referred to the web version of this article.)

Gassiat et al. (2013), Pfunt et al. (2016) and Taherdangkoo et al. (2017). It is common practice and, depending on the geometrical complexity, often the only efficient possibility to treat such fault zones with lower-dimensional models. A modeler parametrizing a real field problem will often face the question of how to consider the fractures in the model. Despite the fact that the assumption of a negligible aperture is not justified, the accuracy of a hybrid-dimensional approach might still be acceptable, as is also indicated by our results.

4.3. Benchmark 3: complex fracture network

This test case considers a small but complex fracture network that includes permeable and blocking fractures. The domain and boundary conditions are shown in Fig. 19. The exact coordinates for the fracture positions are provided in Appendix C. The fracture network contains ten straight immersed fractures, grouped in disconnected networks. The aperture is $\varepsilon = 10^{-4}$ for all fractures, and the permeability is $k_{\mathrm{f,n}} = k_{\mathrm{f,t}} = 10^{4}$ for all fractures except for fractures 4 and 5, which are blocking fractures with $k_{\mathrm{f,n}} = k_{\mathrm{f,t}} = 10^{-4}$. The matrix permeability is again set to $\mathbb{K}_{\mathrm{m}} = \mathbb{I}$. Note that we are considering two sub-cases, a) and b). with a pressure gradient which is predominantly vertical and horizontal, respectively, to better highlight the impact of the blocking fractures. The corresponding reference solutions are depicted in Fig. 20.

Table 7 lists the number of degrees of freedom, matrix elements and fracture elements for all the participating methods. The corresponding grids are visualized in Fig. 21.

The P-XFEM method could not participate in this benchmark example. Its current implementation requires that each matrix element face is cut by at most one fracture branch. While it would be possible to construct a matrix grid that satisfies this requirement, this would contradict the promised advantage of admitting independent fracture and matrix grids.

Table 7
Grids for Benchmark 3.

Method	d.o.f.	♯-matr	♯-frac
Box	1373	2664 triangles	152
TPFA	1420	1332 triangles	88
TPFA*	1425	1332 triangles	93
MPFA	1500	1332 triangles	88
EDFM	1572	1369 quads	203
Flux-Mortar	3349	1230 triangles	89
D-XFEM	7180	1922 triangles	199
MFD	3,471,040	2,260,352 triangles	52,608

4.3.1. Flow from top to bottom

We first consider the setup depicted in Fig. 19(a), resulting in the reference solution visualized in Fig. 20(a). Table 8 lists the errors for this first variant, namely, the flow from top to bottom.

The pressure profiles along the line $(0, 0.5) - (1, 0.9)$, computed by the different methods, are represented in Fig. 22: one can observe that most methods are in good agreement with the reference solution, except for EDFM and the Box method that cannot represent the behaviour of the blocking fractures. Even though this is still a synthetic case, we can see that the geometry of the network starts to be an issue: relatively small intersection angles are present, for instance, between fractures 1 and 2. Another difficulty consists in the coexistence of permeable and blocking fractures which intersect each other: on one hand, some of the methods are not well suited to describe a blocking behaviour, on the other hand, the coupling conditions at the intersection become less trivial in these cases. All the participating methods that account explicitly for the effect of permeability at the fracture intersections have adopted the harmonic average in the case of a permeable and a

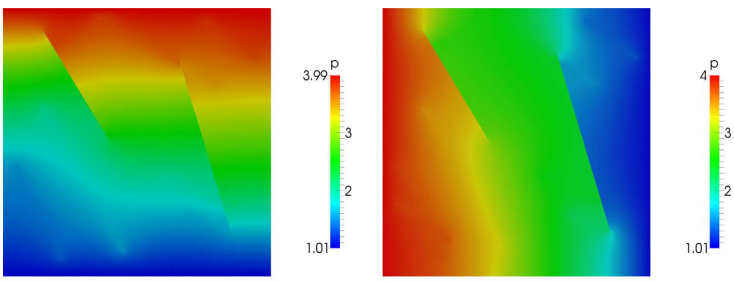

(a) Flow from top to bottom. (b) Flow from left to right.

Fig. 20. Benchmark 3: reference solution for cases a) and b).

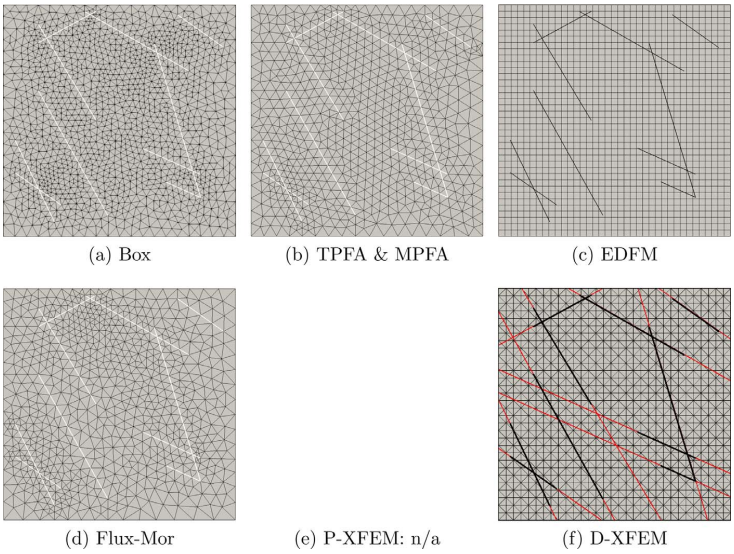

Fig. 21. Benchmark 3: the grids used by the different methods. In the DXFEM grid the red lines indicate the virtual extension of the fractures up to the boundary. (For interpretation of the references to colour in this figure legend, the reader is referred to the web version of this article.)

Table 8
Errors and matrix characteristics for the first variant of Benchmark 3.

Method	err_m	err_f	nnz/size^2	$\|\cdot\|_2$-cond
Box	4.9e−2	3.4e−2	4.9e−3	4.3e3
TPFA	2.7e−2	2.9e−2	2.8e−3	2.6e4
TPFA*	1.3e−2	1.1e−2	2.8e−3	7.9e4
MPFA	2.5e−2	2.8e−2	8.5e−3	2.5e4
EDFM	3.8e−2	4.5e−2	3.1e−3	1.2e6
Flux-Mortar	1.0e−2	8.2e−3	1.6e−3	1.3e4
D-XFEM	1.9e−2	2.9e−2	8.2e−4	8.1e3

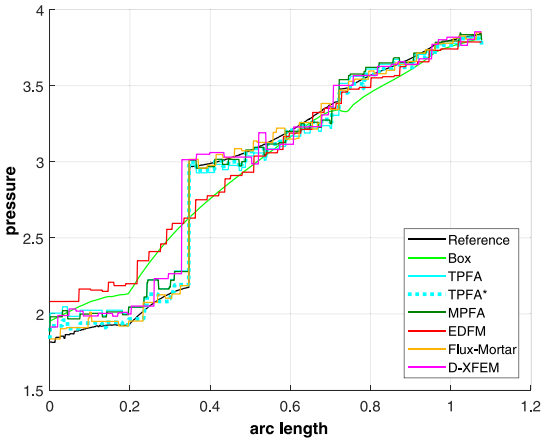

Fig. 22. Benchmark 3, first variant: pressure values along the line (0.0, 0.5) − (1.0, 0.9).

blocking fracture crossing each other. The errors reported in Table 8 show that the methods requiring the continuity of pressure (EDFM and the Box) exhibit slightly higher errors in the matrix. However, the difference is not particularly sharp, since in this sub-case the average pressure gradient is almost parallel to the blocking fractures. The elimination of the fracture intersection cells in the TPFA and MPFA methods is ill-suited for cases where fractures of different permeability cross. Therefore, we include a solution TPFA* in which we have not performed the removal. The corresponding results show a far smaller error compared to the TPFA with elimination, but also demonstrate that the elimination significantly increases the condition number.

Like for Benchmark 1, we investigate the errors in the matrix and in the fracture network, see Fig. 23 and detailed numbers in Appendix D. We have not considered Box and EDFM, since the corresponding errors stagnate due to the presence of blocking fractures, as already discussed in Section 4.1.2. Surprisingly at first sight, now also TPFA and MPFA do not converge. This is an implication of the facts mentioned above, namely, that the intersection cells are removed for both methods together with the appearance of intersecting conductive and blocking fractures. When these cells are included, convergence can be achieved. Only TPFA* and Flux-Mortar exhibit a linear decay of the matrix error, while D-XFEM shows considerably higher absolute numbers and an inferior convergence rate. As already observed for the blocking variant of Benchmark 2, linear convergence cannot be achieved for the fracture error.

4.3.2. Flow from left to right

We now investigate the more challenging setup from Fig. 19(b) and its corresponding reference solution depicted in Fig. 20(b). The errors for this second variant are summarized in Table 9. The pressure profiles along the line (0, 0.5) − (1, 0.9), computed by the different methods for are represented in Fig. 24. As in the previous sub-case EDFM and the Box method are not able to capture the pressure jumps across the blocking fractures. Moreover, the D-XFEM method underestimates the second pressure jump. This behaviour will also reflect in a poor convergence rate (see Fig. 25). In this second case, since we impose pressure on the sides of the square domain, the solution is more challenging. As we can observe from Fig. 20, the gap between continuous and discontinuous methods increases.The errors remain of the same order of magnitude, indicating that all the methods capture the overall trend of the solution. Nevertheless, the difference between TPFA/MPFA and TPFA* becomes larger, indicating that it is even more important to treat

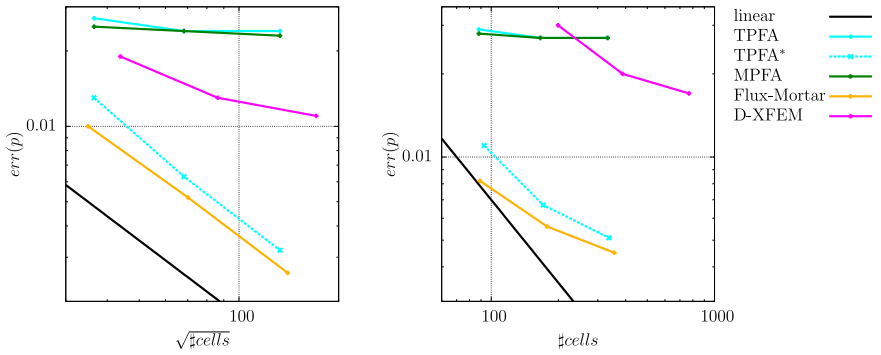

(a) Matrix error err_{m}. (b) Fracture error err_{f}.

Fig. 23. Benchmark 3, flow from top to bottom: evolution of the matrix and fracture errors over grid refinement.

Table 9
Errors and matrix characteristics for the second variant of Benchmark 3.

method	err_{m}	err_{f}	nnz/size^2	$\|\cdot\|_2$-cond
Box	7.5e−2	6.3e−2	4.9e−3	5.3e3
TPFA	5.1e−2	6.7e−2	2.8e−3	3.1e4
TPFA*	1.3e−2	1.1e−2	2.8e−3	2.0e5
MPFA	5.1e−2	6.7e−2	8.5e−3	3.1e4
EDFM	5.8e−2	8.9e−2	3.1e−3	1.2e6
Flux-Mortar	1.4e−2	1.3e−2	1.6e−3	1.4e4
D-XFEM	2.2e−2	3.6e−2	8.2e−4	8.1e3

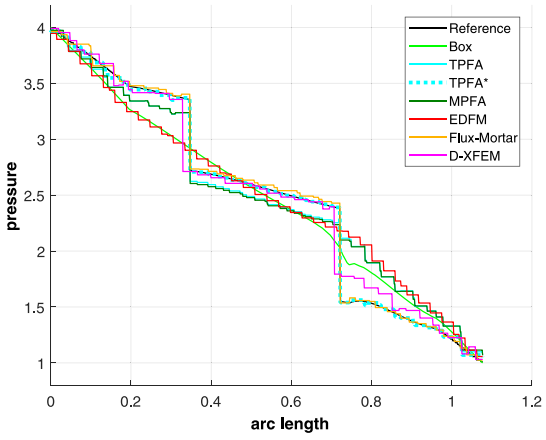

Fig. 24. Benchmark 3, second variant: pressure values along the line (0.0, 0.5) − (1.0, 0.9).

properly the intersections of conductive and blocking fractures.

The error plots associated with this second variant are shown in Fig. 25. They are very similar to the first variant, the only remarkable difference being the stagnation in the numbers for D-XFEM. This is once again caused by the intersections between fractures with different permeabilities, particularly in the “virtual” extensions of the fractures to the boundary.

4.4. Benchmark 4: a realistic case

In this last test case we consider a real set of fractures from an interpreted outcrop in the Sotra island, near Bergen in Norway. The set is composed of 64 fractures grouped in 13 different connected networks, ranging from isolated fractures up to tens of fractures each. In the interpretation process two fractures were composed by more than one segment. However, since the implementation of some methods relay on the fact that one fracture is represented by a single geometrical object, we substitute them by a single segment. It is worth to notice that we are changing the connectivity of the system, nevertheless our goal is to make a comparison of the previous schemes on a complex and realistic set of fractures. The interpreted outcrop and the corresponding set of fractures are represented in Fig. 26. The size of the domain is 700 m × 600 m with uniform matrix permeability $\mathbb{K}_{\mathrm{m}} = 10^{-14}\mathbb{I}\,\mathrm{m}^2$. For simplicity all the fractures have the same scalar permeability $k_{\mathrm{f,n}} = k_{\mathrm{f,t}} = 10^{-8}\ \mathrm{m}^2$, and aperture 10^{-2} m. We consider no-flow boundary condition on top and bottom, pressure 1013250 Pa on the left, and pressure 0 Pa on the right of the boundary of the domain. Due to the high geometrical complexity of the fracture network not all involved numerical schemes/simulators could be used. Nevertheless, it is worth to point out that for the others the main difficulty in handling such geometry is an implementation issue rather than a limitation of the scheme. It is also a very tedious task to create a full-dimensional description of the fracture network and a corresponding equi-dimensional grid of the whole computational domain. Therefore, we refrain from calculating a reference solution with the MFD method and perform a direct comparison of the hybrid-dimensional methods. Since all fractures are conductive and their aperture is negligibly small, we consider all participating methods to be verified by means of the benchmark cases above.

Table 10 lists the number of degrees of freedom, the density of the associated matrix, and its condition number for the different methods. Due to the geometrical difficulties of the network the request of having a similar number of degrees of freedom among the methods is relaxed, as Table 10 indicates. Considering Fig. 27, the solutions are reported for the four methods. We notice that, except for the top right part of the domain in the Box method, the solutions are similar and comparable, which is an indication of their correctness. Compared to the previous test cases the mesh generation is the main concern and some of the methods require a fine tuning to avoid non-physical connections among

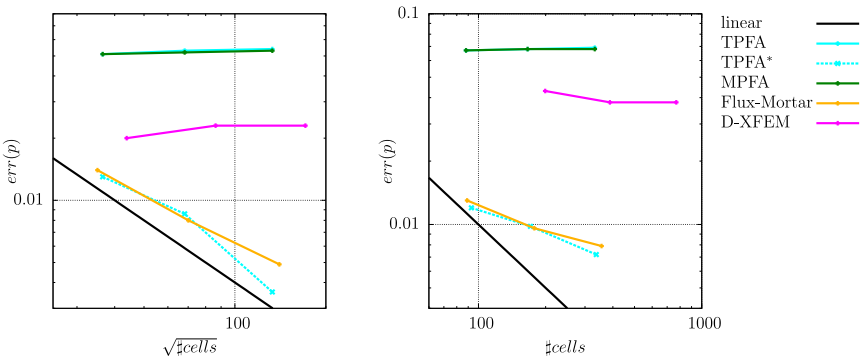

(a) Matrix error err_{m}. (b) Fracture error err_{f}.

Fig. 25. Benchmark 3, flow from left to right: evolution of the matrix and fracture errors over grid refinement.

elements where the fracture are close. An example can be found in the middle of the domain and reported in Fig. 28. Only EDFM is more robust with respect to this constraint. To present a more detailed comparison among the methods, Fig. 29 represents the pressure solution along two different lines: for $y = 500$ m and for $x = 625$ m. We note that the methods behave similarly, and the Box slightly overestimates some peaks. The oscillation of the methods are related to mesh effects.

5. Summary and outlook

Four benchmark cases for single-phase flow in fractured porous media have been proposed and employed to compare the performances of several state-of-the-art hybrid-dimensional discrete-fracture-matrix models. If we consider the cases where all the methods are employed within the applicability range for which they were originally developed, the results are in quite good agreement. In particular, fracture networks exhibiting a larger permeability than the surrounding matrix can be accurately described by all methods. On the other hand, not all methods are capable of modeling blocking fractures. In this case, some methods fail to predict the correct flow patterns for the corresponding scenarios. These observations are confirmed by investigating the behaviour of the errors with respect to the equi-dimensional reference solution under mesh refinement. For purely conductive fracture networks, all methods exhibit a linear decay for both the error in the matrix and the fractures, and the total numbers are very similar. The

Table 10
Discretization and matrix characteristics for Benchmark 4.

Method	d.o.f.	♯-matr	♯-frac	nnz/size^2	$\|\cdot\|_2$-cond
Box	5563	10,807 triangles	1386	1.2e−3	9.3e5
TPFA	8481	7614 triangles	867	4.9e−4	5.3e6
MPFA	8588	7614 triangles	867	1.6e−3	4.9e6
EDFM	3599	2491 quads	1108	1.4e−3	4.7e6
Flux-Mortar	25,258	8319 triangles	1317	2.0e−4	2.2e17

fact that some methods cannot deal with blocking fractures is reflected by a stagnation of the corresponding errors. In the presence of blocking fractures, the order of convergence for the fracture error decreases for all methods. Moreover, the fracture error for the XFEM methods has been observed to be considerably larger than for the other convergent methods. Even if a method can handle conductive and blocking fractures, the intersection of a conductive with a blocking fracture branch poses additional challenges. In this case, a method may not converge if it doesn't treat these intersections carefully enough. Of the eight participating methods, only two, TPFA* and Flux-Mortar, proved to be convergent through all considered cases.

Apart from the discretization error, another component of the total error is the modeling error resulting from the assumption that the fracture apertures are negligibly small. For the Hydrocoin benchmark, this component obviously dominated the measured error. More detailed

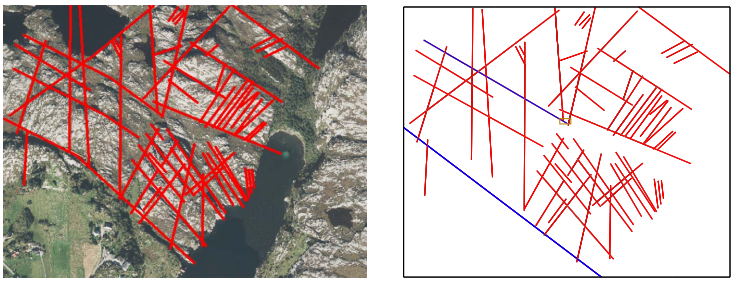

Fig. 26. In the left the interpretation of the set of fractures superimposed to the map. In the right the geometry used in the simulations. The rectified fractures are depicted in blue. (For interpretation of the references to colour in this figure legend, the reader is referred to the web version of this article.)

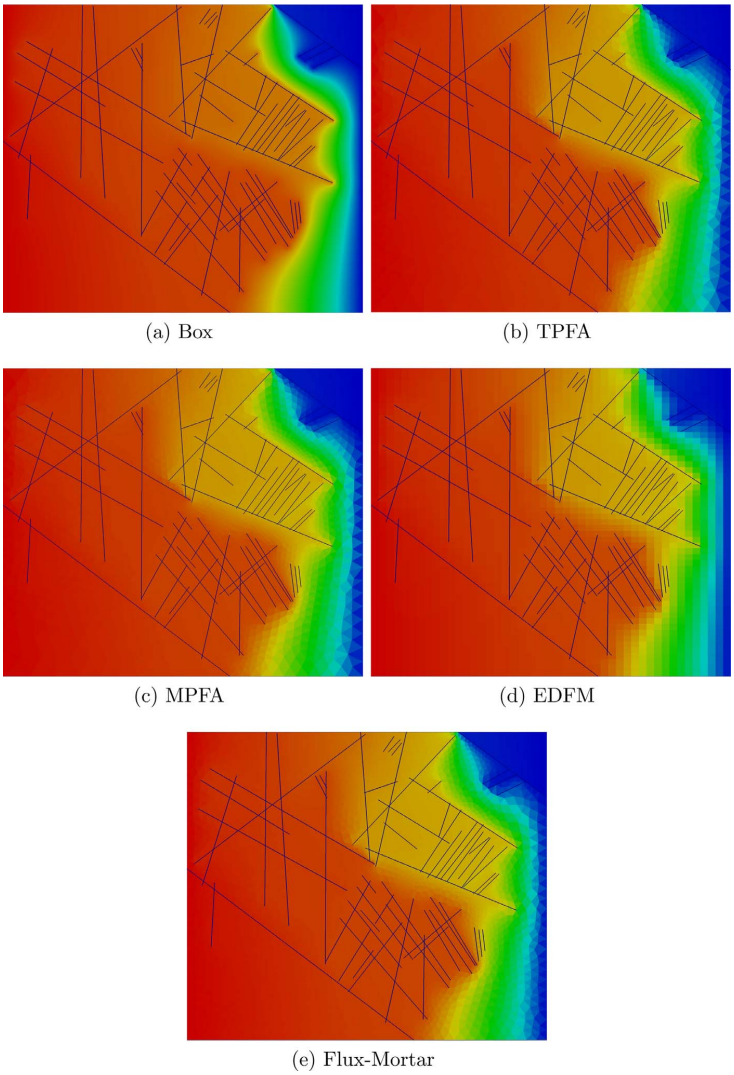

Fig. 27. Representation of the matrix pressures field for the realistic case. The solution values range between 0 and 1013250 Pa.

investigations on the relation between these two components is an interesting topic for future work.

Especially noteworthy are the large differences in the condition numbers of the associated system matrices. The effect of these differences on the behaviour of linear solvers is difficult to quantify in a comparable manner, since the different methods pose different requirements for such solvers.

In principle, all participating methods should have been able to run all proposed cases. However, due to implementation restrictions, some methods could not perform the cases with more complex fracture network geometries. Even if the methodology is general enough, technical difficulties can become crucial obstacles to tackling realistic scenarios.

All the investigated benchmarks are restricted to simple physics and two-dimensional computational domains. This should give other researchers developing DFM models the chance to perform comparison studies for their methods. We encourage the scientific community to contribute their results for the benchmarks to a corresponding Git repository at https://git.iws.uni-stuttgart.de/benchmarks/fracture-flow.

Further benchmark cases may be developed in the near future. In particular, we are very interested in enhancing the purely single-phase single-component flow physics by adding transport, deformation and/or reaction processes. We aim to carry out these efforts in a broader context by means of international workshops. A first such workshop "Modeling and benchmarking of fractured porous media: flow, transport and deformation" was organized by the authors and held in June 2017 at the University of Bergen. First future steps already have been discussed there.

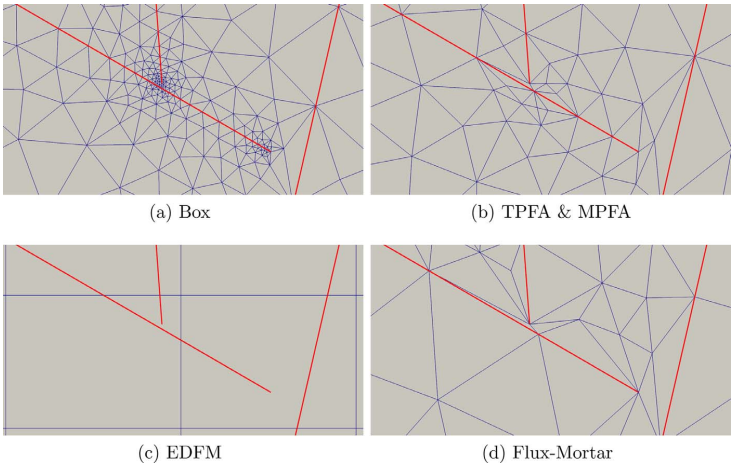

(a) Box (b) TPFA & MPFA

(c) EDFM (d) Flux-Mortar

Fig. 28. Benchmark 4: Representation of mesh in the middle of the domain. The size of the picture is approximately 30 m × 15 m centred in (360, 350). It is represented by the small rectangle in the centre of Fig. 26 left.

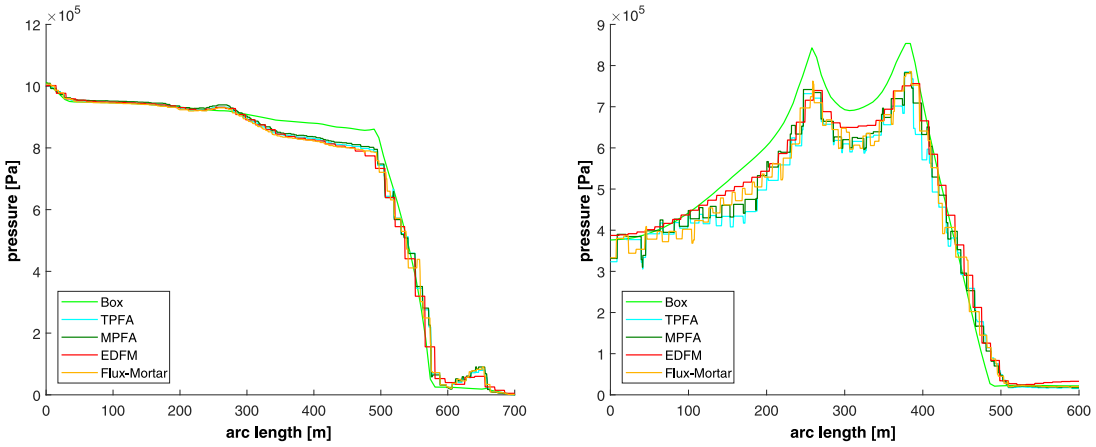

(a) $y = 500\,\mathrm{m}$ (b) $x = 625\,\mathrm{m}$

Fig. 29. Benchmark 4: Pressure solutions of the 4 methods plotted over lines (a) $y = 500$ m, and (b) $x = 625$ m.

Acknowledgement

The authors warmly thank Luisa F. Zuluaga, from University of Bergen, for constructing and providing the real fracture network for the example in Section 4.4. The authors wish to thank also Luca Pasquale and Stefano Zonca.

The second author acknowledges financial support from the GeoStim project from the Research Council of Norway (project no. 228832) through the ENERGIX program. The third author was supported by Norwegian Research Council grant 233736. The fourth author acknowledges financial support from the ANIGMA project from the Research Council of Norway (project no. 244129/E20) through the ENERGIX program.

Appendix A. Details for the convergence study in Benchmark 1

Detailed numbers for the convergence studies carried out in Section 4.1 are provided by means of tables for the errors in matrix and fracture, calculated according to (7). In particular, the index k in $err_{\mathrm{m},\,k}$ and $err_{\mathrm{f},\,k}$ refers to the refinement level. The number of elements is indicated correspondingly by $n_{\mathrm{m},\,k}$ and $n_{\mathrm{f},\,k}$ for matrix and fracture, respectively. The experimental orders of convergence $eoc_{\mathrm{m},\,k}$ and $eoc_{\mathrm{f},\,k}$ are calculated by

$$eoc_{\mathrm{m},k} = 2\frac{\log \dfrac{err_{\mathrm{m},k}}{err_{\mathrm{m},k-1}}}{\log \dfrac{n_{\mathrm{m},k-1}}{n_{\mathrm{m},k}}}, \qquad eoc_{\mathrm{f},k} = \frac{\log \dfrac{err_{\mathrm{f},k}}{err_{\mathrm{f},k-1}}}{\log \dfrac{n_{\mathrm{f},k-1}}{n_{\mathrm{f},k}}}.$$

A1. Conductive fracture network

Method	$n_{m,0}$	$err_{m,0}$	$n_{m,1}$	$err_{m,1}$	$eoc_{m,1}$	$n_{m,2}$	$err_{m,2}$	$eoc_{m,2}$
Box	1078	1.1e−02	4312	5.3e−03	1.05	17,248	2.7e−03	0.97
TPFA	1386	1.1e−02	4269	8.1e−03	0.54	14,866	4.1e−03	1.09
TPFA*	–	–	–	–	–	–	–	–
MPFA	1348	1.1e−02	4673	5.5e−03	1.12	17,632	2.8e−03	1.02
EDFM	1369	6.5e−03	5625	2.7e−03	1.24	22,801	1.4e−03	0.94
Flux-Mortar	1280	1.0e−02	5120	5.2e−03	0.94	20,480	2.6e−03	1.00
P-XFEM	961	9.3e−03	3969	5.2e−03	0.82	16,129	1.9e−03	1.44
D-XFEM	1250	9.6e−03	4802	4.9e−03	1.00	19,602	2.5e−03	0.96

Method	$n_{f,0}$	$err_{f,0}$	$n_{f,1}$	$err_{f,1}$	$eoc_{f,1}$	$n_{f,2}$	$err_{f,2}$	$eoc_{f,2}$
Box	74	1.9e−04	148	1.8e−04	0.08	296	1.7e−04	0.08
TPFA	95	4.4e−03	169	2.8e−03	0.78	317	1.6e−03	0.89
TPFA*	–	–	–	–	–	–	–	–
MPFA	91	4.5e−03	169	2.4e−03	1.02	332	1.2e−03	1.03
EDFM	132	4.0e−03	266	1.8e−03	1.14	532	8.3e−04	1.12
Flux-Mortar	75	6.9e−03	131	3.4e−03	1.27	277	1.6e−03	1.01
P-XFEM	164	7.3e−03	292	4.4e−03	0.88	548	7.6e−04	2.79
D-XFEM	126	8.9e−03	246	4.4e−03	1.05	486	2.2e−03	1.02

A2. Blocking fracture network

Method	$n_{m,0}$	$err_{m,0}$	$n_{m,1}$	$err_{m,1}$	$eoc_{m,1}$	$n_{m,2}$	$err_{m,2}$	$eoc_{m,2}$
Box	1078	4.1e−01	4312	4.1e−01	0.00	17,248	4.1e−01	0.00
TPFA	1386	5.6e−03	4269	4.6e−03	0.35	14,866	2.5e−03	0.98
TPFA*	–	–	–	–	–	–	–	–
MPFA	1348	4.4e−03	4673	2.4e−03	0.98	17,632	1.2e−03	1.04
EDFM	1369	2.9e−01	5625	2.9e−01	0.00	22,801	2.9e−01	0.00
Flux-Mortar	1280	4.3e−03	5120	2.1e−03	1.03	20,480	1.1e−03	0.93
P-XFEM	961	2.7e−03	3969	1.4e−03	0.93	16,129	7.8e−04	0.83
D-XFEM	1250	1.0e−02	4802	1.1e−02	−0.14	19,602	7.7e−03	0.51

Method	$n_{f,0}$	$err_{f,0}$	$n_{f,1}$	$err_{f,1}$	$eoc_{f,1}$	$n_{f,2}$	$err_{f,2}$	$eoc_{f,2}$
Box	74	3.2e−01	148	3.2e−01	0.00	296	3.2e−01	0.00
TPFA	95	4.4e−03	169	3.6e−03	0.35	317	2.4e−03	0.64
TPFA*	–	–	–	–	–	–	–	–
MPFA	91	3.6e−03	169	2.3e−03	0.72	332	1.7e−03	0.45
EDFM	132	3.2e−01	266	3.2e−01	0.00	532	3.2e−01	0.00
Flux-Mortar	75	4.6e−03	131	2.6e−03	1.02	277	1.7e−03	0.57
P-XFEM	164	2.4e−02	292	1.7e−02	0.60	548	1.2e−02	0.55
D-XFEM	126	1.8e−02	246	3.3e−02	−0.91	486	2.2e−02	0.60

Appendix B. Domain modifications for Benchmark 2

Table B.11 provides the exact coordinates of the points from Fig. 16.

In comparison to the original setup, the plateaus close to the upper left and right corners 1 and 9 have been omitted. Moreover, the upper ends of the two fractures have been modified according to Fig. B.30 which amounts to the changes of nodes 2–4 and 6–8.

Finally, the position of nodes 16–19 has been recalculated with higher precision. The hybrid-dimensional models do not take into account nodes 2,4,6,8 and 16–19 and combine nodes 11,12 and 13,14, since the two-dimensional fracture regions have been reduced to two intersecting straight lines.

Table B.11
Coordinates of the numbered points in the modeled region of the problem depicted in Fig. 16.

pt	x (m)	z (m)	pt	x (m)	z (m)
1	0	150	11	1505	−1000
2′	394.285714286	100.714285714	12	1495	−1000
3′	400	100	13	1007.5	−1000
4′	404.444444444	100.555555556	14	992.5	−1000
5	800	150	15	0	−1000
6′	1192.66666667	100.916666667	16	1071.34615385	−566.346153846
7′	1200	100	17	1084.03846154	−579.038461538
8′	1207.6744186	100.959302326	18	1082.5	−587.5
9	1600	150	19	1069.80769231	−574.807692308
10	1600	−1000			

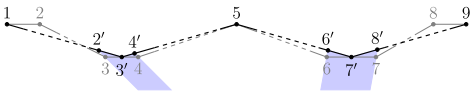

Fig. B.30. Modifications of the Hydrocoin model domain compared to the original formulation (Swedish Nuclear Power Inspectorate (SKI), 1987). The original upper boundary is drawn with grey thin lines, while thick black lines are used for the modified boundary. Modified node locations are indicated by numbers superscripted with ′. The shaded regions show the upper parts of the two slightly extended equi-dimensional fractures.

Appendix C. Fracture coordinates for Benchmark 3

The coordinates are listed in Table C.12.

Table C.12
Benchmark 3: Fracture coordinates

Nf	xA	yA	xB	yB
1	0.0500	0.4160	0.2200	0.0624
2	0.0500	0.2750	0.2500	0.1350
3	0.1500	0.6300	0.4500	0.0900
4	0.1500	0.9167	0.4000	0.5000
5	0.6500	0.8333	0.849723	0.167625
6	0.7000	0.2350	0.849723	0.167625
7	0.6000	0.3800	0.8500	0.2675
8	0.3500	0.9714	0.8000	0.7143
9	0.7500	0.9574	0.9500	0.8155
10	0.1500	0.8363	0.4000	0.9727

Appendix D. Details for the convergence study in Benchmark 3

Detailed numbers for the convergence studies carried out in Section 4.3 are provided by means of tables for the errors in matrix and fracture, analogously to Appendix A.

D1. Flow from top to bottom

Method	$n_{m,0}$	$err_{m,0}$	$n_{m,1}$	$err_{m,1}$	$eoc_{m,1}$	$n_{m,2}$	$err_{m,2}$	$eoc_{m,2}$
Box	2664	4.9e−02	10,656	5.0e−02	−0.03	42,624	5.0e−02	0.00
TPFA	1332	2.7e−02	4650	2.4e−02	0.19	17,690	2.4e−02	0.00
TPFA*	1332	1.3e−02	4650	6.3e−03	1.16	17,690	3.2e−03	1.01
MPFA	1332	2.5e−02	4650	2.4e−02	0.07	17,690	2.3e−02	0.06
EDFM	–	–	–	–	–	–	–	–
Flux-Mortar	1230	1.0e−02	4920	5.2e−03	0.94	19,680	2.6e−03	1.00
P-XFEM	–	–	–	–	–	–	–	–
D-XFEM	1922	1.9e−02	7442	1.3e−02	0.56	29,282	1.1e−02	0.24

Method	$n_{f,0}$	$err_{f,0}$	$n_{f,1}$	$err_{f,1}$	$eoc_{f,1}$	$n_{f,2}$	$err_{f,2}$	$eoc_{f,2}$
Box	152	3.4e−02	292	3.5e−02	−0.04	576	3.6e−02	−0.04
TPFA	88	2.9e−02	166	2.7e−02	0.11	332	2.7e−02	0.00

TPFA*	93	1.1e−02	171	6.7e−03	0.81	337	5.1e−03	0.40
MPFA	88	2.8e−02	166	2.7e−02	0.06	332	2.7e−02	0.00
EDFM	–	–	–	–	–	–	–	–
Flux-Mortar	89	8.2e−03	178	5.6e−03	0.55	356	4.5e−03	0.32
P-XFEM	–	–	–	–	–	–	–	–
D-XFEM	199	3.0e−02	388	2.0e−02	0.61	769	1.7e−02	0.24

D2. Flow from left to right

Method	$n_{m,0}$	$err_{m,0}$	$n_{m,1}$	$err_{m,1}$	$eoc_{m,1}$	$n_{m,2}$	$err_{m,2}$	$eoc_{m,2}$
Box	2664	7.4e−02	10,656	7.6e−02	−0.04	42,624	7.7e−02	−0.02
TPFA	1332	5.1e−02	4650	5.3e−02	−0.06	17,690	5.4e−02	−0.03
TPFA*	1332	1.3e−02	4650	8.6e−03	0.66	17,690	3.6e−03	1.30
MPFA	1332	5.1e−02	4650	5.2e−02	−0.03	17,690	5.3e−02	−0.03
EDFM	–	–	–	–	–	–	–	–
Flux-Mortar	1230	1.4e−02	4920	8.0e−03	0.81	19,680	4.9e−03	0.71
P-XFEM	–	–	–	–	–	–	–	–
D-XFEM	1922	2.0e−02	7442	2.3e−02	−0.21	29,282	2.3e−02	0.00

Method	$n_{f,0}$	$err_{f,0}$	$n_{f,1}$	$err_{f,1}$	$eoc_{f,1}$	$n_{f,2}$	$err_{f,2}$	$eoc_{f,2}$
Box	152	6.3e−02	292	6.7e−02	−0.09	576	6.9e−02	−0.04
TPFA	88	6.7e−02	166	6.8e−02	−0.02	332	6.9e−02	−0.02
TPFA*	93	1.2e−02	171	9.8e−03	0.33	337	7.2e−03	0.45
MPFA	88	6.7e−02	166	6.8e−02	−0.02	332	6.8e−02	0.00
EDFM	–	–	–	–	–	–	–	–
Flux-Mortar	89	1.3e−02	178	9.6e−03	0.44	356	7.9e−03	0.28
P-XFEM	–	–	–	–	–	–	–	–
D-XFEM	199	4.3e−02	388	3.8e−02	0.19	769	3.8e−02	0.00

References

Aavatsmark, I., 2002. An introduction to multipoint flux approximations for quadrilateral grids. Computat. Geosci. 6 (3), 405–432.

Ahmed, R., Edwards, M.G., Lamine, S., Huisman, B.A., Pal, M., 2015. Control-volume distributed multi-point flux approximation coupled with a lower-dimensional fracture model. J. Comput. Phys. 284, 462–489.

de Araujo Cavalcante Filho, J.S., Shakiba, M., Moinfar, A., Sepehrnoori, K., 2015. Implementation of a preprocessor for embedded discrete fracture modeling in an IMPEC compositional reservoir simulator. SPE Reservoir Simulation Symposium, 23–25 February, Houston, Texas, USA. Society of Petroleum Engineershttp://dx.doi.org/10.2118/173289-MS.

Bastian, P., Blatt, M., Dedner, A., Engwer, C., Klöfkorn, R., Kornhuber, R., Ohlberger, M., Sander, O., 2008. A generic grid interface for parallel and adaptive scientific computing. part II: implementation and tests in DUNE. Computing 82 (2–3), 121–138.

Bastian, P., Heimann, F., Marnach, S., 2010. Generic implementation of finite element methods in the distributed and unified numerics environment (DUNE). Kybernetika 46 (2), 294–315.

Berkowitz, B., 2002. Characterizing flow and transport in fractured geological media: a review. Adv. Water Resour. 25 (8–12), 861–884.

Bogdanov, I., Mourzenko, V., Thovert, J.-F., Adler, P., 2003. Two-phase flow through fractured porous media. Phys. Rev. E 68 (2), 026703.

Boon, W. M., Nordbotten, J. M., Yotov, I., 2016. Robust discretization of flow in fractured porous media. ArXiv:1601.06977 [math.NA].

Brenner, K., Groza, M., Guichard, C., Lebeau, G., Masson, R., 2016. Gradient discretization of hybrid dimensional darcy flows in fractured porous media. Numerische Mathematik 134 (3), 569–609.

Brenner, K., Hennicker, J., Masson, R., Samier, P., 2017. Gradient discretization of hybrid-dimensional darcy flow in fractured porous media with discontinuous pressures at matrixfracture interfaces. IMA J. Numer. Anal. 37 (3), 1551–1585. http://dx.doi.org/10.1093/imanum/drw044.

Brezzi, F., Lipnikov, K., Simoncini, V., 2005. A family of mimetic finite difference methods on polygonal and polyhedral meshes. Math. Mod. Meth. Appl. S. 15 (10), 1533–1551.

Caers, J., 2013. A special issue on benchmark problems, datasets and methodologies for the computational geosciences. Comput. Geosci. 50, 1–3. http://dx.doi.org/10.1016/j.cageo.2012.11.001.

Class, H., Ebigbo, A., Helmig, R., Dahle, H.K., Nordbotten, J.M., Celia, M.A., Audigane, P., Darcis, M., Ennis-King, J., Fan, Y., Flemisch, B., Gasda, S.E., Jin, M., Krug, S., Labregere, D., Naderi Beni, A., Pawar, R.J., Sbai, A., Thomas, S.G., Trenty, L., Wei, L., 2009. A benchmark study on problems related to CO2 storage in geologic formations: summary and discussion of the results. Computat. Geosci. 13 (4), 409–434.

D'Angelo, C., Scotti, A., 2012. A mixed finite element method for darcy flow in fractured porous media with non-matching grids. ESAIM: Math. Modell. Numer. Anal. 46 (2), 465–489.

De Dreuzy, J.-R., Pichot, G., Poirriez, B., Erhel, J., 2013. Synthetic benchmark for modeling flow in 3d fractured media. Comput. Geosci. 50, 59–71.

Dietrich, P., Helmig, R., Sauter, M., Hötzl, H., Köngeter, J., Teutsch, G., 2005. Flow and Transport in Fractured Porous Media. Springer.

Eymard, R., Gallouët, T., Herbin, R., 2000. Finite Volume Methods. In: Ciarlet, P.G., Lions, J.L. (Eds.), Solution of Equation in $\mathscr{R}^n$ (Part 3), Techniques of Scientific Computing (Part 3). Handbook of Numerical Analysis 7. Elsevier, pp. 713–1018. http://dx.doi.org/10.1016/S1570-8659(00)07005-8.

Firoozabadi, A., Monteagudo, J.E.P., 2004. Control-volume method for numerical simulation of two-phase immiscible flow in two- and three-dimensional discrete-fractured media. Water Resour. Res. 40, W07405. http://dx.doi.org/10.1029/2003WR002996.

Flauraud, E., Nataf, F., Faille, I., Masson, R., 2003. Domain decomposition for an asymptotic geological fault modeling. Comptes Rendus Mécanique 331 (12), 849–855.

Flemisch, B., Darcis, M., Erbertseder, K., Faigle, B., Lauser, A., Mosthaf, K., Müthing, S., Nuske, P., Tatomir, A., Wolff, M., Helmig, R., 2011. DuMu^x: DUNE for multi-{phase, component, scale, physics, ...} flow and transport in porous media. Adv. Water Resour. 34 (9), 1102–1112. http://dx.doi.org/10.1016/j.advwatres.2011.03.007.

Flemisch, B., Fumagalli, A., Scotti, A., 2016. A review of the xfem-based approximation of flow in fractured porous media. In: Ventura, G., Benvenuti, E. (Eds.), Advances in Discretization Methods: Discontinuities, Virtual Elements, Fictitious Domain Methods. Springer International Publishing, Cham, pp. 47–76. http://dx.doi.org/10.1007/978-3-319-41246-7_3.

Flemisch, B., Helmig, R., 2008. Numerical investigation of a mimetic finite difference method. In: Eymard, R., Hérard, J. (Eds.), Finite Volumes for Complex Applications V – Problems and Perspectives. Wiley - VCH, pp. 815–824.

Formaggia, L., Fumagalli, A., Scotti, A., Ruffo, P., 2014. A reduced model for Darcy's problem in networks of fractures. ESAIM: Math. Modell. Numer. Analysis 48, 1089–1116. http://dx.doi.org/10.1051/m2an/2013132.

Frih, N., Martin, V., Roberts, J.E., Saâda, A., 2012. Modeling fractures as interfaces with nonmatching grids. Computat. Geosci. 16 (4), 1043–1060.

Fumagalli, A., Pasquale, L., Zonca, S., Micheletti, S., 2016. An upscaling procedure for fractured reservoirs with embedded grids. Water Resour. Res. 52 (8), 6506–6525. http://dx.doi.org/10.1002/2015WR017729.

Fumagalli, A., Scotti, A., 2014. An efficient XFEM approximation of Darcy flows in fractured porous media. Oil Gas Sci. Technol. - Revue d'IFP Energies Nouvelles 69.4, 555–564.

Gassiat, C., Gleeson, T., Lefebvre, R., McKenzie, J., 2013. Hydraulic fracturing in faulted sedimentary basins: numerical simulation of potential contamination of shallow aquifers over long time scales. Water Resour. Res. 49 (12), 8310–8327. http://dx.doi.org/10.1002/2013WR014287.

Geiger, S., Dentz, M., Neuweiler, I., 2013. A novel multi-rate dual-porosity model for improved simulation of fractured and multiporosity reservoirs. SPE J. 18 (4), 670–684.

Hajibeygi, H., Karvounis, D., Jenny, P., 2011. A hierarchical fracture model for the iterative multiscale finite volume method. J. Comput. Phys. 230 (24), 8729–8743.

Hansbo, A., Hansbo, P., 2002. An unfitted finite element method, based on Nitsche's method, for elliptic interface problems. Comput. Methods Appl. Mech. Eng. 191 (47–48), 5537–5552.

Helmig, R., 1997. Multiphase Flow and Transport Processes in the Subsurface: A Contribution to the Modeling of Hydrosystems, 1 ed. Springer.

Hoteit, H., Firoozabadi, A., 2008. Numerical modeling of two-phase flow in heterogeneous permeable media with different capillarity pressures. Adv. Water Resour. 31 (1), 56–73.

Huang, H., Long, T.A., Wan, J., Brown, W.P., 2011. On the use of enriched finite element method to model subsurface features in porous media flow problems. Computat. Geosci. 15 (4), 721–736.

Karimi-Fard, M., Durlofsky, L.J., Aziz, K., 2004. An efficient discrete-fracture model applicable for general-purpose reservoir simulators. SPE J. 9 (2), 227–236.

Kolditz, O., Shao, H., Wang, W., Bauer, S., 2015. Thermo-Hydro-Mechanical-Chemical Processes in Fractured Porous Media: Modelling and Benchmarking. Springer.

Li, L., Lee, S.H., 2008. Efficient field-scale simulation of black oil in a naturally fractured reservoir through discrete fracture networks and homogenized media. SPE Reservoir Eval. Eng 11, 750–758. http://dx.doi.org/10.2118/103901-PA.

Lie, K.-A., Krogstad, S., Ligaarden, I.S., J. R. Natvig, H.M.N., Skaflestad, B., 2012. Open source matlab implementation of consistent discretisations on complex grids. Computat. Geosci. 16 (2), 297–322.

Logg, A., Mardal, K.-A., Wells, G.N., et al., 2012. Automated Solution of Differential Equations by the Finite Element Method. Springerhttp://dx.doi.org/10.1007/978-3-642-23099-8.

Martin, V., Jaffré, J., Roberts, J.E., 2005. Modeling fractures and barriers as interfaces for flow in porous media. SIAM J. Sci. Comput. 26 (5), 1667–1691.

Moinfar, A., Narr, W., Hui, M.-H., Mallison, B.T., Lee, S.H., 2011. Comparison of discrete-fracture and dual-permeability models for multiphase flow in naturally fractured reservoirs. SPE Reservoir Simulation Symposium. Society of Petroleum Engineers.

Moinfar, A., Varavei, A., Sepehrnoori, K., Johns, R.T., 2014. Development of an efficient embedded discrete fracture model for 3d compositional reservoir simulation in fractured reservoirs. SPE J. 19 (2), 289–303.

Müthing, S., 2015. A Flexible Framework for Multi Physics and Multi Domain PDE Simulations. University of Stuttgart Ph.D. thesis.

Neumann, S.P., 2005. Trends, prospects and challenges in quantifying flow and transport through fractured rocks. Hydrogeol. J. 13, 124–147.

Nordbotten, J., Flemisch, B., Gasda, S., Nilsen, H., Fan, Y., Pickup, G., Wiese, B., Celia, M., Dahle, H., Eigestad, G., Pruess, K., 2012. Uncertainties in practical simulation of CO2 storage. Int. J. Greenhouse Gas Control 9, 234–242. http://dx.doi.org/10.1016/j.ijggc.2012.03.007.

Panfili, P., Cominelli, A., 2014. Simulation of miscible gas injection in a fractured carbonate reservoir using an embedded discrete fracture model. Abu Dhabi International Petroleum Exhibition and Conference, 10–13 November, Abu Dhabi, UAE. Society of Petroleum Engineershttp://dx.doi.org/10.2118/171830-MS.

Panfili, P., Cominelli, A., Scotti, A., 2013. Using Embedded Discrete Fracture Models (EDFMs) to simulate realistic fluid flow problems. Second EAGE Workshop on Naturally Fractured Reservoirs, Muscat, Oman.

Pfunt, H., Houben, G., Himmelsbach, T., 2016. Numerical modeling of fracking fluid migration through fault zones and fractures in the north german basin. Hydrogeol. J. 24 (6), 1343–1358. http://dx.doi.org/10.1007/s10040-016-1418-7.

Reichenberger, V., Jakobs, H., Bastian, P., Helmig, R., 2006. A mixed-dimensional finite volume method for two-phase flow in fractured porous media. Adv. Water Resour. 29 (7), 1020–1036. http://dx.doi.org/10.1016/j.advwatres.2005.09.001.

Sahimi, M., 2011. Flow and Transport in Porous Media and Fractured Rock: From Classical Methods to Modern Approaches. John Wiley & Sons.

Sandve, T.H., Berre, I., Nordbotten, J.M., 2012. An efficient multi-point flux approximation method for discrete fracture-matrix simulations. J. Comput. Phys. 231 (9), 3784–3800. http://dx.doi.org/10.1016/j.jcp.2012.01.023.

Schwenck, N., 2015. An XFEM-Based Model for Fluid Flow in Fractured Porous Media. University of Stuttgart Ph.D. thesis.

Schwenck, N., Flemisch, B., Helmig, R., Wohlmuth, B., 2015. Dimensionally reduced flow models in fractured porous media: crossings and boundaries. Computat. Geosci. 19 (6), 1219–1230. http://dx.doi.org/10.1007/s10596-015-9536-1.

Singhal, B.B.S., Gupta, R.P., 2010. Applied Hydrogeology of Fractured Rocks. Springer Science & Business Media.

Swedish Nuclear Power Inspectorate (SKI), 1987. The International Hydrocoin Project–Background and Results. Paris, France: Organization for Economic Co-operation and Development.

Taherdangkoo, R., Tatomir, A., Taylor, R., Sauter, M., 2017. Numerical investigations of upward migration of fracking fluid along a fault zone during and after stimulation. Energy Procedia 125, 126–135. http://dx.doi.org/10.1016/j.egypro.2017.08.093.

Tatomir, A.-B., 2012. From Discrete to Continuum Concepts of Flow in Fractured Porous Media. Ph.D. thesis. University of Stuttgart.

Tene, M., Bosma, S.B., Kobaisi, M.S.A., Hajibeygi, H., 2017. Projection-based embedded discrete fracture model (pEDFM). Adv. Water Resour. 105, 205–216. http://dx.doi.org/10.1016/j.advwatres.2017.05.009.

Tunc, X., Faille, I., Gallouët, T., Cacas, M.C., Havé, P., 2012. A model for conductive faults with non-matching grids. Computat. Geosci. 16 (2), 277–296.

Paper C

C

Verification benchmarks for single-phase flow in three-dimensional fractured porous media

Bernd Flemisch, Inga Berre, Wietse Boon, Alessio Fumagalli, Dennis Gläser, Eirik Keilegavlen, Anna Scotti, Ivar Stefansson, Alexandru Tatomir, Konstantin Brenner, Samuel Burbulla, Philippe Devloo, Omar Duran, Marco Favino, Julian Hennicker, I-Hsien Lee, Konstantin Lipnikov, Roland Masson, Klaus Mosthaf, Maria Giuseppina Chiara Nestola, Chuen-Fa Ni, K. Nikitin, Philipp Schaedle, Daniil Svyatskiy, Ruslan Yanbarisov, Patrick Zulian

Advances in Water Resources
DOI: doi.org/10.1016/j.advwatres.2020.103759

Advances in Water Resources 147 (2021) 103759

Contents lists available at ScienceDirect

Advances in Water Resources

journal homepage: www.elsevier.com/locate/advwatres

Verification benchmarks for single-phase flow in three-dimensional fractured porous media

Inga Berre[a], Wietse M. Boon[b], Bernd Flemisch[c,*], Alessio Fumagalli[a,d], Dennis Gläser[c], Eirik Keilegavlen[a], Anna Scotti[d], Ivar Stefansson[a], Alexandru Tatomir[e,f], Konstantin Brenner[g], Samuel Burbulla[h], Philippe Devloo[i], Omar Duran[i], Marco Favino[j], Julian Hennicker[k], I-Hsien Lee[l,m], Konstantin Lipnikov[n], Roland Masson[g], Klaus Mosthaf[o], Maria Giuseppina Chiara Nestola[p], Chuen-Fa Ni[l,m], Kirill Nikitin[q], Philipp Schädle[r], Daniil Svyatskiy[n], Ruslan Yanbarisov[q], Patrick Zulian[p]

[a] Department of Mathematics, University of Bergen, Allégaten 41, Bergen 5007, Norway
[b] Department of Mathematics, KTH Royal Institute of Technology, Lindstedtsvägen 25, Stockholm 11428, Sweden
[c] Department of Hydromechanics and Modelling of Hydrosystems, University of Stuttgart, Pfaffenwaldring 61, Stuttgart 70569, Germany
[d] Laboratory for Modeling and Scientific Computing MOX, Politecnico di Milano, p.za Leonardo da Vinci 32, Milano 20133, Italy
[e] Department of Applied Geology, Geosciences Center, University of Göttingen, Goldschmidtstrasse 3, Göttingen 3707, Germany
[f] Department of Earth Sciences, Uppsala University, Villavägen 16, Uppsala S-75236, Sweden
[g] University of Côte d'Azur, CNRS, INRIA, LJAD, Nice, France
[h] Institute of Applied Analysis and Numerical Simulation, University of Stuttgart, Pfaffenwaldring 57, Stuttgart 70569, Germany
[i] FEC-Universidade Estadual de Campinas, R. Josiah Willard Gibbs 85 - Cidade Universitäria, Campinas SP, Brazil, CEP 13083-839
[j] Institute of Earth Sciences, University of Lausanne, Building Geopolis, UNIL-Mouline, Lausanne 1015, Switzerland
[k] Section de Mathématiques, University de Genäve, 2–4 rue du Liävre, CP 64, Genäve 1211, Switzerland
[l] Graduate Institute of Applied Geology, National Central University, Taiwan
[m] Center for Environmental Studies, National Central University, Taiwan
[n] Los Alamos National Laboratory, New Mexico, USA
[o] Department of Environmental Engineering, Technical University of Denmark, Bygningstorvet, Building 115, Lyngby 2800 Kgs., Denmark
[p] Numerical Simulation in Science, Medicine and Engineering Group, Institute of Computational Science, University della Svizzera italiana Via G. Buffi 13, Lugano Ticino 6900, Switzerland
[q] Marchuk Institute of Numerical Mathematics of Russian Academy of Sciences, Moscow, Russia
[r] ETH Zürich, Geothermal Energy and Geofluids Group, Institute of Geophysics, Zürich 8092, Switzerland

A B S T R A C T

Flow in fractured porous media occurs in the earth's subsurface, in biological tissues, and in man-made materials. Fractures have a dominating influence on flow processes, and the last decade has seen an extensive development of models and numerical methods that explicitly account for their presence. To support these developments, four benchmark cases for single-phase flow in three-dimensional fractured porous media are presented. The cases are specifically designed to test the methods' capabilities in handling various complexities common to the geometrical structures of fracture networks. Based on an open call for participation, results obtained with 17 numerical methods were collected. This paper presents the underlying mathematical model, an overview of the features of the participating numerical methods, and their performance in solving the benchmark cases.

1. Introduction

Flow in fractured porous media is characterized by an interaction between the fractures and the surrounding porous medium, commonly referred to as the matrix. The strong influence of fracture network geometry on flow patterns has motivated the development of mathematical models and numerical methods that explicitly account for the geometry of fractures (Berre et al., 2019). Considering flow both in the fractures and in the surrounding porous medium, these models are based on the conceptual discrete-fracture-matrix (DFM) representation of the fractured porous media.

With the development of a wealth of simulation tools for flow in fractured porous media, a need for verification benchmarks for numerical methods has emerged. To accommodate this need, four research groups working in the field initiated a comparison study, which led to the presentation of a suite of two-dimensional benchmark tests and corresponding results for a range of numerical methods (Flemisch et al., 2018). The methods were probed on test cases featuring known

* Corresponding author.
E-mail address: bernd@iws.uni-stuttgart.de (B. Flemisch).

https://doi.org/10.1016/j.advwatres.2020.103759
Received 17 February 2020; Received in revised form 15 September 2020; Accepted 21 September 2020
0309-1708/

difficulties for numerical methods, including fracture intersections and combinations of blocking and conducting fractures. The study exposed the relative strengths and weaknesses between the participating methods, both in terms of accuracy and computational cost. After the publication of the results, these benchmark cases have been widely applied by the scientific community in testing numerical methods and new simulation tools (Arrarás et al., 2019; Budisa and Hu, 2019; Köppel et al., 2019a; 2019b; Odsæter et al., 2019; Schädle et al., 2019).

Based on the reception of the first benchmark study (Flemisch et al., 2018) and the capabilities of three-dimensional modeling in the research community, the next phase in the work on verification benchmarks was launched with a call for participation (Berre et al., 2018). The purpose of this call was to extend the platform of verification benchmarks for numerical methods to three-dimensional problems. In addition, the studies were extended to include simulations of linear tracer transport as a means to highlight additional nuances in the comparison of the calculated flow fields. The present paper discusses the results received as answers to this call.

The paper is organized as follows. In Section 2, an overview of the participation process is given. Section 3 describes the mathematical models for fluid flow and transport in fractured porous media. Section 4 briefly describes the participating numerical methods as well as the discretization of the transport problem. The four test cases are described in Section 5, with each description followed by a presentation and discussion of the corresponding results. Section 6 summarizes the discussion of the results, and Section 7 provides concluding remarks.

2. Benchmark process

The verification benchmark study was laid out as a four-stage process: the development of benchmark cases, a call for participation, collection and synchronization of the results by the participants, and a final discussion and reporting.

The process started with the participants of the first benchmark study (Flemisch et al., 2018) developing four new test cases. These were designed to test the capabilities of numerical methods for DFM representations of flow in three-dimensional fracture networks. The design of each test case was rendered by the "benchmark case designers" listed in the CRediT author statement at the end of the paper. An open call for participation was launched in September 2018 (Berre et al., 2018), followed by a dedicated mini-symposium at the SIAM Conference on Mathematical and Computational Issues in the Geosciences, March 2019, Houston. Researchers interested in participating in the benchmark followed a predefined registration procedure, were approved by the authors issuing the call, and were asked to sign a participation agreement. During this process, applications concerning 15 additional numerical methods were submitted, all of which were approved by the call authors. Finally, the results of 12 of these methods were submitted and included in the study.

The case descriptions presented in the call (Berre et al., 2018) were accompanied by data in the form of geometry descriptions, existing simulation results, and plotting scripts, all available in the Git repository https://git.iws.uni-stuttgart.de/benchmarks/fracture-flow-3d.git. This repository was reused in the fully transparent collection and synchronization phase. During this phase, the results were uploaded and made available to all participants, and recomputations and adjustments were allowed until August 2019. In the fourth phase, all participants contributed to the reporting of the results presented in Section 5. The last two phases were led by assigned "benchmark case coordinators". While access to the Git repository was restricted to the benchmark participants during the phase of collection and comparison of the results, all data have been made publicly available upon submission of this manuscript. In addition to the data and plotting scripts, five Jupyter notebooks are provided, four focusing on reproducing the figures encountered in Section 5, and one for facilitating the comparison of new results.

3. Mathematical models

This section introduces two models for flow and transport in fractured media. First, the flow model is presented in the conventional equi-dimensional setting, allowing a natural introduction to the physical parameters. From this formulation, an appropriate reduction of the equations results in the mixed-dimensional model that forms the focus of this study. Finally, the equi- and mixed-dimensional transport models are presented.

3.1. Equi-dimensional flow model

Consider a steady-state, incompressible, single-phase flow through a porous medium described by Darcy's law. With the imposition of mass conservation, the governing system of equations is given by

$$\begin{aligned} \boldsymbol{u} + \mathbb{K}\nabla h &= 0, \\ \nabla \cdot \boldsymbol{u} &= q, \end{aligned} \quad \text{in } \Lambda. \tag{1a}$$

Here, $\boldsymbol{u}$ denotes the fluid velocity in m/s, $\mathbb{K}$ is hydraulic conductivity measured in m/s, h is hydraulic head measured in m, and q represents a source/sink term measured in 1/s. The domain $\Lambda \subset \mathbb{R}^3$ will be called the equi-dimensional domain. The following boundary conditions on the boundary $\partial\Lambda$ of Λ complete model (1a):

$$\begin{aligned} h &= \overline{h} \quad && \text{on } \partial\Lambda_h, \\ \boldsymbol{u}\cdot\boldsymbol{n} &= \overline{u} \quad && \text{on } \partial\Lambda_u. \end{aligned} \tag{1b}$$

Assume $\partial\Lambda = \partial\Lambda_h \cup \partial\Lambda_u$, $\partial\Lambda_h \cap \partial\Lambda_u = \emptyset$, and $\partial\Lambda_h \neq \emptyset$. $\overline{h}$ is the hydraulic head imposed on the boundary $\partial\Lambda_h$, while $\overline{u}$ is the prescribed Darcy velocity normal to the boundary $\partial\Lambda_u$ with respect to the outer unit normal vector $\boldsymbol{n}$.

By substituting Darcy's law in the mass conservation, the dual problem (1) can be recast in its primal formulation, given by

$$\begin{aligned} -\nabla\cdot\mathbb{K}\nabla h &= q \ \text{ in } \ \Lambda, \\ h &= \overline{h} \ \text{ on } \ \partial\Lambda_h, \\ -\mathbb{K}\nabla h\cdot\boldsymbol{n} &= \overline{u} \ \text{ on } \partial\Lambda_u. \end{aligned} \tag{2}$$

Problems (1) and (2) are equivalent, however, the two formulations (primal and mixed) require different numerical approximation schemes: for instance, while standard FEM can be applied to (2) a mixed approximation scheme is needed for (1). The reader is referred to Chavent and Jaffré (1986) for more details on the formulation, and to Raviart and Thomas (1977), Brezzi and Fortin (1991), Roberts and Thomas (1991), and Ern and Guermond (2004) for an introduction to mixed methods.

Assume that Λ contains several fractures, i.e., thin inclusions in the domain. The fracture walls are assumed to be planar with smooth boundaries. The fractures have two distinguishing features: a) the thickness, measured by the aperture ϵ, is small compared to the spatial extent of the fracture; and b) the hydraulic conductivity may differ significantly from that of the rest of Λ. The latter implies that the fractures may have a significant impact on the flow in Λ.

In the setting of equi-dimensional flow, we further make the assumption that the principal directions of the local hydraulic conductivity tensor are aligned with the orientation of the fractures. In particular, the hydraulic conductivity in the matrix ($\mathbb{K}_3$), the fractures ($\mathbb{K}_2$), as well as in the intersections between two fractures ($\mathbb{K}_1$) and at the crossings of intersections ($\mathbb{K}_0$) are (3×3)-tensors and allow for the following decompositions:

$$\mathbb{K}_3 = K_3^{eq}, \quad \mathbb{K}_2 = \begin{bmatrix} K_2^{eq} & & 0 \\ & & 0 \\ 0 & 0 & \kappa_2^{eq} \end{bmatrix},$$

$$\mathbb{K}_1 = \begin{bmatrix} K_1^{eq} & 0 & 0 \\ 0 & \kappa_1^{eq} & 0 \\ 0 & 0 & \kappa_1^{eq} \end{bmatrix}, \quad \mathbb{K}_0 = \begin{bmatrix} \kappa_0^{eq} & 0 & 0 \\ 0 & \kappa_0^{eq} & 0 \\ 0 & 0 & \kappa_0^{eq} \end{bmatrix}.$$

Here, K_{d}^{eq} denotes the tangential hydraulic conductivity for $d = 1, \dots, 3$ and is thus given by a symmetric, positive definite $(d \times d)$-tensor. Moreover, κ_d^{eq} represents the normal hydraulic conductivity, given by a positive scalar. Note that the normal bundle of a line in 3D is two-dimensional whereas all three basis vectors of $\mathbb{R}^3$ are normal to an intersection point. The actual meaning of "tangential" and "normal" hydraulic conductivity will be clear in the subsequent part. The superscript *eq* indicates that these quantities are related to the equi-dimensional model. The subscript d, on the other hand, indicates that these parameters will be used on d-dimensional objects in the reduced model, which the next section derives.

3.2. Mixed-dimensional flow model

The small aperture of the fractures justifies a reduction of dimensionality to a representation where fractures and their intersections are approximated by lower-dimensional objects. For more details on the derivation of mixed-dimensional models for flow in fractured porous media, the reader is referred to Martin et al. (2005), Angot et al. (2009) and to Kumar et al. (2020), Brenner et al. (2018), Ahmed et al. (2017), List et al. (2020) for extensions concerning two-phase and unsaturated flows.

The mixed-dimensional decomposition of Λ is Ω. It contains the three-dimensional domain Ω_3 that represents the (possibly unconnected) matrix, and, furthermore, up to three lower-dimensional, open subdomains, namely, the union of fracture planes Ω_2, their intersection lines Ω_1 and intersection points Ω_0. Individual lower-dimensional features are referred to as $\Omega_{d,i}$ with d its dimension and i a uniquely assigned counting index. Finally, $\Gamma_d = \Omega_d \cap \partial\Omega_{d+1}$ is the set of d-interfaces between neighboring subdomains of codimension one. Each interface $\Gamma_{d,j}$ is endowed with a unit normal vector $\boldsymbol{n}$. To be mathematically precise, $\boldsymbol{n}$ is chosen from the tangent bundle of the higher-dimensional neighbor $\Omega_{d+1,i}$, is normal to $\Gamma_{d,j}$, and is oriented outward with respect to $\Omega_{d+1,i}$.

Remaining consistent with the notation convention above, data and unknowns will also be annotated with a subscript related to the dimension. As a first example, on a d-dimensional subdomain $\Omega_{d,i}$, let $\epsilon_{d,i}$ denote the cross-sectional volume, area, or length of the corresponding physical domain for $d = 0, \dots, 2$, respectively. It has the unit of measure $\mathrm{m}^{3-\mathrm{d}}$ and its definition extends to the three-dimensional bulk as $\epsilon_3 = 1$. Moreover, a typical length $a_{d,i}$ is defined such that $\epsilon_{d,i} = a_{d,i}^{3-d}$.

The continuation of this subsection presents the reduced model associated with (1) in the two-dimensional fractures Ω_2 followed by its generalization for all $d = 0, \dots, 3$.

3.2.1. Flow in fractures

To present the flow model, the derivation done in Martin et al. (2005) and Boon et al. (2018) has been considered. The variables in this formulation are the velocity $\boldsymbol{u}_3 = \boldsymbol{u}$ and hydraulic head $h_3 = h$ in the rock matrix Ω_3, as well as the integrated tangential velocity $\boldsymbol{u}_2$ and average hydraulic head h_2 in the fracture. These are given pointwise for $x \in \Omega_2$ by

$$\boldsymbol{u}_2(x) = \int_{\epsilon_2(x)} \boldsymbol{u}_{\parallel} \quad \text{and} \quad h_2(x) = \frac{1}{\epsilon_2(x)} \int_{\epsilon_2(x)} h.$$

Here, $\boldsymbol{u}_{\parallel}$ denotes the components of $\boldsymbol{u}$ tangential to Ω_2. The integrals are computed in the normal direction of the fracture, and thus, the corresponding units of measurement are m^3/s and m for $\boldsymbol{u}_2$ and h_2, respectively.

Averaging and integrating, respectively, over the direction normal to the fractures derives the reduced Darcy's law and mass balance equation. Recall that the vector $\boldsymbol{n}$ here refers to the normal unit vector oriented outward from Ω_3. We have

$$\begin{aligned} \tfrac{1}{\epsilon_2}\boldsymbol{u}_2 + K_2^{eq}\nabla_2 h_2 &= 0 \\ \nabla_2 \cdot \boldsymbol{u}_2 - [\![\boldsymbol{u}_3 \cdot \boldsymbol{n}]\!] &= q_2 \end{aligned} \quad \text{in } \Omega_2, \tag{3a}$$

where ∇_2 is the del-operator in the tangential directions and q_2 is the integrated source term, i.e., $q_2(s) = \int_{\epsilon_2(s)} q$.

Note the assumption that K_2^{eq} is constant in the direction normal to Ω_2. The jump operator is defined as $[\![\boldsymbol{u}_3 \cdot \boldsymbol{n}]\!]|_{\Omega_d} = \sum(\boldsymbol{u}_3 \cdot \boldsymbol{n}|_{\Gamma_2})$, thus representing the mass exchange between fracture and matrix. In particular, for each subdomain $\Omega_{2,i} \subseteq \Omega_2$, all flux contributions are summed over sections of Γ_2 that coincide geometrically with $\Omega_{2,i}$. These fluxes are assumed to satisfy the following Darcy-type law given by a finite difference between the hydraulic head in Ω_2 and on $\partial\Omega_3$:

$$\boldsymbol{u}_3 \cdot \boldsymbol{n} + \kappa_2^{eq} \frac{2}{a_d}(h_2 - h_3) = 0 \quad \text{on } \Gamma_2. \tag{3b}$$

3.2.2. Generalization to intersections and complete model

The following generalizes the equations described above to domains of all dimensions, thus including the intersection lines and points. For that purpose, the integrated velocity $\boldsymbol{u}_d$ for $d = 1$ and average hydraulic head h_d with $d = 0, 1$ are introduced, and given pointwise for $x \in \Omega_d$ by

$$\boldsymbol{u}_1(x) = \int_{\epsilon_1(x)} \boldsymbol{u}_{\parallel} \quad \text{and} \quad h_d(x) = \frac{1}{\epsilon_d(x)} \int_{\epsilon_d(x)} h, \text{ for } d = 0, 1.$$

Again, $\boldsymbol{u}_{\parallel}$ denotes the components of $\boldsymbol{u}$ tangential to Ω_1. The corresponding units of measurement are m^2/s and m for $\boldsymbol{u}_1$ and h_d, respectively. The analogs of (3a) on these lower-dimensional manifolds are then given by

$$\begin{aligned} \frac{1}{\epsilon_1}\boldsymbol{u}_1 + K_1^{eq}\nabla_1 h_1 &= 0 \\ \nabla_1 \cdot \boldsymbol{u}_1 - [\![\boldsymbol{u}_2 \cdot \boldsymbol{n}]\!] &= q_1 \quad \text{in } \Omega_1, \\ -[\![\boldsymbol{u}_1 \cdot \boldsymbol{n}]\!] &= q_0 \quad \text{in } \Omega_0. \end{aligned} \tag{4}$$

Here, ∇_1 denotes the del-operator, i.e., the derivative, in Ω_1. For each $\Omega_{d,i}$, the linear jump operator $[\![\cdot]\!]$ is naturally generalized to $[\![\boldsymbol{u}_{d+1} \cdot \boldsymbol{n}]\!]|_{\Omega_{d,i}} = \sum(\boldsymbol{u}_{d+1} \cdot \boldsymbol{n}|_{\Gamma_{d,j}})$, where all flux contributions are summed over sections $\Gamma_{d,j} \subseteq \Gamma_d$ that coincide geometrically with $\Omega_{d,i}$. Finally, q_1 and q_0 correspond to the integrated source terms in the intersection lines and points, respectively.

Due to our choice of defining $\boldsymbol{u}_d$ as the integrated velocity, a scaling with ϵ_{d+1} appears in the equation governing the flux across Γ_d:

$$\frac{1}{\epsilon_{d+1}}\boldsymbol{u}_{d+1} \cdot \boldsymbol{n} + \kappa_d^{eq} \frac{2}{a_d}(h_d - h_{d+1}) = 0 \quad \text{on } \Gamma_d, \ d = 0, 1. \tag{5}$$

Recalling that $\epsilon_3 = 1$, it now follows that the effective tangential and normal hydraulic conductivities are given by:

$$K_{\mathrm{d}} = \epsilon_d K_{\mathrm{d}}^{eq}, \qquad \text{in } \Omega_d, \ d = 1, \dots, 3 \tag{6a}$$

$$\kappa_d = \epsilon_{d+1} \frac{2}{a_d} \kappa_d^{eq}, \qquad \text{on } \Gamma_d, \ d = 0, \dots, 2. \tag{6b}$$

From these definitions, it is clear that the units of K_{d} and κ_d are $\mathrm{m}^{4-\mathrm{d}}/\mathrm{s}$ and $\mathrm{m}^{2-\mathrm{d}}/\mathrm{s}$, respectively.

Collecting the above equations gives the generalization of system (3) to subdomains of all dimensions. The system consists of Darcy's law in both tangential and normal directions followed by the mass conservation equations:

$$\boldsymbol{u}_d + K_{\mathrm{d}}\nabla_d h_d = 0, \qquad \text{in } \Omega_d, \ d = 1, \dots, 3, \tag{7a}$$

$$\boldsymbol{u}_{d+1} \cdot \boldsymbol{n} + \kappa_d(h_d - h_{d+1}) = 0, \quad \text{on } \Gamma_d, \ d = 0, \dots, 2, \tag{7b}$$

$$\nabla_d \cdot \boldsymbol{u}_3 = q_3, \qquad \text{in } \Omega_3, \tag{7c}$$

$$\nabla_d \cdot \boldsymbol{u}_d - [\![\boldsymbol{u}_{d+1} \cdot \boldsymbol{n}]\!] = q_d, \qquad \text{in } \Omega_d, \ d = 1, 2, \tag{7d}$$

$$-[\![\boldsymbol{u}_1 \cdot \boldsymbol{n}]\!] = q_0, \qquad \text{in } \Omega_0. \tag{7e}$$

The source term is given by q_3 for the rock matrix and $q_d(x) = \int_{\epsilon_d(x)} q$ measured in $\mathrm{m}^{3-\mathrm{d}}/\mathrm{s}$.

System (7) is then compactly described by:

$$\boldsymbol{u}_d + K_{\mathrm{d}} \nabla_d h_d = 0, \qquad \text{in } \Omega_d,\ d = 1, \dots, 3, \tag{8a}$$

$$\boldsymbol{u}_{d+1} \cdot \boldsymbol{n} + \kappa_d (h_d - h_{d+1}) = 0, \quad \text{on } \Gamma_d,\ d = 0, \dots, 2, \tag{8b}$$

$$\nabla_d \cdot \boldsymbol{u}_d - [\![\boldsymbol{u}_{d+1} \cdot \boldsymbol{n}]\!] = q_d, \qquad \text{in } \Omega_d,\ d = 0, \dots, 3, \tag{8c}$$

in which the nonphysical $\boldsymbol{u}_4$ and $\boldsymbol{u}_0$ are understood as zero. The boundary conditions are inherited from the equidimensional model with the addition of a no-flux condition at embedded fracture endings:

$$h_d = \overline{h} \qquad \text{on } \partial\Omega_d \cap \partial\Lambda_h,\ d = 0, \dots, 3, \tag{9a}$$

$$\boldsymbol{u}_d \cdot \boldsymbol{n} = \varepsilon_d \overline{u} \qquad \text{on } \partial\Omega_d \cap \partial\Lambda_u,\ d = 1, \dots, 3, \tag{9b}$$

$$\boldsymbol{u}_d \cdot \boldsymbol{n} = 0 \qquad \text{on } \partial\Omega_d \backslash (\Gamma_{d-1} \cup \partial\Lambda),\ d = 1, \dots, 3. \tag{9c}$$

Finally, this section presents the primal formulation of the mixed-dimensional fracture flow model. Analogous to (2), this formulation is derived by substituting Darcy's laws (8a) and (8b) into the conservation Eq. (8c):

$$-\nabla_d \cdot K_{\mathrm{d}} \nabla_d h_d + [\![\kappa_d (h_d - h_{d+1})]\!] = q_d, \text{ in } \Omega_d,\ d = 0, \dots, 3. \tag{10}$$

Again, the divergence term is interpreted as zero if $d = 0$ and the jump term as zero if $d = 3$. The boundary conditions are given by

$$h_d = \overline{h} \qquad \text{on } \partial\Omega_d \cap \partial\Lambda_h,\ d = 0, \dots, 3, \tag{11a}$$

$$-K_{\mathrm{d}} \nabla_d h_d \cdot \boldsymbol{n} = \varepsilon_d \overline{u} \qquad \text{on } \partial\Omega_d \cap \partial\Lambda_u,\ d = 1, \dots, 3, \tag{11b}$$

$$-K_{\mathrm{d}} \nabla_d h_d \cdot \boldsymbol{n} = 0 \qquad \text{on } \partial\Omega_d \backslash (\Gamma_{d-1} \cup \partial\Lambda),\ d = 1, \dots, 3. \tag{11c}$$

Many discretization schemes presented in this study ignore flow in the one-dimensional fracture intersections and zero-dimensional intersections thereof. Although these correspond to discretizing a simpler model, this is perfectly in line with the proposed study.

3.3. Equi-dimensional transport model

A scalar quantity c with the unit of measure m^{-3} is transported through the porous medium subject to the velocity field resulting from the flow model presented in the previous sections. The purely advective transport of c is described by the conservation equation:

$$\phi \frac{\partial c}{\partial t} + \nabla \cdot (c \boldsymbol{u}) = q_c \quad \text{in } \Lambda, \tag{12}$$

where ϕ is the porosity of the medium and q_c is a source/sink term for c given in m^{-3}/s. Boundary segments where inflow occurs have Dirichlet boundary conditions, i.e.,

$$c|_{\partial\Lambda_c} = \overline{c} \quad \text{on } \partial\Lambda_c, \quad \partial\Lambda_c = \{x \in \partial\Lambda : \ \boldsymbol{u} \cdot \boldsymbol{n} < 0\}, \tag{13}$$

with $\overline{c}$ being the value for c prescribed on the boundary $\partial\Lambda_c$.

3.4. Mixed-dimensional transport model

Analogous to Section 3.2, the average value for c is chosen as the primary variable, which is defined as $c_3 = c$ in Ω_3 and for the lower dimensional objects (with $d \leq 2$) as

$$c_d(s) = \frac{1}{\varepsilon_d(s)} \int_{\varepsilon_d(s)} c.$$

Following the derivation of the mixed-dimensional flow model presented in Section 3.2, the resulting mixed-dimensional transport model reads as:

$$\varepsilon_d \phi_d \frac{\partial c_d}{\partial t} + \nabla_d \cdot \left(c_d \boldsymbol{u}_d \right) - [\![\tilde{c}_{d+1} \left(\boldsymbol{u}_{d+1} \cdot \boldsymbol{n} \right)]\!] = q_{c,d} \quad \text{in } \Omega_d, \quad d = 0, \dots, 3. \tag{14}$$

Note that for $d = 0$, the divergence term is void and for $d = 3$ the contribution of the jump operator is set to null. Here, the porosity is simply $\phi_d = \phi^{eq}$ and $\tilde{c}_{d+1}$ is evaluated on the basis of a first-order upwind scheme, i.e.,

$$\tilde{c}_{d+1} = \begin{cases} c_{d+1} & \text{if } \ \boldsymbol{u}_{d+1} \cdot \boldsymbol{n}|_{\Gamma_d} > 0 \\ c_d & \text{if } \ \boldsymbol{u}_{d+1} \cdot \boldsymbol{n}|_{\Gamma_d} < 0. \end{cases} \tag{15}$$

As in the flow model, the jump operator represents the sum of the fluxes over all contributions defined on sections of Γ_d that coincide geometrically with $\Omega_{d,i}$.

4. Participating discretization methods

The intent of this benchmark study is to quantitatively evaluate different discretization schemes for the mixed-dimensional flow models (8)-(11). The modeling error resulting from averaging the underlying equi-dimensional models is deliberately disregarded. In the sense of this study, the solution to be approximated by the participating methods is the solution to the corresponding mixed-dimensional model, not the equi-dimensional one. For a detailed benchmark study taking into account the modeling error from averaging, see Flemisch et al. (2018). As a means of evaluating a discrete solution, the velocities were inserted into a standard cell-centered, first-order upwind scheme for the transport Eq. (14). The temporal discretization is given by the implicit Euler method with a fixed time-step prescribed for each test case. The main properties of the discretization methods covered by the benchmark are summarized in Tables 1 and 2, which also contain references for further details. The majority of the methods followed the mixed-dimensional flow model and the specified transport discretization, with the following exceptions:

The schemes `NCU_TW-Hybrid_FEM` and `DTU-FEM_COMSOL` describe the flow along the fractures by additional terms defined on the fracture surfaces. This effectively adds connectivity between the degrees of freedom located on fractures without introducing additional degrees of freedom. This means that these schemes do not solve the mass balances (8c) for $d < 3$. Moreover, this approach implies continuity of the hydraulic head across the fractures and therefore replaces the coupling condition (8b). Other schemes participating in this study also assume continuity of the hydraulic head across the fractures, and a complete overview is given in Table 2.

The scheme `UNIL_USI-FE_AMR_AFC` is an equi-dimensional approach, meaning that the fractures, their intersections, and intersections of intersections are discretized with three-dimensional elements using locally refined grids. Therefore, the lower-dimensional mass balances (8c) for $d < 3$ and the coupling conditions (8b) are not relevant for this scheme.

Finally, the schemes `ETHZ_USI-FEM_LM` and `UNIL_USI-FE_AMR_AFC` do not use a first-order upwind scheme but apply an algebraic flux correction technique for the stabilization of a finite element discretization of the transport model (Kuzmin et al., 2012). Such stabilization techniques provide a similar discretization as the given upwind scheme.

5. Benchmark cases and results

This section presents the benchmark cases and compares the submitted results. For each case, the hydraulic head and tracer concentration are compared using several predefined macroscopic metrics. In Section 5.1, a benchmark case containing a single fracture problem is considered. Section 5.2 presents a benchmark based on a synthetic network composed of nine regularly arranged fractures. The benchmark case in Section 5.3 considers the geometrically challenging case of almost intersecting fractures, fractures with small intersections, and other features that a fracture network may exhibit. Finally, Section 5.4 studies a case with 52 fractures selected from a real network.

Table 1
Names, acronyms, references and test cases covered for all participating discretization methods.

Acronym	References	Open source code	Run scripts	Test cases
	Two-point flux approximation			
UiB-TPFA	Keilegavlen et al. (2019) and Nordbotten et al. (2019)	✓[a]	✓[b]	1–4
	Multi-point flux approximation			
UiB-MPFA	Keilegavlen et al. (2019) and Nordbotten et al. (2019)	✓[a]	✓[b]	1–4
	Lowest order mixed virtual element method			
UiB-MVEM	Keilegavlen et al. (2019) and Nordbotten et al. (2019)	✓[a]	✓[b]	1–4
	Lowest order Raviart-Thomas mixed finite elements			
UiB-RT0	Keilegavlen et al. (2019), Nordbotten et al. (2019), and Boon et al. (2018)	✓[a]	✓[b]	1–4
	Multi-point flux approximation			
USTUTT-MPFA	Koch et al. (2020)	✓[c]	✓[d]	1–4
	Two-point flux approximation			
USTUTT-TPFA_Circ	Koch et al. (2020)	✓[c]	✓[d]	1–4
	Mimetic Finite Differences			
LANL-MFD	Lipnikov et al. (2014)	✓[e]	×	1–4
	Hybrid finite element method			
NCU_TW-Hybrid_FEM	Lee and Ni (2015) and Lee et al. (2019)	×	×	1
	Vertex Approximate Gradient continuous hydraulic head			
UNICE_UNIGE-VAG_Cont	Brenner et al. (2016a)	×	×	1–4
	Hybrid Finite Volumes continuous hydraulic head			
UNICE_UNIGE-HFV_Cont	Brenner et al. (2016a)	×	×	1–4
	Vertex Approximate Gradient discontinuous hydraulic head			
UNICE_UNIGE-VAG_Disc	Brenner et al. (2016b)	×	×	1–4
	Hybrid Finite Volumes discontinuous hydraulic head			
UNICE_UNIGE-HFV_Disc	Brenner et al. (2016b)	×	×	1–4
	Lagrange multiplier - L2-projection finite elements			
ETHZ_USI-FEM_LM	Schädle et al. (2019), Köppel et al. (2019b), and Krause and Zulian (2016)	✓Zulian et al. (2016)	×	1–4
	Hybrid H(div)			
UNICAMP-Hybrid_Hdiv	Devloo et al. (2019) and Durán et al. (2019)	✓[f]	✓[f]	1–4
	Flux-corrected finite element method and adaptive mesh refinement			
UNIL_USI-FE_AMR_AFC	Favino et al. (2020) and Kuzmin et al. (2012)	✓Zulian et al. (2016)	×	1–3
	Embedded discrete fracture method			
INM-EDFM	Nikitin and Yanbarisov (2020)	×	×	1,3
	First-order Lagrangian finite elements (COMSOL)			
DTU-FEM_COMSOL	COMSOL (2019)[g]	×	✓Berre et al. (2020)	1–4

[a] https://github.com/pmgbergen/porepy. 2019.
[b] https://github.com/pmgbergen/arXiv_1809_06926. 2019.
[c] https://git.iws.uni-stuttgart.de/dumux-repositories/dumux. 2019.
[d] https://git.iws.uni-stuttgart.de/dumux-pub/berre2020. 2020.
[e] https://github.com/amanzi. 2019.
[f] https://github.com/labmec/HDiv/tree/master/HDiv_Benchmarks. 2019.
[g] https://www.comsol.com/release/5.4. 2019.

The reasoning behind the design of the four cases is to isolate typical challenges encountered in practice by means of dedicated synthetic scenarios. The focus is always on the behavior of the discretization methods in the presence of fractures. While considering a full geologically relevant outcrop model would be interesting, adding such a case would make it impossible to track down the reasons for differences in the results and is therefore out of scope for this study. For similar reasons, investigating strong local heterogeneities in the matrix itself as well as upscaling approaches are excluded.

5.1. Case 1: Single fracture

5.1.1. Description

Fig. 1 illustrates the first benchmark case, with a geometry that is slightly modified from works Zielke et al. (1991) and Barlag et al. (1998). The domain Ω is a cube-shaped region (0m, 100m) × (0m, 100m) × (0m, 100m) which is crossed by a planar fracture, Ω_2, with a thickness of 0.01m. The matrix domain consists of subdomains $\Omega_{3,1}$ above the fracture and $\Omega_{3,2}$ and $\Omega_{3,3}$ below. The subdomain $\Omega_{3,3}$ represents a heterogeneity within the rock matrix. Inflow

Table 2
Numerical properties for the discretization methods. An entry in the column "conforming" can be "fully" if each fracture element needs to coincide with a facet shared by two neighboring matrix elements, "geometrically" if each fracture needs to be a union of element facets from each of the two neighboring matrix subdomain meshes, or "none" if fracture and matrix meshes can be completely independent of each other.

Acronym	Degrees of freedom	Local mass conservation	Allows h discontinuity	Conformity	Subdomain dimensions
UiB-TPFA	h (elem), λ (mortar flux)	✓	✓	Geometrically	0–3
UiB-MPFA	h (elem), λ (mortar flux)	✓	✓	Geometrically	0–3
UiB-MVEM	h (elem), $\boldsymbol{u}$ (faces), λ (mortar flux)	✓	✓	Geometrically	0–3
UiB-RT0	h (elem), $\boldsymbol{u}$ (faces), λ (mortar flux)	✓	✓	Geometrically	0–3
USTUTT-MPFA	h (elem)	✓	✓	Fully	2–3
USTUTT-TPFA_Circ	h (elem)	✓	✓	Fully	2–3
LANL-MFD	h (faces)	✓	✓	Fully	2–3
NCU_TW-Hybrid_FEM	h, $\boldsymbol{u}$ (nodes)	✓	×	Fully	2–3
UNICE_UNIGE-VAG_Cont	h (nodes), (fracture faces)	✓	×	Conforming	2–3
UNICE_UNIGE-VAG_Disc	h (nodes), (fracture faces)	✓	✓	Conforming	2–3
UNICE_UNIGE-HFV_Cont	h (faces), (fracture edges)	✓	×	Conforming	2–3
UNICE_UNIGE-HFV_Disc	h (faces), (fracture edges)	✓	✓	Conforming	2–3
ETHZ_USI-FEM_LM	h (nodes) λ (nodes)	×	×	None	2–3
UNICAMP-Hybrid_Hdiv	h, $\boldsymbol{u}$ (elem), λ (faces)	✓	✓	Geometrically	0–3
UNIL_USI-FE_AMR_AFC	h (nodes)	✓	×	Not applicable	equi-dim.
INM-EDFM	h (elem)	✓	×	None	2–3
DTU-FEM_COMSOL	h (nodes)	✓	×	Fully	2–3

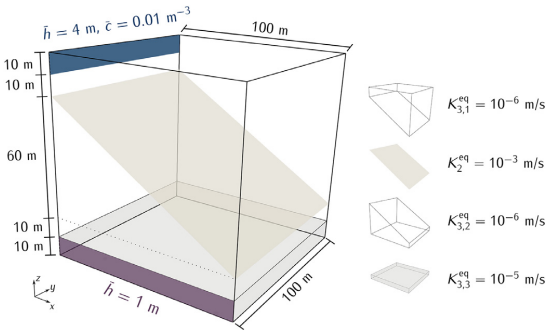

Fig. 1. Conceptual model and geometrical description of the domain for Case 1 of Section 5.1. Inlet and outlet part of the boundary are indicated in blue and purple, respectively. (For interpretation of the references to color in this figure legend, the reader is referred to the web version of this article.)

into the system occurs through a narrow band defined by {0m} × (0m, 100m) × (90m, 100m). Similarly, the outlet is a narrow band defined by (0m, 100m) × {0m} × (0m, 10m).

At the inlet and outlet bands, the hydraulic head is set to $h_{in} = 4$m and $h_{out} = 1$m respectively, and $c_{in} = 0.01\text{m}^{-3}$ is set at the inlet for the transport problem. All remaining parts of the boundary are assigned no-flow conditions. The parameters for conductivity, porosity, and aperture are listed in Table 3 together with the overall simulation time and time-step size.

5.1.2. Results

Three different simulations were carried out with approximately 1k, 10k and 100k cells for the 3d domain. The precise number of cells and degrees of freedom for each method are listed in Table A.7 and will be discussed in Section 5.1.2.7. The basis for comparison of the methods is computed pressure head and concentration, plotted along prescribed lines. The first comparison, represented in Section 5.1.2.1, depicts the hydraulic head along a line crossing the 3d matrix domain, while the solutions reported in 5.1.2.2 and 5.1.2.3 visualize the matrix and fracture concentration along lines at the final simulation time. The purpose of these three plots is to visualize the spread of the solutions, in particular its reduction upon grid refinement. To this end, for a quantity such as the concentration c let $c^{[i]}$ denote the i-th percentile of the provided numerical solutions. The quantification of the spread of the solutions along a given line ξ is based on the following measures:

$$\sigma_c^{[i]} = \frac{c^{[i]} - c^{\text{ref}}}{\bar{c}^{\text{ref}}}, \qquad \sigma_c = \frac{\int_\xi \left(c^{[90]} - c^{[10]}\right) \mathrm{d}x}{\int_\xi c^{\text{ref}} \, \mathrm{d}x}. \tag{16}$$

Here, c^{ref} is the reference solution and $\bar{c}^{\text{ref}}$ is its average over ξ. We note that σ_c is equal to the mean of $(\sigma_c^{[90]} - \sigma_c^{[10]})$ over ξ.

Plots in Section 5.1.2.4 and 5.1.2.5 depict integrated matrix and fracture concentrations over time, respectively. Finally, Section 5.1.2.6 presents comparison of concentration fluxes across the outlet over time.

Table 3
Parameters used in Case 1 of Section 5.1.

Matrix hydraulic conductivity $K_{3,1}$, $K_{3,2}$	$1 \times 10^{-6} \boldsymbol{I}$	m/s
Matrix hydraulic conductivity $K_{3,3}$	$1 \times 10^{-5} \boldsymbol{I}$	m/s
Fracture effective tangential hydraulic conductivity K_2	$1 \times 10^{-3} \boldsymbol{I}$	m^2/s
Fracture effective normal hydraulic conductivity κ_2	20	1/s
Matrix porosity $\phi_{3,1}$, $\phi_{3,2}$	2×10^{-1}	
Matrix porosity $\phi_{3,3}$	2.5 × 10−1	
Fracture porosity ϕ_2	4×10^{-1}	
Fracture cross-sectional length ϵ_2	1×10^{-2}	m
Total simulation time	1×10^9	s
Time-step Δt	1×10^7	s

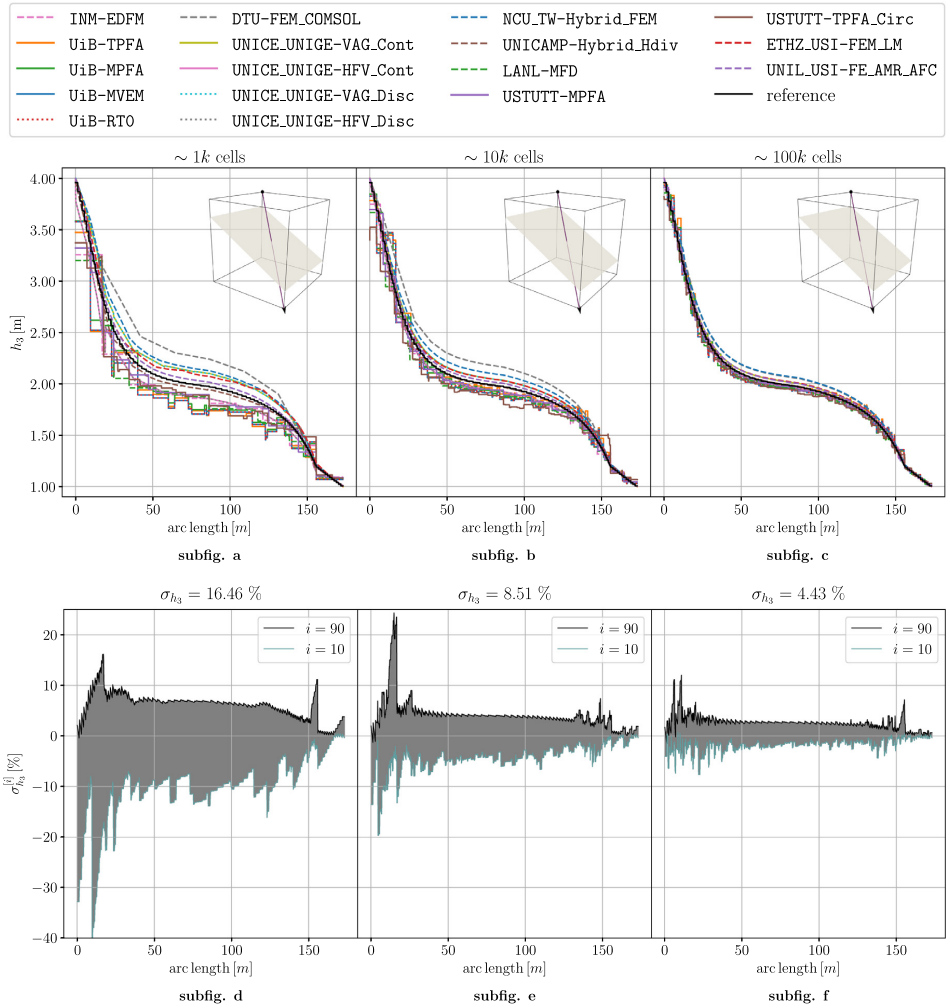

Fig. 2. Case 1 of Section 5.1. On the top, the hydraulic head h_3 in the matrix over the line (0m, 100m, 100m) - (100m, 0m, 0m) for three refinements (coarse to fine). The reference was computed with the USTUTT-MPFA scheme on a refined grid with 1,991,176 cells Gläser (2020). On the bottom, the deviations $\sigma^{[90]}_{h_3}$ and $\sigma^{[10]}_{h_3}$ from the reference solution are illustrated, as defined in (16). Results of Section 5.1.2.1.

5.1.2.1. Hydraulic Head Over Line. Fig. 2 depicts the hydraulic head h_3 in the matrix along the line (0m, 100m, 100m) − (100m, 0m, 0m). Each plot corresponds to one of the three refinement levels.

At the coarsest level of around 1000 cells, all methods already show reasonable agreement. As expected, differences between the methods as well as to the reference solution decrease with increasing refinement level. Two classes of methods can be distinguished in these plots. First, the methods that use cellwise constant values exhibit staircase-like patterns. On the other hand, methods using nodal values are interpolated within each cell and yield a smoother appearance.

To quantify the differences between the participating methods and their convergence behavior over all refinement levels, the spread of the associated data sets is evaluated as outlined above and visualized in the bottom row of pictures. The number σ_{h_3} in each picture's title is calculated by (16) and quantifies the observed convergence behavior. The spikes in the local differences obviously result from the cellwise constant solution values. While a possible post-processing procedure could have reduced these differences, it would obscure the differences in the raw result data and is therefore excluded deliberately.

5.1.2.2. Matrix Concentration Over Line. The pictures at the top of Fig. 3 illustrate the concentration c_3 in the matrix at the final simulation time along the line (0m, 100m, 100m) − (100m, 0m, 0m), again for the different refinement levels. The behavior is similar to that in 5.1.2.1 in the sense that the differences between most of the methods decrease with increasing refinement level. However, two methods show more pronounced deviations from the rest: ETHZ_USI-FEM_LM exhibits oscillations that can be attributed to the fact that the employed algebraic flux correction stabilization scheme does not suppress all spurious oscillations. The NCU_TW-Hybrid_FEM does not capture the curve behavior at all. The obviously larger spread in the results is visualized more explicitly in the bottom row of Fig. 3, showing much slower convergence compared to

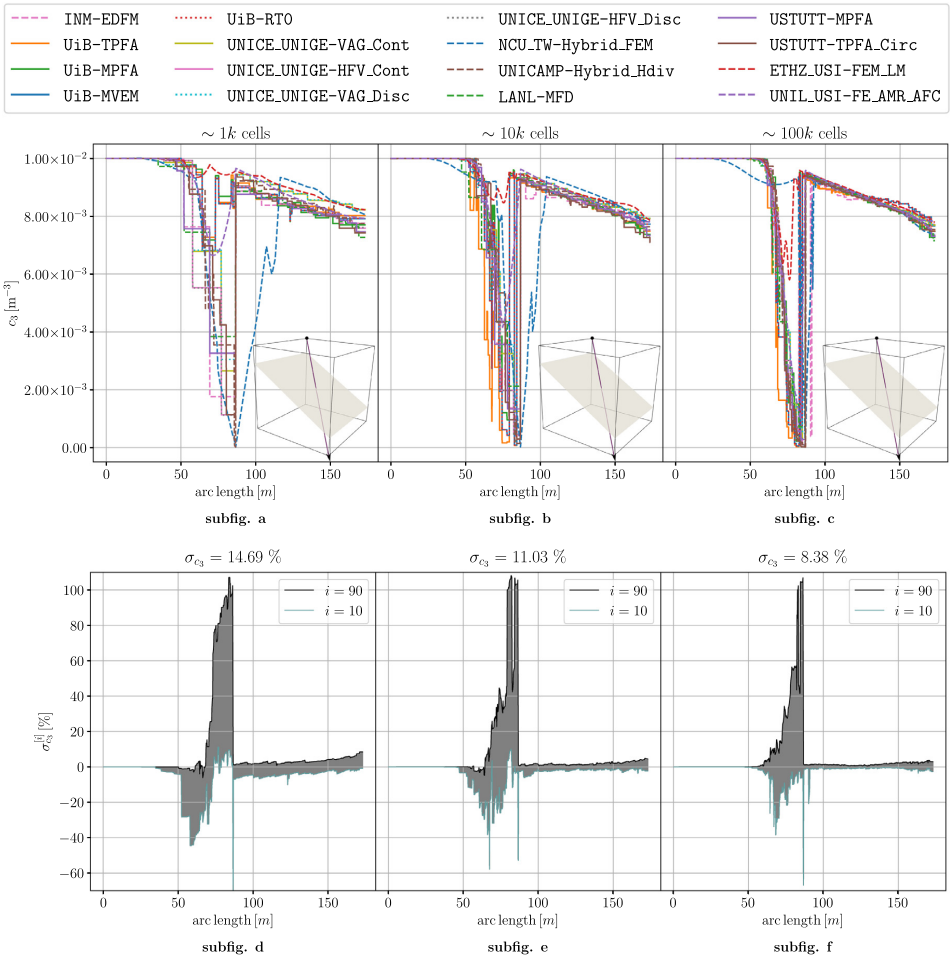

Fig. 3. Case 1 of Section 5.1. On the top, concentration c_3 in the matrix, at the final simulation time, along the line (0m, 100m, 100m) - (100m, 0m, 0m) for three refinements (coarse to fine). On the bottom, the deviations $\sigma_{c_3}^{[90]}$ and $\sigma_{c_3}^{[10]}$ from the median $c_3^{\text{ref}} = c_3^{[50]}$ of the solutions on the finest grid are illustrated. Results of Section 5.1.2.2.

Section 5.1.2.1. The magnitude of the local spread is clearly influenced by the presence of the fracture.

5.1.2.3. Fracture Concentration Over Line. Fig. 4 shows the concentration c_2 within the fracture at the final simulation time along the line (0m, 100m, 80m) − (100m, 0m, 20m).

Again, almost all methods appear to converge with increasing refinement. NCU_TW-Hybrid_FEM exhibit the largest deviations over all refinement levels. Close to the outlet boundary, ETHZ_USI-FEM_LM yields rather different values than the rest of the methods, but it clearly approaches the other methods with increasing refinement. Minor deviations close to the outlet can also be observed for INM-EDFM, UiB-RT0 and UiB-MVEM which become more pronounced for higher refinement levels. Moreover, UiB-TPFA obviously underestimates the concentration in the medium observed arc length for the finest grids. Looking at the bottom row of Fig. 4, the convergence behavior of the spread is better than that of the matrix concentration reported in Section 5.1.2.2, yet worse than for the matrix hydraulic head in Section 5.1.2.1. Since the inflow boundary with an associated Dirichlet boundary condition is located at the beginning of the line, the spread is considerably lower there and increases over the arc length, i.e., the distance to this boundary.

5.1.2.4. Integrated Matrix Concentration Over Time. Unlike the first three plots in 5.1.2.1–5.1.2.3, Fig. 5 illustrates an integrated quantity over time, namely, the integrated matrix concentration $\int_{\Omega_{3,3}} \phi_3 c_3 \, \mathrm{d}x$. Correspondingly, all curves appear much smoother than above. Over the three refinement levels, most methods again exhibit decreasing differences between each other. Remarkably, the UiB-TPFA shows a pronounced underestimation that increases over time. This can be explained by the inconsistency of the employed two-point flux approximation on the tetrahedral grids. Additionally, the NCU_TW-Hybrid_FEM and ETHZ_USI-FEM_LM again exhibit larger differences.

5.1.2.5. Integrated Fracture Concentration Over Time. Analogously, the integrated fracture concentration $\int_{\Omega_2} \epsilon_2 \phi_2 c_2 \, \mathrm{d}x$ for each time-step is visualized in Fig. 6. The behavior of the curves is generally different from that reported in Section 5.1.2.4, as the fracture fills up completely before the final simulation time. Here, the UiB-TPFA is in

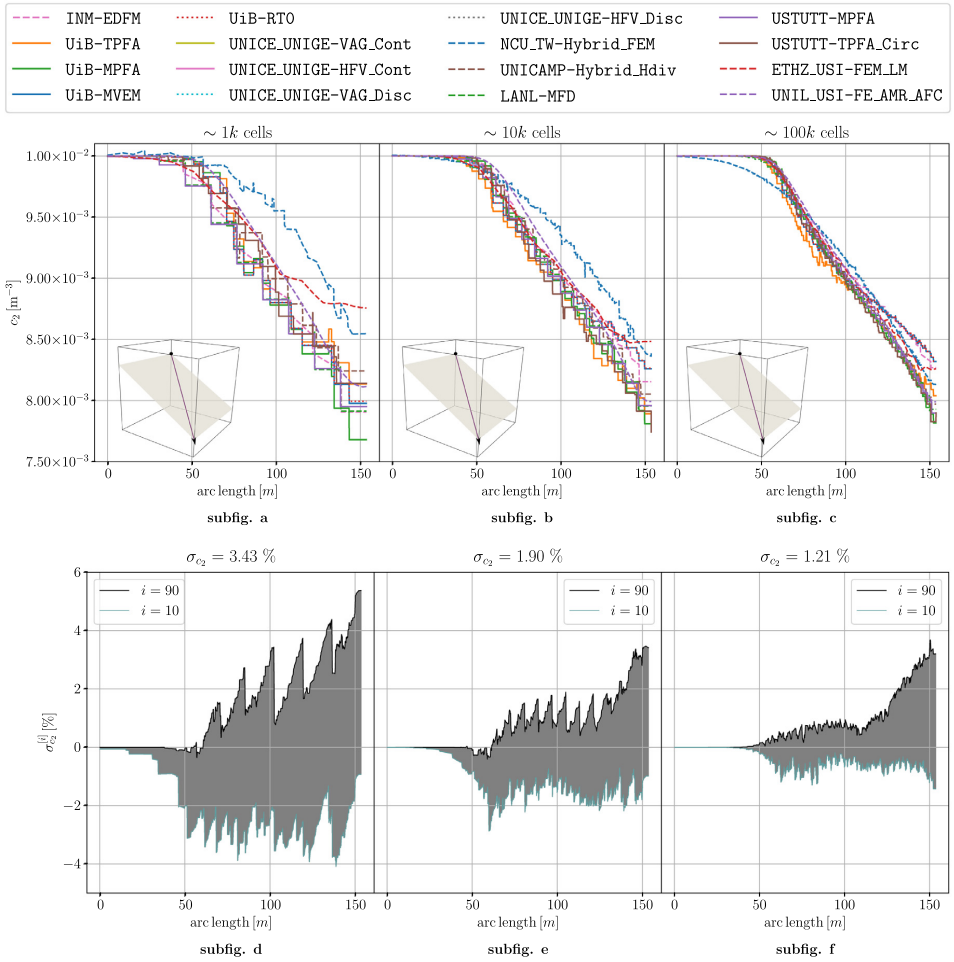

Fig. 4. Case 1 of Section 5.1. On the top, concentration c_2 within the fracture, at the final simulation time, along the line (0m, 100m, 80m) − (100m, 0m, 20m) for three refinements (coarse to fine). On the bottom, the deviations $\sigma_{c_2}^{[90]}$ and $\sigma_{c_2}^{[10]}$ are illustrated, as defined in (16). Here, the median $c_2^{[50]}$ of the solutions on the finest grid is used as the reference solution c_2^{ref}. Results of Section 5.1.2.3.

line with the other methods whereas the NCU_TW-Hybrid_FEM and ETHZ_USI-FEM_LM both deviate from the majority.

5.1.2.6. Concentration Flux Across the Outlet Over Time. Finally, Fig. 7 depicts the integrated concentration flux across the outlet boundary over time. Compared to the results in Section 5.1.2.5, the agreement between the methods appears to be poorer. In particular, the two-point flux approximation of the UiB-TPFA results in an underestimation similar to that reported in 5.1.2.4. Again, ETHZ_USI-FEM_LM and NCU_TW-Hybrid_FEM yield considerably different results at all refinement levels.

5.1.2.7. Computational Cost. Indicators for the computational costs associated with the different methods are presented in Table A.7. Most methods satisfy the prescribed numbers of elements. The most notable exception is given by the NCU_TW-Hybrid_FEM, where six to ten times as many tetrahedral elements have been employed, to compensate for the fact that the degrees of freedom are associated with the vertices. The number of vertices are in line with the prescribed cell numbers. The relations of the number of degrees of freedom to the number of cells vary considerably between the different schemes, reflecting the characteristics from Table 2. The lowest of such numbers are for the purely head- and vertex-based schemes on tetrahedra for the NCU_TW-Hybrid_FEM and DTU-FEM_COMSOL, while the highest ones result from the schemes that have head and velocity values as degrees of freedom. Additionally, the ratios of the number of nonzero entries to the number of degrees of freedom exhibit a large variability, ranging from approximately 5 (TPFA on tetrahedrons) to 30 (MPFA schemes with only head degrees of freedom).

5.2. Case 2: Regular fracture network

5.2.1. Description

The second benchmark is a three-dimensional analog of the two-dimensional test case 4.1 from the benchmark study (Flemisch et al., 2018). The domain is given by the unit cube $\Omega = (0\text{m}, 1\text{m})^3$ and contains

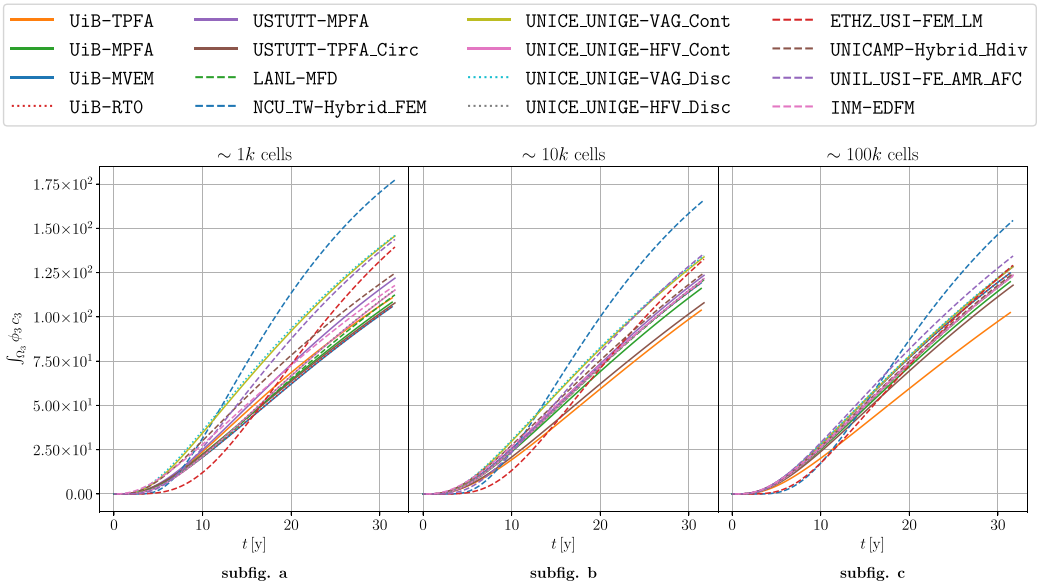

Fig. 5. Case 1 of Section 5.1. Integrated matrix concentration $\int_{\Omega_3} \phi_3 c_3 \, \mathrm{d}x$ for three refinements (coarse to fine). Results of Section 5.1.2.4.

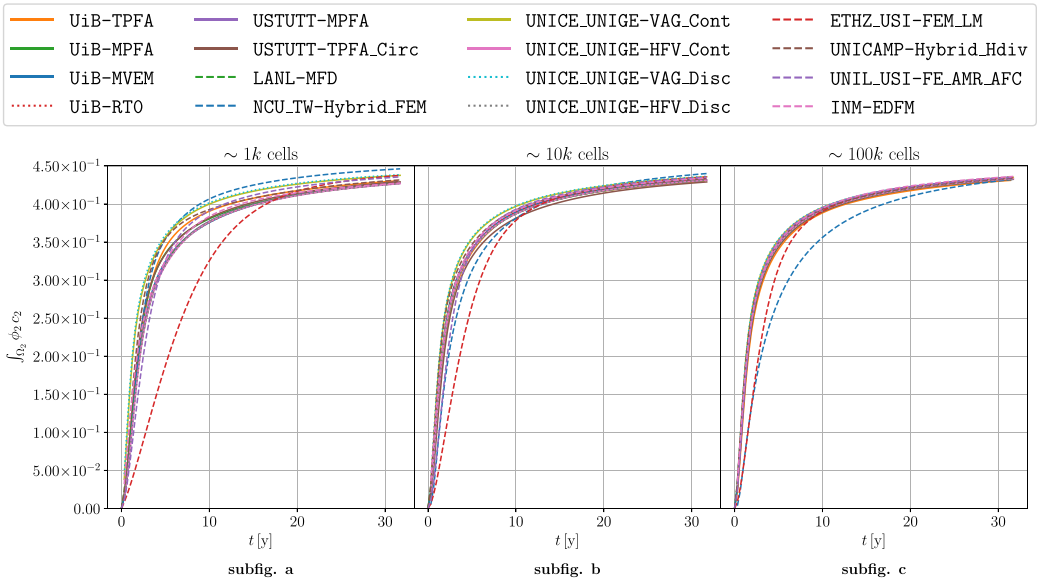

Fig. 6. Case 1 of Section 5.1. Integrated fracture concentration $\int_{\Omega_2} \epsilon_2 \phi_2 c_2 \, \mathrm{d}x$ over time for three refinements (coarse to fine). Results of Section 5.1.2.5.

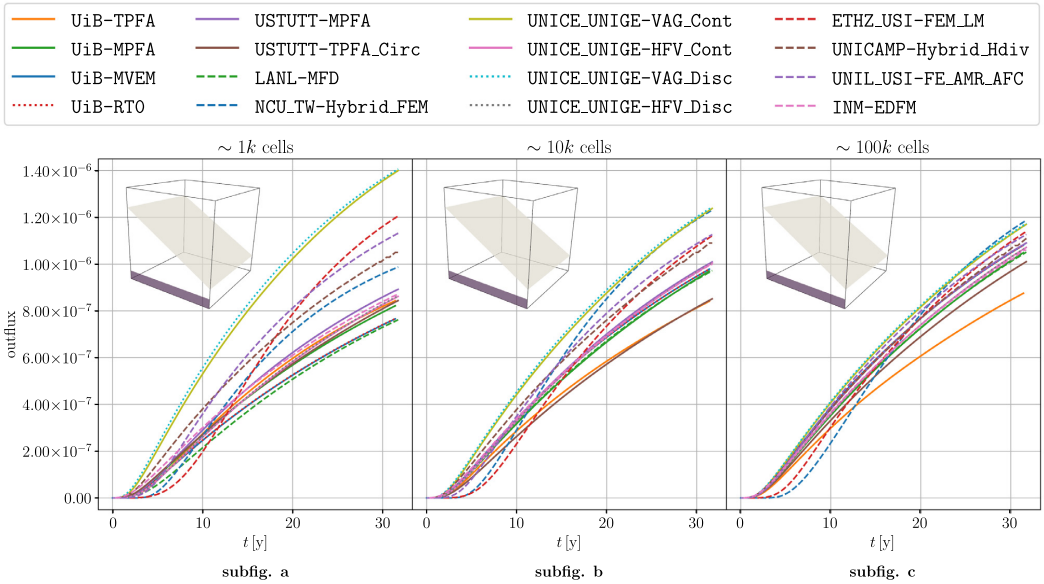

Fig. 7. Case 1 of Section 5.1. Integrated flux of c across the outlet boundary over time for three refinements (coarse to fine). Results of Section 5.1.2.6.

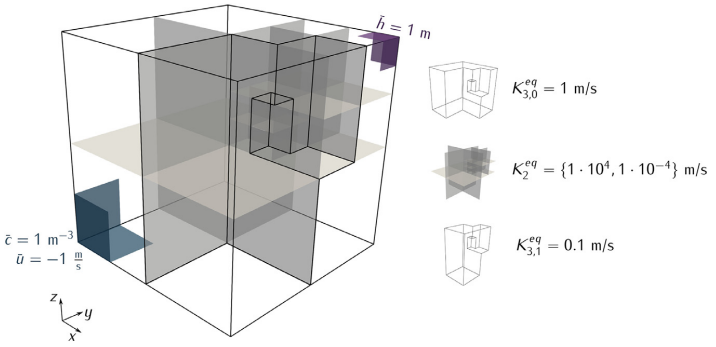

Fig. 8. Representation of the domain ($\Omega_3 = (0\text{m}, 1\text{m})^3$) and the fractures for Case 2 of Section 5.2. The inlet and outlet boundaries are colored in blue and purple, respectively, and on the right side, the permeability distributions among Ω_3 and Ω_2 are illustrated. (For interpretation of the references to color in this figure legend, the reader is referred to the web version of this article.)

9 regularly oriented fractures, as illustrated in Fig. 8. The boundary $\partial\Omega$ is decomposed into three parts, each corresponding to a chosen boundary condition (see Fig. 8). First, $\partial\Omega_h = \{(x, y, z) \in \partial\Omega : x, y, z > 0.875\text{m}\}$ is the part of the boundary where $\bar{h} = 1\text{m}$. Second, a flux boundary condition is set on $\partial\Omega_{in} = \{(x, y, z) \in \partial\Omega : x, y, z < 0.25\text{m}\}$ by imposing $\bar{u} = -1\text{m/s}$. On the remainder of the boundary of Ω, no-flow conditions are imposed.

Two variants of the test case are considered: Case 2.1 has highly conductive fractures and Case 2.2 has blocking fractures. In both cases, different hydraulic conductivities are prescribed in the following matrix subregions:

$$\begin{aligned}
\Omega_{3,0} &= \Omega_3 \setminus \Omega_{3,1} \\
\Omega_{3,1} &= \{(x, y, z) \in \Omega_3 : x > 0.5\text{m} \cap y < 0.5\text{m}\} \\
&\quad \cup \{(x, y, z) \in \Omega_3 : x > 0.75\text{m} \cap 0.5\text{m} < y < 0.75\text{m} \cap z > 0.5\text{m}\} \\
&\quad \cup \{(x, y, z) \in \Omega_3 : 0.625\text{m} < x < 0.75\text{m} \cap 0.5\text{m} \\
&\quad < y < 0.625\text{m} \cap 0.5\text{m} < z < 0.75\text{m}\}.
\end{aligned}$$

The right part of Fig. 8 illustrates these regions. A complete overview of the parameters used in this test case is given in Table 4.

Finally, for the transport problem, a unitary concentration is imposed at the inflow boundary $\partial\Omega_{in}$.

5.2.2. Results

The results were collected for a sequence of 3 simulations by discretizing the 3d domain using approximately 500, 4k, and 32k cells. The number of cells and degrees of freedom used by the participating methods are reported in Table A.8. In the following, results are discussed on the basis of line profiles of the hydraulic head in the 3d matrix as well as plots of the average concentrations within specified subregions of the 3d matrix.

5.2.2.1. Hydraulic Head Over Line. Fig. 9 shows the hydraulic head h_3 plotted along the diagonal line segment (0m, 0m, 0m)-(1m, 1m, 1m) for all grid refinements and for both Case 2.1 and Case 2.2. In the case of conductive fractures the spread and the differences to the reference solution decrease significantly upon grid refinement, although some noticeable differences still prevail for the finest grid.

Table 4
Parameters used in Case 2 of Section 5.2.

	Case 2.1		Case 2.2	
Matrix hydraulic conductivity $\boldsymbol{K}_3\|_{\Omega_{3,0}}$	$\boldsymbol{I}$	m/s	$\boldsymbol{I}$	m/s
Matrix hydraulic conductivity $\boldsymbol{K}_3\|_{\Omega_{3,1}}$	$1 \times 10^{-1}\boldsymbol{I}$	m/s	$1 \times 10^{-1}\boldsymbol{I}$	m/s
Fracture effective tangential hydraulic conductivity K_2	$\boldsymbol{I}$	m^2/s	$1 \times 10^{-8}\boldsymbol{I}$	m^2/s
Fracture effective normal hydraulic conductivity κ_2	2×10^{8}	1/s	2	1/s
Intersection effective tangential hydraulic conductivity K_1	1×10^{-4}	m^3/s	1×10^{-12}	m^3/s
Intersection effective normal hydraulic conductivity κ_1	2×10^{4}	m/s	2×10^{-4}	m/s
Intersection effective normal hydraulic conductivity κ_0	2	m^2/s	2×10^{-8}	m^2/s
Matrix porosity ϕ_3	1×10^{-1}		1×10^{-1}	
Fracture porosity ϕ_2	9×10^{-1}		1×10^{-2}	
Intersection porosity ϕ_1	9×10^{-1}		1×10^{-2}	
Fracture cross-sectional length ϵ_2	1×10^{-4}	m	1×10^{-4}	m
Intersection cross-sectional area ϵ_1	1×10^{-8}	m^2	1×10^{-8}	m^2
Intersection cross-sectional volume ϵ_0	1×10^{-12}	m^3	1×10^{-12}	m^3
Total simulation time	2.5×10^{-1}	s		
Time-step Δt	2.5×10^{-3}	s		

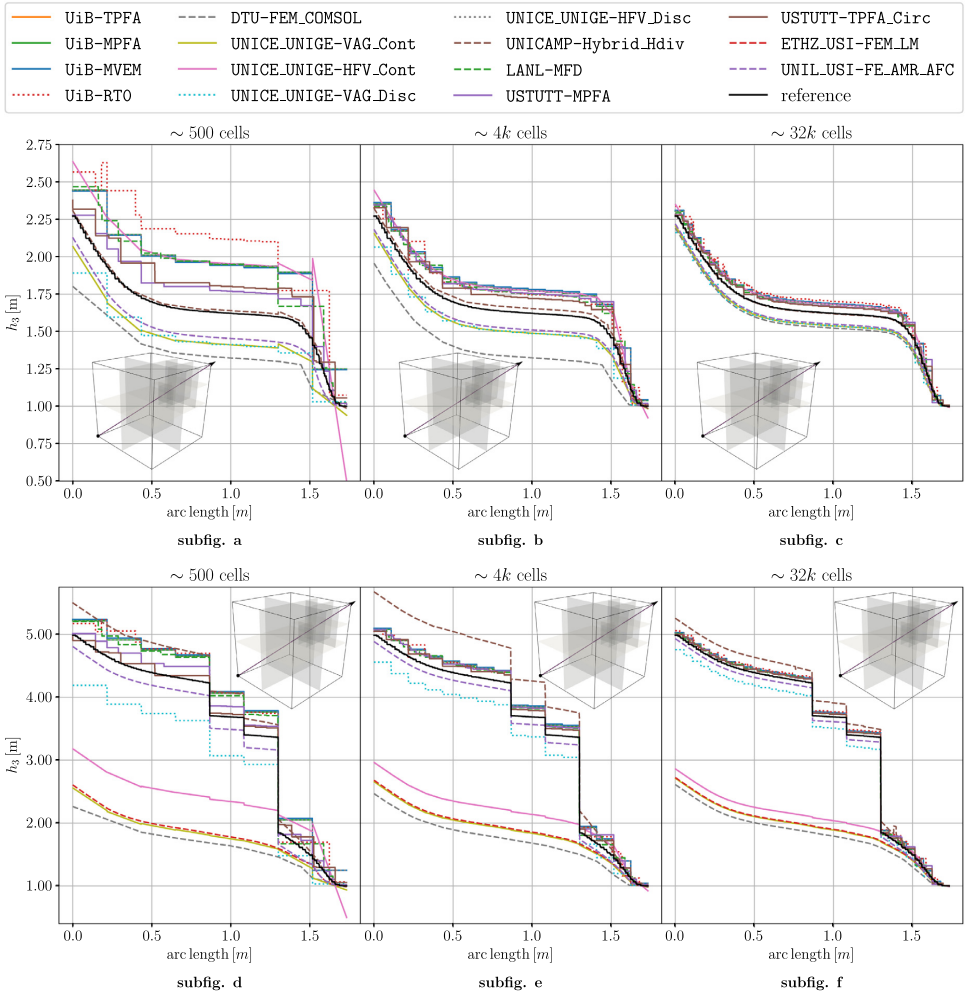

Fig. 9. Case 2 of Section 5.2. Plots of the hydraulic head h_3 along the line (0m, 0m, 0m) - (1m, 1m, 1m) for the different refinement levels (grid refinement increases from left to right) for the case of conductive fractures (Case 2.1, upper row) and blocking fractures (Case 2.2, lower row). The reference was computed with the USTUTT-MPFA scheme on a refined grid with 1,046,566 cells. Results of Section 5.2.2.1.

In the case of blocking fractures, the highest discrepancies are shown by the schemes that assume continuity of the hydraulic head across the fractures. As expected, these methods cannot capture the jump in the hydraulic head present in this test case. On the other hand, the remaining schemes approach the reference solution. The UNICE_UNIGE-VAG_Disc and the UNIL_USI-FE_AMR_AFC produce slightly lower and the UNICAMP-Hybrid_Hdiv scheme slightly higher hydraulic heads, but the deviations tend to diminish with increasing grid refinement.

The UNICE_UNIGE-VAG_Cont and UNICE_UNIGE-VAG_Disc methods incorporate Dirichlet boundary conditions on the vertices rather than on faces. This may explain, in part, the deviations in hydraulic head observed on coarse meshes for these methods. As expected, these differences decrease with mesh refinement. For the UNIL_USI-FE_AMR_AFC method, the differences might come from the representation of the fractures, which have the same spatial dimension as the background matrix. In particular, each fracture consists of a layer of elements that is refined at least twice by using adaptive mesh refinement.

5.2.2.2. Mean Matrix Concentration Over Time. The second comparison in Case 2 concerns the solution of the transport equation over time. These solutions are computed only on the second level of mesh refinement, i.e., using approximately 4000 cells. For the simulation of the transport model, the upwind scheme is employed for all methods except UNIL_USI-FE_AMR_AFC and ETHZ_USI-FEM_LM, which employ a finite element discretization with an algebraic flux correction Kuzmin et al. (2012).

The top of Fig. 10 depicts the temporal evolution of the mean tracer concentrations in three matrix regions for the case of highly conductive fractures. These regions were selected to form a representative illustration of the spread between the schemes. It can be seen that the majority of the schemes produce rather low concentrations in the first region, on the order of 2.5% at the final simulation time. In contrast, the ETHZ_USI-FEM_LM and the UNIL_USI-FE_AMR_AFC schemes produce significantly higher concentrations with values above 10% at the end of the simulation. In general, the temporal evolution of the concentrations in these three regions agrees very well among the majority of participating schemes, while the ETHZ_USI-FEM_LM and the UNIL_USI-FE_AMR_AFC schemes show significant deviations. These might be related to the flow discretization methods, but could also be affected by the different discretization that is employed for the transport discretization related to these methods, and, for UNIL_USI-FE_AMR_AFC, also the underlying equi-dimensional model.

For the case of blocking fractures, the concentrations in the same matrix regions are illustrated in the bottom row of Fig. 10. In general, a larger spread of the computed concentrations can be observed. For the first region, the schemes that assume continuity of the hydraulic head produce significantly lower concentrations, while the remaining schemes produce solutions that agree rather well. However, for the second and third regions, the concentrations at the final simulation time show a wide spread among all participating schemes.

As a general trend, it can be observed that the differences in computed concentrations increase with time. Additionally, differences increase with the regions' distance from the inflow boundary. As expected, for the case of conductive fractures, the differences are smaller than in the case of blocking fractures.

5.3. Case 3: Network with small features

5.3.1. Description

This test case is designed to probe accuracy in the presence of small geometric features, which may cause trouble for conforming meshing strategies. The domain is the box $\Omega = (0\text{m}, 1\text{m}) \times (0\text{m}, 2.25\text{m}) \times (0\text{m}, 1\text{m})$, containing eight fractures (see Fig. 11).

Table 5
Parameters used in Case 3 of Section 5.3.

Matrix hydraulic conductivity K_3	$\boldsymbol{I}$	m/s
Fracture effective tangential hydraulic conductivity K_2	$1 \times 10^2 \boldsymbol{I}$	m^3/s
Fracture effective normal hydraulic conductivity κ_2	2×10^6	1/s
Intersection effective tangential hydraulic conductivity K_1	1	m^2/s
Intersection effective normal hydraulic conductivity κ_1	2×10^4	m/s
Matrix porosity ϕ_3	2×10^{-1}	
Fracture porosity ϕ_2	2×10^{-1}	
Intersection effective porosity ϕ_1	2×10^{-1}	
Fracture cross-sectional length ϵ_2	1×10^{-2}	m
Intersection cross-sectional area ϵ_1	1×10^{-4}	m^2
Total simulation time	1×10^0	s
Time-step Δt	1×10^{-2}	s

The inlet and outlet boundaries are defined as follows:

$$\begin{aligned}
\partial\Omega_N &= \partial\Omega \setminus \left(\partial\Omega_{in} \cup \partial\Omega_{out}\right) \\
\partial\Omega_{in} &= (0\text{m}, 1\text{m}) \times \{0\text{m}\} \times (1/3\text{m}, 2/3\text{m}) \\
\partial\Omega_{out} &= \partial\Omega_{out,0} \cup \partial\Omega_{out,1} \\
\partial\Omega_{out,0} &= (0\text{m}, 1\text{m}) \times \{2.25\text{m}\} \times (0\text{m}, 1/3\text{m}) \\
\partial\Omega_{out,1} &= (0\text{m}, 1\text{m}) \times \{2.25\text{m}\} \times (2/3\text{m}, 1\text{m})
\end{aligned}$$

The boundary conditions for flow are zero Dirichlet conditions on $\partial\Omega_{out}$ and uniform unit inflow on $\partial\Omega_{in}$, so that $\int_{\partial\Omega_{in}} \mathbf{u}_3 \cdot \mathbf{n} dS = -1/3\text{m}^2/\text{s}$, and zero Neumann conditions on $\partial\Omega_N$. For the transport problem, the initial condition is zero in Ω, and the boundary condition is a unit concentration at $\partial\Omega_{in}$. A complete overview of the parameters used in Case 3 is given in Table 5.

5.3.2. Results

Similar to the previous cases, the methods are compared on the basis of a) the hydraulic head of the matrix domain along two lines, b) the integrated fracture concentration over time, c) the fluxes out of the domain and d) computational cost. Two different simulations with approximately 30k and 150k cells for the 3d domain were performed. It was seen as infeasible to include one more level of refinement for all methods. However, refined versions of the USTUTT-MPFA with up to approximately 10^6 matrix cells were produced. At this stage, there were no noticeable differences between solutions on different grids, and the finest solution was included as a reference solution.

5.3.2.1. Hydraulic Head Over Line. Fig. 12 shows the profile of the hydraulic head h_3 in the matrix along the line $(0.5\text{m}, 1.1\text{m}, 0\text{m}) - (0.5\text{m}, 1.1\text{m}, 1\text{m})$. This shows considerable differences between the methods for both refinement levels. However, the agreement is better for the second refinement level, where most of the methods are within a relative hydraulic head range of approximately 10%. The UNICE_UNIGE-VAG_Disc, UNICE_UNIGE-VAG_Cont, DTU-FEM_COMSOL, and UNIL_USI-FE_AMR_AFC methods show the highest discrepancies in these plots, but the deviation from the reference solution decreases significantly with higher refinement. The significant difference between the refinements may indicate that the small features of the fracture network geometry are not adequately resolved, at least not by the coarser grids. This is in line with the purpose of the test case.

5.3.2.2. Mean Fracture Concentration Over Time. Data were reported for the integrated concentration $\overline{c_2} = \int_{\Omega_{2,i}} c_2 / |\Omega_{2,i}|$ on each fracture i throughout the simulation. There is a general agreement between the methods, with the method of ETHZ_USI-FEM_LM showing some deviations for some of the fractures. As an example, Fig. 13 shows the plots for both refinement levels for fracture number 3, demonstrating limited difference between the refinement levels.

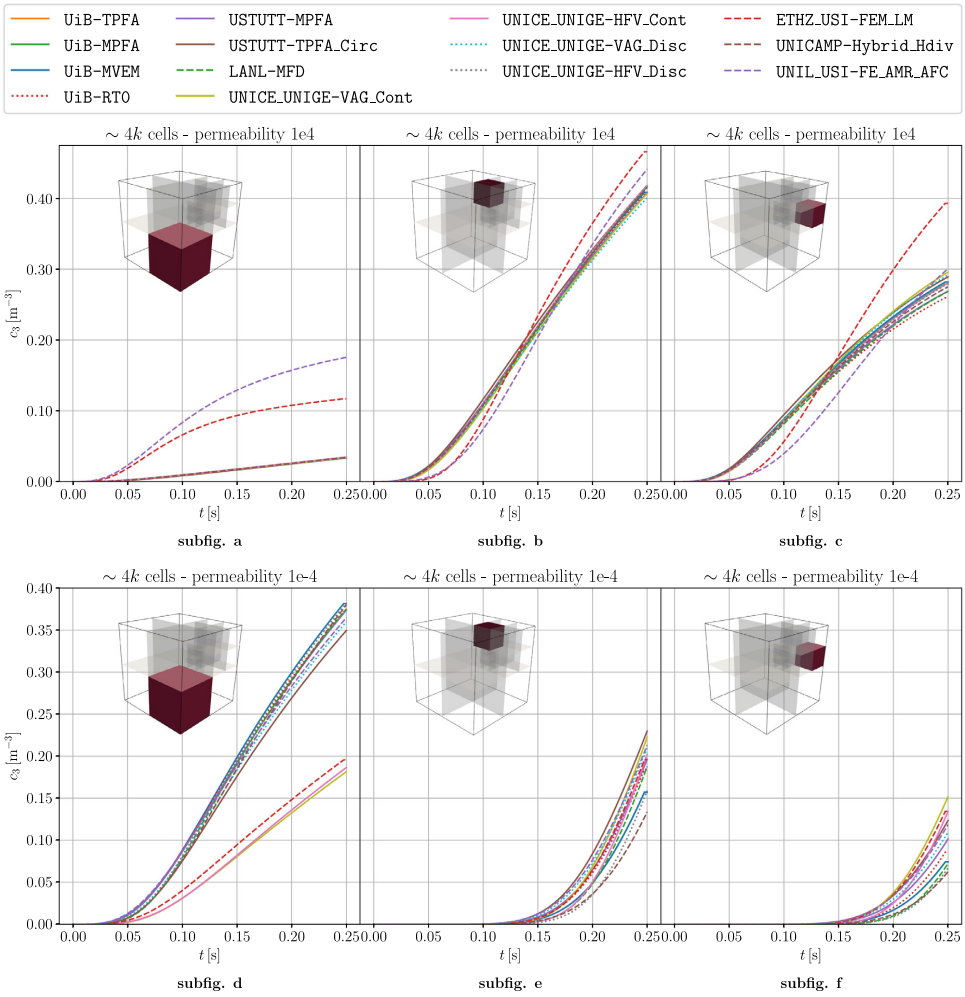

Fig. 10. Case 2 of Section 5.2. On the top, temporal evolution of the average tracer concentration in matrix regions 1, 10 and 11 (from left to right) for the case of conductive fractures (Case 2.1). On the bottom, temporal evolution of the average tracer concentration in the matrix regions 1, 10 and 11 (from left to right) for the case of blocking fractures (Case 2.2). Results of Section 5.2.2.2.

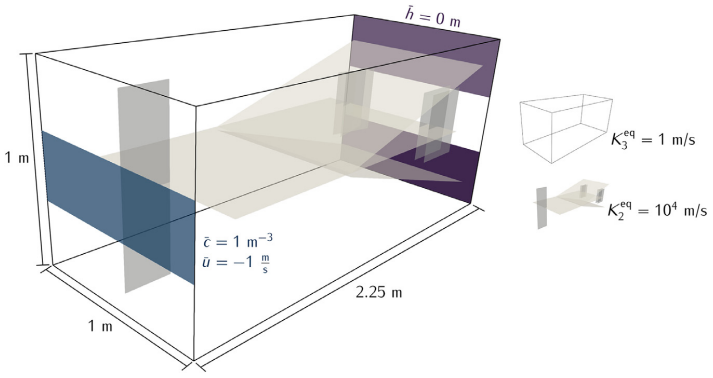

Fig. 11. Representation of the fractures and the outline of the domain for Case 3 of Section 5.3.

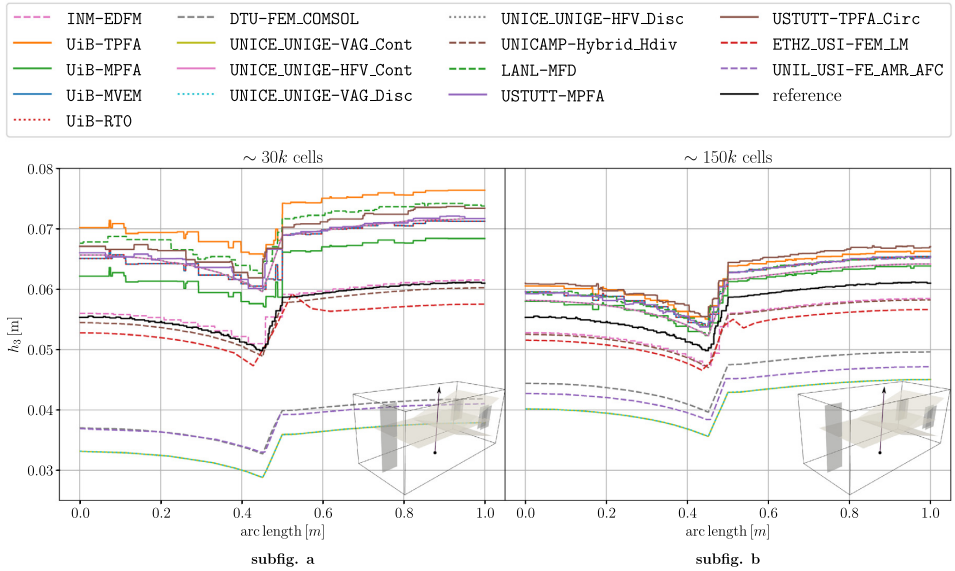

Fig. 12. Case 3 of Section 5.3. Hydraulic head h_3 in the matrix over the line (0.5m, 1.1m, 0m) − (0.5m, 1.1m, 1m) for the coarse (left) and fine (right) grid. The solid black line shows the solution obtained with the USTUTT-MPFA scheme on a grid with approximately 10^6 matrix cells. Results of Section 5.3.2.1.

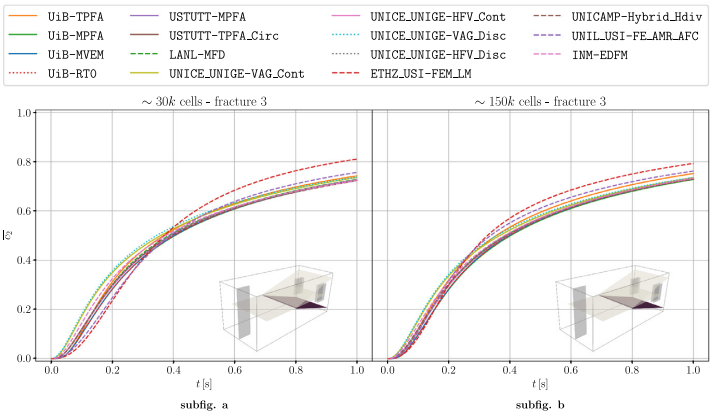

Fig. 13. Case 3 of Section 5.3. Mean concentration within fracture number 3 throughout the simulation time for the coarse (left) and fine (right) grid. Results of Section 5.3.2.2.

5.3.2.3. Boundary Fluxes. The total outflow $\bar{u}_{out} = \int_{\partial\Omega_{out}} \boldsymbol{u}_3 \cdot \boldsymbol{n} dS$ and the proportion exiting over $\partial\Omega_{out,0}$, i.e., $r_{out} = \int_{\partial\Omega_{out,0}} \boldsymbol{u}_3 \cdot \boldsymbol{n} dS / \bar{u}_{out}$, are shown in Fig. 14. When compared to the prescribed inflow of -1/3m^3/s, the $\bar{u}_{out}$ values reveal a small lack of volume conservation for ETHZ_USI-FEM_LM, but the method improves for the finer grid. The ratio r_{out} provides an indication of whether the flux fields agree. The ratios generally agree well with the refined USTUTT-MPFA, except for the ETHZ_USI-FEM_LM method, which does not approach the reference value for the finest grid.

5.3.2.4. Computational Cost. Based on the data presented in Table A.9, note that the UNIL_USI-FE_AMR_AFC applies 68k and 203k cells for the cases where 30k and 150k cells were prescribed, respectively. The rest of the methods are well within 10% of the prescribed values. As for the other test cases, there are significant variations in the number of degrees of freedom and nonzero matrix entries related to the design of the methods.

5.4. Case 4: Field case

5.4.1. Description

The geometry of the fourth case is based on a postprocessed outcrop from the island of Algerøyna, outside Bergen, Norway, and is a subset of the fracture network presented in Fumagalli et al. (2019). From the outcrop, 52 fractures were selected, extruded in the vertical direction and then cut by a bounding box. The resulting network has 106 fracture intersections, and multiple fractures intersect the domain boundary.

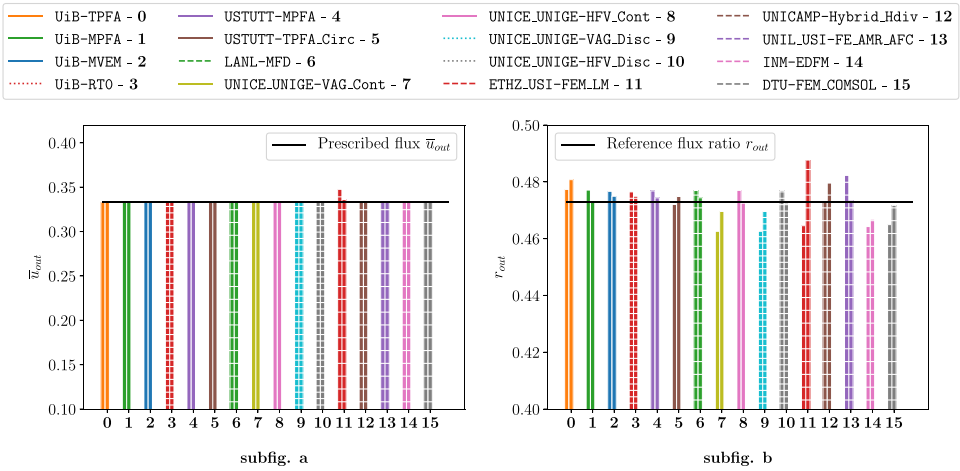

Fig. 14. Case 3 of Section 5.3. Total outflux (left) and ratio exiting over $\partial\Omega_{out,0}$ (right). The bar pairs correspond to the coarse and fine grid, while the reference solution is indicated by the horizontal line. Results of Section 5.3.2.3.

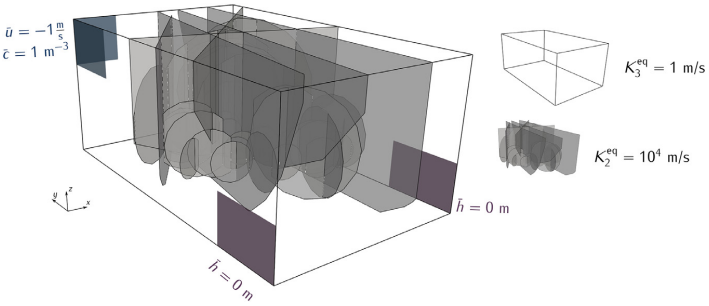

Fig. 15. Case 4 of Section 5.4. Representation of the fractures and the outline of the domain. Inlet boundaries are shown in blue, outlets in purple. (For interpretation of the references to color in this figure legend, the reader is referred to the web version of this article.)

The simulation domain is the box $\Omega = (-500\text{m}, 350\text{m}) \times (100\text{m}, 1500\text{m}) \times (-100\text{m}, 500\text{m})$. The fracture geometry is depicted in Fig. 15.

The inlet and outlet boundaries are defined as follows:

$$\begin{aligned}
\partial\Omega_N &= \partial\Omega \setminus \left(\partial\Omega_{in} \cup \partial\Omega_{out}\right),\\
\partial\Omega_{in} &= \partial\Omega_{in,0} \cup \partial\Omega_{in,1}, \qquad \partial\Omega_{out} = \partial\Omega_{out,0} \cup \partial\Omega_{out,1},\\
\partial\Omega_{in,0} &= (-500\text{m}, -200\text{m}) \times \{1500\text{m}\} \times (300\text{m}, 500\text{m}),\\
\partial\Omega_{in,1} &= \{-500\text{m}\} \times (1200\text{m}, 1500\text{m}) \times (300\text{m}, 500\text{m}),\\
\partial\Omega_{out,0} &= \{-500\text{m}\} \times (100\text{m}, 400\text{m}) \times (-100\text{m}, 100\text{m}),\\
\partial\Omega_{out,1} &= \{350\text{m}\} \times (100\text{m}, 400\text{m}) \times (-100\text{m}, 100\text{m}).
\end{aligned}$$

The boundary conditions for flow are zero Dirichlet conditions on $\partial\Omega_{out}$ and uniform unit inflow on $\partial\Omega_{in}$, so that $\int_{\partial\Omega_{in}} \mathbf{u}_3 \cdot \mathbf{n} dS = -1.2e5\text{m}^3/\text{s}$, and zero Neumann conditions on $\partial\Omega_N$. For the transport problem, the initial condition is zero in Ω, and the boundary condition is a unit concentration at $\partial\Omega_{in}$. The parameters for conductivity, porosity and aperture are given in Table 6, as is the total simulation time and time-step size.

Because of the complex network geometry, grid refinement studies were considered infeasible and the benchmark specified the usage of a single grid. A Gmsh (Geuzaine and Remacle, 2009) configuration file was provided to assist participants with geometry processing and meshing. The use of this predefined grid was optional, but the number of 3d cells should be approximately 260k.

Table 6
Parameter used in Case 4 of Section 5.4.

Matrix hydraulic conductivity K_3	$\boldsymbol{I}$	m/s
Fracture effective tangential hydraulic conductivity K_2	$1 \times 10^2 \boldsymbol{I}$	m^3/s
Fracture effective normal hydraulic conductivity κ_2	2×10^6	1/s
Intersection effective tangential hydraulic conductivity K_1	1	m^2/s
Intersection effective normal hydraulic conductivity κ_1	2×10^4	m/s
Matrix porosity ϕ_3	2×10^{-1}	
Fracture porosity ϕ_2	2×10^{-1}	
Intersection porosity ϕ_1	2×10^{-1}	
Fracture cross-sectional length ϵ_2	1×10^{-2}	m
Intersection cross-sectional area ϵ_1	1×10^{-4}	m^2
Total simulation time	5×10^3	s
Time-step Δt	5×10^1	s

5.4.2. Results

Results were reported for 14 schemes. The two methods that participated in Case 3, which is closest in geometric complexity, but not in Case 4, are `INM-EDFM` and `UNIL_USI-FE_AMR_AFC`. The participating methods are compared in terms of a) hydraulic head of the matrix domain along two lines, b) time series of concentrations in selected fractures and c) computational cost.

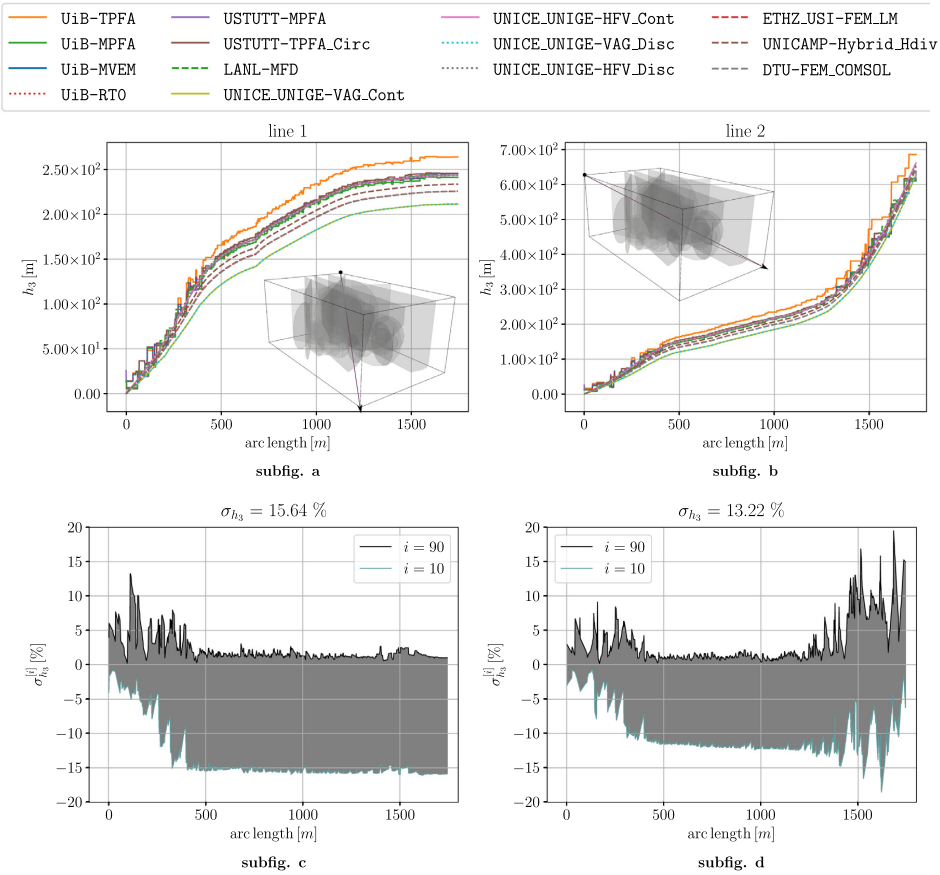

Fig. 16. Case 4 of Section 5.4. Hydraulic head profiles across the domain. Left: Profile from outlet $\partial\Omega_{out,0}$ towards the opposite corner. Right: Profile from outlet $\partial\Omega_{out,1}$ towards $\partial\Omega_{in}$. On the bottom, the deviations $\sigma_{h_3}^{[90]}$ and $\sigma_{h_3}^{[10]}$ are illustrated, as defined in (16). Here, the median $h_3^{[50]}$ of the solutions on the finest grid is used as the reference solution h_3^{ref}. Results of Section 5.4.2.1.

5.4.2.1. Hydraulic Head. Fig. 16 shows the hydraulic head along the two specified lines, together with the spread of the reported results. Both lines start in points at the outflow boundaries where the hydraulic head is set to 0; the first line ends far away from the inlet, while the second ends at the inlet boundary. For the first line there are noticeable deviations for some of the solutions: The `UiB-TPFA` scheme predicts a significantly higher hydraulic head drop, likely caused by the inconsistency of the scheme. Conversely, the `UNICE_UNIGE-VAG_Disc` and `UNICE_UNIGE-VAG_Cont` methods underestimate the drop in hydraulic head compared to the average of the reported results, while there is only minor disagreement among the other methods. On the second line, the `UiB-TPFA` scheme overestimates the drop in hydraulic head over the domain, while the other methods are in very good agreement. The average spread σ_{h_3} calculated according to (16) of around 15% is within a reasonable range, considering the geometrical complexity of the fracture network.

5.4.2.2. Concentration Plots. The quality of the flux field is measured by the time series of average concentrations in the fracture planes, with good agreement among most of the methods. Fig. 17 shows the time evolution of concentration for three of the fractures, numbers 15, 45 and 48, which show the largest differences between the methods. The results produced by the `ETHZ_USI-FEM_LM` deviate slightly from the other methods on two of these figures, while `UNICE_UNIGE-VAG_Disc` also shows a slight deviation for one of the figures.

5.4.2.3. Computational Cost. Measures for the computational cost of the participating methods are given in Table A.10. Most of the groups used the provided mesh file. The `UNICAMP-Hybrid_Hdiv` method used a grid with only approximately 40% of the cells in the provided grid. `DTU-FEM_COMSOL` employed almost seven times more 3d cells for its nodal-based method, yielding a number of degrees of freedom that is in the lower half with respect to all participating methods. As in the previous test cases, there are significant differences in the number of unknowns and nonzero matrix elements among the methods.

6. Summary of results

The performance of each method for all test cases is indicated in Fig. 18. The main points emerging from the discussion of the results in Section 5 are:

1. Of the 17 schemes that participated in at least one of the test cases, 14 presented simulation results on all four cases.

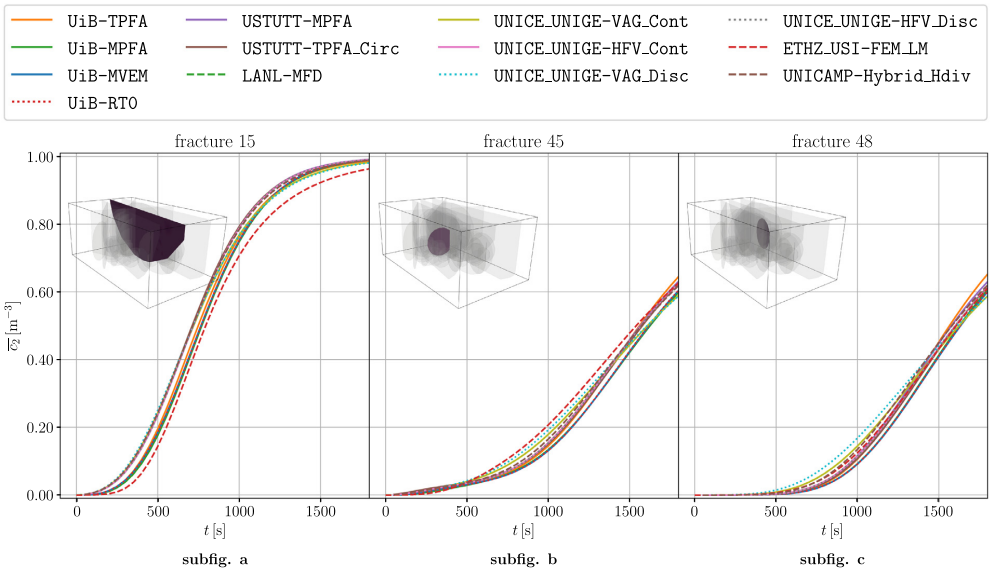

Fig. 17. Case 4 of Section 5.4. Mean concentration over time in three selected fractures with identification 15, 45, and 48. Results of Section 5.4.2.2.

	Case 1						Case 2				Case 3				Case 4		
Method	a	b	c	d	e	f	a1	a2	b1	b2	a	b	c	d	a	b	c
UiB-TPFA																	
UiB-MPFA																	
UiB-MVEM																	
UiB-RT0																	
USTUTT-MPFA																	
USTUTT-TPFA_Circ																	
LANL-MFD																	
NCU_TW-Hybrid_FEM																	
UNICE_UNIGE-VAG_Cont																	
UNICE_UNIGE-HFV_Cont																	
UNICE_UNIGE-VAG_Disc																	
UNICE_UNIGE-HFV_Disc																	
ETHZ_USI-FEM_LM																	
UNICAMP-Hybrid_Hdiv																	
UNIL_USI-FE_AMR_AFC																	
INM-EDFM																	
DTU-FEM_COMSOL																	

No significant deviation
Minor deviation
Major deviation
No results reported

Fig. 18. Summary of the performance of all methods.

2. Cases 3 and 4 pose the highest demands on the methods in terms of geometrical complexity. Taken together, the cases point to the challenges inherent to DFM simulations and indicate the methods' robustness in this respect.
3. Although the prescribed numbers of cells was adhered to for most of the methods, the numbers of degrees of freedom and matrix density reported in Tables A.7 through A.10 vary significantly, indicating differences in computational cost.
4. Not unexpectedly, fractures that act as barriers cause trouble for the methods that assume a continuous hydraulic head over the fracture, as seen in Case 2. Blocking fractures are outside the intended range of validity for these models, and alternative approaches should be sought for those cases.
5. Out of the 17 schemes, one is not mass conservative. There are no signs of the lack of conservation in the reported concentration fields, likely due to successful postprocessing of the flux fields. Nevertheless, for most of the test cases, the concentration fields reported by the nonconforming mesh method `ETHZ_USI-FEM_LM` deviate from the other reported results.
6. The well-known inconsistency of the widely used two-point flux approximation is manifested in the underestimation of permeability in the hydraulic head results reported for `UiB-TPFA`. The

USTUTT-TPFA_Circ method circumvents this inconsistency by locating the hydraulic head values at the circumcenters of the tetrahedrons. However, this poses additional restrictions on the mesh.

The observations herein can to some degree be used as guidance when choosing discretization schemes for practical simulations, with the 7 methods that showed no deviations on any of the benchmark methods being natural candidates. Nevertheless, said observations should not be uncritically transferred to other geometries, problem setups and quantities of interest. The choice of discretization method can also be influenced by aspects not discussed in this benchmark, such as the availability of efficient linear solvers and the ease of implementation. Moreover, the participating methods obviously don't cover the whole range of available DFM discretization approaches.

7. Conclusion and outlook

This paper has presented a set of benchmark cases for the simulation of flow in three-dimensional fractured porous media, assuming Darcy flow in both matrix and fractures. The suite consists of one case with a single fracture, one case with 9 fractures and setups with conductive and blocking fractures, one case with 8 fractures designed to emphasize complex geometric details, and finally a case with 52 fractures, based on a real fracture network. The metrics employed to measure discretization performance are a) the profiles of the hydraulic head, b) the quality of the flux field measured by simulation of passive tracers and c) the computational cost as indicated by the number of degrees of freedom and matrix sparsity pattern. A total of 17 methods participated in the benchmark. While these can't include all discretization schemes proposed for flow in fractured porous media, they nevertheless cover a wide range of numerical approaches.

The benchmark uncovered important differences between the methods, with 10 methods showing significant deviations. While the observations and discussions herein offer some guidance to identifying well-suited methods for practical simulations, such extrapolation requires care and consideration of the particularities of the simulation in question. Moreover, the high number of participating methods and research groups proves that simulations in 3d media are fully feasible for a wide range of schemes and research codes. For further development of discretization methods, 3d cases should therefore become a natural complement to the more traditional 2d simulation results.

To advance the field of numerical methods for physics-based models, there is a need both for creative development of new mathematical models and numerical methods and for rigorous testing and comparison. The current paper presents a contribution to the latter. The provided test cases and data provides researchers with a suite of problems to benchmark methods and implementations for single-phase flow in fractured porous media. With this, researchers in the field are invited to utilize the test cases, results and data from the current study in development of new methods. Further, with recent developments of models and numerical methods for more complex and coupled physics in fractured porous media, the present work can hopefully also serve as inspiration for development of additional benchmark studies in the future.

CRediT author statement

I. Berre, W. Boon, B. Flemisch, A. Fumagalli, D. Gläser, E. Keilegavlen, A. Scotti, I. Stefansson, and A. Tatomir were jointly responsible for conceptualizing, initiating and coordinating the whole benchmark process as described in Section 2. They wrote the initial draft of the manuscript and were responsible for the overall review and editing process. In the roles outlined in Section 2, the following authors acted as "designers" and "coordinators" for the individual benchmark cases:

Case	Designer(s)	Coordinator(s)
1	D. Gläser, A. Tatomir	B. Flemisch, A. Tatomir
2	A. Fumagalli, I. Stefansson	W. Boon, D. Gläser
3	E. Keilegavlen, I. Stefansson	I. Stefansson, A. Fumagalli
4	E. Keilegavlen, A. Fumagalli	E. Keilegavlen

All other authors mainly acted as benchmark participants for one or more discretization methods. This included implementing and executing the benchmark case scenarios, post-processing and uploading the results as well as communicating with the coordinating group. Acting as internal reviewers, they were also involved in editing the manuscript. The following table lists the persons responsible for the participating methods, which naturally also includes authors from the coordinating group:

Author(s)	Method(s)
K. Brenner, J. Hennicker, R. Masson	UNICE_UNIGE-*
S. Burbulla	USTUTT-TPFA_Circ
P. Devloo, O. Duran	UNICAMP-Hybrid_Hdiv
M. Favino, M. Nestola	UNIL_USI-FE_AMR_AFC
A. Fumagalli, E. Keilegavlen, I. Stefansson	UiB-*
D. Gläser	USTUTT-MPFA
I.-H. Lee, C.-F. Ni	NCU_TW-Hybrid_FEM
K. Lipnikov, D. Svyatskiy	LANL-MFD
K. Mosthaf	DTU-FEM_COMSOL
K. Nikitin, R. Yanbarisov	INM-EDFM
P. Schädle, P. Zulian	ETHZ_USI-FEM_LM

Declaration of Competing Interest

The authors declare that they have no known competing financial interests or personal relationships that could have appeared to influence the work reported in this paper.

Acknowledgments

I. Berre, A. Fumagalli, E. Keilegavlen, and I. Stefansson were supported by Norwegian Research Council grants 250223, 244129/E20 and 267908/E20. The contribution of *S. Burbulla* was funded by the Deutsche Forschungsgemeinschaft (DFG, German Research Foundation) - Project Number 327154368 - SFB 1313. *P. Devloo* was supported by Fapesp grant No 2017/15736-3, ANP/Petrobras grant No 2014/00090-2 and CNPq grant No 310369/2006-1. *O. Duran* was supported by ANP/Petrobras grant No 2014/00090-2. *M. Favino* was supported by the Swiss National Science Foundation (SNSF) grant PZ00P2_180112. *M. Nestola and P.Zulian* were supported by the SCCER-SoE and the Pasc Project FASTER. *C.-F. Ni and I.-H. Lee* were partially funded by Institute of Nuclear Energy Research under grant NL1050288 and by Ministry of Science and Technology under grant MOST 108-2116-M-008-004- and MOST 106-2116-M-008-014-. *K. Nikitin and R. Yanbarisov* were supported by Moscow Center for Fundamental and Applied Mathematics (agreement with the Ministry of Education and Science of the Russian Federation No. 075-15-2019-1624). *P. Schädle* thanks the Werner Siemens Foundation for their endowment of the Geothermal Energy and Geofluids group at the Institute of Geophysics, ETH Zurich.

Appendix A. Measures of Computational Cost

This section provides three indicators related to computational cost: the number of cells (0d-3d), the number of degrees of freedom and the number of nonzero matrix entries. There is one table for each test case with data of all the participating methods at all refinement levels. For the equi-dimensional UNIL_USI-FE_AMR_AFC method, the cells

Table A.7
Computational cost indicators for Case 1.

Method	Refinement	0d cells	1d cells	2d cells	3d cells	dofs	nnz
UiB-TPFA	0	0	0	112	1,022	1,358	6,008
	1	0	0	756	9,438	11,706	53,904
	2	0	0	4,576	98,311	112,039	533,547
UiB-MPFA	0	0	0	112	1,022	1,358	62,200
	1	0	0	756	9,438	11,706	672,454
	2	0	0	4,576	98,311	112,039	7,481,237
UiB-MVEM	0	0	0	112	1,022	3,905	24,435
	1	0	0	756	9,438	33,651	222,927
	2	0	0	4,576	98,311	326,561	2,259,630
UiB-RT0	0	0	0	112	1,022	3,905	24,435
	1	0	0	756	9,438	33,651	222,927
	2	0	0	4,576	98,311	326,561	2,259,623
USTUTT-MPFA	0	0	0	100	1,000	1,100	22,626
	1	0	0	400	9,600	10,000	227,354
	2	0	0	3,600	108,000	111,600	2,731,104
USTUTT-TPFA_Circ	0	0	0	193	3,400	3,593	17,373
	1	0	0	448	9,085	9,533	46,505
	2	0	0	2,582	104,578	107,160	530,224
LANL-MFD	0	0	0	100	1,000	4,400	51,720
	1	0	0	400	8,000	34,840	390,840
	2	0	0	1,600	64,000	267,280	3,035,280
NCU_TW-Hybrid_FEM	0	0	0	625	9,572	1,840	25,539
	1	0	0	2,453	65,934	11,537	169,937
	2	0	0	22,262	638,332	104,581	1,603,776
UNICE_UNIGE-VAG_Cont	0	0	0	81	1,134	1,511	34,085
	1	0	0	361	10,108	11,721	288,933
	2	0	0	1,849	103,544	111,233	2,877,105
UNICE_UNIGE-HFV_Cont	0	0	0	81	1,134	3,870	39,060
	1	0	0	361	10,108	32,319	340,879
	2	0	0	1,849	103,544	320,221	3,454,921
UNICE_UNIGE-VAG_Disc	0	0	0	81	1,134	1,943	43,519
	1	0	0	361	10,108	13,483	328,867
	2	0	0	1,849	103,544	119,771	3,073,987
UNICE_UNIGE-HFV_Disc	0	0	0	81	1,134	4,077	40,041
	1	0	0	361	10,108	33,231	345,135
	2	0	0	1,849	103,544	324,779	3,475,475
ETHZ_USI-FEM_LM	0	0	0	120	1,000	1,617	38,834
	1	0	0	480	10,115	12,714	335,023
	2	0	0	1,920	93,150	103,470	2,775,270
UNICAMP-Hybrid_Hdiv	0	0	0	526	1,054	5,968	11,4924
	1	0	0	2,884	10,589	62,164	1,249,536
	2	0	0	15,052	100,273	604,019	12,448,629
UNIL_USI-FE_AMR_AFC	0	0	0	720	540	1,857	49,417
	1	0	0	10,880	38,180	56,947	1,545,935
	2	0	0	39,520	108,671	579,837	16,878,449
INM-EDFM	0	0	0	140	1,000	1,140	7666
	1	0	0	720	10,000	10,720	73,364
	2	0	0	3,800	100,000	103,800	719,292
DTU-FEM_COMSOL	0	0	0	0	1,006	259	3,082
	1	0	0	0	10,091	1,931	26,771
	2	0	0	0	100,014	17,850	258,202

Table A.8
Computational cost indicators for Case 2.

Method	Refinement	0d cells	1d cells	2d cells	3d cells	dofs	nnz
UiB-TPFA	0	27	90	252	512	1,820	8,253
	1	27	180	1,008	4,096	8,074	43,513
	2	27	360	4,032	32,768	46,622	281,717
UiB-MPFA	0	27	90	252	512	1,820	8,609
	1	27	180	1,008	4,096	8,074	44,984
	2	27	360	4,032	32,768	46,622	287,565
UiB-MVEM	0	27	90	252	512	4,706	20,795
	1	27	180	1,008	4,096	24,862	118,620
	2	27	360	4,032	32,768	161,414	806,000
UiB-RT0	0	27	72	226	612	3,970	21,687
	1	27	159	1,192	5,339	24,727	153,263
	2	27	270	4,536	39,157	148,245	980,955
USTUTT-MPFA	0	0	0	284	843	1,127	42,060
	1	0	0	686	3,076	3,762	207,260
	2	0	0	4,578	38,877	43,455	2,918,322
USTUTT-TPFA_Circ	0	0	0	312	978	1,290	7,488
	1	0	0	1,206	4,286	5,492	31,402
	2	0	0	4,578	38,877	43,455	226,201
LANL-MFD	0	0	0	434	628	2,758	23,246
	1	0	0	1,736	5,024	18,610	150,314
	2	0	0	6,944	40,192	134,812	1,062,572
UNICE_UNIGE-VAG_Cont	0	0	0	252	512	974	22,324
	1	0	0	1,008	4,096	5,902	143,470
	2	0	0	4,032	32,768	39,908	1,014,088
UNICE_UNIGE-HFV_Cont	0	0	0	252	512	2,223	22,599
	1	0	0	1,008	4,096	15,048	157,980
	2	0	0	4,032	32,768	109,368	1,172,592
UNICE_UNIGE-VAG_Disc	0	0	0	252	512	2,102	46,348
	1	0	0	1,008	4,096	10,223	238,891
	2	0	0	4,032	32,768	56,607	1,390,939
UNICE_UNIGE-HFV_Disc	0	0	0	252	512	2,730	24,138
	1	0	0	1,008	4,096	17,076	164,148
	2	0	0	4,032	32,768	117,480	1,197,288
ETHZ_USI-FEM_LM	0	0	0	1,212	512	3,159	67,183
	1	0	0	1,212	4,096	7,343	182,793
	2	0	0	1,212	32,768	38,367	1,036,960
UNICAMP-Hybrid_Hdiv	0	27	69	534	923	6,018	123,312
	1	27	90	1,896	3,912	23,988	479,322
	2	27	249	10,744	38,742	236,868	4,830,288
UNIL_USI-FE_AMR_AFC	0	1,331	2,787	6,513	1,745	16,283	410,491
	1	1,331	5,211	20,673	8,129	45,257	1,180,333
	2	1,331	10,059	72,033	47,553	161,805	4,274,281
DTU-FEM_COMSOL	0	0	0	0	550	129	1,561
	1	0	0	0	3,881	836	10,900
	2	0	0	0	32,147	6,060	84,954

Table A.9
Computational cost indicators for Case 3.

Method	Refinement	0d cells	1d cells	2d cells	3d cells	dofs	nnz
UiB-TPFA	0	0	50	4,305	31,644	44,786	207,295
	1	0	86	13,731	138,446	180,024	849,349
UiB-MPFA	0	0	50	4,305	31,644	44,786	2,596,061
	1	0	86	13,731	138,446	180,024	11,196,843
UiB-MVEM	0	0	50	4,305	31,644	120,696	818,151
	1	0	86	13,731	138,446	496,032	3,438,098
UiB-RT0	0	0	50	4,305	31,644	120,696	818,151
	1	0	86	13,731	138,446	496,032	3,438,098
USTUTT-MPFA	0	0	0	4,321	31,942	36,263	2,459,195
	1	0	0	12,147	131,488	143,635	10,157,331
USTUTT-TPFA_Circ	0	0	0	4,321	31,942	36,263	191,147
	1	0	0	12,147	131,488	143,635	745,375
LANL-MFD	0	0	0	5,617	21,056	75,878	607,730
	1	0	0	22,468	168,448	555,887	4,367,379
UNICE_UNIGE-VAG_Cont	0	0	0	4,321	31,870	10,213	130,781
	1	0	0	7,711	150,083	35,485	479,105
UNICE_UNIGE-HFV_Cont	0	0	0	4,321	31,870	71,708	504,872
	1	0	0	7,711	150,083	319,175	2,206,691
UNICE_UNIGE-VAG_Disc	0	0	0	4,321	31,870	23,302	400,876
	1	0	0	7,711	150,083	59,187	966,849
UNICE_UNIGE-HFV_Disc	0	0	0	4,321	31,870	80,538	532,114
	1	0	0	7,711	150,083	335,599	2,259,971
ETHZ_USI-FEM_LM	0	0	0	750	29,295	33,270	899,809
	1	0	0	3,000	150,930	163,430	4,421,700
UNICAMP-Hybrid_Hdiv	0	0	38	5,580	24,351	153,519	3,180,847
	1	0	51	23,607	162,773	994,243	20,600,135
UNIL_USI-FE_AMR_AFC	0	0	3,877	323,779	68,386	86,594	1,206,048
	1	0	3,877	323,779	547,088	148,993	2,202,947
INM-EDFM	0	0	0	4,036	29,952	33,988	240,398
	1	0	0	10,732	149,760	160,492	1,133,364
DTU-FEM_COMSOL	0	0	0	0	30,984	5,641	80,669
	1	0	0	0	150,524	30,379	469,447
USTUTT-MPFA-refined	5	0	0	49,428	980,212	1,029,640	75,207,825

Table A.10
Computational cost indicators for Case 4.

Method	0d cells	1d cells	2d cells	3d cells	dofs	nnz
UiB-TPFA	0	1,601	52,618	259,409	424,703	1,950,313
UiB-MPFA	0	1,601	52,618	259,409	424,703	22,953,336
UiB-MVEM	0	1,601	52,618	259,409	1,082,740	7,342,691
UiB-RT0	0	1,601	52,618	259,409	1,082,740	7,342,691
USTUTT-MPFA	0	0	52,618	259,420	312,038	21,227,071
USTUTT-TPFA_Circ	0	0	52,618	259,420	312,038	1,721,932
LANL-MFD	0	0	52,070	260,417	783,158	7,953,396
UNICE_UNIGE-VAG_Cont	0	0	52,070	260,431	95,930	1,237,714
UNICE_UNIGE-HFV_Cont	0	0	52,070	260,431	600,561	4,349,901
UNICE_UNIGE-VAG_Disc	0	0	52,070	260,431	252,326	4,497,980
UNICE_UNIGE-HFV_Disc	0	0	52,070	260,431	704,813	4,663,105
ETHZ_USI-FEM_LM	0	0	52,618	212,040	223,532	5,817,930
UNICAMP-Hybrid_Hdiv	0	938	24,853	94,294	629,065	13,233,581
DTU-FEM_COMSOL	0	0	0	1,860,063	319,489	4,709,565

listed as “0d-2d cells” are also three-dimensional cells that correspond to the fractures (“2d”), intersections of fractures (“1d”) and intersections of such intersections (“0d”).

Supplementary material

Supplementary material associated with this article can be found, in the online version, at doi:10.1016/j.advwatres.2020.103759.

References

Ahmed, E., Jaffré, J., Roberts, J.E., 2017. A reduced fracture model for two-phase flow with different rock types. Math. Comput. Simul. 137, 49–70.

Angot, P., Boyer, F., Hubert, F., 2009. Asymptotic and numerical modelling of flows in fractured porous media. ESAIM: Math. Modell. Numeric. Anal.-Modélisat. Mathématique et Anal. Numér. 43 (2), 239–275.

Arrarás, A., Gaspar, F.J., Portero, L., Rodrigo, C., 2019. Mixed-dimensional geometric multigrid methods for single-phase flow in fractured porous media. SIAM J. Sci. Comput. 41 (5), B1082–B1114. https://doi.org/10.1137/18M1224751.

Barlag, C., Hinkelmann, R., Helmig, R., Zielke, W., 1998. Adaptive methods for modelling transport processes in fractured subsurface systems. 3rd International Conference on Hydroscience and Engineering, Cottbus.

Berre, I., Boon, W., Flemisch, B., Fumagalli, A., Gläser, D., Keilegavlen, E., Scotti, A., Stefansson, I., Tatomir, A., 2018. Call for participation: verification benchmarks for single-phase flow in three-dimensional fractured porous media. arXiv e-prints 1809.06926.

Berre, I., Boon, W. M., Flemisch, B., Fumagalli, A., Gläser, D., Keilegavlen, E., Scotti, A., Stefansson, I., Tatomir, A., Brenner, K., Burbulla, S., Devloo, P., Duran, O., Favino, M., Hennicker, J., Lee, I.-H., Lipnikov, K., Masson, R., Mosthaf, K., Nestola, M. G. C., Ni, C.-F., Nikitin, K., Schädle, P., Svyatskiy, D., Yanbarisov, R., Zulian, P., 2020. Data repository of this work. https://git.iws.uni-stuttgart.de/benchmarks/fracture-flow-3d.git.

Berre, I., Doster, F., Keilegavlen, E., 2019. Flow in fractured porous media: a review of conceptual models and discretization approaches. Transp. Porous Media 130 (1), 215–236. https://doi.org/10.1007/s11242-018-1171-6.

Boon, W.M., Nordbotten, J.M., Yotov, I., 2018. Robust discretization of flow in fractured porous media. SIAM J. Numer. Anal. 56 (4), 2203–2233. https://doi.org/10.1137/17M1139102.

Brenner, K., Groza, M., Guichard, C., Lebeau, G., Masson, R., 2016. Gradient discretization of hybrid dimensional darcy flows in fractured porous media. Numerische Mathematik 134 (3), 569–609. https://doi.org/10.1007/s00211-015-0782-x.

Brenner, K., Hennicker, J., Masson, R., Samier, P., 2016. Gradient discretization of hybrid-dimensional Darcy flow in fractured porous media with discontinuous pressures at matrix-fracture interfaces. IMA J. Numeric. Anal. 37 (3), 1551–1585. https://doi.org/10.1093/imanum/drw044.

Brenner, K., Hennicker, J., Masson, R., Samier, P., 2018. Hybrid-dimensional modelling of two-phase flow through fractured porous media with enhanced matrix fracture transmission conditions. J. Comput. Phys. 357, 100–124.

Brezzi, F., Fortin, M., 1991. Mixed and Hybrid Finite Element Methods. Computational Mathematics, 15. Springer Verlag, Berlin.

Budisa, A., Hu, X., 2019. Block preconditioners for mixed-dimensional discretization of flow in fractured porous media. arXiv e-prints 1905.13513.

Chavent, G., Jaffré, J., 1986. Mathematical models and finite elements for reservoir simulation: Single phase, multiphase and multicomponent flows through porous media. Elsevier Science.

Devloo, P., Teng, W., Zhang, C.-S., 2019. Multiscale hybrid-mixed finite element method for flow simulation in fractured porous media. Comput. Model. Eng. Sci. 119 (1), 145–163. https://doi.org/10.32604/cmes.2019.04812.

Durán, O., Devloo, P.R., Gomes, S.M., Valentin, F., 2019. A multiscale hybrid method for darcy’s problems using mixed finite element local solvers. Comput. Methods. Appl. Mech. Eng. 354, 213–244. https://doi.org/10.1016/j.cma.2019.05.013.

Ern, A., Guermond, J.-L., 2004. Theory and Practice of Finite Elements. Applied mathematical sciences, 159. Springer. https://doi.org/10.1007/978-1-4757-4355-5.

Favino, M., Hunziker, J., Caspari, E., Quintal, B., Holliger, K., Krause, R., 2020. Fully-automated adaptive mesh refinement for media embedding complex heterogeneities: application to poroelastic fluid pressure diffusion. Comput. Geosci. 2020. https://doi.org/10.1007/s10596-019-09928-2.

Flemisch, B., Berre, I., Boon, W., Fumagalli, A., Schwenck, N., Scotti, A., Stefansson, I., Tatomir, A., 2018. Benchmarks for single-phase flow in fractured porous media. Adv. Water Resour. 111, 239–258. https://doi.org/10.1016/j.advwatres.2017.10.036.

Fumagalli, A., Keilegavlen, E., Scialò, S., 2019. Conforming, non-conforming and non-matching discretization couplings in discrete fracture network simulations. J. Comput. Phys. 376, 694–712. https://doi.org/10.1016/j.jcp.2018.09.048.

Geuzaine, C., Remacle, J.-F., 2009. Gmsh: a 3-d finite element mesh generator with built-in pre- and post-processing facilities. Int. J. Numer. Methods Eng. 79 (11), 1309–1331. https://doi.org/10.1002/nme.2579.

Gläser, D., 2020. Case1 - Single Fracture. 10.18419/darus-862.

Keilegavlen, E., Berge, R., Fumagalli, A., Starnoni, M., Stefansson, I., Varela, J., Berre, I., 2020. PorePy: an open-Source software for simulation of multiphysics processes in fractured porous media. Comput. Geosci.. https://doi.org/10.1007/s10596-020-10002-5.

Koch, T., Gläser, D., Weishaupt, K., Ackermann, S., Beck, M., Becker, B., Burbulla, S., Class, H., Coltman, E., Emmert, S., Fetzer, T., Grüninger, C., Heck, K., Hommel, J., Kurz, T., Lipp, M., Mohammadi, F., Scherrer, S., Schneider, M., Seitz, G., Stadler, L., Utz, M., Weinhardt, F., Flemisch, B., 2020. DuMux 3 - an open-source simulator for solving flow and transport problems in porous media with a focus on model coupling. Comput. Math. Appl. 2020. https://doi.org/10.1016/j.camwa.2020.02.012.

Krause, R., Zulian, P., 2016. A parallel approach to the variational transfer of discrete fields between arbitrarily distributed unstructured finite element meshes. SIAM J. Sci. Comput. 38, C307–C333. https://doi.org/10.1137/15M1008361.

Kumar, K., List, F., Pop, I.S., Radu, F.A., 2020. Formal upscaling and numerical validation of unsaturated flow models in fractured porous media. J. Comput. Phys. 407, 109138.

Kuzmin, D., Löhner, R., Turek, S. (Eds.), 2012. Flux-corrected transport: Principles, algorithms, and applications. Springer. https://doi.org/10.1007/978-94-007-4038-9.

Köppel, M., Martin, V., Jaffré, J., Roberts, J.E., 2019. A lagrange multiplier method for a discrete fracture model for flow in porous media. Comput. Geosci. 23 (2), 239–253. https://doi.org/10.1007/s10596-018-9779-8.

Köppel, M., Martin, V., Roberts, J.E., 2019. A stabilized lagrange multiplier finite-element method for flow in porous media with fractures. GEM - Int. J. Geomath. 10 (1), 7. https://doi.org/10.1007/s13137-019-0117-7.

Lee, I.-H., Ni, C.-F., 2015. Fracture-based modeling of complex flow and CO2 migration in three-dimensional fractured rocks. Comput. Geosci. 81, 64–77. https://doi.org/10.1016/j.cageo.2015.04.012.

Lee, I.-H., Ni, C.-F., Lin, F.-P., Lin, C.-P., Ke, C.-C., 2019. Stochastic modeling of flow and conservative transport in three-dimensional discrete fracture networks. Hydrol. Earth Syst. Sci. 23, 19–34. https://doi.org/10.5194/hess-23-19-2019.

Lipnikov, K., Manzini, G., Shashkov, M., 2014. Mimetic finite difference method. J. Comput. Phys 257, 1163–1227. https://doi.org/10.1016/j.jcp.2013.07.031.

List, F., Kumar, K., Pop, I.S., Radu, F.A., 2020. Rigorous upscaling of unsaturated flow in fractured porous media. SIAM J. Math. Anal. 52 (1), 239–276.

Martin, V., Jaffré, J., Roberts, J.E., 2005. Modeling fractures and barriers as interfaces for flow in porous media. SIAM J. Sci. Comput. 26 (5), 1667–1691. https://doi.org/10.1137/S1064827503429363.

Nikitin, K.D., Yanbarisov, R.M., 2020. Monotone embedded discrete fractures method for flows in porous media. J. Comput. Appl. Math. 364, 112353. https://doi.org/10.1016/j.cam.2019.112353.

Nordbotten, J.M., Boon, W.M., Fumagalli, A., Keilegavlen, E., 2019. Unified approach to discretization of flow in fractured porous media. Comput. Geosci. 23 (2), 225–237. https://doi.org/10.1007/s10596-018-9778-9.

Odsæter, L.H., Kvamsdal, T., Larson, M.G., 2019. A simple embedded discrete fracture-matrix model for a coupled flow and transport problem in porous media. Comput. Methods Appl. Mech. Eng. 343, 572–601. https://doi.org/10.1016/j.cma.2018.09.003.

Raviart, P.A., Thomas, J.M., 1977. A mixed finite element method for 2-nd order elliptic problems. In: Galligani, I., Magenes, E. (Eds.), Mathematical Aspects of Finite Element Methods. Springer Berlin Heidelberg, pp. 292–315. https://doi.org/10.1007/BFb0064470.

Roberts, J.E., Thomas, J.-M., 1991. Mixed and hybrid methods. In: Ciarlet, P.G., Lions, J.L. (Eds.), Handbook of Nnumerical Analysis, Vol. II. North-Holland, Amsterdam, pp. 523–639. https://doi.org/10.1016/S1570-8659(05)80041-9.

Schädle, P., Zulian, P., Vogler, D., Bhopalam, S.R., Nestola, M.G., Ebigbo, A., Krause, R., Saar, M.O., 2019. 3d non-conforming mesh model for flow in fractured porous media using lagrange multipliers. Comput. Geosci. 132, 42–55. https://doi.org/10.1016/j.cageo.2019.06.014.

Zielke, W., Helmig, R., Krohn, K., Shao, H., Wollrath, J., 1991. Discrete modelling of transport processes in fractured porous rock. In: 7th ISRM Congress, pp. 57–60.

Zulian, P., Kopanicáková, A., Nestola, M. C. G., Fink, A., Fadel, N., Magri, V., Schneider, T., Botter, E., 2016. Utopia: a C++ embedded domain specific language for scientific computing. Git repository.

Paper D

PorePy: an open-source software for simulation of multiphysics processes in fractured porous media

Eirik Keilegavlen, Runar Berge, Alessio Fumagalli, Michele Starnoni, Ivar Stefansson, Jhabriel Varela, Inga Berre

D

Computational Geosciences
DOI: 10.1007/s10596-020-10002-5

Computational Geosciences
https://doi.org/10.1007/s10596-020-10002-5

ORIGINAL PAPER

PorePy: an open-source software for simulation of multiphysics processes in fractured porous media

Eirik Keilegavlen[1] · Runar Berge[1] · Alessio Fumagalli[1,2] · Michele Starnoni[1,3] · Ivar Stefansson[1] · Jhabriel Varela[1] · Inga Berre[1]

Received: 26 August 2019 / Accepted: 10 September 2020

Abstract
Development of models and dedicated numerical methods for dynamics in fractured rocks is an active research field, with research moving towards increasingly advanced process couplings and complex fracture networks. The inclusion of coupled processes in simulation models is challenged by the high aspect ratio of the fractures, the complex geometry of fracture networks, and the crucial impact of processes that completely change characteristics on the fracture-rock interface. This paper provides a general discussion of design principles for introducing fractures in simulators, and defines a framework for integrated modeling, discretization, and computer implementation. The framework is implemented in the open-source simulation software PorePy, which can serve as a flexible prototyping tool for multiphysics problems in fractured rocks. Based on a representation of the fractures and their intersections as lower-dimensional objects, we discuss data structures for mixed-dimensional grids, formulation of multiphysics problems, and discretizations that utilize existing software. We further present a *Python* implementation of these concepts in the PorePy open-source software tool, which is aimed at coupled simulation of flow and transport in three-dimensional fractured reservoirs as well as deformation of fractures and the reservoir in general. We present validation by benchmarks for flow, poroelasticity, and fracture deformation in porous media. The flexibility of the framework is then illustrated by simulations of non-linearly coupled flow and transport and of injection-driven deformation of fractures. All results can be reproduced by openly available simulation scripts.

Keywords Fractured reservoirs · Mixed-dimensional geometry · Numerical simulations · Multiphysics · Discrete fracture matrix models · Open-source software · Reproducible science

1 Introduction

Simulation of flow, transport, and deformation of fractured rocks is of critical importance to several applications such as subsurface energy extraction and storage and waste disposal. While the topic has received considerable attention in the last decade, the development of reliable simulation tools remains a formidable challenge. Many reasons can be given for this; we here pinpoint four possible causes: First, while natural fractures are thin compared to the characteristic length of the domains of interest, their extent can span the entire domain [1]. The high aspect ratio makes the geometric representation of fractures in the simulation model challenging. Second, the strongly heterogeneous properties of fractures compared to the matrix with respect to flow and mechanics call for methods that can handle strong parameter discontinuities as well as different governing physics for the fractures and the matrix, see for instance [2–4]. Third, phenomena of practical interest tend to involve multiphysics couplings, such as interaction between flow, temperature evolution, geo-chemical effects, and fracture deformation [5]. Correspondingly, there is an ongoing effort to develop and introduce multiphysics

Electronic supplementary material The online version of this article (https://doi.org/10.1007/s10596-020-10002-5) contains supplementary material, which is available to authorized users.

✉ Eirik Keilegavlen
Eirik.Keilegavlen@uib.no

[1] Department of Mathematics, University of Bergen, Pb 7800, 5020 Bergen, Norway

[2] Present address: MOX Laboratory, Department of Mathematics, Politecnico di Milano, via Bonardi 9, 20133 Milan, Italy

[3] Present address: Department of Environment, Land and Infrastructure Engineering, Politecnico di Torino, Turin, Italy

Published online: 14 October 2020

couplings within simulation models [6]. Fourth, fracture networks have highly complex intersection geometries, which must be accounted for in the simulation models. Although the geometry of the walls of individual fractures can be complex by themselves, we will not consider this in any detail, but rather assume that averaged apertures are available at the scale of discretizations.

Traditionally, simulation of flow-driven dynamics in fractured media has been based on two conceptual models. The first is the upscaled representation, where the fracture network geometry and dynamical processes taking place in the network are replaced by equivalent continuum models, which resemble those used in non-fractured porous media. As these models do not resolve the fracture geometry, they are computationally efficient, and have been extended to cover a wide range of multiphysics couplings, as exemplified by the TOUGH2 family of codes [7] as well as PFLOTRAN [8]. The accuracy of the simulations is however highly dependent on the quality of the upscaled model, which in turn depends on the fractured domain's resemblance of a continuous medium with respect to the nature of the physical processes. In practice, the upscaling process ranges from treatable by analytical means for simple fracture geometries and dynamics [9, 10], to extremely challenging in the case of multiphysics couplings and complex fracture geometries [11, 12].

The second traditional class of models, known as the discrete fracture network (DFN) models, is constructed using an explicit representation of the fracture network in the simulation model, while ignoring the surrounding rock mass. The models combine highly accurate representation of dynamics in the fractures with computational efficiency from not having to deal with the rock matrix. DFN simulation models with a high level of sophistication have been developed, notably for coupled flow and transport, see for instance [13–15]. By themselves, DFN models cannot represent processes outside the fracture network; however, the models can be combined with continuum models to achieve fracture-matrix couplings.

The respective limitations of continuum and DFN models have, over the last decade, led to an increased interest in the class of discrete fracture matrix (DFM) models. In DFM models, the fractures are sorted in two classes according to their importance for the dynamics in question [16]. The most important fractures are represented explicitly, while upscaled models are applied for the remaining fractures and the host rock. As such, DFM models represent a flexible compromise between upscaling and explicit representations. The models can represent governing equations in the rock matrix, fractures, and generally also in the intersections between fractures. For computational efficiency, it is common to represent fractures and their intersections as lower-dimensional objects embedded in the three-dimensional rock matrix [17, 18]. We refer to such representation as a mixed-dimensional model [19], and conversely refer to a model of a domain where only a single dimension is considered fixed dimensional.

DFM models can further be divided into two subgroups, according to whether they explicitly represent the fracture surfaces in the computational grid [16]. Models that apply non-conforming gridding include the embedded discrete fracture matrix model (EDFM) [20], and extended finite element methods (XFEM) [21, 22]. These methods avoid the complexities of conforming grid generation discussed below, but must instead incorporate the fracture-matrix interaction in what becomes complex modifications of the numerical method for XFEM [23], or by constructing an upscaled representation, e.g., [24], where the latter approach faces challenges reminiscent of those in continuum-type models. For this reason, our interest herein is DFM methods with conforming grids. Construction of these grids can be challenging for complex fracture networks, particularly in 3d, and the high cell count that may result can put limits in the amount of fractures that can be explicitly represented. Nevertheless, this type of DFM models has been developed for flow and transport, as well as mechanics and poroelasticity, and the explicit representation is particularly useful when the fractures deform. Simulation models that incorporate DFM principles include DuMuX [25], CSMP [26], MOOSE-FALCON [27, 28], OpenGeoSys [29], and Flow123d [30].

The utility of a rapid prototyping framework is illustrated by the wide usage of the Matlab Reservoir Simulation Toolbox (MRST) [31, 32], mainly for non-fractured porous media. Similarly, research into strongly coupled processes in mixed-dimensional geometries will benefit from software of similar flexibility and with a structure tailored to the specific challenges related to fractured porous media.

The goal of this paper is twofold: First, we review challenges related to design of simulation frameworks for multiphysics couplings in mixed-dimensional geometries. Our aim is to discuss design choices that must be made in the implementation of any DFM simulator, including data structures for mixed-dimensional geometries, and representation and discretization of multiphysics problems. Second, we describe a framework for integrated modeling, discretization, and implementation, and an open-source software termed PorePy adhering to this framework. Key to our approach is a decomposition of the geometry into separate objects for rock matrix, individual fractures, and fracture intersections. Governing equations can then be defined separately on each geometric object, as well as on the connection between the objects. This allows for significant code reuse from the discretization of fixed-dimensional problems; thus, our design principles are also applicable to more general PDE software frameworks, such as FEniCS [33], Dune [34], and FireDrake [35]. Furthermore, for scalar and vector elliptic problems

(flow and deformation), the models rest on a solid mathematical formulation [36–38].

Built on the mixed-dimensional geometry, PorePy offers several discretization schemes for mathematical models of common processes, such as flow, transport, and mechanical deformation. Multiphysics couplings are easily formulated, and their discretization depends on the availability of appropriate discretization schemes. Moreover, the framework allows for different geometric objects to have different primary variables and governing equations. The software can be used for linear and non-linear problems, with the latter treated by automatic differentiation. PorePy offers automatic gridding of fractured domains in 2d and 3d, relying on the third-party software Gmsh [39] to construct the grid. PorePy is fully open-source (see www.github.com/pmgbergen/porepy) and is released under the GNU General Public License (GPL) version 3.

The paper is structured as follows: In Section 2, we present the principles whereupon we have built the mixed-dimensional framework in PorePy. Section 3 presents models for physical processes central to fractured porous media: single-phase flow, heat transport, and poroelastic rock deformation coupled with fracture deformation modeled by contact mechanics. The implementation of PorePy is presented in Section 4. In Section 5, we benchmark our approach and the PorePy library against well-established test cases. In Section 6, we present two complex applications to illustrate the potential of the framework with respect to advanced physical processes, followed by conclusions in Section 7.

2 Design principles for mixed-dimensional simulation tools

Developing a simulation model for a specific process in mixed-dimensional media requires three main ingredients: A representation of the mixed-dimensional geometry, governing equations for dynamics within and between the geometric objects (rock matrix, fractures, and fracture intersections), and a strategy for discretization and assembly of the equations on the geometry. This in turn leads to decisions on how much of the mixed-dimensional geometry to represent, which type of couplings between different geometric objects to permit, and how to establish communication between the geometric objects.

In this section, we discuss principles for modeling of coupled processes between dimensions in a general context of fractured rocks, together with representation of the geometry in a continuous and discrete setting. The general discussion herein is supplemented by concrete examples of modeling of the important processes presented in Section 3, while discretizations and implementation are discussed in Section 4.

2.1 Representation of a mixed-dimensional geometry

We consider the representation of a fracture network embedded in a 3d domain. The dimension of the fractures is reduced to 2. Similarly, fracture intersections are reduced to 1d objects and intersections of intersection lines to 0d, producing a hierarchy of objects of dimensions 0 to 3. For a fracture network in a 2d domain, the natural simplification applies, i.e., fractures will be objects of dimension 1 and intersections objects of dimension 0. An important modeling choice is which parts of the geometry to represent in the model. We emphasize that, as our focus herein is DFM models with explicit fracture representation, it is assumed that at least the dominating fractures and the matrix will be explicitly represented in the simulation model, and furthermore that the simulation grid will conform to the fractures.

We distinguish between two approaches for the representation of the fracture geometry: The first explicitly represents the full hierarchy of geometric objects (3d–0d). However, for many processes, one can to a good approximation assume that the main dynamics take place in the matrix or in the fractures, while objects of co-dimension more than 1 (intersection lines and points) mainly act as transition zones between fractures. This observation motivates the second approach: The matrix and fractures are represented explicitly, together with some model for direct fracture-fracture interaction.

Representation only of matrix and fractures and not the intersections in some sense constitutes the minimal modification to an existing fixed-dimensional model and has been a popular choice, e.g., for flow and transport problems [40]. The strategy has also been taken a long way towards practical applications, see for instance [41]. There are however drawbacks, notably in the treatment of fracture intersections: Without explicit access to the intersection objects, modeling of interaction between two fractures can be challenging. As an example, for flow, the model does not allow for specifying the permeability of the intersection between two fractures. Significantly, the difficulties tend to increase with increasing complexity of the dynamics, such as countercurrent flow due to gravity and capillary forces, and when transitioning from 2d domains to 3d, i.e., the dimension of the intersections increases from zero to one. This has important consequences for model and method development, as issues related to ad hoc treatment of intersection dynamics may not manifest until relatively late in the development process. For these reasons, we prefer the first approach, where all geometric objects are treated (or "represented") equally, independent of their dimension.

To illustrate our geometry representation, consider Fig. 1a showing three fractures that intersect pairwise along three

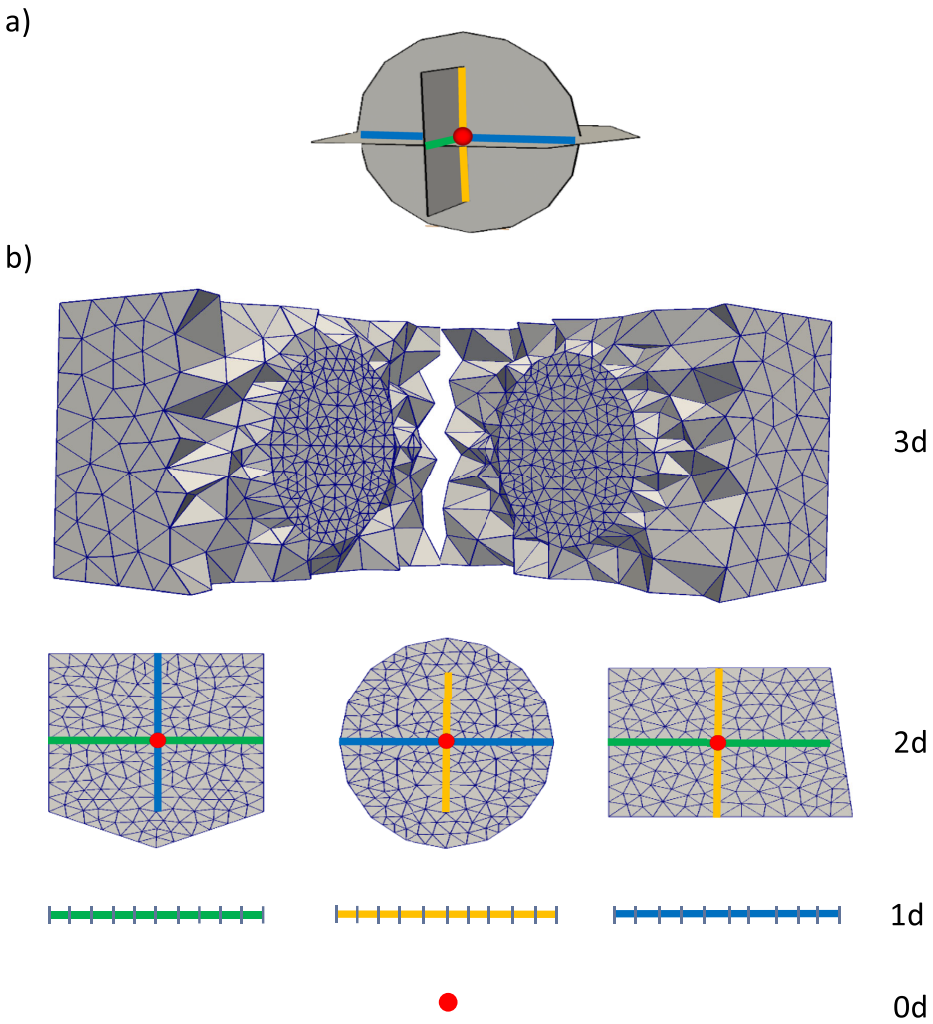

Fig. 1 Conceptual illustration of a fracture network, including grids and lower-dimensional representation. **(a)** Fracture network, the rock matrix is not visualized. (**b**) Grids of all subdomains. Fracture intersections (1d) are represented by colored lines, the 0d grid by a red circle. The 3d grid is cut to expose the circular fracture

lines, which in turn intersect in a point. The fracture network thus defines a set of objects of dimensions $\{0, 1, 2\}$, while the surrounding host medium (not shown) is 3d. We shall refer to each object as a subdomain and denote a generic subdomain by Ω_i. Note that all subdomains of dimension less than 3 are embedded in at least one subdomain of one dimension more, for instance, all lines in the geometry lie on at least two fracture surfaces.

Figure 1b shows the computational grid constructed for each subdomain. The grid on each subdomain conforms to any lower-dimensional subdomains embedded within it, illustrated by the faces in the 3d grid that match the circular fracture. We will discuss grid construction in more detail in Section 4.1.

To finalize the description of the geometry, we introduce the notation for an interface between two subdomains. With reference to Fig. 2, we denote by Ω_h and Ω_l two subdomains one dimension apart so that Ω_l is embedded in Ω_h, and let $\partial_j\Omega_h$ be the part of the boundary of Ω_h that geometrically coincides with Ω_l. Furthermore, we introduce the interface Γ_j on the boundary between $\partial\Omega_h$ and Ω_l. From the dimension reduction, it follows that Γ_j, Ω_l, and $\partial_j\Omega_h$ all coincide geometrically. For completeness, we note that the mathematical framework [36] on which our models are based considers the two sides of Ω_l as

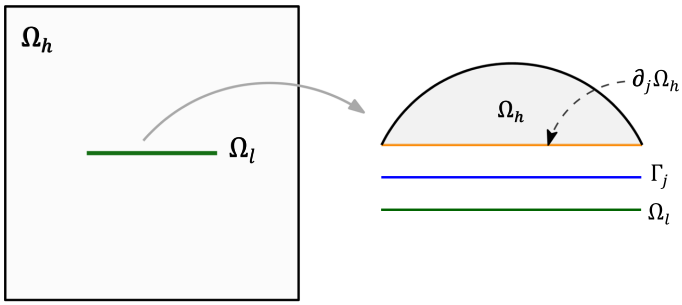

Fig. 2 Mixed-dimensional geometric objects. A higher-dimensional subdomain Ω_h is connected to a lower-dimensional subdomain Ω_l through the interface Γ_j. The part of the boundary of Ω_h geometrically coinciding with Ω_l is denoted by $\partial_j\Omega_h$. The interface Γ_k on the lower side of Ω_l is not shown

different interfaces, Γ_j and Γ_k. Throughout, we will let Γ_j denote a generic interface and use the triplet (Γ_j, Ω_h, Ω_l) to represent an interface and its higher- and lower-dimensional neighbor.

2.2 Permissible coupling structures for mixed-dimensional processes

For modeling purposes, it is important to establish which types of couplings between variables on subdomains and interfaces are permitted. In our framework, we impose the following constraints on the modeling of dynamic processes:

1. There is only coupling between subdomains that are exactly one dimension apart.
2. Interaction between subdomains is formulated as a model on the interface between the subdomains.
3. A model on an interface can depend on variables on the interface and the immediate subdomain neighbors, but not on variables associated with other subdomains or interfaces.

These choices have two important consequences: First, our framework explicitly rules out direct 3d-1d couplings. Second, our model does not permit direct coupling between objects of the same dimension, say, two fractures; the communication must go via a lower- or higher-dimensional object. On the other hand, the imposed constraints make the structure of the equations on a subdomain relatively simple, as the dynamics depend only on variables internal to the subdomain and on neighboring interfaces.

In some cases, it can be of interest to also consider couplings between subdomains of equal dimension, for instance to implement domain decomposition solvers. This can be realized by a secondary partitioning of the subdomains. When such a strategy is applied, the above constraints should be applied only on the interface between subdomains of different dimensions. On interfaces between subdomains of the same dimension, standard continuity conditions can be applied.

3 Model problems

In this section, we use the modeling framework defined in Section 2 to present three sets of governing equations, each of which is of high relevance for fractured porous media: the elliptic pressure equation, fully coupled flow and transport, and fracture deformation coupled with poroelastic deformation of the host medium. Since most of the involved fixed-dimensional processes are well established, our main purpose is to apply the modeling framework described in Section 2 to the mixed-dimensional setting.

We introduce the following notation for variables and subdomains: Variables in a generic subdomain Ω_i are marked by the subscript i, while the subscript j identifies interface variables on Γ_j. For a subdomain Ω_i, the set of neighboring interfaces is split into interfaces towards subdomains of higher dimensions, denoted $\widehat{S}_i$, and interfaces towards subdomains of lower dimensions, denoted by $\check{S}_i$ (see Fig. 3).

Communication between an interface and its neighboring subdomains is handled by projection operators. In the subsequent parts, we will apply four different classes of projections. We indicate the mapping from an interface to the related subdomains by Ξ, with a subscript indicating the index of the interface and a superscript denoting the index of the subdomain, as illustrated in Fig. 4. We also introduce the projection operators from subdomains neighboring of an interface to the interface itself, denoted by the symbol Π with the same convention as before for sub- and superscripts. The actual definition of these objects is scope-dependent and will be specified when needed. The construction of the projection needs to consider the nature of the variable to project, being of intensive or extensive kind, that is, whether the projections should average or sum the variables, respectively.

3.1 Flow in fractured media

We first consider incompressible flow in mixed-dimensional geometries, where we assume a Darcy-type relation between

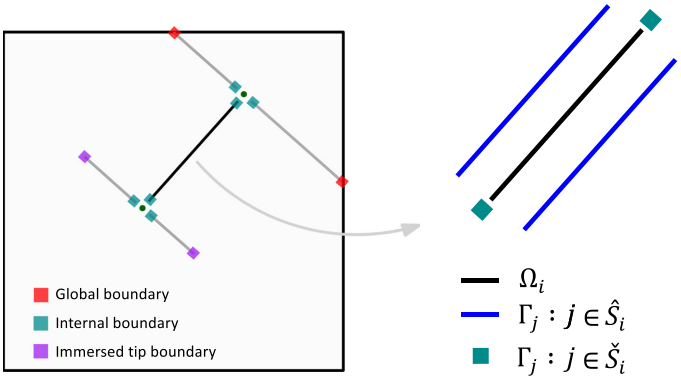

Fig. 3 Intersecting fractures, interfaces, and types of boundary conditions. The 2d domain contains three fractures (1d lines) that intersect in two intersection points (dots). The fractures have three types of boundaries: internal (green squares), immersed tips (purple squares), and endings at the external boundary (red squares). A close-up of the black fracture Ω_i shows the interfaces associated with its higher-dimensional (blue lines) and lower-dimensional (green squares) neighboring subdomains. The sets of such interfaces are denoted respectively by $\hat{S}_i$ and $\check{S}_i$

the flux and the pressure gradient in all subdomains. The model has been presented several times before, see, e.g., [2, 42, 43].

First, consider a domain with a single interface Γ_j with neighboring subdomains Ω_h and Ω_l. In addition to the pressure p_i and flux q_i in each subdomain, we denote the flux on Γ_j by λ_j and formally write $\lambda_j = \Pi_j^h \, tr \, q_h \cdot n_h$, with n_h the unit normal on $\partial_j\Omega_h$ pointing from Ω_h to Ω_l, and tr a suitable trace operator mapping from Ω_h to $\partial_j\Omega_h$, referring to Fig. 4. The strong form of the Darcy problem for Ω_l reads: find (q_l, p_l) such that

$$\begin{aligned} q_l + \frac{\mathcal{K}_l}{\mu_l}\nabla p_l &= 0, \\ \nabla \cdot q_l - \Xi_j^l \lambda_j &= f_l \end{aligned}, \tag{3.1}$$

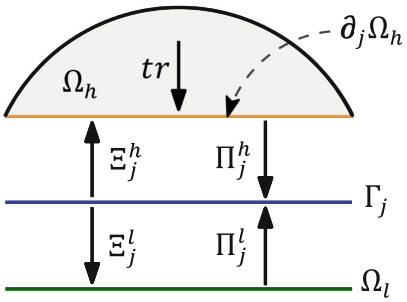

Fig. 4 Representation of a generic coupling between two subdomains. An interface Γ_j is coupled to a higher-dimensional subdomain Ω_h and a lower-dimensional subdomain Ω_l. The projection operators are denoted by Ξ (interface to subdomains) and Π (subdomains to interface) with subscripts indicating the interface and superscripts indicating the subdomain. The trace operator tr maps quantities from Ω_h to its boundary $\partial_j\Omega_h$

where the differential operators are defined on the tangent space of Ω_l and Ξ_j^l maps from Γ_j to Ω_l. We have indicated with f_l a source or sink term, μ_l is the fluid viscosity, while $\mathcal{K}_l$ represents the effective tangential permeability tensor scaled by the aperture as described in [42]. An analogous problem is written for (q_h, p_h), with the exception that $\Xi_j^h \lambda_j$ is mapped to a boundary condition on $\partial_j\Omega_h$,

$$q_h \cdot n_h|_{\partial_j\Omega_h} = \Xi_j^h \lambda_j. \tag{3.2}$$

The flux λ_j is given by an interface condition on Γ_j, which reads

$$\lambda_j + \frac{\kappa_j}{\mu_j}\left(\Pi_j^l p_l - \Pi_j^h tr\, p_h\right) = 0. \tag{3.3}$$

Here, κ_j indicates the normal effective permeability. Equation (3.3) can be seen as a Darcy law in the normal direction of Γ_j. Different types of boundary conditions can be imposed on the external boundary of Ω_h and Ω_l. Moreover, we impose null flux if Ω_l has an immersed tip boundary.

The extension to problems with many subdomains is now immediate: The flux on an interface is still formulated in terms of variables on its two neighboring subdomains, while for a subdomain Ω_i summation over all neighboring interfaces gives the problem: Find (q_i, p_i) so that

$$\begin{aligned} q_i + \frac{\mathcal{K}_i}{\mu_i}\nabla p_i &= 0, \\ \nabla \cdot q_i - \textstyle\sum_{j \in S} \Xi_j^i \lambda_j &= f_i, \\ q_i \cdot n_i|_{\partial_j\Omega_i} &= \Xi_j^i \lambda_j \quad \forall j \in \check{S}_i \end{aligned} \tag{3.4}$$

In the case of $d = 0$, most of the above terms are void, and we are left with the balance between the source term and fluxes from higher dimensions, while for the case $d = 3$, the term involving interface fluxes from higher dimensions is void.

3.2 Fully coupled flow and transport

We next turn to modeling of fully coupled flow and transport, as an example of a multiphysics problem with variable coupling within and between subdomains. We consider a single-phase flow of an incompressible fluid with two components that mix ideally. We denote by c_i the mass fraction of a component associated with Ω_i; the closure relation for the mass fractions implies that we can calculate the other value by $1 - c_i$. The governing equation of the fluid is given by Darcy's law and the fluid mass conservation as in Eq. (3.4). However, we let the viscosity of the fluid depend on the mass fraction,

$$\mu_i = \mu_i(c_i). \tag{3.5}$$

The conservation equations for the components can be formulated as

$$\phi_i \frac{\partial c_i}{\partial t} + \nabla \cdot (c_i q_i - \mathcal{D}_i \nabla c_i) - \sum_{j \in \check{S}_i} \Xi_j^i \left(\eta_j + \beta_j \right) = g_i. \tag{3.6}$$

Here, ϕ_i represents the effective porosity, $\mathcal{D}_i$ is the effective diffusivity, and g_i denotes sources and sinks. A sum of advective, η_j, and diffusive, β_j, fluxes from the higher-dimensional domains is included in the conservation equation. As for the flow problem, flow over lower-dimensional interfaces Γ_j, $j \in \check{S}_i$, enters as Neumann boundary conditions. We note that the governing equations are coupled via the mass fraction dependency of viscosity and the presence of the Darcy flux in the advective transport.

Let us now consider the interaction between two neighboring subdomains Ω_h and Ω_l via the common interface Γ_j. The flow over Γ_j, denoted by λ_j, is given by Eq. (3.3), where the interface viscosity μ_j is modeled as a function of the mean of the mass fractions on the two sides,

$$\mu_j = \mu_j \left(\frac{\Pi_j^l c_l + \Pi_j^h tr\, c_h}{2} \right). \tag{3.7}$$

The component flux over Γ_j is again governed by an advection-diffusion relation: The diffusion term β_j is, in analogy with the corresponding term for the Darcy flux, given by

$$\beta_j + \delta_j \left(\Pi_j^l c_l - \Pi_j^h tr\, c_h \right) = 0, \tag{3.8}$$

with δ_j representing the effective diffusivity over the interface Γ_j. For the advective term η_j, we introduce an upstream-like operator based on the Darcy interface flux:

$$Up(c_h, c_l; \lambda_j) = \begin{cases} \Pi_j^h tr\, c_h, & \text{if } \lambda_j \geq 0 \\ \Pi_j^l c_l, & \text{if } \lambda_j < 0. \end{cases} \tag{3.9}$$

With this, the advective interface flux η_j is given by the relation

$$\eta_j - \lambda_j Up(c_h, c_l; \lambda_j) = 0. \tag{3.10}$$

Finally, global boundary conditions are imposed in the standard way for elliptic and advection-diffusion problems, see, e.g., [44]. Equations (3.5)–(3.10) define the governing equations in all subdomains and on all interfaces, with the exception of 0d domains, where the diffusion operator again is void.

3.3 Poroelastic fracture deformation by contact mechanics

Our final set of model equations considers poroelastic deformation of a fractured medium, where the fractures may open or, if the frictional forces are insufficient to withstand tangential forces on the fracture surface, undergo slip. This process is important in applications such as geothermal energy extraction and CO_2 storage. Modeling of the process is non-trivial due to (i) the coupled poroelastic processes, (ii) the heterogeneous governing equations between subdomains, (iii) the need to use non-standard constitutive laws to relate primary variables during sliding, and (iv) the non-smooth behavior of the constitutive laws in the transition between sticking and sliding and between open and closed fractures. Modeling of this process is an active research field, see, e.g., [45–47], and thus represents an example where the availability of a flexible prototyping framework is highly useful. Due to the complexity in deformation of intersecting fractures, we limit our exposition to media with non-intersecting fractures.

Flow and deformation in the rock matrix, represented by the subdomain Ω_h, are governed by Biot's equations for poroelasticity [48].

$$\begin{aligned} &\nabla \cdot (\mathcal{C}_h \nabla_s u_h - \alpha_h p_h I) = b_h, \\ &\alpha_h \frac{\partial (\nabla \cdot u_h)}{\partial t} + \theta_h \frac{\partial p_h}{\partial t} - \nabla \cdot \left(\frac{\mathcal{K}_h}{\mu_h} \nabla p_h \right) = f_h \end{aligned} \tag{3.11}$$

Here, the first equation represents conservation of momentum, with the acceleration term neglected, while the second equation expresses conservation of mass. The primary variables are the displacement, u_h, and the fluid pressure, p_h. The stiffness matrix $\mathcal{C}_h$ can for linear isotropic media be expressed purely in terms of the first and second Lamé parameters, and the elastic stress can be computed as

$$\sigma_h = \mathcal{C}_h \nabla_s u_h,$$

where ∇_s is the symmetric gradient. Furthermore, α_h is the Biot constant, I the second-order identity tensor, b_h denotes body forces, and θ_h the effective storage term. We also assume boundary conditions are given on the global boundary.

Next, to model relative motion of the fracture walls, it is necessary to consider both interfaces between Ω_h and Ω_l. In a slight abuse of notation, we will let u_j denote the displacement variable on both interfaces. We emphasize that u_j is a vector in $\mathbb{R}^n$, that is, it represents the displacement in both the tangential and normal direction of Ω_l. We will require continuity between u_h and u_j, expressed as $\Pi_j^h tr\, u_h = u_j$, where we recall that the trace operator maps to $\partial_j\Omega_h$. We also introduce the jump in displacement, $[\![u_j]\!]$, between the two interfaces on opposing sides of Ω_l (see Fig. 5). The jump is decomposed into the tangential jump $[\![u_j]\!]_\tau$ and the normal jump $[\![u_j]\!]_n$.

The mechanical state in Ω_l is described by the contact traction σ_l, which also is a vector in $\mathbb{R}^n$, with normal and tangential components $\sigma_{l,n}$ and $\sigma_{l,\tau}$, respectively. Our model also includes fluid flow in the fracture Ω_l, which is governed by conservation of mass

$$\frac{\partial}{\partial t}\left(a([\![u_j]\!])\right) + \theta_l \frac{\partial p_l}{\partial t} - \nabla \cdot \left(\frac{\mathcal{K}_l}{\mu_l}\nabla p_l\right) - \Xi_j^l \lambda_j = f_l. \quad (3.12)$$

Here, the time derivative of the aperture $a([\![u_j]\!]) = a_0 - [\![u_j]\!]_n$ represents changes in the available volume due to changes in the displacement jump, with a_0 denoting the residual hydraulic aperture. The negative sign on the normal jump is related to the sign convention in (3.14) below. As in the previous sections, the relation between the fluid pressures in Ω_h and Ω_l is governed by a flux law of the type (3.3).

The relation between σ_l and $[\![u_j]\!]$ is modeled by borrowing techniques from contact mechanics as summarized here (for a full discussion, see [49]). Balance of tractions between the poroelastic stress in Ω_h and the contact traction in Ω_l is for the two sides expressed as

$$\begin{aligned}\Pi_{j_1}^h n_h \cdot (\sigma_h - \alpha_h p_h I) &= \Pi_{j_1}^l \sigma_l - \left(\Pi_{j_1}^h n_h\right) \cdot \left(I\Pi_{j_1}^l \alpha_l p_l\right)\\ \Pi_{j_2}^h n_h \cdot (\sigma_h - \alpha_h p_h I) &= -\Pi_{j_2}^l \sigma_l - \left(\Pi_{j_2}^h n_h\right) \cdot \left(I\Pi_{j_2}^l \alpha_l p_l\right)\end{aligned} \quad (3.13)$$

The contact traction is zero whenever the normal displacement jump is nonzero, that is

$$[\![u_j]\!]_n \le 0, \quad \sigma_{l,n} \le 0, \quad [\![u_j]\!]_n \sigma_{l,n} = 0. \quad (3.14)$$

For closed fractures, the motion in the tangential direction is controlled by the ratio between the tangential traction $\sigma_{l,\tau}$ and the maximum available frictional traction $F\sigma_{l,n}$, where F is the friction coefficient. The time derivative of the displacement jump is zero until the frictional traction is overcome; for larger tangential tractions, the time derivative of the displacement jump and tangential traction are parallel:

$$\begin{aligned}\|\sigma_{l,\tau}\| &\le -F\sigma_{l,n},\\ \|\sigma_{l,\tau}\| &< -F\sigma_{l,n} \rightarrow [\![u_j]\!]_\tau = 0,\\ \|\sigma_{l,\tau}\| &= -F\sigma_{l,n} \rightarrow \exists \gamma \in \mathbb{R}, \sigma_{l,\tau} = -\gamma^2 [\![u^j]\!]_\tau.\end{aligned} \quad (3.15)$$

Here $\|\cdot\|$ represents the Euclidean norm, and $[\![u_j]\!]_\tau$ the sliding velocity. We emphasize that the tangential contact conditions are formulated in terms of the contact traction σ_l, with no contribution from the fluid pressure p_l.

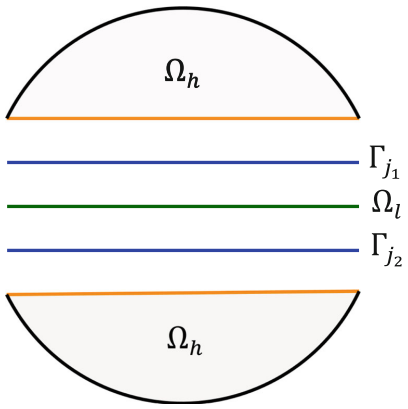

Fig. 5 Illustration of a lower-dimensional domain, Ω_l, that has two interfaces, Γ_{j_1} and Γ_{j_2}, with a higher-dimensional domain, Ω_h

4 Implementation

This section describes the implementation of the mixed-dimensional simulation framework outlined above in the open-source simulator PorePy. Our emphasis is on three topics that are particular to this type of DFM simulation models: Gridding, discretization of subdomain couplings, and how to deal with parameters, variables, and linear systems for multiphysics problems that are defined on an arbitrary number of subdomains and dimensions. The ability to treat these components with relatively simple input is the main distinguishing feature of PorePy, and thus, the section gives an overview of the important properties of the implemented simulator.

Figure 6 displays the main components of PorePy, with emphasis on the mixed-dimensional aspects of the code. The implementation follows the principles of locality of variables and equations described in the previous sections. Specifically, equations and discretizations are assigned on individual subdomains, and the implementation of specific discretization schemes closely resembles that applied to fixed-dimensional problems. Similarly, the stencil of interface couplings is

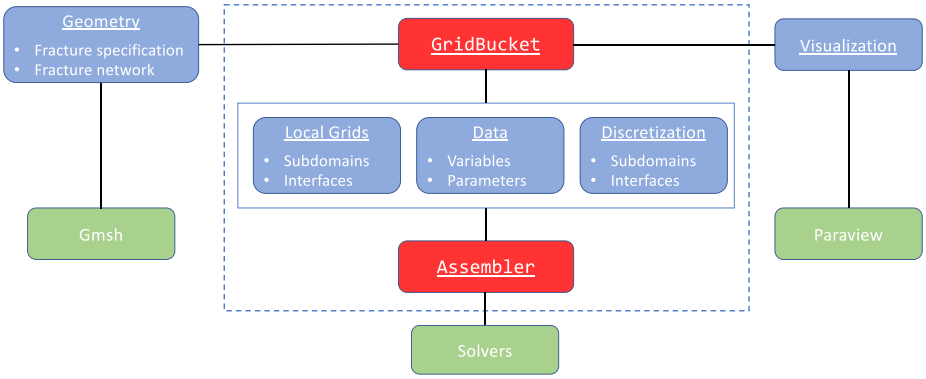

Fig. 6 Outline of the architecture of PorePy: The main mixed-dimensional components are the GridBucket class, which is a combined grid and data manager, and the Assembler class, which acts as a degree of freedom manager. Variables, parameters, and discretizations are local to subdomains and interfaces. Geometry specification and grid construction is handled in part by communication with Gmsh, while visualization is available through export to Paraview. Green boxes represent external dependencies

limited to the interface and the immediate neighboring subdomains. The connection between the subdomains is handled in a top-down manner and implemented in two core classes: The GridBucket class keeps track of the relation between neighboring subdomains and interfaces, and it also acts as a facility for storage of parameters and variables. The Assembler class can be considered a global degree of freedom manager which also has methods for global discretization and assembly. These core mixed-dimensional components are supplemented by functionality for grid construction, assisted by Gmsh, while visualization and linear solvers must be handled by external packages.

A typical workflow for a mixed-dimensional simulation will consist of the following steps:

1. Specify the problem geometry. Use this to create a GridBucket object, that is, a mixed-dimensional grid.
2. On the individual subdomains and interfaces in the GridBucket, specify variables, parameters, and discretizations (thus implicitly define governing equations).
3. Create an Assembler object, use this for initial discretization and assembly of linear system.
4. Solve the mixed-dimensional problem.

Depending on the problem characteristics, the last point can entail non-linear iterations, time stepping, etc.

The rest of this section presents design choices and concrete implementation details of the individual steps. As an illustration of the usage of the resulting simulation framework, Fig. 7 provides an example PorePy code for the setup, discretization, and solution of the mixed-dimensional compressible flow problem. We emphasize that to change the problem geometry, e.g., the fracture network, it is sufficient to change the pink section, while governing equations, parameters, and/or discretization schemes are altered by modifications to the green section. Several examples of the latter are given in Section 5.

4.1 Mixed-dimensional geometry and gridding

Grid construction is one of the main technical bottlenecks for the application of conforming DFM models. The translation of a geometric description of the fracture network into a computational grid consists of three steps: Identification of intersection lines and points, construction of the mixed-dimensional grid, and post-processing of the grid into a format that is suited for the discretization approaches described in Section 4.2. The first and third of these tasks are technically challenging, and one of the strengths of PorePy is that it provides a robust implementation with a simple interface. The second item, grid construction, is a highly advanced research topic in its own; in PorePy, this is handled by a Gmsh backend.

4.1.1 Geometry processing

In PorePy, fractures are described as lines (for 2d domains) or convex planar polygons (in 3d). Curved objects are not supported, as this would significantly complicate the task of identifying intersections; however, piecewise linear approximations are possible. The fractures are specified by their endpoints (in 2d) or vertexes (in 3d). Individual fractures are collected into FractureNetwork2d and FractureNetwork3d classes.

Before passing the fracture network to a gridding software, all fracture intersections must be found. In principle, the computation of fracture intersections is straightforward, following

Section 4.1

```
import porepy as pp
import numpy as np
from scipy.sparse.linalg import spsolve

## Define fractures and fracture network
f1 = pp.Fracture(np.array([[0, 1, 1, 0], [0, 0, 1, 1], [0, 0, 0, 0]]))
f2 = pp.Fracture(np.array([[0, 0, 0, 0], [0, 1, 1, 0], [0, 0, 1, 1]]))
network = pp.FractureNetwork3d([f1, f2])

# Construct GridBucket using prescribed mesh size parameters
gb = network.mesh({'mesh_size_frac': 0.1, 'mesh_size_bound': 1, 'mesh_size_min':0.01})
```

Section 4.2

```
## Define parameters and discretizations
diffusion_discr = pp.Mpfa('flow')  # Discretization for diffusion term
accumulation_discr = pp.MassMatrix('flow')
for g, d in gb:  # Loop over all subdomain grids (g) and their associated data (d)
    pp.initialize_default_data(g, d, 'flow')  # Default parameters for flow problem
    d[pp.PRIMARY_VARIABLES] = {'p': {'cells': 1}}  # Primary var. p, one dof per cell

    # Assign discretizations for accumulation and diffusion terms
    d[pp.DISCRETIZATION] = {'p': {'accumulation': accumulation_discr,
                                  'diffusion': diffusion_discr}}

for e, d in gb.edges():  # Loop over all interfaces (e) and their associated data (d)
    g_l, g_h = gb.nodes_of_edge(e)   # Get grids of neighboring subdomains
    mg = d['mortar_grid']            # Get hold of mortar grid
    data = {'normal_diffusivity': 1} # Declare interface parameters
    pp.initialize_data(mg, d, 'flow', data)  # Default parameters for flow problem
    d[pp.PRIMARY_VARIABLES] = {'mortar_flux': {'cells': 1}}  # Primary variable
    # The interface discretization has access to associated subdomain discretizations
    interface_discr = pp.RobinCoupling('flow', diffusion_discr, diffusion_discr)
    # Define coupling term through variables and terms/discretizations on the
    # interface and the neighboring subdomains
    d[pp.COUPLING_DISCRETIZATION] = { 'interface_flux':  # identifier of this term
        {g_h: ('p', 'diffusion'),               # variable and term on Omega_h
         g_l: ('p', 'diffusion'),               # variable and term on Omega_l
         e: ('mortar_flux', interface_discr)}}  # variable and term on Gamma_j
```

Section 4.3

```
## Create object for global assembly and discretization
assembler = pp.Assembler(gb)
assembler.discretize()                  # Call discretize on all local discretizations
A, b = assembler.assemble_matrix_rhs()  # Assemble global discretization matrices
```

Section 4.4

```
## Solve linear system and export results
p = spsolve(A, b)                 # Solve sparse linear system
assembler.distribute_variable(p)  # Distribute variables to subdomains and interfaces

# Set up an exporter to write the mixed-dimensional pressure field to vtk
paraview_exporter = pp.Exporter(gb, file_name='foo')
# Write data to vtk, ready for import in Paraview.
paraview_exporter.write_vtk('p')
```

Fig. 7 Setup of a full PorePy simulation, illustrated by a mixed-dimensional compressible flow problem solved with a single time step. The background colors indicate different simulation stages, which are discussed in detail in the indicated subsections

for instance [50]. However, to reduce the complexity of the grid construction and limit the number of cells in the resulting grid, it can be useful to alter the geometry to avoid small details, such as almost intersecting fractures. PorePy automatically merges objects that are closer than a user-specified tolerance, and also cuts dangling fracture ends. While such modifications can alter the connectivity of the network, we have found that it is a critical ingredient for dealing with fracture networks that originate from sources that have not removed such small details, for instance networks exported from geological processing software or stochastic fracture network generators.

4.1.2 Gridding

The computational grid should conform to all fractures, and by extension also to their intersection lines and points. This is a difficult problem; however, algorithms [51–53] and high-quality implementations [54, 55] are available. PorePy relies on Gmsh [39] for the grid construction, as this allows for a unified approach in both 2d and 3d domains. While Gmsh allows for a nuanced specification of grid sizes, only a limited set of this functionality is exposed in the PorePy interface: A grid size can be set for the fracture network and the far field; more advanced settings can be accessed by direct manipulations in Gmsh. Still, the specified geometry implicitly sets conditions on the grid size; if the fracture network contains fractures that are close relative to the specified grid size, Gmsh will attempt to construct a grid with reasonable quality, and thereby override the user preferences if necessary.

4.1.3 Construction of grids, mortar grids, and projection operators

The grids provided by Gmsh must be post-processed to be of use for our mixed-dimensional simulations. First, grids for individual subdomains must be extracted. Second, mortar grids must be constructed on the interface between subdomain grids, together with projection operators between the grids. Third, the resulting sets of grids must be arranged in the mixed-dimensional GridBucket.

Subdomains of different dimensions can be identified from Gmsh tags that for each cell identify the geometric object to which the cell belongs (matrix, fracture, or intersection). However, to avoid direct connection between cells that lie on different sides of lower-dimensional objects, faces must be split, and nodes duplicated before the grids are arranged in the GridBucket. This process is illustrated in Fig. 8, which also shows the resulting lower-dimensional grids. Note that while all (d–1)-dimensional faces are split in two, the number of duplicates of a node depends on whether it is located on an intersection, a fracture tip or a global boundary, or in the interior of the subdomain. After this modification, the cells that belong to the same geometric objects are collected into subdomain grids. These are implemented as standard fixed-dimensional grids, so that when a discretization scheme is applied to a subdomain, this is indistinguishable from the traditional fixed-dimensional operation. In this spirit, the grid structure used for individual grids is agnostic to spatial dimension, with an implementation heavily inspired by that of MRST [32].

The mortar grids constructed under post-processing of the Gmsh output are associated with the interfaces. They match with the lower-dimensional grid, and thereby also with the split faces of the higher-dimensional grid. The mortar grids also have methods for the construction of projection matrices between themselves and the lower- and higher-dimensional neighboring subdomains, with separate methods for the mapping of extensive and intensive quantities. Only the lowest order projection operators are available in PorePy, which for matching grids simply identify the split faces of Ω_h with cells in Γ_j, and cells in Γ_j with cells in Ω_i. However, non-matching grids can be introduced by replacing individual subdomain and mortar grids. Specifically, computational speedups can often be achieved by combining fine grids in fractures, which are often the main venue for dynamical processes, with relatively coarse grids in the matrix. During the replacement, the projection operators are automatically updated to account for the resulting non-matching grids.

The individual subdomains and mortar grids are collected in the GridBucket class. This is implemented as a graph, where each subdomain grid Ω_i defines a node, while the interface Γ_j is represented as an edge in the graph, and is identified by the pairing of its neighboring subdomains (Ω_h, Ω_l). In addition to keeping track of geometric information, the GridBucket also provides flexible data storage in the form of dictionaries on subdomains and interfaces. These are used for parameters, discretizations, simulation results, and other data if relevant.

4.2 Primary variables, parameters, and discretization

To define a problem to be discretized in PorePy, one must define primary variables, governing equations, and problem

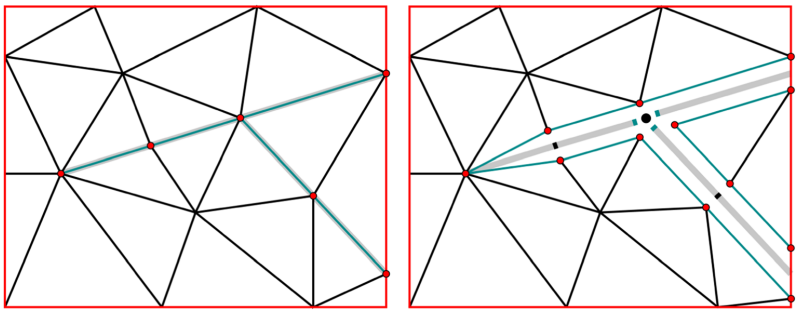

Fig. 8 The process of splitting the faces and nodes of the grid. The faces and nodes of the 2d grid that coincide with the 1d grids (gray lines) are split and define an internal boundary of the grid. Similarly, the faces and nodes of the 1d grids that coincide with the 0d grid (black dot) are split. Note that the split nodes and faces coincide geometrically but have been shifted in the right figure for illustrative purposes

parameters. PorePy is designed to allow for maximum flexibility in these specifications. Variables and parameters are defined on individual subdomains and interfaces. Governing equations are specified in terms of their discretizations: Each variable can be assigned one or several discretizations corresponding to different terms in the equation. As with the variable specification, discretizations are specified locally on subdomains and interfaces, thus heterogeneous governing equations or discretization schemes can readily be assigned. It is up to the user to ensure that the specified combination of variables, equations, and discretizations is mathematically well posed on the given mixed-dimensional grid.

In terms of implementation, the data structures for parameters and solution vectors are stored locally to each subdomain and interface. Specifically, variables are represented as numpy arrays and parameters as a combination of numpy arrays and dedicated classes.

4.2.1 Discretization classes

For the implementation of discretizations, it is useful to differ between the schemes themselves, their implementation, and the application of a discretization object to a specific grid and parameter set, which produces a discretization matrix. All discretization schemes are implemented as classes which are designed to act on individual subdomains or interfaces. In most cases, there is a one-to-one correspondence between terms in the governing equations and discretization. As an example, the compressible flow equation on a subdomain will be specified by assigning discretizations of the accumulation and diffusion term to a pressure variable, as is shown in Fig. 7.

A compatible discretization class should implement a method for discretization, which computes coefficients that will enter into a discretization matrix. Furthermore, the class needs a method for assembly of matrix and right-hand side. The act of discretization and assembly should together produce a local discretization matrix, usually in the form of a sparse matrix represented using the SciPy library and a right-hand side represented as a numpy array.

There are important differences between discretization classes for subdomains and interfaces: Subdomain discretizations have access only to the subdomain grid and its associated data and assemble a matrix local to the subdomain. An interface discretization is responsible for coupling variables on the neighboring subdomains, and it therefore has access to the relevant subdomain discretizations and data in addition to information local to the interface. Thus, an interface discretization may put additional requirements on a subdomain discretization, see Section 4.2.2 for an example. The assembly method in the interface discretization should treat both the interface equation and the discrete couplings of the interface law to the neighboring subdomains.

In PorePy, subdomain discretization schemes are available for diffusion, advection, and mechanical deformation, as well as mass matrices for accumulation terms. Specifically, diffusion processes can be discretized by the lowest order Raviart-Thomas mixed finite elements combined with a piecewise constant pressure approximation (RT0-P0) [56], the lowest order mixed virtual element method (MVEM) combined with a piecewise constant pressure approximation [57, 58], and by two finite volume schemes: the two- and multipoint flux approximations (TPFA and MPFA, respectively). Advection terms can be discretized by a first-order upstream scheme. Mechanical deformation is discretized by the multipoint stress approximation (MPSA) [59, 60], also extended to poroelasticity [61] and thermo-poroelasticity [62].

On interfaces, discretization schemes in PorePy cover the interface diffusion law (3.3), and an upstream scheme for the advection term (3.9). The discretization of the contact mechanics (Eqs. (3.14) and (3.15)) is implemented by a semi-smooth Newton method to deal with the discontinuities in the solution, for details we refer to [49, 63]. The available discretizations on subdomains and interfaces can also be used as building blocks for more complex problems; for instance, the simulations of thermo-poroelasticity with fracture deformation reported in [64] utilized several of the discretization schemes mentioned above.

In the following, we present the implementation of two examples of combined subdomain and interface discretizations, allowing us to discuss different aspects in the design and implementation of mixed-dimensional problems.

4.2.2 Subdomain coupling for discretization of mixed-dimensional flow

3.1, focusing on the division of responsibilities between subdomain and interface discretizations. The discretization of the interface law (3.3) is implemented in the class RobinInterfaceLaw, which in itself is simple, but has an instructive approach to communication with the adjacent subdomain discretizations. From the model in Section 3.1, we see that for a discretization on a generic subdomain Ω_i to interact with the interface problem, we need to provide operators which:

1) Handle Neumann boundary data on the form $\Xi_j^i \lambda_j$ for all interfaces Γ_j for which Ω_i is the higher-dimensional neighbor.
2) Handle source terms $\Xi_j^i \lambda_j$ from interfaces Γ_j for which Ω_i is the lower-dimensional neighbor.
3) Provide a discrete operator $tr\, p_i$ to be combined with Π_j^i to project the pressure to interfaces Γ_j, $j \in \check{S}_i$.
4) Provide a pressure p_i that can be projected to interfaces Γ_j, $j \in \widehat{S}_i$ using Π_j^i.

RobinInterfaceLaw assumes that the subdomain discretization has dedicated methods, with specified names, that handle each of these four operations. Thus, any discretization class aimed at individual subdomains can be made compatible with RobinInterfaceLaw, and thus applicable to mixed-dimensional problems, provided the four required methods are implemented. Moreover, all of these are readily available in any reasonable implementation of a discretization scheme for elliptic equations. Examples of how RobinInterfaceLaw is set up to interact with subdomain discretizations can be found in Figs. 7 and 10.

It is instructive to write out the structure of the coupled system for our case with two subdomains Ω_h and Ω_l separated by an interface Γ_j. Denote by y_h, y_l, and ξ_j the vectors of discrete unknowns in Ω_h, Ω_l, and on Γ_j, respectively. As we make no assumptions that the same discretization scheme is applied in both subdomains, these may contain different sets of unknowns. The discrete system can then be represented on the generic form

$$\begin{pmatrix} A_h & 0 & N_h\Xi_j^h \\ 0 & A_l & S_l\Xi_j^l \\ -\Pi_j^h P_h & \Pi_j^l P_l & M_j \end{pmatrix} \begin{pmatrix} y_h \\ y_l \\ \xi_j \end{pmatrix} = \begin{pmatrix} f_h \\ f_l \\ 0 \end{pmatrix}. \tag{4.1}$$

Here, A_h and A_l are the fixed-dimensional discretizations on the subdomains and f_h and f_l the corresponding source and sink terms. N_h is the discretization of Neumann boundary conditions on Ω_h, and S_l is the discretization of source terms in Ω_l. Furthermore, P_h provides a discrete representation of the pressure trace operator on Ω_h and P_l gives the pressure unknowns in Ω_l; the latter is an identity operator for the integral formulations presented on primal form and strips away flux unknowns in the dual formulation. Finally, M_j represents the normal permeability term in (3.3) and is discretized directly by RobinCoupling. In accordance with the second constraint on mixed-dimensional modeling discussed in Section 2.2, there is no direct coupling between Ω_h and Ω_l as seen from the 0 entries in the matrix.

The PorePy implementation of the above method represents the mortar variable by piecewise constant functions. Our implementation for the coupled mixed-dimensional problem relies on the analysis carried out in [39], which provides a theoretical background to obtain a stable global scheme with full flexibility in choosing heterogeneous discretization schemes between the subdomains. We also note that the interface discretization for many other classes of equations, such as the advection-diffusion problem presented in Section 3.2, follows a similar approach.

4.2.3 Subdomain couplings for contact mechanics in poroelastic media

As a second example of the matrix structure produced by a subdomain and interface coupling, we consider the model for fracture deformation introduced in Section 3.3. This can be considered a complex model, in that the traction balance on the interface involves multiple variables on Ω_h, Ω_l, and Γ_j. Specifically, the equations for the momentum balance presented in Section 3.3 can be represented in matrix form as

$$\begin{pmatrix} A_h & B_h & D_h\Xi_j^h & 0 & 0 \\ 0 & 0 & U_l\Xi_j^l & 0 & T_l \\ \Pi_j^h T_h & \Pi_j^h G_h & \Pi_j^h S_h \Xi_j^h & -\Pi_j^l G_l & \pm\Pi_j^l \end{pmatrix} \begin{pmatrix} u_h \\ p_h \\ u_j \\ p_l \\ \sigma_l \end{pmatrix} = \begin{pmatrix} b_h \\ r \\ 0 \end{pmatrix}. \tag{4.2}$$

Here, the first row represents the momentum balance with the contribution of the mortar displacement variables on the momentum balance in Ω_h. In practice, this takes the form of a Dirichlet boundary condition discretized as D_h, while A_h, B_h, and b_h represent discretization of poroelasticity in Ω_h. In the second row, the matrices U_l and T_l represent the linearized fracture conditions, i.e., the relation between u_j and σ_l stated in Eqs. (3.14) and (3.15), with contributions from the previous Newton iteration and time step entering in $r = r(u_j, \sigma_l)$. The third row represents Newton's third law over the interfaces, and thus is a discretization of Eq. (3.13). The first three terms provide the traction on the two fracture walls reconstructed from the variables on $\partial_j^* \Omega_h$ and Γ_j, where S_h represents a mapping from the Dirichlet boundary condition to tractions. The two last terms relate these tractions to the variables in Ω_l, where G_l represents $n_h \alpha_l$, while the $\pm$ in the last term accounts for the fracture side. We emphasize that neither the inter-dimensional contributions to mass conservation nor the coupling for mass conservation is included in (4.2); this is handled by the corresponding internal subdomain discretizations and additional coupling discretizations in the form discussed in Section 4.2.2.

In terms of implementation, the interface equations in (4.2) are in fact split into three different classes: One which handles the interaction between u_h, u_j, and σ_l and two that represent the fluid traction on Γ_j from p_h and p_l, respectively. The most interesting of these classes is the first, termed PrimalContactCoupling, which is used for purely mechanical problems; the discretization of the contact problem that produces the matrices U_l and T_l for the current state of $[\![u_j]\!]$ and σ_l is outsourced to a separate class ColoumbContact. An illustration of how PrimalContactCoupling is set up to interact with the surrounding variables and discretizations is given in the context of Sneddon's problem of fracture deformation (see Fig. 16 in Section 5.3).

4.3 Global assembly of mixed-dimensional multiphysics problems

As discussed in Section 4.2, PorePy requires only specification of variables and discretizations locally on subdomains and interfaces. The global organization is left to the Assembler class, which has the following responsibilities: First, to assign a global numbering of the degrees of freedom of all local variables. Second, to apply all assigned discretization schemes. Third, to assemble the sparse global linear system. The user interface to the Assembler is simple;

numbering of degrees of freedom is handled in the object initialization, while the class has dedicated methods for discretization and assembly. The underlying implementation of these methods is elaborate and involves nested loops over the GridBucket. For global discretization, all local discretization objects are identified, and their respective discretization methods invoked. In the assembly operation, the local discretization matrices are placed in the global linear system according to the degree of freedom of the associated local variable(s).

It is instructive to consider the structure of the global linear system in the setting of a multiphysics problem with more than one primary variable. It has a double block structure, with one set of blocks stemming from the geometric division into subdomains and interfaces. Within each subdomain and interface, there is a second set of blocks, with one block per variable or variable pair (for off-diagonal blocks). This information, which is useful for design of tailored preconditioners and linear solvers as well as post-processing and visualization, can be accessed through the Assembler. We emphasize that the implementation of the Assembler is general in the sense that it can be applied to new discretizations and governing equations without modification.

The bottom-up approach to the assembly of variables and discretizations to some degree favors flexibility over computational speed. The overhead in construction and manipulation of matrices, independent of matrix size and separate from the cost of discretization, is minor but can become notable when repeated many times, e.g., in time-dependent and non-linear problems. For problems with many subdomains, the cost in using local assembly can become prohibitively high. Specifically, the cost has been pronounced in simulations of non-linearly coupled flow and transport, as reported in [65] and also in Section 6.1. As a remedy, which is also compatible with the automatic differentiation (AD) module in PorePy, the Assembler also provides methods to construct global discrete operators.

4.4 Solvers and visualization

PorePy has no native support for linear solvers, but instead relies on external libraries for solving linear systems. The structure of the linear systems obtained for mixed-dimensional is non-standard compared with that of similar fixed-dimensional problems. Thus, if the linear system is to be solved by iterative methods, traditional preconditioners cannot be expected to perform well, and specialized methods may be preferable. Preconditioners for mixed-dimensional problems are an immature research field, see however [66, 67] for examples on how PorePy can be combined with dedicated solvers for mixed-dimensional problems.

Finally, visualization is handled by an export filter to the vtk/vtu format, which can be read for instance by Paraview [68]. To aid analysis of simulation results, the export preserves the link between the data and its associated dimensions.

5 Validation

In this section, we validate our modeling framework and its implementation in PorePy by probing discretization schemes, multiphysics problems, and time-dependent problems through three test cases: a benchmark for flow problems in 2d fractured media, Mandel's problem for poroelasticity, and Sneddon's problem for fracture deformation in elastic media. The cases thus supplement previous testing of PorePy, reported in [38, 69–71]. The supplementary material provides detailed setups, including parameters, for all simulations in Sections 5 and 6. Scripts that reproduce all results reported herein can be accessed at [72], see that reference or the supplementary material for installation instructions.

5.1 Flow in 2d fractured porous media

To validate the mixed-dimensional flow discretization, we consider Benchmark 3 of [73], which describes the incompressible single-phase flow problem in a fractured domain presented in Section 3.1. The fracture network contains intersecting and isolated fractures (see Fig. 9). The network contains both highly conductive and blocking fractures, see the supplementary material for parameter details.

The aim of this case is twofold — we benchmark our code against well-established methods in the literature and illustrate PorePy's flexibility in assigning heterogeneous subdomain discretizations. We consider four groups of discretization schemes and simulation grids: first, three homogeneous (the same for all the subdomains) discretizations: TPFA, MPFA, and RT0-P0. Second, a case with the MVEM, where the cells of the rock matrix are constructed by a clustering procedure starting from a more refined simplicial grid, see [70] for details. Third, two heterogeneous discretizations where RT0-P0 and MVEM for the rock matrix are combined with TPFA for the fractures. Fourth, a case where the fracture grid is twice as fine as the matrix grid, with the mortar grids non-conforming to the surrounding grids (labeled Non-Matching) discretized using the RT0-P0 scheme. We use simplex grids in all cases that do not involve MVEM. A code snippet that highlights the assignment of heterogeneous discretizations is given in Fig. 10.

Figure 9 shows the domain with fractures, boundary conditions, and a representative numerical solution. The figure also depicts a plot of the pressure along the line $(0, 0.5) - (1, 0.9)$. We observe good agreement between the solutions obtained in PorePy and the reference solution of [73], which is a solution of the equi-dimensional problem computed on a very fine grid. We also perform a refinement study using a sequence of three grids to compute the error relative to the

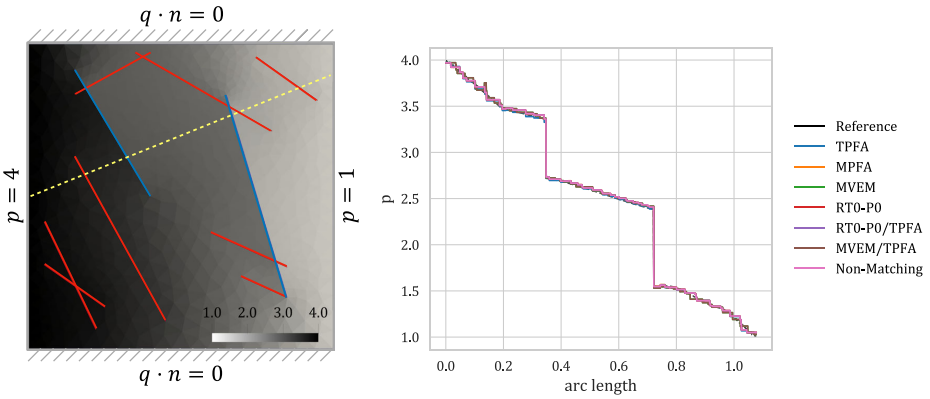

Fig. 9 Left: A solution obtained with MPFA on the coarsest grid showing the fracture network and the problem setup. The red lines represent conductive fractures whereas the blue lines are blocking fractures. The yellow line indicates the line of the pressure profile. Right: Pressure profiles for the discretization schemes used in the validation

reference solution, as done in the original benchmark. Figure 11 shows the decay of the normalized L^2 error for the rock matrix and the union of the fracture subdomains. In the former, we notice a first order of convergence for all the considered methods. The convergence rate for the fracture subdomains is sublinear, as was also observed in the original benchmark.

5.2 Mandel's problem in poroelasticity

The next test case considers a poroelastic material, with a setup defined by Mandel's problem [74, 75], for which an analytical solution is available. While the problem geometry does not include lower-dimensional objects, the case tests the implementation of the poroelastic code and shows the framework's flexibility to

```
matrix_discr = pp.RT0('flow')     # Discretization in the matrix
fracture_discr = pp.Tpfa('flow')  # Discretization in fractures and intersections

for g, d in gb:
    if g.dim == 2:  # This is the matrix grid
        # RT0 has both cell and face unknowns
        d[pp.PRIMARY_VARIABLES] = {'p': {'cells': 1, 'faces': 1}}
        d[pp.DISCRETIZATION] = {'p': {'diffusion': matrix_discr}}
    else:  # Fracture or fracture intersection grid.
        # TPFA has only cell unknowns
        d[pp.PRIMARY_VARIABLES] = {'p': {'cells': 1}}
        d[pp.DISCRETIZATION] = {'p': {'diffusion': fracture_discr}}

for e, d in gb.edges():  # Loop over all interfaces (e) and their associated data (d)
    g_l, g_h = gb.nodes_of_edge(e)  # Get grids of neighboring subdomains
    d[pp.PRIMARY_VARIABLES] = {'mortar_flux': {'cells': 1}}  # Primary variable

    if g_h.dim == 2:  # Adapt interface discretization to neighboring subdomains
        interface_discr = pp.RobinCoupling('flow', matrix_discr, fracture_discr)
    else:  # Omega_l is an intersection point
        interface_discr = pp.RobinCoupling('flow', fracture_discr, fracture_discr)

    # Define coupling
    d[pp.COUPLING_DISCRETIZATION] = { 'interface_flux':  # Identifier of this term
        {g_h: ('p', 'diffusion'),
         g_l: ('p', 'diffusion'),
         e: ('mortar_flux', interface_discr)}}
```

Fig. 10 Code snippet of the discretization assignment for the combination of RT0-P0 and TPFA. The code can be used as a partial replacement of the green section in Fig. 7. Note that the parameter definition is not included in the snippet

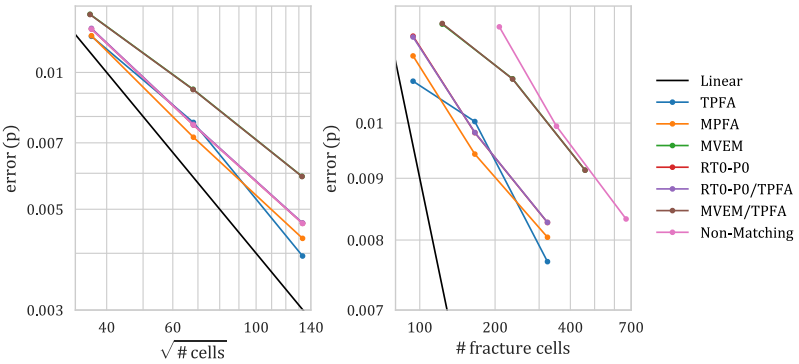

Fig. 11 Left: Convergence of the pressure unknown for the matrix subdomain for the simulations reported in Section 5.1. Right: Convergence for the pressure unknown for the fracture subdomains

deal with coupled problems and time-dependent mixed boundary conditions. The original problem consists of an isotropic poroelastic slab of width $2a$ and height $2b$ sandwiched by two rigid plates (Fig. 12). Initially, two compressive constant loads of intensity $2F$ are applied to the slab at $y = \pm b$. At $x = \pm a$, fluid is free to drain, and edges are stress free. Gravity contributions are neglected.

The problem is modeled using the quasi-static Biot equations, as presented in Section 3.3. Exploiting the symmetry of the problem, we focus on the positive quarter domain Ω', rather than the full domain Ω, see Fig. 12 for an illustration and for boundary conditions. Note that the vertical displacement at the top of the domain is time-dependent and given by the exact solution, see [76].

The simulation parameters were taken from [77], see also the supplementary material for details. The coupled problem is discretized in space using MPSA and MPFA for the mechanics and flow, respectively. For the time discretization, we use implicit Euler. The computational grid is unstructured and composed of 622 triangular elements. The results are shown in Fig. 13 in terms of dimensionless quantities and are in good agreement with [77] for both pressure and displacement.

In Fig. 14, we show a code snippet illustrating the assembly of a generic poroelastic problem using MPSA/MPFA in PorePy. One primary variable for each subproblem must be specified, namely displacement for the mechanics (variable 0) and pressure for the flow (variable 1). There are five terms (plus one stabilization term) involved in the discretization of the Biot equations. We label them with subscripts kl identifying the impact on variable k from variable l. The numbering also corresponds to the placement in the 2×2 block discretization matrix, with the first row representing the momentum balance and the second row the mass balance.

The Mpsa class is used to obtain the divergence of the stress (term_00), which corresponds to the first diagonal block. For the second diagonal block, term_11_0 and term_11_1 refer to the discretization of the fluid accumulation and fluid flux (after applying implicit Euler) obtained using the classes ImplicitMassMatrix and ImplicitMpfa, respectively. In addition, term_11_2 is a stabilization term arising naturally from the discretization process [61].

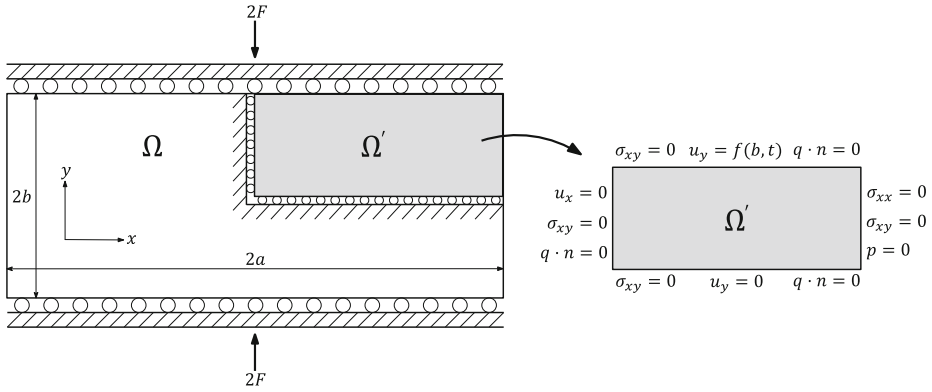

Fig. 12 Mandel's problem. Left: Schematic representation of the full and positive quarter domains, Ω and Ω'. Right: Quarter domain showing the boundary conditions

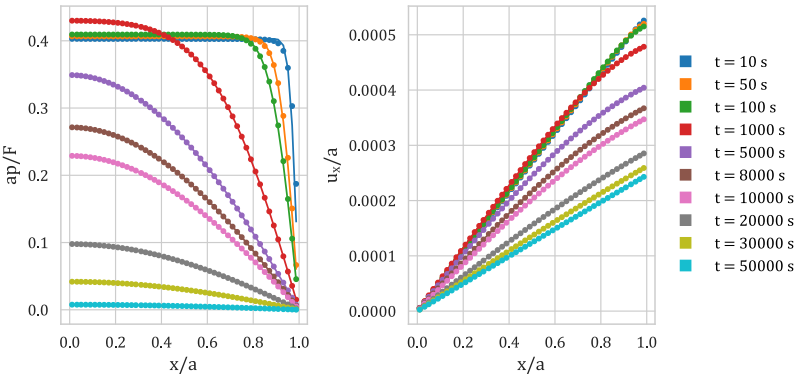

Fig. 13 Analytical (solid lines) and MPSA/MPFA (dots) solutions to Mandel's problem. The dimensionless profiles for the pressure (left) and the horizontal displacement (right) are shown for several times

Lastly, term_01 and term_10 are the off-diagonal coupling blocks representing respectively the terms involving the pressure gradient (obtained with GradP) and the divergence of the displacement field (obtained with DivU).

5.3 Sneddon's problem of fracture deformation

In this example, a square domain with a single fracture located in the middle is considered. The fracture forms an angle β with the horizontal direction (see Fig. 15) and is subjected to a constant pressure p_0, which can be interpreted as a pair of normal forces acting on either side of the fracture. An analytical solution for the relative normal displacement along the fracture was derived by Sneddon [78] for an infinite domain, and has the following form:

$$[\![u_j]\!]_n(d_f) = \frac{(1-\nu)p_0 L}{G}\sqrt{1-\frac{d_f^2}{\left(\frac{L}{2}\right)^2}}, \tag{5.1}$$

```
## Primary variables for poroelasticity problems
v_0 = 'u'  # displacement
v_1 = 'p'  # pressure

## Name of the five terms of the equation + additional stabilization term
term_00 = 'stress_divergence'       # div symmetric grad u
term_11_0 = 'fluid_mass'            # d/dt beta p
term_11_1 = 'fluid_flux'            # div (rho g - K grad p)
term_11_2 = 'stabilization'
term_01 = 'pressure_gradient'       # alpha grad p
term_10 = 'displacement_divergence' # d/dt alpha div u

## Store in the data dictionary and specify discretization objects
d[pp.PRIMARY_VARIABLES] = {v_0: {'cells': g.dim}, v_1: {'cells': 1}}
d[pp.DISCRETIZATION] = {
    # Momentum balance equation
    v_0: {term_00: pp.Mpsa(kw_m)},
    # Mass conservation equation
    v_1: {
        term_11_0: pp.ImplicitMassMatrix(kw_f, v_1),
        term_11_1: pp.ImplicitMpfa(kw_f),
        term_11_2: pp.BiotStabilization(kw_f, v_1),
    },
    # Pressure contribution to the momentum balance equation
    v_0 + '_' + v_1: {term_01: pp.GradP(kw_m)},
    # Displacement contribution to the mass conservation equation
    v_1 + '_' + v_0: {term_10: pp.DivU(kw_m, kw_f, v_0)},
}
```

Fig. 14 Code snippet illustrating the terms involved in the assembly of a poroelastic problem using MPSA/MPFA in PorePy. The snippet highlights assignment of discretizations for multiphysics problems within a subdomain

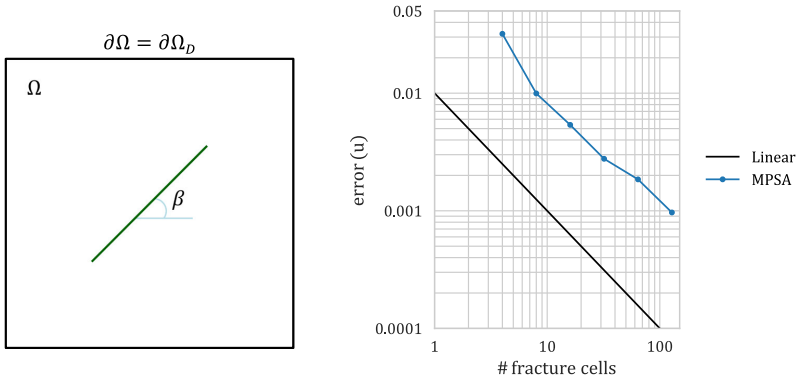

Fig. 15 Setup and convergence of Sneddon's problem. Left: Schematic representation of the domain. Right: Average convergence behavior of the relative normal displacement along the fracture. Each dot corresponds to the average of 140 simulations

where ν and G are the Poisson's ratio and shear modulus, respectively, L is the fracture length, and d_f denotes the distance from the center of the fracture.

In our calculations, the condition of infinite domain is replaced with a Dirichlet boundary, where the prescribed displacement is set equal to the analytical solution calculated using the procedure illustrated in [79]. The accuracy of the numerical solution is very sensitive to the discretization, specifically the cell configuration at the fracture tips [46]. To reduce the dependency on specific grid realizations, the values of the numerical solution reported in Fig. 16 are the average of a group of $20 \times 7 = 140$ computations per level of grid resolution, with 7 different fracture angles β in the range 0°–30° and 20 grid realizations per fracture. With six levels of grid refinement, the full study contains $20 \times 7 \times 6 = 840$ simulations. Figure 16 summarizes the results in the form of the error in relative normal displacement between the analytical solution (5.1) and the numerical solution as a function of the fracture resolution, i.e., number of fracture elements. The method provides first-order convergence on average.

Finally, the code snippet in Fig. 16 indicates the key parts of the variable and discretization assignment for the contact mechanics problem. The classes to note are ColoumbContact, which represents Eqs. (3.14) and (3.15), and the interface discretization PrimalContactCoupling, see also the discussion in Section 4.2.3.

6 Applications: multiphysics simulations

Having established the accuracy of PorePy for central test cases that involve mixed-dimensional geometries, we proceed to present two multiphysics cases of high application relevance: A non-linearly coupled flow and transport problem, and fracture reactivation caused by fluid injection. The motivation for the simulations is to illustrate further capabilities of the modeling framework and its PorePy implementation, including simulations on complex 3d fracture networks, automatic differentiation applied to non-linear problems, non-matching grids, and simulation of fracture deformation in a poroelastic setting.

6.1 Fully coupled flow and transport

We consider the injection of a more viscous fluid into a domain initially filled with a less viscous fluid. The two fluids are miscible and have equal densities; thus, they can be modeled as two components in a single-phase system, as described in Section 3.2. The viscosity of the mixture of fluids given by $\mu_i(c_i) = \exp(c_i)$, for the mass fraction $c_i \in [0, 1]$, which is 0 if only the less viscous fluid is present and 1 if only the more viscous fluid is present. In the parameter regime studied in this example, the transport in the fractures is advection dominated, while the transport in the rock matrix is dominated by diffusion, see the supplementary material for details.

The time derivative is approximated using an implicit Euler method, which gives a fully implicit scheme for the primary variables pressure and mass fraction. The spatial terms are discretized by a finite volume method, with simple upstream for advective terms, and TPFA for fluxes and diffusive terms. We apply forward automatic differentiation implemented in PorePy to obtain the Jacobian of the global system of equations, which is then used in a standard Newton method to solve the non-linear problem. The convergence criterion is given by the maximum norm of the residual vector with a tolerance 10^{-9}.

The mixed-dimensional domain considered in this example consists of one 3d domain, 15 2d fracture domains, 62 1d domains, and 9 0d domains. On this geometry, two computational grids are constructed: The first has matching grids in all dimensions, with in total 20,812 cells, out of which 16,766 are 3d cells and 3,850 are 2d fracture cells. The second mixed-dimensional grid has a 3d grid identical to the first grid, whereas the lower-dimensional objects are assigned refined grids with in total 13,839 2d fracture cells; thus, the 3d-2d interfaces have non-matching grids. The combination of the

```
Nd = gb.dim_max()  # Get ambient dimension
# For the 2d domain we solve linear elasticity with MPSA
mpsa = pp.Mpsa('mechanics')

# The assembler expects that all variables are assigned a discretization. Create a
# void discretization object; the friction discretization is set via the interface law
empty_discr = pp.VoidDiscretization('friction', Nd)

# Define discretization parameters
for g, d in gb:
    if g.dim == Nd:  # Omega_i is the matrix
        d[pp.PRIMARY_VARIABLES] = {'u': {'cells': Nd}}
        d[pp.DISCRETIZATION] = {'u': {'mpsa': mpsa}}
    else:  # Omega_i is a fracture
        d[pp.PRIMARY_VARIABLES] = {'contact': {'cells': Nd}}
        d[pp.DISCRETIZATION] = {'contact': {'empty': empty_discr}}

# For the 1d domain we define a contact condition
coloumb = pp.ColoumbContact('friction', Nd)
# Define a contact condition on the mortar grid
contact = pp.PrimalContactCoupling('friction', mpsa, coloumb)

# Loop over all interfaces (e) and their associated data (d)
for e, d in gb.edges():
    g_l, g_h = gb.nodes_of_edge(e)

    d[pp.PRIMARY_VARIABLES] = {'interface_u': {'cells': Nd}}
    d[pp.COUPLING_DISCRETIZATION] = {'friction': {
        g_h: ('u', 'mpsa'),
        g_l: ('contact', 'empty'),
        (g_h, g_l): ('interface_u', contact)}}
```

Fig. 16 Code snippet that illustrates variable and discretization assignment for Sneddon's problem, discretized using the contact mechanics functionality in PorePy. The code can be used as a partial replacement of the green section in Fig. 7

non-linearity and the non-matching grids provides a challenging test for the robustness of the PorePy implementation of subdomain couplings and provides an illustration of the framework's flexibility.

Figure 17 shows the average mass fraction profile in the fractures for the two grids. There are no significant differences between the two cases, indicating the stability of the implementation of the non-matching case. Figure 18 shows a snapshot of the mass fraction in the fractures and the rock matrix at time $t = 20$. The diffusive front in the rock matrix has only moved a few grid cells at the break-through; however, due to the diffusion and advection from the fractures to the rock matrix, the mass fraction has increased in considerable parts of the rock matrix. We observe no irregularities for the solution produced on the non-matching grid in this case, suggesting PorePy's ability to deal with non-standard grid couplings also for challenging physical regimes.

6.2 Poroelasticity and fracture deformation

The final example aims at demonstrating the modeling framework's and PorePy's applicability to non-standard combinations of physical processes in different domains and thereby its potential for method development and prototyping. With the critical events taking place on individual fractures as a result of processes in the rock matrix, it also serves as an example of the importance of incorporating dynamics of both the matrix and explicitly represented fractures, as done in DFM models.

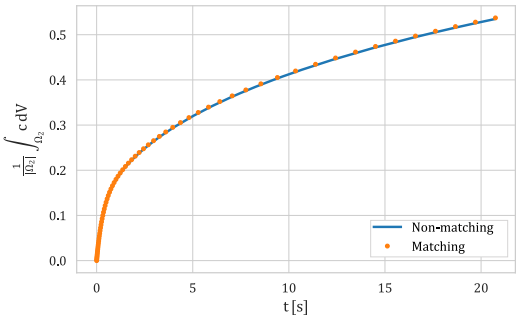

Fig. 17 Fully coupled flow and transport: Comparison of average mass fraction in the fracture network for a simulation with matching grids and a simulation with non-matching grids

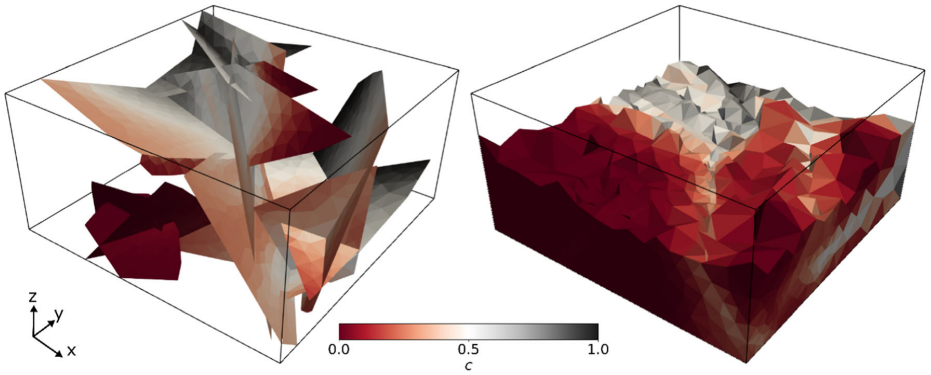

Fig. 18 Fully coupled flow and transport: Mass fraction in the fractures (left) and in the rock matrix (right) for the coupled flow and transport problem given in Section 3.2 at the end time of the simulation ($t = 20$). In the right figure, the rock matrix domain is cropped, and the fractures removed to reveal the mass fraction inside the domain. The black lines indicate the domain boundary. Non-matching grids are used with the fracture grids being much finer than the grid in the rock matrix

Specifically, we consider the model equations for coupled poroelasticity and fracture deformation presented in Section 3.3. The poroelastic deformation of the host rock is discretized with MPSA, while the fluid flow in the fractures is discretized with MPFA. The discretization of the contact mechanics follows the structure outlined in Section 4.2.3, and temporal discretization is performed using implicit Euler.

We consider a reservoir of idealized geometry containing three non-intersecting fractures numbered from 1 through 3, whereof the first contains an injection well (see Fig. 19). On this geometry, we solve the governing equations presented in Section 3.3. We impose injection over a 25-day period and an anisotropic background stress regime, producing a scenario well suited to demonstrate different fracture dynamics. We investigate the dynamics both during the injection phase and during the subsequent 25-day relaxation phase, at the end of which the pressure has almost reached equilibrium once more. The full set of parameters may be found in the supplementary material.

The dynamics on the fractures throughout the simulation are summarized in Fig. 19, while the spatial distribution of the fracture displacement jumps at the end of the injection phase is shown in Fig. 20. The figures show how the simulation captures the complex dynamics both during and after injection, and thus highlight how the explicit fracture representation allows for detailed studies of fracture deformation.

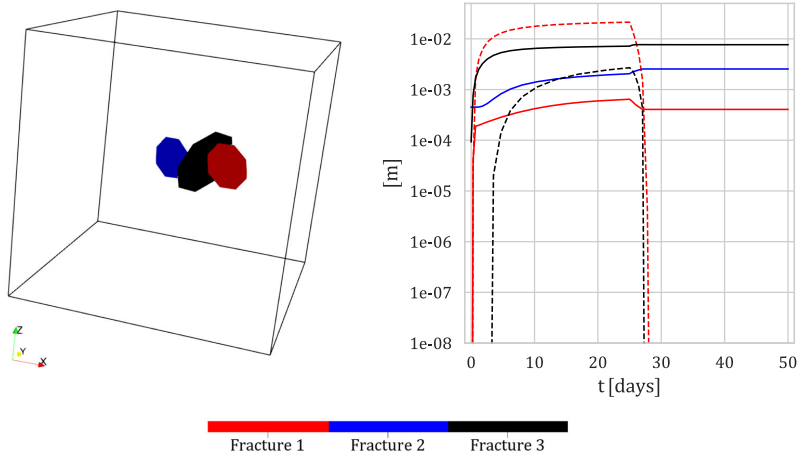

Fig. 19 Left: Domain geometry with numbering of the three fractures. Fluid is injected in fracture 1 during the first 25 days, after which the well is shut. Right: L^2-norm normalized by fracture area of the normal (dashed lines) and tangential (solid lines) displacement jumps for each fracture

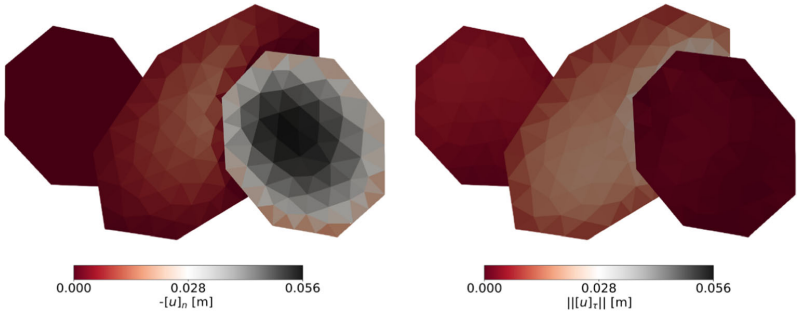

Fig. 20 Normal and tangential displacements jump on the fractures at the end of the injection phase to the left and right, respectively. The orientation of the fracture network corresponds to that in Fig. 12, with the injection fracture to the right

7 Conclusions

The complexity in modeling and simulation of multiphysics processes in fractured porous media, combined with a strong current research focus and corresponding developments, calls for flexible simulation tools that facilitate rapid prototyping of models and discretization methods. This paper presents design principles for such software together with their implementation in the open-source simulation tool PorePy. The combined framework for modeling and simulation is based on the discrete fracture matrix model, where fractures and their intersections are represented as separate lower-dimensional geometric objects. The framework facilitates flexibility for multiphysics dynamics and reuse of existing code written for non-fractured domains; hence, it is well suited for extending other software packages to mixed-dimensional problems.

The open-source software PorePy demonstrates the capabilities of the suggested framework: It provides automatic gridding of complex fracture networks in two and three dimensions, and contains implemented numerical methods for flow, transport, poroelastic deformation of the rock, and fracture deformation modeled by contact mechanics. The implementation performs well for benchmark problems in flow, poroelastic deformation, and fracture deformation. Furthermore, multiphysics simulations of fully coupled flow and non-linear transport and of fracture deformation under poroelastic deformation of a domain demonstrate the versatility of the software.

Acknowledgments The authors thank two anonymous reviewers for the comments and suggestions that helped to improve the quality of the paper.

Funding Open Access funding provided by University of Bergen. This work has been funded in part by Norwegian Research Council grant 250223, 244129/E20, 267908/E20, and 274883, and by a VISTA Scholarship from the Norwegian Academy of Science and Letters.

References

1. Berkowitz, B.: Characterizing flow and transport in fractured geological media: a review. Adv. Water Resour. **25**(8–12), 861–884 (2002). https://doi.org/10.1016/S0309-1708(02)00042-8
2. Martin, V., Jaffré, J., Roberts, J.E.: Modeling fractures and barriers as interfaces for flow in porous media. SIAM J. Sci. Comput. **26**(5), 1667–1691 (2005). https://doi.org/10.1137/S1064827503429363
3. Barton, N., Bandis, S., Bakhtar, K.: Strength, deformation and conductivity coupling of rock joints. Int. J. Rock Mech. Min. Sci. Geomech. Abstr. **22**(3), 121–140 (1985). https://doi.org/10.1016/0148-9062(85)93227-9
4. Frih, N., Roberts, J.E., Saada, A.: Modeling fractures as interfaces: a model for Forchheimer fractures. Comput. Geosci. **12**(1), 91–104 (2008). https://doi.org/10.1007/s10596-007-9062-x
5. Rutqvist, J., Wu, Y.-S., Tsang, C.-F., Bodvarsson, G.: A modeling approach for analysis of coupled multiphase fluid flow, heat transfer, and deformation in fractured porous rock. Int. J. Rock Mech. Min. Sci. **39**(4), 429–442 (2002). https://doi.org/10.1016/S1365-1609(02)00022-9
6. Burnell, J., et al.: Geothermal supermodels: the next generation of integrated geophysical, chemical and flow simulation modelling tools. Proc World Geotherm. Congr. 7 (2015)
7. Pruess, K.: TOUGH2: a general numerical simulator for multiphase fluid and heat flow. Report LBL-29400 (1991)
8. Hammond, G.E., Lichtner, P.C., Mills, R.T.: Evaluating the performance of parallel subsurface simulators: an illustrative example with PFLOTRAN: evaluating the parallel performance of Pflotran. Water Resour. Res. **50**(1), 208–228 (2014). https://doi.org/10.1002/2012WR013483
9. Barenblatt, G.I., Zheltov, I.P., Kochina, I.N.: Basic concepts in the theory of seepage of homogeneous liquids in fissured rocks [strata]. J. Appl. Math. Mech. **24**(5), 1286–1303 (1960). https://doi.org/10.1016/0021-8928(60)90107-6

10. Arbogast, T., Douglas Jr., J., Hornung, U.: Derivation of the double porosity model of single phase flow via homogenization theory. SIAM J. Math. Anal. **21**(4), 823–836 (1990). https://doi.org/10.1137/0521046
11. Lemonnier, P., Bourbiaux, B.: Simulation of naturally fractured reservoirs. State of the art: part 1 – physical mechanisms and simulator formulation. Oil Gas Sci. Technol. Rev. L'Institut Fr. Pétrole. **65**(2), 239–262 (2010). https://doi.org/10.2516/ogst/2009066
12. Lemonnier, P., Bourbiaux, B.: Simulation of naturally fractured reservoirs. State of the art: part 2 – matrix-fracture transfers and typical features of numerical studies. Oil Gas Sci. Technol. – Rev. L'Institut Fr. Pétrole. **65**(2), 263–286 (2010). https://doi.org/10.2516/ogst/2009067
13. Hyman, J.D., Karra, S., Makedonska, N., Gable, C.W., Painter, S.L., Viswanathan, H.S.: dfnWorks: a discrete fracture network framework for modeling subsurface flow and transport. Comput. Geosci. **84**, 10–19 (2015). https://doi.org/10.1016/j.cageo.2015.08.001
14. Erhel, J., de Dreuzy, J.-R., Poirriez, B.: Flow simulation in three-dimensional discrete fracture networks. SIAM J. Sci. Comput. **31**(4), 2688–2705 (2009). https://doi.org/10.1137/080729244
15. Berrone, S., Pieraccini, S., Scialò, S.: On simulations of discrete fracture network flows with an optimization-based extended finite element method. SIAM J. Sci. Comput. **35**(2), A908–A935 (2013). https://doi.org/10.1137/120882883
16. Berre, I., Doster, F., Keilegavlen, E.: Flow in fractured porous media: a review of conceptual models and discretization approaches. Transp. Porous Media. **130**, 215–236 (2018). https://doi.org/10.1007/s11242-018-1171-6
17. Noorishad, J., Mehran, M.: An upstream finite element method for solution of transient transport equation in fractured porous media. Water Resour. Res. **18**(3), 588–596 (1982). https://doi.org/10.1029/WR018i003p00588
18. Baca, R.G., Arnett, R.C., Langford, D.W.: Modelling fluid flow in fractured-porous rock masses by finite-element techniques. Int. J. Numer. Methods Fluids. **4**(4), 337–348 (1984). https://doi.org/10.1002/fld.1650040404
19. Reichenberger, V., Jakobs, H., Bastian, P., Helmig, R.: A mixed-dimensional finite volume method for two-phase flow in fractured porous media. Adv. Water Resour. **29**(7), 1020–1036 (2006). https://doi.org/10.1016/j.advwatres.2005.09.001
20. Li, L., Lee, S.H.: Efficient field-scale simulation of black oil in a naturally fractured reservoir through discrete fracture networks and homogenized media. SPE Reserv. Eval. Eng. **11**(04), 750–758 (2008). https://doi.org/10.2118/103901-PA
21. Fumagalli, A., Scotti, A.: A reduced model for flow and transport in fractured porous media with non-matching grids. In: Cangiani, A., Davidchack, R.L., Georgoulis, E., Gorban, A.N., Levesley, J., Tretyakov, M.V. (eds.) Numerical Mathematics and Advanced Applications 2011, pp. 499–507. Springer, Berlin (2013)
22. Flemisch, B., Fumagalli, A., Scotti, A.: A review of the XFEM-based approximation of flow in fractured porous media. In: Ventura, G., Benvenuti, E. (eds.) Advances in Discretization Methods, vol. 12, pp. 47–76. Springer International Publishing, Cham (2016)
23. Schwenck, N., Flemisch, B., Helmig, R., Wohlmuth, B.I.: Dimensionally reduced flow models in fractured porous media: crossings and boundaries. Comput. Geosci. **19**(6), 1219–1230 (2015). https://doi.org/10.1007/s10596-015-9536-1
24. Jiang, J., Younis, R.M.: An improved projection-based embedded discrete fracture model (pEDFM) for multiphase flow in fractured reservoirs. Adv. Water Resour. **109**, 267–289 (2017). https://doi.org/10.1016/j.advwatres.2017.09.017
25. Flemisch, B., Darcis, M., Erbertseder, K., Faigle, B., Lauser, A., Mosthaf, K., Müthing, S., Nuske, P., Tatomir, A., Wolff, M., Helmig, R.: DuMux: DUNE for multi-{phase,component,scale, physics,…} flow and transport in porous media. Adv. Water Resour. **34**(9), 1102–1112 (2011). https://doi.org/10.1016/j.advwatres.2011.03.007
26. Matthäi, S.K., Geiger, S., Roberts, S.G., Paluszny, A., Belayneh, M., Burri, A., Mezentsev, A., Lu, H., Coumou, D., Driesner, T., Heinrich, C.A.: Numerical simulation of multi-phase fluid flow in structurally complex reservoirs. Geol. Soc. Lond. Spec. Publ. **292**(1), 405–429 (2007). https://doi.org/10.1144/SP292.22
27. Gaston, D., Newman, C., Hansen, G., Lebrun-Grandié, D.: MOOSE: a parallel computational framework for coupled systems of nonlinear equations. Nucl. Eng. Des. **239**(10), 1768–1778 (2009). https://doi.org/10.1016/j.nucengdes.2009.05.021
28. Breede, K., Dzebisashvili, K., Liu, X., Falcone, G.: A systematic review of enhanced (or engineered) geothermal systems: past, present and future. Geotherm. Energy. **1**(1), 4 (2013). https://doi.org/10.1186/2195-9706-1-4
29. Wang, W., Kolditz, O.: Object-oriented finite element analysis of thermo-hydro-mechanical (THM) problems in porous media. Int. J. Numer. Methods Eng. **69**(1), 162–201 (2007). https://doi.org/10.1002/nme.1770
30. Březina, J., Stebel, J.: Analysis of model error for a continuum-fracture model of porous media flow. In: Kozubek, T., Blaheta, R., Šístek, J., Rozložník, M., Čermák, M. (eds.) High Performance Computing in Science and Engineering, vol. 9611, pp. 152–160. Springer International Publishing, Cham (2016)
31. Lie, K.-A.: An Introduction to Reservoir Simulation Using MATLAB/GNU Octave: User Guide for the MATLAB Reservoir Simulation Toolbox (MRST), 1st edn. Cambridge University Press (2019)
32. Lie, K.-A., Krogstad, S., Ligaarden, I.S., Natvig, J.R., Nilsen, H.M., Skaflestad, B.: Open-source MATLAB implementation of consistent discretisations on complex grids. Comput. Geosci. **16**(2), 297–322 (2012). https://doi.org/10.1007/s10596-011-9244-4
33. Alnæs, M., et al.: The FEniCS Project Version 1.5. Arch. Numer. Softw. **3**, (2015). https://doi.org/10.11588/ans.2015.100.20553
34. Blatt, M., et al.: The distributed and unified numerics environment, Version 2.4. Arch. Numer. Softw. **4**, (2016). https://doi.org/10.11588/ans.2016.100.26526
35. Rathgeber, F., Ham, D.A., Mitchell, L., Lange, M., Luporini, F., Mcrae, A.T.T., Bercea, G.T., Markall, G.R., Kelly, P.H.J.: Firedrake: automating the finite element method by composing abstractions. ACM Trans. Math. Softw. **43**(3), 1–27 (2016). https://doi.org/10.1145/2998441
36. Boon, W.M., Nordbotten, J.M., Vatne, J.E.: Functional analysis and exterior calculus on mixed-dimensional geometries. Ann. Mat. (2020). https://doi.org/10.1007/s10231-020-01013-1
37. Boon, W.M., Nordbotten, J.M.: Stable mixed finite elements for linear elasticity with thin inclusions. arXiv. **1903.01757**, (2019)
38. Nordbotten, J.M., Boon, W.M., Fumagalli, A., Keilegavlen, E.: Unified approach to discretization of flow in fractured porous media. Comput. Geosci. **23**(2), 225–237 (2019). https://doi.org/10.1007/s10596-018-9778-9
39. Geuzaine, C., Remacle, J.-F.: Gmsh: a 3-D finite element mesh generator with built-in pre- and post-processing facilities. Int. J. Numer. Methods Eng. **79**(11), 1309–1331 (2009). https://doi.org/10.1002/nme.2579
40. Karimi-Fard, M.: An efficient discrete-fracture model applicable for general-purpose reservoir simulators. SPE J. **9**(2), (2004). https://doi.org/10.2118/88812-PA
41. Hui, M.-H., Mallison, B., Lim, K.-T.: An innovative workflow to model fractures in a giant carbonate reservoir. Proc. Int. Pet. Tech. Conf. 15 (2008)
42. Berre, I., et al.: Verification benchmarks for single-phase flow in three-dimensional fractured porous media. arXiv. **2002.07005**, (2020)
43. Boon, W.M., Nordbotten, J.M., Yotov, I.: Robust discretization of flow in fractured porous media. SIAM J. Numer. Anal. **56**(4), 2203–2233 (2018). https://doi.org/10.1137/17M1139102

44. Quarteroni, A., Valli, A.: Numerical approximation of partial differential equations, 2nd edn. Springer, Berlin (1997)
45. Garipov, T.T., Karimi-Fard, M., Tchelepi, H.A.: Discrete fracture model for coupled flow and geomechanics. Comput. Geosci. **20**(1), 149–160 (2016). https://doi.org/10.1007/s10596-015-9554-z
46. Ucar, E., Keilegavlen, E., Berre, I., Nordbotten, J.M.: A finite-volume discretization for deformation of fractured media. Comput. Geosci. **22**(4), 993–1007 (2018). https://doi.org/10.1007/s10596-018-9734-8
47. McClure, M.W., Horne, R.N.: An investigation of stimulation mechanisms in Enhanced Geothermal Systems. Int. J. Rock Mech. Min. Sci. **72**, 242–260 (2014). https://doi.org/10.1016/j.ijrmms.2014.07.011
48. Coussy, O.: Poromechanics. Chichester, Wiley (2003)
49. Berge, R.L., Berre, I., Keilegavlen, E., Nordbotten, J.M., Wohlmuth, B.: Finite volume discretization for poroelastic media with fractures modeled by contact mechanics. Int. J. Numer. Methods Eng. **121**(4), 644–663 (2020). https://doi.org/10.1002/nme.6238
50. Dong, S., Zeng, L., Dowd, P., Xu, C., Cao, H.: A fast method for fracture intersection detection in discrete fracture networks. Comput. Geotech. **98**, 205–216 (2018). https://doi.org/10.1016/j.compgeo.2018.02.005
51. Mallison, B.T., Hui, M.H., Narr, W.: Practical gridding algorithms for discrete fracture modeling workflows. presented at the 12th European Conference on the Mathematics of Oil Recovery, Oxford, UK (2010). https://doi.org/10.3997/2214-4609.20144950
52. Holm, R., Kaufmann, R., Heimsund, B.-O., Øian, E., Espedal, M.S.: Meshing of domains with complex internal geometries. Numer. Linear Algebra Appl. **13**(9), 717–731 (2006). https://doi.org/10.1002/nla.505
53. Berge, R.L., Klemetsdal, Ø.S., Lie, K.-A.: Unstructured Voronoi grids conforming to lower dimensional objects. Comput. Geosci. **23**(1), 169–188 (2019). https://doi.org/10.1007/s10596-018-9790-0
54. Shewchuk, J.R.: Triangle: engineering a 2D quality mesh generator and Delaunay triangulator. In: Applied Computational Geometry: Towards Geometric Engineering, vol. 1148, pp. 203–222 (1996)
55. Si, H.: TetGen, a Delaunay-based quality tetrahedral mesh generator. ACM Trans. Math. Softw. **41**(2), 1–36 (2015). https://doi.org/10.1145/2629697
56. Boffi, D., Brezzi, F., Fortin, M.: Mixed finite element methods and applications. Springer, Berlin (2013)
57. da Veiga, L.B., Brezzi, F., Marini, L.D., Russo, A.: Mixed virtual element methods for general second order elliptic problems on polygonal meshes. ESAIM Math. Model. Numer. Anal. **50**(3), 727–747 (2016). https://doi.org/10.1051/m2an/2015067
58. da Veiga, L.B., Brezzi, F., Marini, L.D., Russo, A.: H(div) and H(curl) -conforming virtual element methods. Numer. Math. **133**(2), 303–332 (2016). https://doi.org/10.1007/s00211-015-0746-1
59. Nordbotten, J.M.: Convergence of a cell-centered finite volume discretization for linear elasticity. SIAM J. Numer. Anal. **53**(6), 2605–2625 (2015). https://doi.org/10.1137/140972792
60. Keilegavlen, E., Nordbotten, J.M.: Finite volume methods for elasticity with weak symmetry. Int. J. Numer. Methods Eng. **112**(8), 939–962 (2017). https://doi.org/10.1002/nme.5538
61. Nordbotten, J.M.: Stable cell-centered finite volume discretization for Biot equations. SIAM J. Numer. Anal. **54**(2), 942–968 (2016). https://doi.org/10.1137/15M1014280
62. Nordbotten, J.M., Keilegavlen, E.: An introduction to multi-point flux (MPFA) and stress (MPSA) finite volume methods for thermo-poroelasticity. arXiv. **2001.01990**, (2020)
63. Hüeber, S., Stadler, G., Wohlmuth, B.I.: A primal-dual active set algorithm for three-dimensional contact problems with coulomb friction. SIAM J. Sci. Comput. **30**(2), 572–596 (2008). https://doi.org/10.1137/060671061
64. Stefansson, I., Berre, I., Keilegavlen, E.: A fully coupled numerical model of thermo-hydro-mechanical processes and fracture contact mechanics in porous media. **arXiv:2008.06289**, (2020)
65. Berge, R.L., Berre, I., Keilegavlen, E., Nordbotten, J.M.: Viscous fingering in fractured porous media. **arXiv:1906.10472**, (2019)
66. Budisa, A., Boon, W., Hu, X.: Mixed-dimensional auxiliary space preconditioners. **arXiv:1910.04704**, (2019)
67. Budiša, A., Hu, X.: Block preconditioners for mixed-dimensional discretization of flow in fractured porous media. Comput. Geosci. (2020). https://doi.org/10.1007/s10596-020-09984-z
68. Ahrens, J., Geveci, B., Law, C.: ParaView: an end-user tool for large data visualization
69. Fumagalli, A., Keilegavlen, E., Scialò, S.: Conforming, non-conforming and non-matching discretization couplings in discrete fracture network simulations. J. Comput. Phys. **376**, 694–712 (2019). https://doi.org/10.1016/j.jcp.2018.09.048
70. Fumagalli, A., Keilegavlen, E.: Dual virtual element methods for discrete fracture matrix models. Oil Gas Sci. Technol. – Rev. D'IFP Energ. Nouv. **74**, 41 (2019). https://doi.org/10.2516/ogst/2019008
71. Stefansson, I., Berre, I., Keilegavlen, E.: Finite-volume discretisations for flow in fractured porous media. Transp. Porous Media. **124**(2), 439–462 (2018). https://doi.org/10.1007/s11242-018-1077-3
72. PorePy implementation with runscripts. https://doi.org/10.5281/zenodo.3374624. (2019)
73. Flemisch, B., Berre, I., Boon, W., Fumagalli, A., Schwenck, N., Scotti, A., Stefansson, I., Tatomir, A.: Benchmarks for single-phase flow in fractured porous media. Adv. Water Resour. **111**, 239–258 (2018). https://doi.org/10.1016/j.advwatres.2017.10.036
74. Mandel, J.: Consolidation des sols (étude mathématique). Geotechnique. **3**(7), 287–299 (1953)
75. Abousleiman, Y., Cheng, A.-D., Cui, L., Detournay, E., Rogiers, J.-C.: Mandel's problem revisited. Geotechnique. **46**(2), 187–195 (1996)
76. Cheng, A.H.-D., Detournay, E.: A direct boundary element method for plane strain poroelasticity. Int. J. Numer. Anal. Methods Geomech. **12**(5), 551–572 (1988). https://doi.org/10.1002/nag.1610120508
77. Mikelić, A., Wang, B., Wheeler, M.F.: Numerical convergence study of iterative coupling for coupled flow and geomechanics. Comput. Geosci. **18**(3–4), 325–341 (2014). https://doi.org/10.1007/s10596-013-9393-8
78. Sneddon, I.N.: Fourier Transforms. Dover Publications, New York (1995)
79. Crouch, S.L., Starfield, A.M.: Boundary Element Methods in Solid Mechanics: with Applications in Rock Mechanics and Geological Engineering. Allen & Unwin, London (1983)

Paper E

A fully coupled numerical model of thermo-hydro-mechanical processes and fracture contact mechanics in porous media

Ivar Stefansson, Inga Berre, Eirik Keilegavlen

E

Submitted to Computer Methods in Applied Mechanics and Engineering
Preprint: arXiv:2008.06289 [math.NA]

A fully coupled numerical model of thermo-hydro-mechanical processes and fracture contact mechanics in porous media

Ivar Stefansson[a,*], Inga Berre[a], Eirik Keilegavlen[a]

[a]*University of Bergen, Bergen, Norway*

Abstract

A range of phenomena in the subsurface is characterised by the interplay between coupled thermal, hydraulic and mechanical processes and deforming structures such as fractures. Modelling subsurface dynamics can provide valuable phenomenological understanding, but requires models which faithfully represent the dynamics involved; these models, therefore are themselves highly complex.

This paper presents a mixed-dimensional thermo-hydro-mechanical model designed to capture the process-structure interplay using a discrete-fracture-matrix framework. It incorporates tightly coupled thermo-hydro-mechanical processes based on laws for momentum, mass and entropy in subdomains representing the matrix and the lower-dimensional fractures and fracture intersections. The deformation of explicitly represented fractures is modelled by contact mechanics relations and a Coulomb friction law, with particular attention on coupling of fracture dilation to the governing equations in both fractures and matrix.

The model is discretised using multi-point finite volumes for the balance equations and a semismooth Newton scheme for the contact conditions and is implemented in the open source fracture simulation toolbox PorePy. Finally, simulation studies demonstrate the model's convergence, investigate process-structure coupling effects, explore different fracture dilation models and show an application of the model to a 3d geothermal pressure stimulation and long-term cooling scenario.

Keywords: thermo-hydro-mechanics, fractures, fracture deformation, porous media, multi-point finite volumes, shear dilation, discrete fracture-matrix, mixed-dimensional

1. Introduction

Fluid injection operations into the subsurface are common in e.g. geothermal energy and petroleum production, wastewater disposal, CO_2 storage and groundwater management. Injection can severely alter subsurface hydraulic, mechanical, thermal and chemical conditions. These coupled processes are strongly affected by preexisting fractures, which represent extreme heterogeneities and discontinuities in the formation. The processes may in turn cause deformation of the fractures, giving rise to dynamic and highly complex process-structure interactions.

In some subsurface engineering operations, fracture deformation is deliberately induced, e.g. to enhance permeability through hydraulic stimulation, in which fluid is injected at elevated pressure to overcome a fracture's frictional resistance to slip [1, 2, 3]. There may also be interest in preventing deformation of fractures to, for example, avoid induced seismicity of unacceptable

*Corresponding author

magnitude in disposal of wastewater [4, 5, 6, 7] or during hydraulic stimulation of fractured geothermal reservoirs [8, 9, 10].

As data related to subsurface dynamics are limited, physics-based modelling can complement data analysis in understanding governing mechanisms for fracture deformation. This requires numerical simulation tools that can capture the governing structure of the fractured formation and relevant coupled processes as well as process-structure interactions, which necessitates explicit representation of both the matrix and dominant fractures in the model. Typically, major fractures or faults are represented explicitly while the rest of the domain is represented as a matrix continuum, possibly integrating effects of finer-scale fractures.

In a spatial grid, there are two alternatives for representing such a Discrete-Fracture-Matrix (DFM) conceptual representation: Resolving the width of the fractures in the grid in an equi-dimensional model imposes severe restrictions put on the spatial discretisation of the domain due to the high aspect ratio of the fractures, thereby limiting the number of fractures that can be included in the model. A geometrically simpler alternative, which was introduced for flow models, is a co-dimension one model, where fractures are represented as objects of one dimension lower than the surrounding domain [11, 12, 13, 14]. In contrast to simulation models for coupled flow and mechanics that treat faults as equidimensional zones of different rheology resolved in the grid [15, 16, 17], the co-dimension DFM model facilitates modelling of fracture slip and dilation [18, 19], and can be combined with full mechanical fracture opening [20]. A conceptually simpler alternative to co-dimension one DFM models is to incorporate only the dynamics in the fracture network and either disregard the dynamics in the matrix altogether or approximate them using semi-analytical methods. These approaches are based on Discrete-Fracture-Network (DFN) representations [21, 22] and will be referred to as DFN methods.

Driven by the need to improve the result of injection operations and avoid unacceptable environmental impacts, intense focus has been placed on in physics-based modelling. Early works by Willis-Richards et al. [23], Rahman et al. [24], Kohl and Mégel [25] and Bruel [26] developed DFN-type models considering only deformation and flow in the fractures and using a Coulomb friction law to model fracture slip due to changes in effective stress as a consequence of local change in fluid pressure. Later, Baisch et al. [27] improved on this type of model by including redistribution of shear stress along the fracture as a consequence of slip through a block-spring model. McClure and Horne [28] further developed the modelling of mechanical interaction between fractures with the boundary integral equation method and introduced a rate-and-state friction model. This type of method has been combined with fracture propagation [29, 30]. As only the fracture is discretised when using the boundary integral equation method, models based on this approach can be classified as DFN-type models. Common to all of these approaches is use of semi-analytical approaches and sequential coupling of physical processes.

The last decade has seen developments in the inclusion of dynamics in the matrix as well as improved models and numerical solution schemes for coupling of different dynamics. Building on previously developed DFN-type models, McClure and Horne [28] and McClure [31] introduced a semi-analytical leakoff term to mimic fracture-matrix flow. Norbeck et al. [29] expanded on previous models developed by McClure and Horne [28] and accounted for the interaction between fracture and matrix flow through an embedded discrete fracture model, where flow in the fracture and in the matrix are discretised on non-conforming grids and connected through transfer terms. Hydro-mechanical simulation tools based on co-dimension one DFM models combined with Coulomb friction laws for fracture slip have also been introduced, motivated by applications related to CO_2-storage [32], gas production [33] and hydraulic stimulation of fractured geothermal reservoirs [34, 19].

More recently, thermal effects have been taken into account in deformation of fractured porous media. Based on a DFN-type model, where the boundary integral equation method was used so

that only the fracture is discretised, Ghassemi and Zhou [35] included thermo-poroelastic effects in the matrix. Based on a DFM conceptual model, Pandey et al. [36] and Salimzadeh et al. [37] have presented models with linear thermo-poroelasticity for the matrix combined with flow, heat transfer and deformation of a single fracture. However, none of these works included modelling of fracture slip or shear dilation when fracture surfaces are in contact. Gallyamov et al. [20] consider a conceptually similar model which includes multiphase flow and a fracture-contact-mechanics model combined with opening and propagation of fractures, and present simulation studies with a large number of fractures. Their work considers the impact of the contact traction on the hydraulic aperture of closed fractures. In contrast to the majority of previously mentioned works, where simplifications that impact the solution are made in the solution of the coupled system, they solve the equations fully coupled, i.e. the flow, energy and mechanics equations are solved simultaneously building on the work by Garipov et al. [33].

Recent work by Garipov and Hui [38] combines several previous developments. Their work is based on a DFM model and considers a fully coupled thermo-poroelastic model for the matrix, flow and heat transfer in the fractures and contact mechanics for fractures based on a Coulomb friction law. Energy and mass conservation are discretised by a finite volume (FV) method, while momentum is discretised by a Galerkin finite element method. This work also presents robust treatment of couplings in the model. However, while the work accounts for permeability enhancement due to full opening of fractures as well as shear dilation, stress response due to dilation as a consequence of slip is not included in the model.

This paper presents a mathematical model based on a mixed-dimensional DFM representation of coupled thermo-hydro-mechanical (THM) processes in a porous rock containing deforming fractures with an accompanying discretisation and numerical solution approach. The model fully couples fluid flow and transport in both matrix and fractures, linear thermo-poromechanics in the matrix and nonlinear fracture deformation. Fracture deformation is based on traction balance, nonpenetration and a Coulomb type friction law, and allows for shear slip and dilation as well as complete fracture opening. To the authors' knowledge, this is the first model that consistently and fully coupled represents stress redistribution due to slip-induced dilation of fractures. As demonstrated by the numerical results, the effect of this coupling can be significant.

Based on the modelling of fractures as lower-dimensional surfaces, the domain is decomposed into subdomains of different dimensions corresponding to matrix, fractures and intersections. Model equations, sets of variables and parameters are defined on each subdomain and the interfaces between them. The resulting mixed-dimensional model [39] facilitates systematic modelling on the decomposed structure while incorporating interaction between processes both within and between subdomains. The governing balance equations in each subdomain are discretised based on multi-point FV methods preserving local conservation, using the same spatial grid for discretisation of all processes. The nonlinear fracture deformation equations are discretised using a semismooth Newton scheme formulated as an active set method.

The model is presented in Section 2, and its discretisation is described in Section 3. In both sections, particular emphasis is placed on fracture deformation as well as its impact on the balance equations for the fractures and the back-coupling to the higher-dimensional momentum balance. Three examples are presented in Section 4: The first investigates governing mechanisms and coupling effects and verifies the model and its implementation in a convergence study. In the second, three different models for fracture dilation are compared. In the last example, the model is applied to a 3d hydraulic stimulation and long-term cooling scenario for geothermal energy extraction. Finally, Section 5 provides some concluding remarks.

2. Model

This section describes the model for THM processes in a porous medium with contact mechanics at the fractures. It relies on a DFM model in which the matrix, the fractures and fracture intersections are explicitly represented by individual subdomains. To avoid resolving the small geometric distances introduced to the fracture network geometry by the high aspect ratio of the fractures, the dimensions of the fracture and intersection subdomains are reduced. The subdomains are collected in a hierarchical structure and connected by interfaces to yield the full mixed-dimensional model.

Decomposition into subdomains facilitates tailored modelling of processes in distinct subdomains, while interactions between subdomains take place on the interfaces. Specifically, separate sets of variables, equations and parameters are defined on each subdomain and interface. This procures the flexibility needed to model the highly complex system arising from the coupled THM system posed in both matrix and fractures.

The model consists of balance equations for momentum, mass and entropy and relations governing the fracture deformation posed on the subdomains. These are supplemented by constitutive laws and equations for coupling over the interfaces. The equations are formulated in terms of the primary variables displacement, pressure, temperature and contact traction on the fractures.

Standard THM equations for a mono-dimensional porous medium are introduced succinctly in Section 2.1 following Coussy [40], followed by a more elaborate presentation of the lower-dimensional scalar equations for deforming fractures and intersections emphasising the effect of volume change in Section 2.2. Section 2.3 describes the model for fracture deformation and its relation to volume change.

2.1. Matrix THM model

We first consider the governing equations in the matrix domain consisting of a solid and a fluid phase. The momentum balance equation reads

$$\nabla \cdot \sigma = \boldsymbol{q_u}, \tag{1}$$

with $\boldsymbol{q_u}$ denoting body forces and the thermo-poroelastic stress tensor for infinitesimal deformation modelled as linearly elastic obeying an extended Hooke's law

$$\sigma = \frac{\mathbf{D}}{2}(\nabla \boldsymbol{u} + \nabla \boldsymbol{u}^T) - \alpha p \mathbf{I} - \beta_s K (T - T_0)\mathbf{I}. \tag{2}$$

Here, $\mathbf{D}$ denotes the stiffness tensor, α the Biot coefficient, β the linear thermal expansion and K the bulk modulus, while $\boldsymbol{u}$, p, T and $\mathbf{I}$ are displacement, pressure, temperature and identity matrix. Subscripts 0 and s indicate the initial state of a variable and the solid phase, respectively. Herein, the relations $\frac{\mathbf{D}}{2}(\nabla \boldsymbol{u} + \nabla \boldsymbol{u}^T) = G(\nabla \boldsymbol{u} + \nabla \boldsymbol{u}^T) + K \mathrm{tr}(\nabla \boldsymbol{u})\mathbf{I}$ and $\boldsymbol{q_u} = \rho_s \boldsymbol{g}$ are used, with G denoting the shear modulus, tr() the trace operator, ρ the density and $\boldsymbol{g}$ the gravitational acceleration vector.

Balance of mass reads

$$\left(\phi c + \frac{\alpha - \phi}{K}\right)\frac{\partial p}{\partial t} + \alpha \frac{\partial (\nabla \cdot \boldsymbol{u})}{\partial t} - \beta \frac{\partial T}{\partial t} + \nabla \cdot \boldsymbol{v} = q_p, \tag{3}$$

with porosity ϕ, compressibility c and subscript f which denotes fluid. Fluid flux relative to the solid is denoted by $\boldsymbol{v}$ and volume sources and sinks by q_p. With $\mathcal{K}$ denoting the permeability

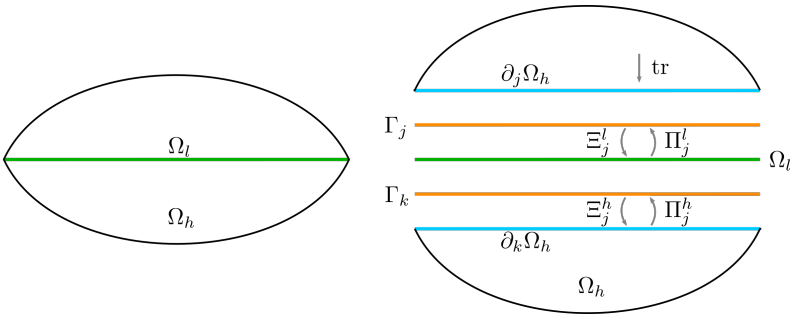

Figure 1: Schematic representation of a two-dimensional matrix subdomain Ω_h and a throughgoing one-dimensional fracture Ω_l. In the expanded representation to the right, the two subdomains are separated by the interfaces Γ_j and Γ_k corresponding to the internal boundaries $\partial_j\Omega_h$ and $\partial_k\Omega_h$. The projection operators used for transfer of variables between the subdomains and interfaces are shown. In the model, Ω_l, Γ_j, Γ_k, $\partial_j\Omega_h$ and $\partial_k\Omega_h$ coincide geometrically.

and μ the viscosity, the flux is modelled according to Darcy's law:

$$\boldsymbol{v} = -\frac{\mathcal{K}}{\mu}\left(\nabla p - \rho \boldsymbol{g}\right). \tag{4}$$

Assuming local thermal equilibrium between the two phases, the entropy balance equation is

$$\frac{\rho C}{T_0}\frac{\partial T}{\partial t} + \beta_s K \frac{\partial(\nabla\cdot\boldsymbol{u})}{\partial t} - \beta\frac{\partial p}{\partial t} + \frac{1}{T_0}\nabla\cdot\boldsymbol{J} = q_T + \frac{\Phi_f}{T}, \tag{5}$$

with ρ, C and β denoting effective density, heat capacity and thermal expansion, respectively. The fluid dissipation $\Phi_f = \frac{\boldsymbol{v}\cdot\boldsymbol{v}}{\mathcal{K}}$ is neglected on an assumption of small velocities [40], while $\boldsymbol{J}$ and q_T are the total heat flux and entropy sources and sinks. The former may be split into continuum scale heat diffusion modelled by Fourier's law and advection along the fluid flow field:

$$\boldsymbol{J} = \boldsymbol{q} + \boldsymbol{w} = -\kappa\nabla T + \rho_f C_f T\boldsymbol{v}, \tag{6}$$

with the effective heat conductivity κ accounting for dispersion due to the tortuous flow in the porous medium. The effective thermal properties are computed as porosity weighted sums [41]

$$\begin{aligned}\rho C &= \phi\rho_f C_f + (1-\phi)\,\rho_s C_s\\ \beta &= \phi\beta_f + (1-\phi)\,\beta_s\\ \beta &= \phi C_f + (1-\phi)\,\kappa_s.\end{aligned} \tag{7}$$

2.2. Mixed-dimensional TH model

This section derives balance equations for mass and entropy for fluid-filled fractures and intersections which may undergo significant relative deformation and volume change giving rise to an additional term compared to equations for static domains. Along with outlining dimension reduction for the mass and entropy equations, the connection between the subdomains of the mixed-dimensional model is presented.

Some notation is needed to describe the mixed-dimensional model of a fractured porous domain of dimension $D = 3$ or $D = 2$ which is split into subdomains corresponding to the rock matrix, the co-dimension one fracture planes and co-dimension two fracture intersections. In the case $D = 3$, the model also generalises to account for intersections of fracture intersection lines, i.e. zero-dimensional points. A subdomain is denoted by Ω_i and its boundary by $\partial\Omega_i$. The subscript i is also used to identify variables defined within Ω_i, but suppressed as context allows. Each part $\partial_j\Omega_i$ of the internal boundary is associated with an interface Γ_j to an immersed lower-dimensional domain Ω_l (see Fig. 1). All lower- and higher-dimensional interfaces of a subdomain are collected in the sets $\check{S}$ and $\tilde{S}$; in particular, the interfaces corresponding to surfaces of fracture i constitute $\hat{S}_i$. Where convenient, the higher- and lower-dimensional neighbours of an interface are denoted by Ω_h and Ω_l, respectively.

Finally, four types of projection operators are needed to transfer variables between interfaces and the neighbouring higher- and lower-dimensional subdomains. As illustrated in Fig. 1, projection from the interface to the subdomains is performed by Ξ_j^h and Ξ_j^l, respectively, whereas Π_j^h and Π_j^l project from the subdomains to the interface.

The thickness of a fracture is characterised by the aperture a [m], which will be related to the fracture deformation in Section 2.3. The aperture of an intersection is taken to be the average of the intersecting higher-dimensional neighbours, i.e.

$$a_l = \frac{1}{|\hat{S}_l|} \sum_{j \in \check{S}_l} \Xi_j^l \Pi_j^h a_h, \tag{8}$$

with $a = 1$ in the matrix for completeness. The specific volume $\mathcal{V} = a^{D-d}$ accounts for the dimension reduction from the deforming equi-dimensional Ω to the corresponding spatially fixed d-dimensional Ω_i so that for a scalar quantity ζ and a vector quantity $\boldsymbol{\iota}$

$$\begin{aligned} &\frac{d}{dt}\int_\Omega \zeta dx = \int_{\Omega_i} \frac{\partial}{\partial t}(\mathcal{V}\zeta_i) dx \\ &\int_{\partial\Omega} \boldsymbol{\iota} \cdot d\boldsymbol{x} = \mathcal{V}\int_{\partial\Omega_i} \boldsymbol{\iota}_i \cdot d\boldsymbol{x} - \sum_{j \in \hat{S}_i} \Xi_j^l \left(\Pi_j^h \mathcal{V}_h \int_{\Gamma_j} \iota_j dx \right), \end{aligned} \tag{9}$$

with $\boldsymbol{n}$ denoting the outwards normal at the boundaries and ι_j the interface flux into the domain. The weighting with $\mathcal{V}_h$ ensures that the interface flux matches the dimension of fluxes of the higher-dimensional neighbour, which are scaled by specific volumes as seen by the expression for the tangential flux. Note that all differentials in reduced integrals should be interpreted as relative to the domain of integration; i.e. dx is two-dimensional for a fracture with $d = 2$.

Suppressing all subscripts f throughout this subsection, the fluid mass balance equation for a deforming domain is

$$\frac{d}{dt}\int_\Omega \rho dx + \int_{\partial\Omega} \rho \boldsymbol{v} \cdot d\boldsymbol{x} = \int_\Omega \rho q_p dx. \tag{10}$$

The boundary flux integral may be split into two parts corresponding to tangential (in-plane) and normal (out-of-plane) components. Averaging in the normal direction for the tangential contribution and replacing the normal part of the boundary by Γ_j, the fluid flux becomes

$$\int_{\partial\Omega} \boldsymbol{v} \cdot d\boldsymbol{x} = \int_{\partial\Omega_i} \mathcal{V}_i \boldsymbol{v}_i \cdot d\boldsymbol{x} - \sum_{j \in \hat{S}_i} \Xi_j^l \left(\Pi_j^h \mathcal{V}_h \int_{\Gamma_j} v_j dx \right). \tag{11}$$

Thus, the inter-dimensional coupling between Ω_h and Ω_l takes the form of interface fluid fluxes v_j, which also appear as a Neumann condition for Ω_h:

$$\boldsymbol{v}_h \cdot \boldsymbol{n}_h = \Xi_j^h v_j \quad \text{on } \partial_j \Omega_h, \tag{12}$$

with $\boldsymbol{n}_h$ denoting the outwards normal on $\partial_j \Omega_h$. Letting $\mathrm{tr}(\cdot)$ denote a suitable trace operator, the interface flux is modelled using a Darcy type law extended from Martin et al. [12] to account for gravity

$$v_j = -\frac{\mathcal{K}_j}{\Pi_j^l \mu_l} \left(\frac{2}{\Pi_j^l a_l} \left(\Pi_j^l p_l - \Pi_j^h \mathrm{tr}(p_h) \right) - \Pi_j^l \rho_l \boldsymbol{g} \cdot \Pi_j^h \boldsymbol{n}_h \right) \quad \text{on } \Gamma_j. \tag{13}$$

Both the weighting by a_l and $\mathcal{V}_h$ and the normal permeability $\mathcal{K}_j$ arise through dimension reduction. The remaining terms of Eq. (10) are averaged in the normal direction using Eq. (9), and

$$\rho = \rho_0 \exp[c(p - p_0) - \beta(T - T_0)] \tag{14}$$

is inserted for the fluid density. Collecting terms, dividing by ρ and assuming Darcy's law for the tangential flux yields the dimensionally reduced mass balance

$$\begin{aligned} \int_{\Omega_i} \mathcal{V}_i \left(c_i \frac{\partial p_i}{\partial t} - \beta \frac{\partial T_i}{\partial t} \right) + \frac{\partial \mathcal{V}_i}{\partial t} dx - \int_{\partial \Omega_i} \mathcal{V}_i \frac{\mathcal{K}}{\mu} \left(\nabla p_i - \rho \boldsymbol{g} \right) \cdot d\boldsymbol{x} - \sum_{j \in \hat{S}_i} \Xi_j^i \left(\Pi_j^h \mathcal{V}_h \int_{\Gamma_j} v_j dx \right) \\ = \int_{\Omega_i} \mathcal{V}_i q_p dx. \end{aligned} \tag{15}$$

The dimension reduction is now performed for the entropy balance, which reads

$$\frac{d}{dt} \int_\Omega \rho s dx + \int_{\partial \Omega} \left(\frac{\boldsymbol{q}}{T} + s \rho \boldsymbol{v} \right) \cdot d\boldsymbol{x} = \int_\Omega q_T + \frac{\Phi}{T} dx. \tag{16}$$

The total dissipation consisting of Φ_f and thermal dissipation $\Phi_T = -\frac{\boldsymbol{q}}{T} \cdot \nabla T$ is combined with the conductive flux to yield

$$\int_{\partial \Omega} \frac{\boldsymbol{q}}{T} \cdot d\boldsymbol{x} - \int_\Omega \frac{\Phi}{T} dx = \int_\Omega \nabla \cdot \left(\frac{\boldsymbol{q}}{T} \right) - \frac{\boldsymbol{v} \cdot \boldsymbol{v}}{\mathcal{K} T} + \frac{\boldsymbol{q}}{T^2} \cdot \nabla T dx = \int_\Omega \frac{\nabla \cdot \boldsymbol{q}}{T} - \frac{\boldsymbol{v} \cdot \boldsymbol{v}}{\mathcal{K} T} dx. \tag{17}$$

The latter term is again neglected, while the former is approximated as $\frac{\nabla \cdot \boldsymbol{q}}{T_0}$. The source term is assumed to equal the entropy of the fluid of the volume source and sink terms, $q_T = \rho s q_p$.

The dimension reduction of the flux terms is

$$\begin{aligned} \int_{\partial \Omega} \left(\frac{\boldsymbol{q}}{T_0} + s \boldsymbol{v} \right) \cdot d\boldsymbol{x} = \int_{\partial \Omega_i} \mathcal{V} \left(\frac{\boldsymbol{q}_i}{T_0} + s T \boldsymbol{v}_i \right) \cdot d\boldsymbol{x} \\ - \sum_{j \in \hat{S}_i} \Xi_j^l \left(\Pi_j^h \mathcal{V}_h \int_{\Gamma_j} \frac{q_j}{T_0} + w_j dx \right), \end{aligned} \tag{18}$$

and the internal boundary conditions are

$$\begin{aligned} \boldsymbol{q}_h \cdot \boldsymbol{n}_h &= \Xi_j^h q_j \\ \boldsymbol{w}_h \cdot \boldsymbol{n}_h &= \Xi_j^h w_j \end{aligned} \quad \text{on } \partial_j \Omega_h. \tag{19}$$

The Fourier-type conductive interface flux is

$$q_j = -\kappa_j \frac{2}{\Pi_j^l a_l}(\Pi_j^l T_l - \Pi_j^h \mathrm{tr}(T_h)) \quad \text{on } \Gamma_j \tag{20}$$

with the normal heat conductivity modelled as $\kappa_j = \Pi_j^l \kappa_{f,l}$ since it originates from the dimension reduction of a fluid-filled domain.

The dimension reduction of the remaining terms of Eq. (16) is a direct analogue to the mass balance derivations above. The equations of state are Eq. (14), and the linearised entropy equation of state

$$s - s_0 = -\beta \frac{p - p_0}{\rho} + \frac{C}{T_0}(T - T_0). \tag{21}$$

Assuming Fourier's law, linearising and retaining only the dominant terms produces the dimension reduced entropy balance

$$\begin{aligned} &\int_{\Omega_i} \frac{C\rho}{T_0}(T_i - T_0)\frac{\partial \mathcal{V}_i}{\partial t} + \frac{C\rho}{T_0}\mathcal{V}_i \frac{\partial T}{\partial t} - \beta \mathcal{V}_i \frac{\partial p_i}{\partial t} dx + \int_{\partial\Omega_i} \mathcal{V}_i \left(\frac{C\rho}{T_0}(T_i - T_0)\boldsymbol{v}_i - \frac{\kappa_i}{T_0}\nabla T_i \right) \cdot d\boldsymbol{x} \\ &- \sum_{j \in \hat{S}_i} \Xi_j^i \left(\Pi_j^h \mathcal{V}_h \int_{\Gamma_j} \frac{q_j}{T_0} + \frac{w_j}{T_0} dx \right) = \int_{\Omega_i} \mathcal{V}_i q_p \frac{C\rho}{T_0}(T - T_0) dx, \end{aligned} \tag{22}$$

with an advective interface flux defined according to the upstream direction of the interface fluid flux:

$$w_j = \begin{cases} v_j \Pi_j^h \mathrm{tr}(\rho_h C_h T_h) & \text{if } v_j > 0 \\ v_j \Pi_j^l \rho_k C_l T_l & \text{if } v_j \leq 0 \end{cases} \quad \text{on } \Gamma_j. \tag{23}$$

2.3. Fracture deformation

The traction balance, nonpenetration condition and friction law posed on a fracture l are formulated in terms of interface displacements and fracture contact traction. The interface displacements on the two surfaces Γ_j and Γ_k are $\boldsymbol{u}_j$ and $\boldsymbol{u}_k$, and the jump between the two sides is

$$[\![\boldsymbol{u}_l]\!] = \Xi_j^l \boldsymbol{u}_j - \Xi_k^l \boldsymbol{u}_k. \tag{24}$$

Since the fracture deformation depends on traction caused by the *contact* between the two surfaces, the contribution from p_l should be subtracted on the fracture surfaces to yield the traction balance posed on the interfaces:

$$\begin{aligned} \Pi_j^l \boldsymbol{\lambda}_l - p_l \mathbf{I} \cdot \boldsymbol{n}_l &= \Pi_j^h \mathrm{tr}(\sigma_h \cdot \boldsymbol{n}_h) && \text{on } \Gamma_j. \\ \Pi_k^l \boldsymbol{\lambda}_l - p_l \mathbf{I} \cdot \boldsymbol{n}_l &= -\Pi_k^h \mathrm{tr}(\sigma_h \cdot \boldsymbol{n}_h) && \text{on } \Gamma_k. \end{aligned} \tag{25}$$

The right-hand sides are the higher-dimensional THM tractions projected to the interfaces. The fracture contact traction $\boldsymbol{\lambda}_l$ will for notational convenience be referred to as $\boldsymbol{\lambda}$ in the following, and is defined according to the normal of the fracture, which is defined as $\boldsymbol{n}_l = \Xi_j^l \Pi_j^h \boldsymbol{n}_h$. Also, a vector $\boldsymbol{i}_l$ defined on a fracture may be decomposed into the normal and tangential components

$$i_n = \boldsymbol{i} \cdot \boldsymbol{n}_l \text{ and } \boldsymbol{i}_\tau = \boldsymbol{i} - i_n \mathbf{I}. \tag{26}$$

The nonpenetration condition reads

$$\begin{aligned} \llbracket \boldsymbol{u} \rrbracket_n - g &\leq 0 \\ \lambda_n(\llbracket \boldsymbol{u} \rrbracket_n - g) &= 0 \\ \lambda_n &\leq 0, \end{aligned} \tag{27}$$

with the gap function g defined to equal the distance between the two fracture interfaces when in contact. The Coulomb friction law is

$$\begin{aligned} ||\boldsymbol{\lambda}_\tau|| &\leq -F\lambda_n \\ ||\boldsymbol{\lambda}_\tau|| &< -F\lambda_n \rightarrow \llbracket \dot{\boldsymbol{u}} \rrbracket_\tau = 0 \\ ||\boldsymbol{\lambda}_\tau|| &= -F\lambda_n \rightarrow \exists\, \zeta \in \mathbb{R}^- : \llbracket \dot{\boldsymbol{u}} \rrbracket_\tau = \zeta \boldsymbol{\lambda}_\tau, \end{aligned} \tag{28}$$

with F denoting the friction coefficient and $\llbracket \dot{\boldsymbol{u}} \rrbracket_\tau$ denoting the tangential displacement increment. In addition to enforcing the traction balance of Eq. (25) and the conditions of Eqs. (27) and (28), a Dirichlet condition is assigned on $\partial_j \Omega_h$ so that

$$\Xi_j^h \boldsymbol{u}_j = \mathrm{tr}(\boldsymbol{u}_h). \tag{29}$$

The aperture introduced in Section 2.2 is a function of displacement jump, $a = a\,(\llbracket \boldsymbol{u} \rrbracket)$. Due to roughness of the fracture surfaces, tangential displacements may induce dilation [42] as illustrated in Fig. 2. The relationship between the dilation and the magnitude of tangential displacement is assumed to be linear and described by the friction angle ψ following Rahman et al. [43]. As modelled herein, the dilation is not merely a hydraulic effect impacting, e.g., the fracture permeability, but a mechanical effect in the sense that the normal distance between the fracture surfaces increases. As such, the dilation must be coupled back to the normal interface displacements and the matrix deformation through Eq. (29), which is achieved by choosing the gap function

$$g = -\tan(\psi)||\llbracket \boldsymbol{u} \rrbracket_\tau||. \tag{30}$$

The update is reversible; if the tangential displacement is reversed, g takes on its initial value.

Small-scale fracture roughness may provide a volume for the fluid to occupy even when the fractures are in an undeformed state. This leads to the following relation between aperture and displacement:

$$a = a_0 - \llbracket \boldsymbol{u} \rrbracket_n, \tag{31}$$

where a_0 denotes the residual aperture in the undeformed state.

In addition to entering the equations as a result of dimension reduction, a governs the tangential permeability of a fracture or intersection line i according to the cubic law [44],

$$\mathcal{K}_i = \frac{a_i^2}{12} \mathbf{I}_i, \tag{32}$$

where $\mathbf{I}_i$ denotes the identity matrix of the fracture dimension. Equation (32) constitutes a strongly nonlinear coupling, especially as $\mathcal{K}_i$ is multiplied by $\mathcal{V}$ in Eq. (15). Finally, the normal permeability of an interface is inherited from the lower-dimensional neighbour:

$$\mathcal{K}_j = \Pi_j^l \mathcal{K}_l. \tag{33}$$

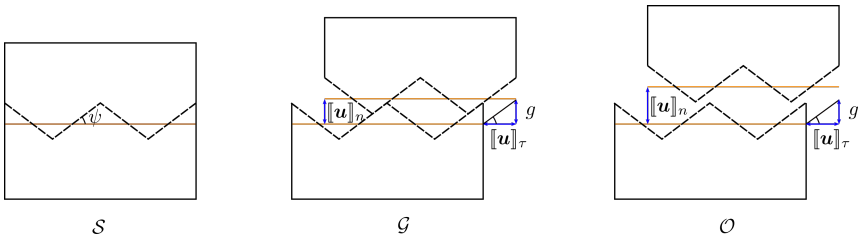

Figure 2: Schematic representation of three fracture configurations: sticking ($\mathcal{S}$), gliding ($\mathcal{G}$) and open ($\mathcal{O}$). In the model, the fracture surfaces are represented as planar interfaces indicated by the orange lines. Idealised fracture roughness is shown by dashed sawtooth lines, with the inclination of the teeth equalling the dilation angle ψ, while the magnitude of displacement jumps and g are indicated by arrows. In the first configuration, the fracture is undisplaced and closed with $g = [\![\boldsymbol{u}]\!]_n = [\![\boldsymbol{u}]\!]_\tau = 0$. In the second configuration, the fracture is still mechanically closed, but tangential displacement has resulted in fracture dilation due to roughness. In the third configuration, there is no mechanical contact across the fracture; that is, the fracture is mechanically open with $[\![\boldsymbol{u}]\!]_n < g$.

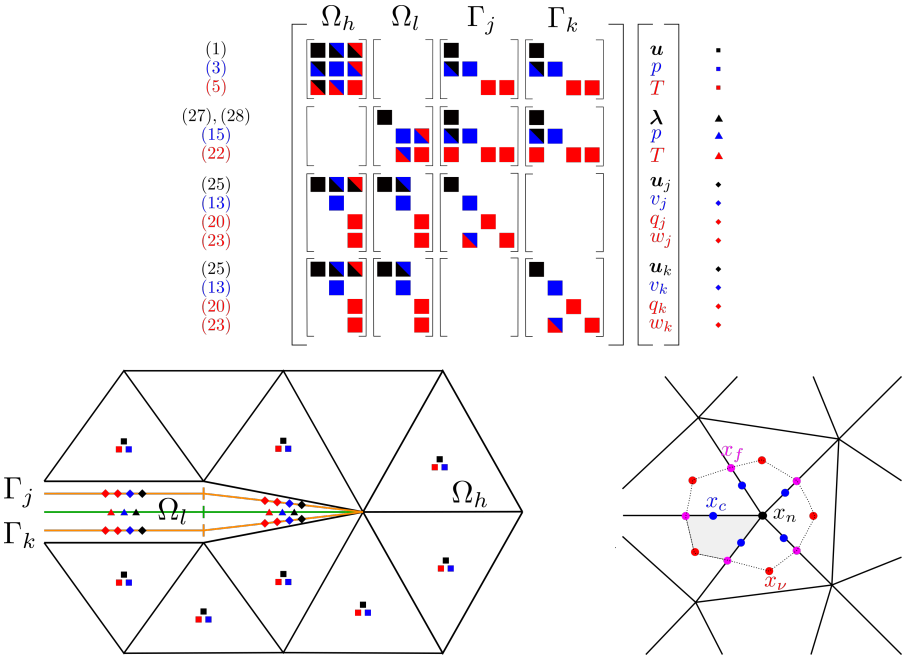

Figure 3: Top: The two-level block system of linear equations for the matrix Ω_h, fracture Ω_l and interfaces Γ_j and Γ_k with corresponding equation numbers shown to the left. Bottom left: Spatial discretisation and spatial location of degrees of freedom for a domain corresponding to the equation system. Matrix, fracture and interface grids are shown in black, green and orange, respectively, and the corresponding degrees of freedom are shown as squares, triangles and diamonds. Black represents displacement, blue pressure and red temperature; the relation between all markers and unknowns is shown at top right. Bottom right: Subgrid around a node x_n of the primary grid, which is shown in solid black lines. The interaction region forming the stencil for the local systems is constructed by connecting the surrounding cell centres x_ν and face centres x_f as indicated by the dotted lines. Continuity of primary variables is enforced in the points x_c; the shaded area indicates a subcell.

3. Discretisation

This section describes the discretisation of the model presented in the previous section. The system is discretised in time using Implicit Euler (IE) and solved monolithically. The spatial grids are simplicial, and are constructed such that the lowerdimensional cells coincide with higher-dimensional faces; grids are generated by Gmsh [45]. The model is implemented in the open source fracture simulation toolbox PorePy presented in Keilegavlen et al. [39].

The mixed-dimensional framework gives rise to a two-level block structure as the equations are discretised. The outer level corresponds to the subdomains and interfaces, with entries internal to the subdomains on the diagonal and entries for the interdimensional coupling on the off-diagonals. The inner level corresponds to the primary variables, with coupling effects between different variables on the off-diagonals. The block structure is illustrated in Fig. 3, which will be used in the following description of discretisation of individual terms by referring to the block in row r and column c as $A_{(r,c)}$ with r and c ranging from 1 to 14.

3.1. Matrix THM discretisation

The spatial discretisation of the diffusive terms of the balance equations is achieved using a family of cell-centred finite volume schemes. The approach is based on the multi-point flux approximation (MPFA) [46] defined for diffusive scalar problems and the multi-point stress approximation (MPSA) for vector problems [47] and their combination for THM problems [48, 49]. The scheme is formulated in terms of discrete displacement (D vectors), pressure and temperature unknowns and is locally momentum, mass and entropy conservative.

The scheme's construction is based on a subdivision of the spatial grid as illustrated in Fig. 3, with the gradients of displacement, pressure and temperature defined as piecewise constants on the subdivision. The fluxes of the conserved quantities momentum, mass and entropy are discretised via Hooke's, Darcy's and Fourier's law, respectively. Continuity is enforced for traction and mass and entropy fluxes over faces of the subgrid and for the primary variables in the continuity points x_c, leading to one local system for each node of the primary grid. Each local system is partially inverted to express gradients in terms of the cell-centre values in nearby cells. A global system is constructed by collecting for each cell all face fluxes as expressed in terms of the cell-centred primary variables. For details, see Nordbotten and Keilegavlen [49].

The coupling between the three equations is achieved by using the thermo-poroelastic stress for the local traction balances, which directly yields the contributions $A_{(1,2)}$ and $A_{(1,3)}$ representing the scalar variables' effect on the momentum balance. $A_{(2,1)}$ and $A_{(3,1)}$, which represent the displacement effects on the scalar balances, are constructed by assembly of the discrete divergence based on the local systems for the displacement gradients.

The standard FV IE discretisation is applied to all time derivatives; that is, both the TH coupling blocks $A_{(2,3)}$ and $A_{(3,2)}$ and the accumulation terms of $A_{(2,2)}$ and $A_{(3,3)}$. The advective term of (5) is discretised using a first-order upwind scheme, i.e. the temperature flux between cells k and l is

$$(\rho_f C_f T \boldsymbol{v})_{k,l} = \begin{cases} C_f \boldsymbol{v}_{k,l} T_k \rho_{f,k} & \text{if } \boldsymbol{v}_{k,l} > 0 \\ C_f \boldsymbol{v}_{k,l} T_l \rho_{f,k} & \text{if } \boldsymbol{v}_{k,l} \leq 0, \end{cases} \tag{34}$$

with the fluid flux from cell k to cell l $\boldsymbol{v}_{k,l}$ and $\rho_{f,k}$ computed from the solution at the previous iteration.

3.2. Mixed-dimensional TH discretisation

All terms of the scalar equations for the lower-dimensional subdomains are discretised using lower-dimensional versions of the corresponding D-dimensional discretisations. For the Darcy and Fourier fluxes, this implies that we use the MPFA scheme, while the advective fluxes are again treated by first-order upwinding. The interdimensional coupling relations are discrete analogues to Eqs. (13), (20) and (23). Thus, they involve reconstruction of p and T on $\partial_j\Omega_h$, which we base on discretisation matrices pertaining to the MPFA discretisations. For the matching grids used herein, the discrete projections are straightforward bijective mappings between faces of Ω_h and cells of Γ_j (Π_j^h and Ξ_j^h) and between the cells of Ω_l and Γ_j (Π_j^l and Ξ_j^l).

The nonlinearities arising through the products involving a and $\mathcal{V}$ are solved iteratively within the Newton scheme for fracture deformation described below. Specifically, the time derivatives are computed as additional right hand side terms based on values from the previous iterate and time step. However, the linear volume-change terms in the fractures are coupled fully implicitly to $\boldsymbol{u}_j$ so that the contribution for each fracture is the jump between the neighbouring higher-dimensional interfaces, as illustrated by the off-diagonal blocks $A_{(5,7)}$, $A_{(5,11)}$, $A_{(6,7)}$ and $A_{(6,11)}$. Densities are computed from the solution at the previous iteration. In some simulations involving strong advection and high temperature gradients, the density dependence in the gravity term of Darcy's law may lead to oscillatory fluxes between Newton iterations. This may result in convergence problems related to the upstream discretisation of the advective term. In these situations, convergence was achieved by damping the updates of the fluid flux of the advective term.

3.3. Fracture deformation

Fracture deformation discretisation is based on the approach presented by Hüeber et al. [50] and Wohlmuth [51] with the frictional contact problem formulated as a variational inequality. The formulation is expanded to account for the $[\![\boldsymbol{u}]\!]_\tau$ dependency of g. Deformation constraints are reformulated as complementary functions $\mathcal{C} = \mathcal{C}(\mathbb{X})$, with $\mathbb{X}$ being the unknowns. The constraints are imposed by solving $\mathcal{C} = 0$ through application of the semismooth Newton method

$$\mathcal{D}(\mathbb{X}^k)(\delta\mathbb{X}^k) = -\mathcal{C}(\mathbb{X}^k), \tag{35}$$

where the increment of a function f between successive iterations k and $k+1$ is $\delta f(\mathbb{X}^k) = f(\mathbb{X}^{k+1}) - f(\mathbb{X}^k)$ and $\mathcal{D}$ is the generalised Jacobian of $\mathcal{C}$, i.e. the convex hull of the standard Jacobian wherever $\mathcal{C}$ is differentiable.

To facilitate imposition of different constraints based on the deformation states defined in Eqs. (27) and (28), three disjoint sets describing the deformation state as open, sticking or gliding are defined:

$$\begin{aligned} \mathcal{O} &= \{b \leq 0\} \\ \mathcal{S} &= \{||-\boldsymbol{\lambda}_\tau + \tilde{c}[\![\dot{\boldsymbol{u}}]\!]_\tau|| < b\} \\ \mathcal{G} &= \{||-\boldsymbol{\lambda}_\tau + \tilde{c}[\![\dot{\boldsymbol{u}}]\!]_\tau|| \geq b > 0\}\,. \end{aligned} \tag{36}$$

Here, $\tilde{c}$ denotes a numerical parameter, the friction bound is $b = F\left(-\lambda_n + \tilde{c}\left([\![\boldsymbol{u}]\!]_n - g\right)\right)$ and $[\![\dot{\boldsymbol{u}}]\!]_\tau$ denotes the increment from the previous time step. Replacing $[\![\dot{\boldsymbol{u}}]\!]_\tau$ by $[\![\boldsymbol{u}]\!]_\tau$ in the above definition yields the cumulative fracture state sets, which are denoted by subscript c.

The normal and tangential complementary functions are

$$\mathcal{C}_n\left([\![\boldsymbol{u}]\!]_n, \lambda_n\right) = -\lambda_n - \frac{1}{F}\max(0, b) \tag{37}$$

and

$$\mathcal{C}_\tau\left([\![\delta\boldsymbol{u}]\!]_\tau, [\![\boldsymbol{u}]\!]_\tau, \boldsymbol{\lambda}\tau\right) = \max(b, ||-\boldsymbol{\lambda}_\tau + \tilde{c}[\![\boldsymbol{u}]\!]_\tau||)\left(-\boldsymbol{\lambda}_\tau\right) - \max(0, b)\left(-\boldsymbol{\lambda}_\tau + \tilde{c}[\![\dot{\boldsymbol{u}}]\!]_\tau\right), \tag{38}$$

and the corresponding generalised Jacobians are

$$\mathcal{D}_n\left([\![\boldsymbol{u}]\!], \lambda_n\right)\left(\delta[\![\boldsymbol{u}]\!], \delta\lambda_n\right) = -\delta\lambda_n - \chi_{\mathcal{S}\cup\mathcal{G}}\frac{1}{F}\delta b \tag{39}$$

and

$$\begin{aligned}\mathcal{D}_\tau\left([\![\boldsymbol{u}]\!], [\![\dot{\boldsymbol{u}}]\!]_\tau, \boldsymbol{\lambda}\right)\left(\delta[\![\boldsymbol{u}]\!], \delta[\![\dot{\boldsymbol{u}}]\!]_\tau, \delta\boldsymbol{\lambda}\right) = &-\max(b, ||-\boldsymbol{\lambda}_\tau + \tilde{c}[\![\dot{\boldsymbol{u}}]\!]_\tau||)\delta\boldsymbol{\lambda}_\tau \\ &- \chi_{\mathcal{O}\cup\mathcal{G}}\frac{\boldsymbol{\lambda}_\tau\left(-\boldsymbol{\lambda}_\tau + \tilde{c}[\![\dot{\boldsymbol{u}}]\!]_\tau\right)^T}{||-\boldsymbol{\lambda}_\tau + \tilde{c}[\![\dot{\boldsymbol{u}}]\!]_\tau||}\left(-\delta\boldsymbol{\lambda}_\tau + \tilde{c}\delta[\![\dot{\boldsymbol{u}}]\!]_\tau\right) \\ &- \chi_{\mathcal{S}\cup\mathcal{G}}\, b\left(-\delta\boldsymbol{\lambda}_\tau + \tilde{c}\delta[\![\dot{\boldsymbol{u}}]\!]_\tau\right) \\ &- \chi_{\mathcal{S}}\,\delta b\boldsymbol{\lambda}_\tau \\ &- \chi_{\mathcal{S}\cup\mathcal{G}}\,\delta b\left(-\boldsymbol{\lambda}_\tau + \tilde{c}[\![\dot{\boldsymbol{u}}]\!]_\tau\right).\end{aligned} \tag{40}$$

Here, $\chi_\star$ is the characteristic function of a set $\star$ for a fracture cell ν,

$$\chi_\star = \begin{cases} 1 & \text{if } \nu \in \star \\ 0 & \text{if } \nu \notin \star, \end{cases} \tag{41}$$

while the increment of the friction bound is

$$\delta b = F\left[-\delta\lambda_n + \tilde{c}\left(\delta[\![\boldsymbol{u}]\!]_n - \frac{dg}{d[\![\boldsymbol{u}]\!]_\tau}\delta[\![\boldsymbol{u}]\!]_\tau\right)\right]. \tag{42}$$

Hence, sorting each cell according to Eq. (36) and imposing Eq. (35) results in the following constraints:

$$\begin{aligned}\boldsymbol{\lambda}^{\nu,k+1} &= \boldsymbol{0} && \nu \in \mathcal{O} \\ [\![\boldsymbol{u}^{\nu,k+1}]\!]_n - \left(\frac{dg}{d[\![\boldsymbol{u}]\!]_\tau}\right)^{\nu,k}[\![\dot{\boldsymbol{u}}^{\nu,k+1}]\!]_\tau &= g^{\nu,k} - \left(\frac{dg}{d[\![\boldsymbol{u}]\!]_\tau}\right)^{\nu,k}[\![\dot{\boldsymbol{u}}^{\nu,k}]\!]_\tau && \nu \in \mathcal{G}\cup\mathcal{S} \\ [\![\dot{\boldsymbol{u}}^{\nu,k+1}]\!]_\tau - \frac{F[\![\dot{\boldsymbol{u}}^{\nu,k}]\!]_\tau}{b^{\nu,k}}\lambda_n^{\nu,k+1} &= [\![\dot{\boldsymbol{u}}^{\nu,k}]\!]_\tau && \nu \in \mathcal{S} \\ \boldsymbol{\lambda}_\tau^{\nu,k+1} + L^{\nu,k}[\![\dot{\boldsymbol{u}}t^{\nu,k+1}]\!]_\tau + F\boldsymbol{\nu}^{\nu,k}\lambda_n^{\nu,k+1} &= \boldsymbol{r}^{\nu,k} + b^{\nu,k}\boldsymbol{\nu}^{\nu,k} && \nu \in \mathcal{G}\end{aligned} \tag{43}$$

The coefficients L, $\boldsymbol{\nu}$ and $\boldsymbol{r}$ are functions of $[\![\dot{\boldsymbol{u}}^k]\!]_\tau$ and $\boldsymbol{\lambda}^k$, and can thus be computed from the previous iterate. For the exact expressions and further details of the discretisation and implementation of the fracture deformation equations, see Berge et al. [52].

The effect of letting g depend on $[\![\boldsymbol{u}]\!]_\tau$ only appears in the normal condition in the two terms involving the derivative $\frac{dg}{d[\![\boldsymbol{u}]\!]_\tau}$. The two cases $g = 0$ and Eq. (30) will be considered below. The former obviously gives $\frac{dg}{d[\![\boldsymbol{u}]\!]_\tau} = 0$ while the latter gives

$$\frac{dg}{d[\![\boldsymbol{u}]\!]_\tau} = \begin{cases} -\tan(\psi)\frac{[\![\boldsymbol{u}]\!]_\tau^T}{||[\![\boldsymbol{u}]\!]_\tau||} & \text{if} \quad ||[\![\boldsymbol{u}]\!]_\tau|| > 0 \\ 0 & \text{if} \quad ||[\![\boldsymbol{u}]\!]_\tau|| = 0, \end{cases} \tag{44}$$

which may be inserted into Eq. (43) to finally yield $A_{(4,4)}$, $A_{(4,7)}$ and $A_{(4,11)}$ of Fig. 3.

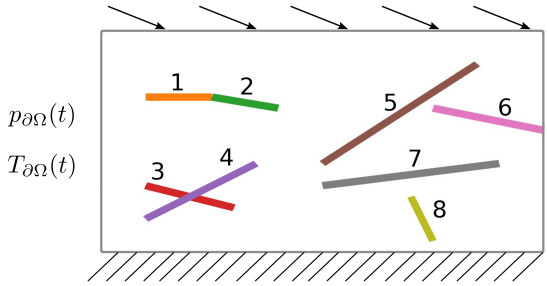

Figure 4: Fracture geometry and the boundary conditions driving the dynamics for examples 1 and 2. The colour scheme for the fractures is used throughout Sections 4.1 and 4.2. The domain is fixed at the bottom and displaced at the top, while temporally varying pressure and temperature values $p_{\partial\Omega}$ and $T_{\partial\Omega}$ are prescribed at the left boundary.

4. Results

This section presents three sets of simulations aimed at demonstrating the model's representation of complex process-structure interactions. In the first example, a convergence study is presented and coupling mechanisms investigated. The second example explores different modelling choices for the relationship between displacement jumps and apertures. Finally, the model is applied to a geothermal scenario with a pressure stimulation phase and long-term cooling during a production phase. Run scripts for the example simulations and animations showing temporal evolution of the solutions may be found in a dedicated GitHub repository [53].

4.1. Example 1 - Convergence study

Starting from a coarse grid of 398 2d cells, 38 1d cells and two 1d cells, a sequence of six grids is produced by nested conforming refinement. The finest grid, which has 407 552 2d cells resulting in a total of 1 647 254 unknowns, is used as the reference solution for the convergence study and forms the basis of the process discussion of coupling mechanisms.

The geometry of the 2d domain with eight fractures is a modified version of a geometry presented in Berge et al. [52] and is shown in Fig. 4. It contains a kink formed by two fractures, an intersection formed by two other fractures and nearly intersecting fractures, as well as both immersed fractures and one fracture extending to the boundary. These features can be expected to challenge the accuracy of numerical simulations.

Simulating three different phases allows us to distinguish between the influence of mechanical, hydraulic and thermal driving forces. The three phases are defined through the boundary conditions as follows: Fixing the bottom and setting homogeneous stress conditions on the left and right boundary, a Dirichlet displacement value of $(5 \times 10^{-4}, -2 \times 10^{-4})^T$ m is applied at the top throughout the simulation and is the only driving force during phase I. Phase II begins when a pressure gradient of 4×10^7 Pa is applied from left to right. Once the solution has reached equilibrium, a boundary temperature 15 K lower than the initial temperature is prescribed at the left boundary marking the onset of phase III. The initial values are $p_0 = 0$ Pa, $T_0 = 300$ K and $a_0 = 5 \times 10^{-4}$; no gravity effects are included in this example.

Figure 5 shows convergence results for the end of the three phases. For each phase, we

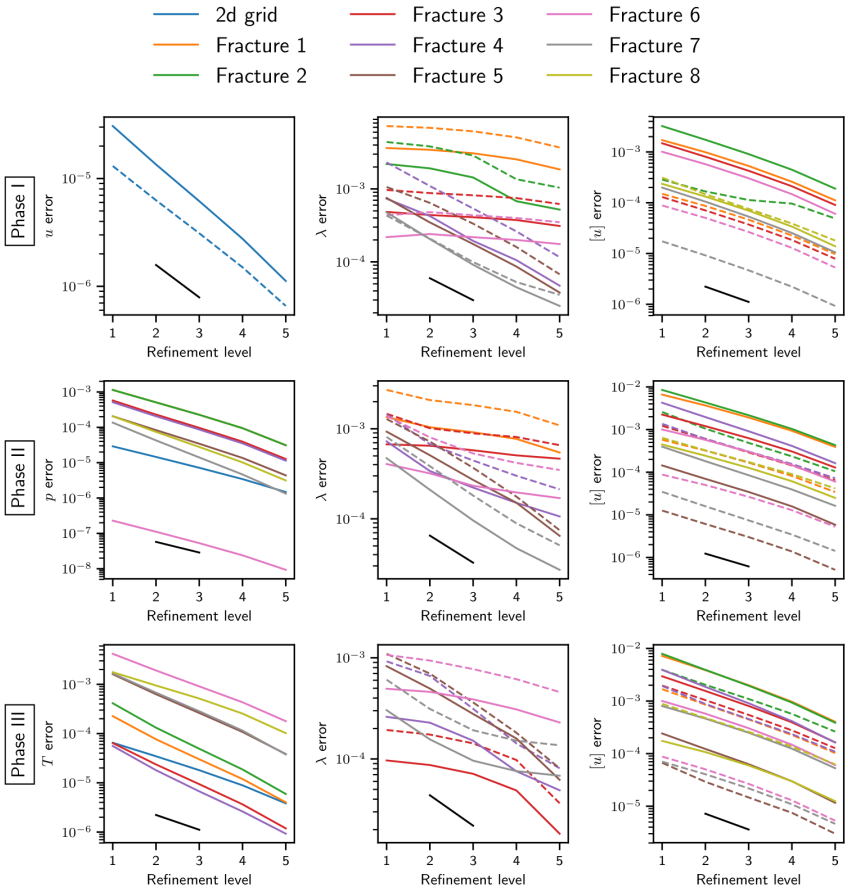

Figure 5: Example 1: Errors relative to reference grid solution for solutions on five coarser grids at the end of the three phases, shown top to bottom. The three columns correspond to the variable of the main driving force, contact traction and displacement jumps. Solid and dashed lines correspond to x and y component in the matrix and tangential and normal component in the fractures. The black lines indicate first order.

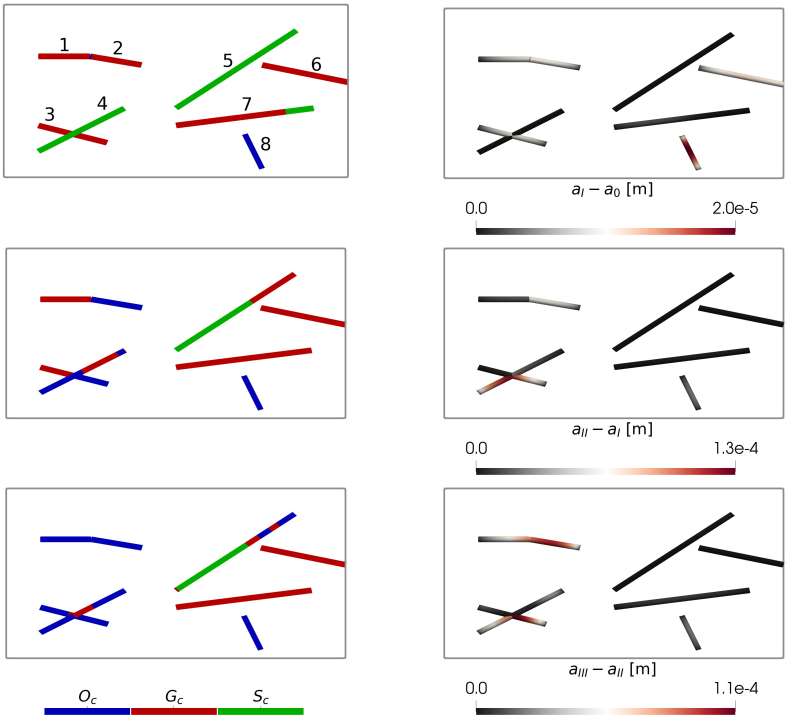

Figure 6: Example 1: Left: Fracture states according to cumulative displacement jumps at the end of phases I through III shown top to bottom. Right: Aperture increments throughout each of the three phases I through III shown top to bottom.

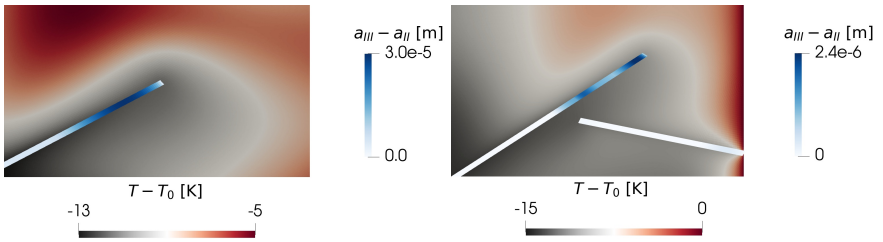

Figure 7: Example 1: Matrix temperature with superimposed fracture aperture increment in the region surrounding fracture 4 (left) and fractures 5 and 6 (right). The temperature solutions are 8/3 h and 22/3 h into phase III, at which point the cold temperature front has not yet moved past the respective regions. The subscripts on a indicate the value at the end of the corresponding phase, i.e. the values are the increments throughout phase III.

plot the errors for three primary variables on individual subdomains for the different refinement levels. The variables are displacement jumps, contact tractions and the variable related to the main driving force of the phase. The error is computed by projecting the cell-centre value of the coarse grids onto the reference grid and then computing the L^2 norm of the difference between coarse and fine solution. Errors are normalised by the number of reference cells in the subdomain multiplied by a weight k representing the magnitude of the global range of the variable in question. The weights are obtained from the boundary conditions and are $k_{\boldsymbol{u}} = ||(5 \times 10^{-4}, -2 \times 10^{-4})||$ m, $k_p = 4 \times 10^7$ Pa, k_T =15 K and $k_{\boldsymbol{\lambda}} = \mathrm{E} k_{\boldsymbol{u}}$ with E denoting Young's modulus.

In general, the expected first order convergence is observed. The exception is traction on some of the fractures (1, 2, 3 and 6). These local errors may be attributed to the geometrical challenges posed by those fractures: Fractures 1 and 2 meet in a kink, which seems to lead to relatively large errors compared to the remaining fractures as discussed by Berge et al. [52]. Fracture 3 intersects fracture 4, while the error on fracture 6 is concentrated around the leftmost tip, which is close to the neighbouring fracture 5. However, the traction solutions converge for all fractures without small transition regions and the challenging geometrical features have no discernible effect on the convergence in the other primary variables. Therefore, taken together, the presented results serve as a verification of the model.

Figure 6 shows the fracture deformation for each of the three phases, and thus demonstrates the effect of each of the three driving forces. The richness in physical processes and the complexity of coupling in the fractured THM problem is well illustrated by a phenomenon observed towards the end of phase III around fractures 5 and 6 (see Fig. 7). The role of fractures as preferential flow pathways leads to high flow rates and cooling in the region where fluid leaves fracture 5, both at the tip closest to the right boundary and in the area closest to fracture 6. This, in turn, leads to local contraction of the matrix and fracture dilation - in this particular case both through shear displacement and normal opening as seen from the final deformation state (bottom left in Fig. 6. The dilation further increasing the fracture conductivity can be expected to enhance the effect, which is also observed at the tip of fracture 4 somewhat earlier in the simulation. This phenomenon of enhanced cooling-induced aperture increase in regions where the fluid enters or leaves a fracture can be expected to be of a general character.

K	Bulk modulus	2.2×10^{10} Pa
G	Shear modulus	1.7×10^{10} Pa
μ	Viscosity	1.0×10^{-3} Pa s
$\mathcal{K}$	Permeability	1.0×10^{-15} m^2
α	Biot coefficient	0.8
F	Friction coefficient	0.5
β_s	Solid thermal expansion	8.0×10^{-6} K^{-1}
β_f	Fluid thermal expansion	4.0×10^{-4} K^{-1}
κ_s	Solid thermal conductivity	3.0 W m^{-1} K^{-1}
κ_f	Fluid thermal conductivity	0.6 W m^{-1} K^{-1}
C_s	Solid specific heat capacity	790 J K^{-1}
C_f	Fluid specific heat capacity	4.2×10^3 J K^{-1}
ϕ	Porosity	1.0×10^{-2}
c_f	Fluid compressibility	4.0×10^{-10} Pa^{-1}
ρ_f	Solid density	2.7×10^3 kg m^{-1}
$\rho_{f,0}$	Reference fluid density	1.0×10^3 kg m^{-1}

Table 1: Model parameters for the example simulations.

4.2. Example 2 - Fracture dilation models

The second example is a study of different models for fracture dilation based on simulation of the case described in Section 4.1 with two simplified aperture models. In the first simplified model, M_0, there is no coupling between shear displacement and dilation, i.e. $g = 0$ and $a = a_0 - [\![\boldsymbol{u}]\!]_n$. In the second simplified model, M_1, the aperture is related to the tangential displacement as $a = a_0 - [\![\boldsymbol{u}]\!]_n - \tan(\psi)||[\![\boldsymbol{u}]\!]_\tau||$ while g is kept constant. This represents a naive one-way coupling which accounts for the dilation effect for the apertures and fracture permeability. We emphasise that neglecting the back-coupling to normal displacement - and thus to the matrix momentum balance - makes this model inconsistent. The model of 4.1, where dilation is coupled to the displacement solution through the gap function according to Eq. (30), represents the full two-way dilation coupling and will be referred to as M_2. Thus, subscripts correspond to the number of directions of couplings accounted for by the models.

A comparison in terms of the final spatial distribution of aperture increase and tangential displacement jump on each of the closed fractures is shown in Fig. 8. As the dilation relations are irrelevant for open fractures, analysis is based on the mostly closed fractures 5 through 7. Fractures 6 and 7 clearly demonstrate how the dilation coupling in M_2 reduces tangential displacement compared to the simplified methods, as the induced normal displacement increases the normal traction on the fractures. Interestingly, the apertures displayed in Fig. 8 show overestimation for the one-way coupling due to the above-mentioned overestimation of the tangential jumps. M_0 obviously yields no shear dilation. The M_0 aperture increase of fracture 5 is thus related to the fracture being open. Note that part of this region is closed for M_2 (cf. the bottom left illustration of Fig. 6) demonstrating how inconsistency affects the results beyond the prediction of a. While the results demonstrate qualitative and consistent effects of how accurately the coupling is modelled, the magnitude of the discrepancy must be expected to depend on the problem at hand, particularly the dilation angle.

4.3. Example 3 - Hydraulic stimulation and long-term cooling of a geothermal reservoir

The third example shows hydraulic stimulation of a geothermal reservoir, followed by an injection and production phase leading to long-term reservoir cooling for the 3d geometry in Fig. 9. The domain is the box $(-750\,\mathrm{m}, 750\,\mathrm{m}) \times (-750\,\mathrm{m}, 750\,\mathrm{m}) \times (-1750\,\mathrm{m}, -250\,\mathrm{m})$ and contains three fractures, two of which intersect along a line, and two wells. The initial values are $p_0 = p_H = \rho_{f,0}\boldsymbol{g}z$ Pa, $T_0 = 350\,\mathrm{K}$ and $a_0 = 2 \times 10^{-3}$, with the positive direction of the z axis pointing upwards. After letting the system reach equilibrium under the mechanical boundary conditions representing an anisotropic background stress in phase I, we simulate a pressure stimulation phase (II) and a production and long-term cooling phase (III). In the 10 hour stimulation phase, the flow rates of the injection and production wells are 75 and $0\,\mathrm{L\,s^{-1}}$, respectively. During the 15 year production phase, both rates are $20\,\mathrm{L\,s^{-1}}$. The injection temperature is 70 K below the reservoir temperature. The wells are incorporated as source terms in the fracture cells intersected by the well paths, with upwind discretisation for the entropy equation in the production cell. Hydrostatic Dirichlet boundary conditions $p = p_H$ apply for the pressure. An anisotropic compressive background stress is imposed with the following non-zero stress tensor values

$$\sigma_{xx} = \frac{3}{4}\rho_s G z \qquad \sigma_{yy} = \frac{3}{2}\rho_s G z \qquad \sigma_{zz} = \rho_s G z, \tag{45}$$

where G denotes the gravitational constant. While the remaining parameters listed in the Table 1 are plausible for geothermal reservoirs, they do not correspond to a specific site.

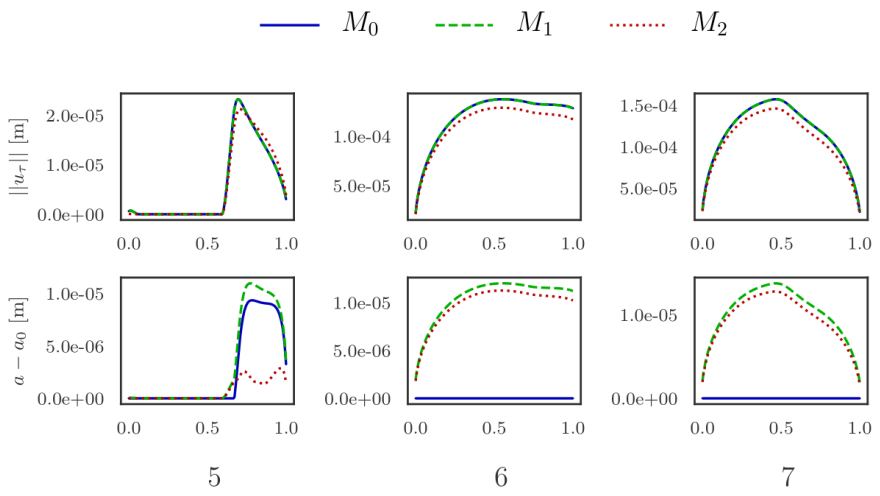

Figure 8: Example 2: Final tangential displacement jumps (top) and apertures (bottom) along three (partially) closed fractures with the three different models for the relationship between a and $[\![\boldsymbol{u}]\!]$. The cells are sorted from lowest to highest x coordinate and the fracture number is shown at the bottom.

The results are summarised through the temporal evolution of the norm of the displacement jumps on the three fractures shown in Fig. 9. Significant stimulation effects appear in both phases, with the magnitude of the jumps somewhat larger during the cooling; dynamics initiate latest on the injection fracture due to its orientation relative to the background stress. Also shown are the number of Newton iterations for each time step, which show that convergence is achieved within 30 iterations for all time steps. The spikes are related to the nonlinearity involving advective fluxes discussed in Section 3.2.

Figure 10 shows spatial plots of pressure, temperature, aperture, displacement jumps and deformation state. The plots demonstrate the model's cell-wise spatial resolution of the dynamics both in fractures and matrix. For all three phases, displacement jumps are orientated in agreement with the background stress field and are very closely aligned. The only cells in $\mathcal{O}$ are around the intersection towards in phase III. For the remaining cells, the (relatively small) normal components of the orientation arrows are due solely to shear dilation.

During phase II, aperture increments are most pronounced on fracture 2, which has no wells within fracture 2. However, its intersection with fracture 1 where injection occurs leads to a significant pressure increase. Despite negligible pressure perturbation in fracture 3, some slip is observed due to stress redistribution following the deformation of fracture 2. The location of the slip in fracture 3, away from the stress shadow of fracture 2, highlights the complex mechanical interplay between fractures in a network.

During phase III, some displacement jumps are induced in fracture 1 close to the intersection, whereas there is significant aperture increase throughout fracture 2 as a result of cooling of the surrounding rock. Along fracture 3, the deforming region is different from the previous phase, with displacement occurring in the region closest to fracture 2, where the surrounding matrix has

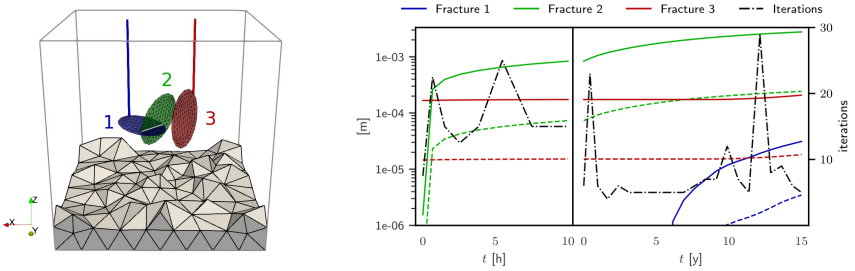

Figure 9: Example 3: Left: Fracture network geometry and well paths. The grey lines indicate the domain boundary and the white line is the 1d fracture intersection, while the injection and production wells are indicated by blue and red lines, respectively. Also shown are the 2d grid cells and some coarse 3d grid cells close to the boundary, indicating grid refinement in the region of interest. Right: L^2 norm of tangential (solid lines) and normal (dashed lines) displacement jumps on each fracture during phases II and III. The values are normalised by the number of fracture cells. The black dashed line shows the number of Newton iterations needed for convergence.

been cooled the most. This conforms with the observations in Section 4.1 of aperture increases in regions of fluid entry or departure from the fractures.

5. Conclusion

A model for fully coupled thermo-hydro-mechanical processes in porous media with deforming fractures is presented. Using the discrete-fracture-matrix approach, the matrix, the fractures and the fracture intersections are represented by subdomains of different dimensions connected by interfaces in a mixed-dimensional model. Balance equations for entropy and mass in all subdomains are coupled by fluxes on the interfaces, while the momentum balance in the matrix and traction balance and non-penetration for the fracture surfaces are coupled through interface displacements. These governing equations are supplemented with constitutive laws, including a Coulomb type friction law and a linear shear dilation relation for the fractures. For the latter, a novel model consistently coupling slip and shear dilation of the fractures with the stress response of the matrix is presented. The resulting set of model equations is discretised using cell-centred multi-point finite volume schemes and a semismooth Newton method for fracture deformation and solved fully coupled.

The model and its implementation are verified through a convergence study displaying first-order convergence for all primary variables and subdomains, except for the expected local reduction of convergence in the transition between contact regimes. An exploration of three different shear-dilation models reveals significant discrepancies, demonstrating the importance of accurate and consistent modelling of the underlying physical mechanisms and their couplings.

Investigations of 2d and 3d examples identify a mechanism by which cooling-induced dilation preferentially occurs in regions where fluid leaves or enters a fracture. The investigations also show the complexity of the process-structure interactions which may arise: in particular, how fracture deformation and resulting fracture dilation is induced by both mechanical, hydraulic and thermal driving forces. This confirms the need for models which explicitly incorporate all relevant processes and structural features as well as the resulting process-structure interactions. Furthermore, it demonstrates the proposed model's prowess in capturing such highly complex interactions and identifying their governing mechanisms. Extensions such as chemical processes

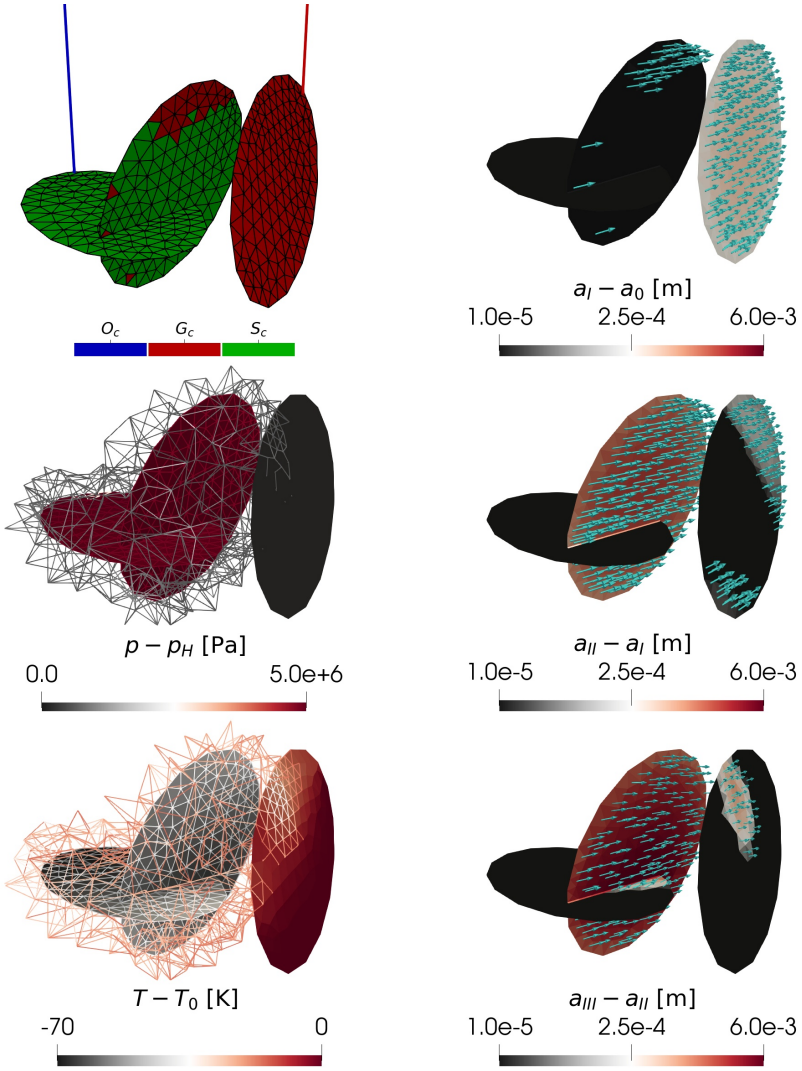

Figure 10: Example 3: Left: Deformation state according to the cumulative displacement jumps at the end of phase I (top). Perturbation from hydrostatic pressure at the end of phase II for the fractures and matrix cells satisfying $p - p_H > 5 \times 10^5$ Pa (centre). Final fracture temperature and matrix cells satisfying $T - T_0 < -15$ K (bottom). Right: Aperture increments and glyphs indicating the direction of the displacement jumps for each of the three phases top to bottom. Note that the logarithmic scale for the aperture increments is truncated at 1×10^{-5} m for visualisation purposes. The j interface of fracture 1 is on the bottom, whereas it is on the front right for fractures 2 and 3, i.e. those sides have displaced according to the arrows relative to the other side according to Eq. (24).

and more advanced friction models and dilation relations could readily be accommodated in the applied mixed-dimensional framework.

6. Acknowledgements

Funding: This work was supported by the Research Council of Norway and Equinor ASA through grant number 267908.

Bibliography

[1] R. Pine, A. Batchelor, Downward migration of shearing in jointed rock during hydraulic injections, in: International Journal of Rock Mechanics and Mining Sciences & Geomechanics Abstracts, volume 21, Elsevier, 1984, pp. 249–263.

[2] J. Rutqvist, O. Stephansson, The role of hydromechanical coupling in fractured rock engineering, Hydrogeology Journal 11 (2003) 7–40.

[3] K. Evans, H. Moriya, H. Niitsuma, R. Jones, W. Phillips, A. Genter, J. Sausse, R. Jung, R. Baria, Microseismicity and permeability enhancement of hydrogeologic structures during massive fluid injections into granite at 3 km depth at the Soultz HDR site, Geophysical Journal International 160 (2005) 388–412.

[4] K. M. Keranen, M. Weingarten, G. A. Abers, B. A. Bekins, S. Ge, Sharp increase in central Oklahoma seismicity since 2008 induced by massive wastewater injection, Science 345 (2014) 448–451.

[5] J. De Waal, A. Muntendam-Bos, J. Roest, Production induced subsidence and seismicity in the Groningen gas field - can it be managed?, Proceedings of the International Association of Hydrological Sciences 372 (2015) 129.

[6] L. Improta, L. Valoroso, D. Piccinini, C. Chiarabba, A detailed analysis of wastewater-induced seismicity in the Val d'Agri oil field (Italy), Geophysical Research Letters 42 (2015) 2682–2690.

[7] K. M. Keranen, M. Weingarten, Induced seismicity, Annual Review of Earth and Planetary Sciences (2018).

[8] L. Dorbath, N. Cuenot, A. Genter, M. Frogneux, Seismic response of the fractured and faulted granite of Soultz-sous-Forêts (France) to 5 km deep massive water injections, Geophysical Journal International 177 (2009) 653–675.

[9] W. L. Ellsworth, D. Giardini, J. Townend, S. Ge, T. Shimamoto, Triggering of the Pohang, Korea, Earthquake (m w 5.5) by Enhanced Geothermal System Stimulation, Seismological Research Letters 90 (2019) 1844–1858.

[10] M. O. Häring, U. Schanz, F. Ladner, B. C. Dyer, Characterisation of the basel 1 enhanced geothermal system, Geothermics 37 (2008) 469–495.

[11] M. Karimi-Fard, L. J. Durlofsky, K. Aziz, An Efficient Discrete-Fracture Model Applicable for General-Purpose Reservoir Simulators, SPE Journal 9 (2003) 227–236.

[12] V. Martin, J. Jaffré, J. E. Roberts, Modeling Fractures and Barriers as Interfaces for Flow in Porous Media, SIAM J. Sci. Comput. 26 (2005) 1667–1691. URL: http://scitation.aip.org/getabs/servlet/GetabsServlet?prog=normal&id=SJOCE3000026000005001667000001&idtype=cvips&gifs=yes. doi:10.1137/S1064827503429363.

[13] V. Reichenberger, H. Jakobs, P. Bastian, R. Helmig, A mixed-dimensional finite volume method for two-phase flow in fractured porous media, Advances in Water Resources 29 (2006) 1020–1036.

[14] J. M. Nordbotten, W. M. Boon, A. Fumagalli, E. Keilegavlen, Unified approach to discretization of flow in fractured porous media, Computational Geosciences 23 (2019) 225–237.

[15] J. Rutqvist, J. Birkholzer, C.-F. Tsang, Coupled reservoir–geomechanical analysis of the potential for tensile and shear failure associated with CO_2 injection in multilayered reservoir–caprock systems, International Journal of Rock Mechanics and Mining Sciences 45 (2008) 132–143.

[16] J. Rutqvist, A. P. Rinaldi, F. Cappa, G. J. Moridis, Modeling of fault reactivation and induced seismicity during hydraulic fracturing of shale-gas reservoirs, Journal of Petroleum Science and Engineering 107 (2013) 31–44.

[17] B. Wassing, J. Van Wees, P. Fokker, Coupled continuum modeling of fracture reactivation and induced seismicity during enhanced geothermal operations, Geothermics 52 (2014) 153–164.

[18] F. Cappa, J. Rutqvist, Modeling of coupled deformation and permeability evolution during fault reactivation induced by deep underground injection of CO_2, International Journal of Greenhouse Gas Control 5 (2011) 336–346.

[19] E. Ucar, I. Berre, E. Keilegavlen, Three-dimensional numerical modeling of shear stimulation of fractured reservoirs, Journal of Geophysical Research: Solid Earth 123 (2018) 3891–3908.

[20] E. Gallyamov, T. Garipov, D. Voskov, P. Van den Hoek, Discrete fracture model for simulating waterflooding processes under fracturing conditions, International Journal for Numerical and Analytical Methods in Geomechanics 42 (2018) 1445–1470.

[21] A. M. Shapiro, J. Andersson, Simulation of steady-state flow in three-dimensional fracture networks using the boundary-element method, Advances in Water Resources 8 (1985) 106–110.

[22] J. C. Long, P. Gilmour, P. A. Witherspoon, A model for steady fluid flow in random three-dimensional networks of disc-shaped fractures, Water Resources Research 21 (1985) 1105–1115.

[23] J. Willis-Richards, K. Watanabe, H. Takahashi, Progress toward a stochastic rock mechanics model of engineered geothermal systems, Journal of Geophysical Research: Solid Earth 101 (1996) 17481–17496.

[24] M. Rahman, M. Hossain, S. Rahman, A shear-dilation-based model for evaluation of hydraulically stimulated naturally fractured reservoirs, International Journal for Numerical and Analytical Methods in Geomechanics 26 (2002) 469–497.

[25] T. Kohl, T. Mégel, Predictive modeling of reservoir response to hydraulic stimulations at the European EGS site Soultz-sous-Forêts, International Journal of Rock Mechanics and Mining Sciences 44 (2007) 1118–1131.

[26] D. Bruel, Using the migration of the induced seismicity as a constraint for fractured hot dry rock reservoir modelling, International Journal of Rock Mechanics and Mining Sciences 44 (2007) 1106–1117.

[27] S. Baisch, R. Vörös, E. Rothert, H. Stang, R. Jung, R. Schellschmidt, A numerical model for fluid injection induced seismicity at Soultz-sous-Forêts, International Journal of Rock Mechanics and Mining Sciences 47 (2010) 405–413.

[28] M. W. McClure, R. N. Horne, Investigation of injection-induced seismicity using a coupled fluid flow and rate/state friction model, Geophysics 76 (2011) WC181–WC198.

[29] J. H. Norbeck, M. W. McClure, J. W. Lo, R. N. Horne, An embedded fracture modeling framework for simulation of hydraulic fracturing and shear stimulation, Computational Geosciences 20 (2016) 1–18.

[30] F. Ciardo, B. Lecampion, Effect of dilatancy on the transition from aseismic to seismic slip due to fluid injection in a fault, Journal of Geophysical Research: Solid Earth 124 (2019) 3724–3743.

[31] M. W. McClure, Generation of large postinjection-induced seismic events by backflow from dead-end faults and fractures, Geophysical Research Letters 42 (2015) 6647–6654.

[32] B. Jha, R. Juanes, Coupled multiphase flow and poromechanics: A computational model of pore pressure effects on fault slip and earthquake triggering, Water Resources Research 50 (2014) 3776–3808.

[33] T. Garipov, M. Karimi-Fard, H. Tchelepi, Discrete fracture model for coupled flow and geomechanics, Computational Geosciences 20 (2016) 149–160.

[34] E. Ucar, I. Berre, E. Keilegavlen, Postinjection normal closure of fractures as a mechanism for induced seismicity, Geophysical Research Letters 44 (2017) 9598–9606.

[35] A. Ghassemi, X. Zhou, A three-dimensional thermo-poroelastic model for fracture response to injection/extraction in enhanced geothermal systems, Geothermics 40 (2011) 39–49.

[36] S. Pandey, A. Chaudhuri, S. Kelkar, A coupled thermo-hydro-mechanical modeling of fracture aperture alteration and reservoir deformation during heat extraction from a geothermal reservoir, Geothermics 65 (2017) 17–31.

[37] S. Salimzadeh, A. Paluszny, H. M. Nick, R. W. Zimmerman, A three-dimensional coupled thermo-hydro-mechanical model for deformable fractured geothermal systems, Geothermics 71 (2018) 212 – 224. URL: http://www.sciencedirect.com/science/article/pii/S0375650517301013. doi:https://doi.org/10.1016/j.geothermics.2017.09.012.

[38] T. Garipov, M. Hui, Discrete fracture modeling approach for simulating coupled thermo-hydro-mechanical effects in fractured reservoirs, International Journal of Rock Mechanics and Mining Sciences 122 (2019) 104075. URL: http://www.sciencedirect.com/science/article/pii/S1365160918311018. doi:https://doi.org/10.1016/j.ijrmms.2019.104075.

[39] E. Keilegavlen, R. Berge, A. Fumagalli, M. Starnoni, I. Stefansson, J. Varela, I. Berre, Porepy: An open-source software for simulation of multiphysics processes in fractured porous media, arXiv preprint arXiv:1908.09869 (2019).

[40] O. Coussy, Poromechanics, Wiley, 2004. URL: https://books.google.no/books?id=Nm_RNf7paz4C.

[41] D. McTigue, Thermoelastic response of fluid-saturated porous rock, Journal of Geophysical Research: Solid Earth 91 (1986) 9533–9542.

[42] M. Hossain, M. Rahman, S. Rahman, et al., A shear dilation stimulation model for production enhancement from naturally fractured reservoirs, SPE Journal 7 (2002) 183–195.

[43] M. K. Rahman, M. M. Hossain, S. S. Rahman, A shear-dilation-based model for evaluation of hydraulically stimulated naturally fractured reservoirs, International Journal for Numerical and Analytical Methods in Geomechanics 26 (2002) 469–497. URL: https://onlinelibrary.wiley.com/doi/abs/10.1002/nag.208. doi:10.1002/nag.208. arXiv:https://onlinelibrary.wiley.com/doi/pdf/10.1002/nag.208.

[44] R. W. Zimmerman, G. S. Bodvarsson, Hydraulic conductivity of rock fractures, Transport in porous media 23 (1996) 1–30.

[45] C. Geuzaine, J.-F. Remacle, Gmsh: A 3-d finite element mesh generator with built-in pre- and post-processing facilities, International Journal for Numerical Methods in Engineering 79 (2009) 1309–1331. URL: https://onlinelibrary.wiley.com/doi/abs/10.1002/nme.2579. doi:10.1002/nme.2579. arXiv:https://onlinelibrary.wiley.com/doi/pdf/10.1002/nme.2579.

[46] I. Aavatsmark, An introduction to multipoint flux approximations for quadrilateral grids, Computational Geosciences 6 (2002) 405–432. doi:10.1023/A:1021291114475.

[47] J. M. Nordbotten, Cell-centered finite volume discretizations for deformable porous media, International Journal for Numerical Methods in Engineering 100 (2014) 399–418. URL: https://onlinelibrary.wiley.com/doi/abs/10.1002/nme.4734. doi:10.1002/nme.4734. arXiv:https://onlinelibrary.wiley.com/doi/pdf/10.1002/nme.4734.

[48] J. Nordbotten, Stable cell-centered finite volume discretization for biot equations, SIAM Journal on Numerical Analysis 54 (2016) 942–968. doi:10.1137/15M1014280.

[49] J. Nordbotten, E. Keilegavlen, An introduction to multi-point flux (mpfa) and stress (mpsa) finite volume methods for thermo-poroelasticity, arXiv preprint arXiv:2001.01990 (2020).

[50] S. Hüeber, G. Stadler, B. I. Wohlmuth, A primal-dual active set algorithm for three-dimensional contact problems with coulomb friction, SIAM Journal on Scientific Computing 30 (2008) 572–596.

[51] B. Wohlmuth, Variationally consistent discretization schemes and numerical algorithms for contact problems, Acta Numerica 20 (2011) 569–734. doi:10.1017/S0962492911000079.

[52] R. L. Berge, I. Berre, E. Keilegavlen, J. M. Nordbotten, B. Wohlmuth, Finite volume discretization for poroelastic media with fractures modeled by contact mechanics, International Journal for Numerical Methods in Engineering 121 (2020) 644–663. URL: https://onlinelibrary.wiley.com/doi/abs/10.1002/nme.6238. doi:10.1002/nme.6238. arXiv:https://onlinelibrary.wiley.com/doi/pdf/10.1002/nme.6238.

[53] Run scripts for porepy simulations, https://github.com/IvarStefansson/A-fully-coupled-numerical-model-of-thermo-hydro-mechanical-processes-and-fracture-contact-mechanics-, 2020.

Paper F

Fault slip in hydraulic stimulation of geothermal reservoirs: governing mechanisms and process-structure interaction

Inga Berre, Ivar Stefansson, Eirik Keilegavlen

F

The Leading Edge
DOI: 10.1190/tle39120893.1

Paper G

Numerical modelling of convection-driven cooling, deformation and fracturing of thermo-poroelastic media

Ivar Stefansson, Eirik Keilegavlen, Sæunn Halldórsdóttir, Inga Berre

G

In preparation for Transport in Porous Media
Preprint: arXiv:2012.06493 [math.NA]

Numerical modelling of convection-driven cooling, deformation and fracturing of thermo-poroelastic media

Ivar Stefansson Eirik Keilegavlen Sæunn Halldórsdóttir
Inga Berre

Abstract

Convection-driven cooling in porous media influences thermo-poromechanical stresses, thereby causing deformation. These processes are strongly influenced by the presence of fractures, which dominate flow and heat transfer. At the same time, the fractures deform and propagate in response to changes in the stress state. Mathematically, the model governing the physics is tightly coupled and must account for the strong discontinuities introduced by the fractures. Over the last decade, and motivated by a number of porous media applications, research into such coupled models has advanced modelling of processes in porous media substantially.

Building on this effort, this work presents a novel model that couples flow, heat transfer, deformation, and propagation of fractures with flow, heat transfer, and thermo-poroelasticity in the matrix. The model is based on explicit representation of fractures in the porous medium, and discretised using multi-point finite volume methods. Frictional contact and non-penetration conditions for the fractures are handled through active set methods, while a propagation criterion based on stress intensity factors governs fracture extension. Considering both forced and natural convection processes, the numerical results show the intricate nature of thermo-poromechanical fracture deformation and propagation.

1 Introduction

For a porous medium, possibly containing fractures, the interplay between flow, thermal transport, and deformation can be strong. In particular, cooling of the medium induces thermal stress that can lead to deformation and fracturing. Furthermore, fractures deform and propagate as a result of the coupled dynamics. The result is coupled thermo-hydro-mechanical (THM) processes in the intact porous medium, interacting with flow and thermal transport in fractures as well as fracture deformation and propagation. Such coupled process-structure interaction is characteristic for a wide range of natural and engineered processes in natural and manufactured materials. For example, the structural and functional

performance of concrete structures, like dams, bridges, nuclear and liquefied natural gas containers, and cement sheaths of subsurface well bore constructions, are affected by the time evolution of their properties under variable THM loads [5, 14, 44, 18, 19, 45]. In the subsurface, THM processes interact with deformation and propagation of fractures in fluid injection operations [58, 32, 64]. The coupled dynamics is also hypothesised to be crucial in heat transfer from the deep roots of geothermal systems by deepening natural convection through evolving fractures [46, 13, 11, 12]. Common to all these applications is that tight coupling in the dynamics limits the knowledge which can be gained from analysis of individual processes and mechanisms in isolation. This motivates development of simulation models that acknowledge the coupled nature of the physics.

Since its foundation by Biot [10], the theory of poroelasticity has successfully been applied to model coupled hydro-mechanical processes. The extention to thermo-poroelasticity [23] is also widely applied, including in geomechanics [56]. More recently, models accounting for discontinuities in the form of fractures in poroelastic and thermo-poroelastic media have been developed. Typically, the development has focused either on deformation of preexisting fractures or the mechanical fracturing of the materials. The models can be distinguished based on whether fractures are represented explicitly as discrete objects embedded in the porous medium, or represented as part of the porous medium itself. The latter incorporate the effect of the extent to which the material is fractured by use of smeared or distributed representations. Such models include phase-field and damage approaches for fracture [16] and continuum and multi-continuum approaches for flow models [9].

Approaches based on explicit representation of the fractures can further be distinguished by how the fractures are represented in discretisation, specifically on whether a conforming or non-conforming representation of the fractures is used in the grid [9]. Non-conforming methods represent the fracture through an enriched representation. For poromechanics, combinations of the embedded discrete fracture method, extended finite element methods and/or embedded finite element methods have been applied [52, 24, 35]. Such non-conforming approaches have also been extended to include tensile fracture propagation based on extended finite element [42] and embedded discrete fracture methods [27]. Conforming methods use a representation where the fractures coincide with matrix faces. Considering fractures that have a negligible aperture compared to the modelled domain, this representation can be combined with an approach where fractures are modelled as lower-dimensional structures [47, 39] and discretised with elements of zero thickness [43, 15, 28, 8]. For poroelastic media with fractures, this allows for the application of standard finite element [55], finite volume [62, 7] and combined finite element/finite volume schemes [34, 57, 33], more recently also including fracture contact mechanics [34, 31, 30] and tensile fracture propagation [57, 55]. Thermal effects on fracture deformation and propagation in poroelastic media are less studied, although some recent studies model deformation of existing fractures in thermo-poroelastic media [54, 60, 33].

Motivated by the development of increasingly sophisticated THM models for

fractured porous media, our goal in the present paper is to extend numerical modeling of THM to also incorporate fracture propagation, and thereby contribute to bridge the gap between fracture mechanics models and coupled THM models for porous media. Specifically, we consider mathematical and numerical modelling of fracture deformation and propagation resulting from coupled THM-processes. Our focus is on convection-driven cooling in the subsurface, where forced or natural fluid convection induces thermo-poromechanical stress changes leading to fracture deformation and propagation. The dynamics is characterised by tight coupling between physical processes and strong interaction between the physical processes and the (evolving) geometry of the fracture network. Accordingly, our model and simulation approach is designed to faithfully represent these couplings, including fracture deformation and propagation.

The fractured thermo-poroelastic medium is represented using a discrete fracture-matrix model, where fractures are represented as lower-dimensional discontinuities in an otherwise continuous thermo-poroelastic medium. Deformation of existing fractures is modelled through contact mechanics relations based on a Coulomb friction criterion for slip along the fractures and a non-penetration condition [37, 7]. This is combined with a simple criterion for fracture propagation based on the mode I stress intensity factor, which we compute directly from the displacement jump in the vicinity of the fracture tip using a variant [48] of the displacement correlation method [21]. To adjust the grid to an arbitrary fracture propagation path is highly technical [51, 25], and we instead make the assumption that fractures propagate along existing faces in the matrix grid. This constrains the numerical representation of an evolving fracture and makes it difficult to preserve reasonable fracture geometries for general propagation scenarios, in particular for three-dimensional problems. We therefore further limit ourselves to tensile fracturing, where the possible propagation path is easy to predict and the grid can be constructed to accommodate the propagation.

We discretise the model using a control volume framework for fracture contact mechanics in thermo-poroelastic media [60]. The control volume approach builds on a combination of the multi-point stress approximation method for Biot poroelasticity [49, 41] with the multi-point flux approximation method for flow [2]. This combination is previously applied for numerical modelling of fractured poroelastic media [62] with a simplified model for deformation along fractures. The fracture contact mechanics builds on work by Berge et al. [7], who formulated the contact conditions on the fracture using Lagrange multipliers representing the contact tractions [63]. Using this approach, the variational inequality representing the contact problem can be rewritten using complementary functions, and the resulting system of equations solved by a semi-smooth Newton method [37, 7]. Our model is implemented in the open-source simulator PorePy [40], which is designed for multiphysics problems in fractured porous media.

We assess the reliability of our simulation tool by tests that probe the approximations of both the onset of fracturing and the speed of fracture propagation. We then present two application-related simulations that both involve fracture

propagation driven by convective cooling. The cases include respectively forced convection during production of geothermal energy and natural convection in vertical fractures in the presence of high thermal gradients. Taken together, the results show the importance of developing simulation tools that can accurately represent the tight couplings in THM processes, and also deal with deformation and propagation of fractures.

The paper is structured as follows. Section 2 presents the governing model equations for poroelastic media with deforming and propagating fractures. The discretisation schemes and numerical solution strategy is presented in Section 3. Section 4 presents simulation results, before concluding remarks are given in Section 5.

2 Governing equations

The conceptual model is based on explicit and conforming representation of fractures in the porous medium. Two modes of fracture deformation are considered: Deformation with fixed transverse extension governed by contact mechanics relations and deformation through irreversible fracture propagation. We also impose conservation of mass and energy in matrix and fractures and momentum balance in the matrix.

2.1 Geometrical representation of fractured porous media

The model and governing equations are posed in a mixed-dimensional framework arising from considering fractures as lower-dimensional objects. Hence, in a three-dimensional domain, fractures are represented as two-dimensional surfaces, and in a two-dimansional domain, they are one-dimensional lines. In a D-dimensional domain, we denote the matrix subdomain by Ω_h and fractures are represented by subdomains Ω_l of dimension $D-1$. The matrix and fractures are connected by interfaces denoted by Γ_j, with the subscript pair j, k used to indicate the two interfaces on either side of a fracture, see Fig. 1. The boundary of Ω_i is denoted by $\partial\Omega_i$, and the internal part of it corresponding to Γ_j is $\partial_j\Omega_i$.

We also use subscripts i, h and l to identify the domain of the primary variables, which are displacement, pressure, temperature, contact traction ($\boldsymbol{u}$, p, T and $\boldsymbol{\lambda}$). Similarly, subscript j denotes the four interface variables defined in Sections 2.2 and 2.6. The subscripts are suppressed when context allows, as are the subscripts f and s denoting fluid and solid, respectively.

To model fracture deformation, it is necessary to decompose a vector into its normal and tangential components relative to a fracture. The fracture normal is defined to equal the outwards normal $\boldsymbol{n}_h$ on the j side, i.e. $\boldsymbol{n}_l = \boldsymbol{n}_h|_{\partial_j\Omega_h}$. A vector $\boldsymbol{\iota}_l$ may now be decomposed as

$$\iota_n = \boldsymbol{\iota}_l \cdot \boldsymbol{n}_l \text{ and } \boldsymbol{\iota}_\tau = \boldsymbol{\iota}_l - i_n \boldsymbol{n}_l, \tag{1}$$

where subscripts n and τ denote the normal and tangential direction, respectively.

2.2 Contact mechanics for fracture slip and opening

The contact mechanics relations are a traction balance between the two fracture surfaces and a nonpenetration condition, complemented by a Coulomb friction law governing the relative displacement when the surfaces are in contact. These relations are formulated in the displacement jump $[\![\boldsymbol{u}]\!]$ and the contact traction $\boldsymbol{\lambda}_l$. The higher-dimensional THM traction, $\sigma_h \cdot \boldsymbol{n}_h$, is balanced by the contact traction and the fracture pressure on the two interfaces:

$$\begin{aligned} (\boldsymbol{\lambda}_l - p_l \mathbf{I} \cdot \boldsymbol{n}_l)|_{\Omega_l \cup \Gamma_j} &= \sigma_h \cdot \boldsymbol{n}_h|_{\partial\Omega_h \cup \Gamma_j}, \\ (\boldsymbol{\lambda}_l - p_l \mathbf{I} \cdot \boldsymbol{n}_l)|_{\Omega_l \cup \Gamma_k} &= -\sigma_h \cdot \boldsymbol{n}_h|_{\partial\Omega_h \cup \Gamma_k}. \end{aligned} \tag{2}$$

Here the notation indicating that the variable is taken at the interface $Gamma_j$ or Γ_k should be interpreted as the extension and projection of this variable to the respecitve interface. The displacement jump over the fracture is defined as

$$[\![\boldsymbol{u}_l]\!] = \boldsymbol{u}_k - \boldsymbol{u}_j, \tag{3}$$

with $\boldsymbol{u}_j$ and $\boldsymbol{u}_k$ denoting displacement at Γ_j and Γ_k, cf. Fig. 1. The gap function g is defined as the normal distance between the fracture surfaces when these are in mechanical contact. Following Stefansson [60], we set

$$g = \tan(\psi)||[\![\boldsymbol{u}]\!]_\tau||, \tag{4}$$

with ψ denoting the dilation angle [6], thus accounting for shear dilation of the fracture resulting from tangential displacement $[\![\boldsymbol{u}]\!]_\tau$ of the rough fracture surfaces.

Given that fracture surface interpenetration and positive normal contact traction are prohibited, the following conditions have to be fulfilled:

$$\begin{aligned} [\![\boldsymbol{u}]\!]_n - g &\geq 0, \\ \lambda_n([\![\boldsymbol{u}]\!]_n - g) &= 0, \\ \lambda_n &\leq 0. \end{aligned} \tag{5}$$

Hence, when a fracture is mechanically open and there is no mechanical contact across the fracture, the normal contact force, λ_n, is zero.

The friction law is imposed by enforcing

$$\begin{aligned} ||\boldsymbol{\lambda}_\tau|| &\leq -F\lambda_n, \\ ||\boldsymbol{\lambda}_\tau|| &< -F\lambda_n \rightarrow [\![\dot{\boldsymbol{u}}]\!]_\tau = 0, \\ ||\boldsymbol{\lambda}_\tau|| &= -F\lambda_n \rightarrow \exists\, \zeta \in \mathbb{R}^+ : [\![\dot{\boldsymbol{u}}]\!]_\tau = \zeta \boldsymbol{\lambda}_\tau, \end{aligned} \tag{6}$$

where F and $[\![\dot{\boldsymbol{u}}]\!]_\tau$ denote the friction coefficient and the tangential (shear) displacement increment, respectively. For simplicity, we consider a constant coefficient of friction in this work.

2.3 Fracture propagation

Fracture propagation occurs when the potential energy released by the extension exceeds the energy required to separate the fracture surfaces by breaking atomic

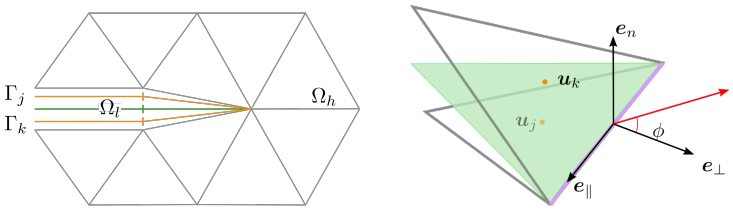

Figure 1: Left: A two-dimensional matrix domain Ω_h and a one-dimensional fracture Ω_l connected by interfaces, all gridded in a conforming way. Right: Local coordinate system at tip of a two-dimensional fracture. The face of the tip cell is shown in purple and the interface cell centres on the j and k sides are shown as orange dots. The red propagation vector forms an angle ϕ with $\boldsymbol{e}_\perp$. The separation between fracture, interfaces and (to the left) matrix faces is for visualisation purposes only, in the model, all coincide geometrically.

bonds [36]. Using concepts of linear elastic fracture mechanics, we evaluate propagation based on computation of stress intensity factors (SIFs). The SIFs are computed directly from the displacement jump in the vicinity of the fracture tip using the variant of the displacement correlation method [48].

Referring to Fig. 1, the local geometry at a fracture tip is described using a coordinate system given by the orthogonal basis vectors $\boldsymbol{e}_\perp$, $\boldsymbol{e}_n$ and $\boldsymbol{e}_\parallel$ (or $\boldsymbol{e}_\perp$ and $\boldsymbol{e}_n$ if $D = 2$). We set $\boldsymbol{e}_n = \boldsymbol{n}_l$, and the tangential ($\tau$) vectors $\boldsymbol{e}_\perp$ and $\boldsymbol{e}_\parallel$ are respectively perpendicular and parallel to $\partial\Omega_l$ at $\partial\Omega_l$ (see Fig. 1). By use of the components of the displacement jump in the local coordinate system, the displacement correlation method gives the three SIFs

$$\begin{aligned} K_I &= \sqrt{\frac{2\pi}{R_d}}\left(\frac{\mu}{\kappa+1}[\![\boldsymbol{u}]\!]_n\right), \\ K_{II} &= \sqrt{\frac{2\pi}{R_d}}\left(\frac{\mu}{\kappa+1}[\![\boldsymbol{u}]\!]_\perp\right), \\ K_{III} &= \sqrt{\frac{2\pi}{R_d}}\left(\frac{\mu}{4}[\![\boldsymbol{u}]\!]_\parallel\right). \end{aligned} \tag{7}$$

Here, μ denotes the shear modulus and $\kappa = 3 - 4\nu$ the Kolosov constant, with ν being the Poisson ratio. R_d is the distance from the fracture tip to the point at which the displacement jump is evaluated. The three stress intensity factors are related to tensile (K_I), shear (K_{II}) and torsional (K_{III}) forces.

As stated in the introduction, we limit ourselves to tensile fracture in this work, and ignore contributions from (K_{II}) and (K_{III}). With this assumption, a tip propagates if the computed mode I factor exceeds a critical value,

$$K_I \geq K_{Ic}, \tag{8}$$

and the propagation angle ϕ illustrated in Fig. 1 is zero. Criteria for more sophisticated mixed-mode propagation, which can be highly relevant for subsurface applications, are reviewed by Richard et al. [53].

2.4 Fracture mass and energy balance

The thickness of a dimensionally reduced fracture is represented by the aperture, which changes as the domain deforms according to

$$a = a_{res} + [\![\boldsymbol{u}]\!]_n, \tag{9}$$

with a_{res} denoting the residual hydraulic aperture in the undeformed state representing the effect of small-scale roughness of the two fracture surfaces. The tangential fracture permeability $\mathcal{K}_l$ is chosen to depend on aperture by the nonlinear relationship $\mathcal{K}_l = a^2/12$, which corresponds to setting the hydraulic aperture of the fracture equal to a [65].

On the assumption that the fractures are completely filled with fluid, the parameters of this subsection equal that of the fluid. We assume single-phase flow according to Darcy's law:

$$\boldsymbol{v} = -\frac{\mathcal{K}}{\mu}\left(\nabla p - \rho \boldsymbol{g}\right), \tag{10}$$

where μ, ρ and $\boldsymbol{g}$ denote viscosity, density and the gravity acceleration. The total heat flux may be split into continuum scale heat diffusion modelled by Fourier's law and advection along the fluid flow field:

$$\begin{aligned} \boldsymbol{q} &= -\kappa \nabla T, \\ \boldsymbol{w} &= \rho C T \boldsymbol{v}, \end{aligned} \tag{11}$$

where κ and C denote thermal conductivity and heat capacity, respectively.

Following Stefansson et al. [60] (see also Brun et al. [20] and Coussy [23]), balance of mass for a fracture Ω_l reads

$$a\left(c\frac{\partial p}{\partial t} - \beta \frac{\partial T}{\partial t}\right) + \frac{\partial a}{\partial t} - \nabla \cdot \left(a\frac{\mathcal{K}}{\mu}\left(\nabla p - \rho \boldsymbol{g}\right)\right) - \sum_{j \in \hat{S}_l} v_j = a q_p, \tag{12}$$

with c, β and q_p denoting compressibility, thermal expansion coefficient and a fluid source or sink term.

Next, assuming local thermal equilibrium between fluid and solid, neglecting viscous dissipation and linearising [60], the energy balance is

$$\begin{aligned} &\frac{C\rho}{T_0}(T - T_0)\frac{\partial a}{\partial t} + \frac{C\rho}{T_0} a \frac{\partial T}{\partial t} - \beta a \frac{\partial p}{\partial t} + \nabla \cdot \left[a\left(\frac{C\rho}{T_0}(T - T_0)\boldsymbol{v} - \frac{\kappa}{T_0}\nabla T\right)\right] \\ &- \sum_{j \in \hat{S}_l} \frac{q_j}{T_0} + \frac{w_j}{T_0} = a q_T, \end{aligned} \tag{13}$$

where we assume thermal sources and sinks to satisfy $aq_T = aq_p \frac{C\rho}{T_0}(T - T_0)$ and T_0 denotes a reference temperature. In Eqs. (12) and (13) the last terms on the right hand sides represents the fluxes from matrix to fractures, which are defined in Section 2.6.

In deriving these equations, the following equations of state are assumed [23] for density

$$\rho = \rho_0 \exp[c(p - p_0) - \beta(T - T_0)] \tag{14}$$

and entropy

$$s - s_0 = -\beta \frac{p - p_0}{\rho} + \frac{C}{T_0}(T - T_0). \tag{15}$$

2.5 Matrix thermo-poroelasticity, energy and mass balance

The following section presents the balance equations and constitutive relations for the matrix problem. The model resembles that of the previous section, with the addition of a momentum balance equation for the thermo-poroelastic medium, yielding three balance equations for Ω_h. For details on the derivations of the equations, we again refer to Coussy [23] and Brun et al. [20]. We first define the following effective parameters [22], arising through the assumption of local thermal equilibrium:

$$\begin{aligned} \kappa_e &= \phi\kappa_f + (1 - \phi)\kappa_s, \\ (\rho C)_e &= \phi\rho_f C_f + (1 - \phi)\rho_s C_s, \\ \beta_e &= \phi\beta_f + (\alpha - \phi)\beta_s. \end{aligned} \tag{16}$$

ϕ and α denote porosity and the Biot coefficient, respectively.

Neglecting inertial terms, the momentum balance is

$$\nabla \cdot \sigma = \boldsymbol{q_u}, \tag{17}$$

with $\boldsymbol{q_u}$ denoting body forces and the linearly thermo-poroelastic stress tensor related to the primary variables by an extended Hooke's law

$$\sigma - \sigma_0 = \frac{\mathbf{D}}{2}(\nabla \boldsymbol{u} + \nabla \boldsymbol{u}^T) - \alpha(p - p_0)\mathbf{I} - \beta_e K(T - T_0)\mathbf{I}. \tag{18}$$

The mass balance equation reads

$$\left(\phi c + \frac{\alpha - \phi}{K}\right)\frac{\partial p}{\partial t} + \alpha \frac{\partial(\nabla \cdot \boldsymbol{u})}{\partial t} - \beta_f \frac{\partial T}{\partial t} + \nabla \cdot \left(\frac{\mathcal{K}}{\mu}(\nabla p - \rho \boldsymbol{g})\right) = q_p, \tag{19}$$

while the energy balance is

$$\frac{(\rho C)_e}{T_0}\frac{\partial T}{\partial t} + \beta_s K \frac{\partial(\nabla \cdot \boldsymbol{u})}{\partial t} - \beta_f \frac{\partial p}{\partial t} + \nabla \cdot \left(\frac{C\rho}{T_0}(T - T_0)\boldsymbol{v} - \frac{\kappa}{T_0}\nabla T\right) = q_T. \tag{20}$$

On $\Omega_h \cup \Gamma_j$, the following internal boundary conditions ensure coupling from Ω_h to the interface variables on Γ_j:

$$\begin{aligned} \boldsymbol{u}_h &= \boldsymbol{u}_j, \\ \boldsymbol{v}_h \cdot \boldsymbol{n}_h &= v_j, \\ \boldsymbol{q}_h \cdot \boldsymbol{n}_h &= q_j, \\ \boldsymbol{w}_h \cdot \boldsymbol{n}_h &= w_j. \end{aligned} \tag{21}$$

The conservation equations are complemented by appropriate boundary conditions on the domain bondary. This applies to both the matrix and fracture domains.

2.6 Interface fluxes between fractures and matrix

Interface flux relations close the mixed-dimensional system of mass and energy balance equations [47, 38]:

$$\begin{aligned} v_j &= -\frac{\mathcal{K}_j}{\mu}\left(\frac{2}{a_l}\left(p_l|_{\Omega_l \cup \Gamma_j} - p_h|_{\partial\Omega_h \cup \Gamma_j}\right) - \rho_l \boldsymbol{g} \cdot \boldsymbol{n}_h\right), \\ q_j &= -\kappa_j \frac{2}{a_l}(T_l|_{\Omega_l \cup \Gamma_j} - T_h|_{\partial\Omega_h \cup \Gamma_j}), \\ w_j &= \begin{cases} v_j \rho_h C_h T_h & \text{if } v_j > 0 \\ v_j \rho_l C_l T_l & \text{if } v_j \leq 0 \end{cases}. \end{aligned} \tag{22}$$

We set the normal permeability and thermal conductivity equal to their tangential counterparts, i.e. $\mathcal{K}_j = \mathcal{K}_l$ and $\kappa_j = \kappa_l$.

3 Discretisation and solution strategy

Discretisation of the governing equations entails devising discrete representation of the conservation equations and of the contact mechanics relations on existing fractures. Moreover, when the propagation criteria are met, the fracture geometry must be modified and the discretisations updated accordingly.

We make the following assumptions on the computational grid: Grids for the subdomains Ω_h and Ω_l and the interface Γ_j are constructed so that faces on $\partial_j \Omega_i$ match with cells in Γ_j and Ω_l. We make no assumptions on the cell types; for the simulations presented in Section 4 we mainly use Cartesian grids as these are most easily fit to a known, straight propagation path, but also consider simplex cells for one simulation.

3.1 Spatial discretisation

Pressure and temperature are represented by their cell centre values in Ω_h and Ω_l, as is the displacement in Ω_h and contact force in Ω_l. The discrete primary variables on Γ are displacements, mass flux and advective and diffusive heat fluxes.

3.1.1 Contact mechanics

The non-linear contact mechanics problem is represented by an active set approach implemented as a semi-smooth Newton method following [37, 7]. The treatment of Eqs. (5) and (6) depends on whether the previous iterates were in an open, sticking or gliding state, with the states evaluated cell-wise in Ω_l. Equation (2) is discretised by relating the cell centre pressures and contact force in Ω_l to the discrete traction on Γ.

3.1.2 Discretisation of balance equations

For Ω_h, the stress term in (17) and the diffusive fluxes in (19) and (20) are all discretised with a family of finite volume multi-point approximations termed MPxA [2, 49, 50]. The methods construct discrete representations of the constitutive relations, Hook's, Darcy's and Fourier's law, in terms of the cell centre variables. These relations are used to enforce conservation of THM traction, mass and (diffusive) heat flux over the cell faces. For faces on the fracture surfaces, the discrete traction enters the contact mechanics discretisation described above. The full heat flux is given by the sum of the discrete Fourier's law and the advective flux, where the latter is discretised by a single-point upstream method. For further information on the MPxA methods, we refer to [50].

In Ω_l, Eqs. (12) and (13) are discretised analogously to the corresponding terms in Ω_h. Finally, fluxes over Γ are computed from discrete versions of Eqs. (22).

3.1.3 Solution of non-linear system

The discretised system of equations is solved by Newton's method, with the terms from the contact conditions handled by a semi-smooth approach following [37, 7]. The termination criterion for the Newton iterations considers the residuals and updates of each of the primary variables $\boldsymbol{u}_h$, $\boldsymbol{u}_j$, p and T. Within each non-linear iteration, the linearised system is solved using a direct sparse solver [26]. While simple, this approach is memory intensive and puts practical constraints on mesh resolution, in particular for three-dimensional problems. A more scalable method would involve iterative solvers with block preconditioners for the THM components of the linear system [17], with a tailored treatment of the contact conditions [29].

3.2 Solution algorithm

The temporal derivatives are discretised by a backward Euler scheme, and the THM contact mechanics problem is solved monolithically, using implicit in time evaluation of all spatial derivatives. When the non-linear solver has converged, we proceed to fracture propagation evaluation.

Stress intensity factors and the fracture propagation criterion are evaluated for each fracture tip faces using Eqs. (7) and (8). The displacement jump is evaluated at the neighbouring cell of the tip face, i.e. R_d is the distance between

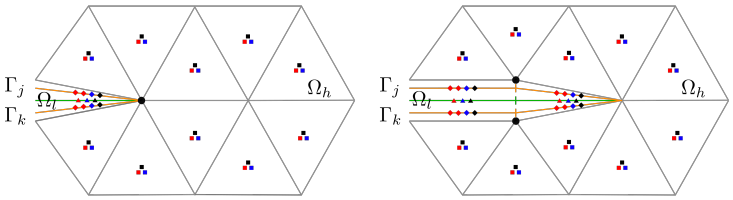

Figure 2: Example grid and unknowns before (left) and after (right) propagation. Unknown shapes reflect the subdomain or interface where they are defined, whereas the colours red, blue and black correspond to heat, mass and deformation, respectively. One vertex (black circle) and the face along which propagation occurs are duplicated as part of the geometry update. The different types of domains are separated for illustration purposes. Figure adapted from [60].

the centre of the tip face and the cell. The fracture is restricted to grow along faces of the matrix grid, no computation of the propagation length is performed. The geometrical update for each identified face now entails i) duplicating the face for the matrix grid, ii) adding a cell in the fracture grid and iii) adding one cell for each of the two interfaces. The three new cells all coincide geometrically with the chosen face, see Fig. 2. Once new cells and faces have been added, connectivity information is updated both within subdomains and between the subdomains and the interface.

Variables are initialised in the new cells using the reference values p_0 and T_0, and new apertures are set to a_{res}. This in effect adds mass to the system, cf. Eq. (14). To compensate, we prescribe an additional term on the right hand side of equation (12) equal to $-a_{res}/dt$ in newly formed fracture cells the subsequent time step, with dt denoting time step size. Since Eq. (13) is derived by considering $s - s_0$, Eq. (15) implies that no right-hand side term arises with the chosen initialisation values.

Before the simulation proceeds to the next time step, all terms are rediscretised to account for modifications of the grids. This can be done locally, i.e. only for the faces and cells where the discretisation is affected by the grid update.

4 Simulation results

The results presented in this section serve to first verify the computational approach, and then to show application to two subsurface cases involving THM processes and fracture propagation. The PorePy toolbox [40, 1] was used for all simulations and run scripts for geometry and parameter setup etc. are available on GitHub [61]. All parameters not specified in the text are listed in Table 1.

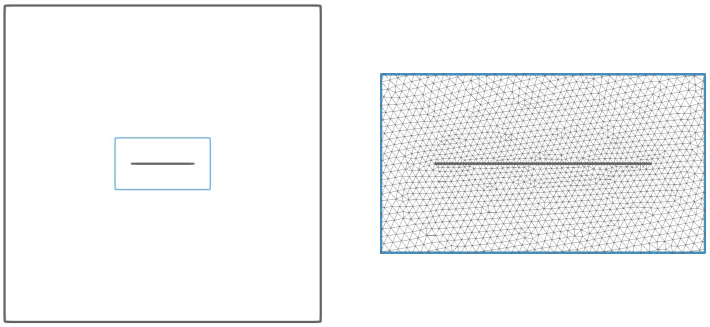

Figure 3: Example 1: Domain geometry (left) and close-up around the fracture showing the matrix mesh for the mesh with $h = 0.25$ (right). The blue box shows the location of the close-up.

4.1 Verification

The verification of the computational approach entails first a test of the numerical stress intensity factors and next a convergence test of the fracture propagation speed.

4.1.1 Example 1: Stress intensity factors

To verify the SIF computation, we consider an analytical solution, first derived by Sneddon [59], for a single crack in an infinite medium with uniform internal pressure on the fracture surfaces. Boundary conditions for the finite simulation domain are computed using the boundary element method following Keilegavlen et al. [40], who also presents a thorough convergence study for the aperture using PorePy. Herein, we compare the SIFs as computed by the displacement correlation method to the analytical solution

$$\begin{aligned} K_{I,an} &= p_f \sqrt{l\pi}, \\ K_{II,an} &= 0. \end{aligned} \tag{23}$$

Here, p_f denotes the internal pressure on the fracture and l denotes fracture length. We use a square domain of side length 50 m, $l = 10$ m and $p_f = 1 \times 10^{-4}$ Pa. We consider a sequence of four grids, the finest of which is shown in Fig. 3. To probe the method for different material parameters, we also use four different Poisson ratios. Based on displacement solutions on each

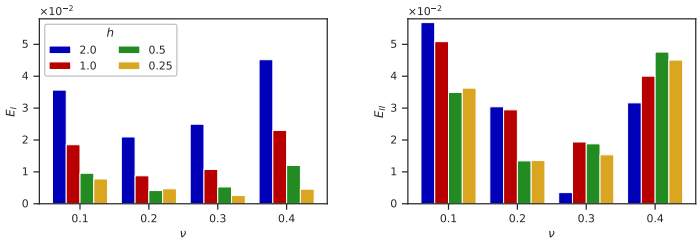

Figure 4: Errors for K_I (left) and K_{II} (right) computed according to Eq. (24) for different values of the Poisson ratio ν and different mesh sizes h.

grid, SIFs are estimated and the normalised L^2 type errors are computed as

$$E_I = \frac{\left[\sum_{j=1}^{2} \left(K_{I,j} - K_{I,an}\right)^2\right]^{1/2}}{2K_{I,an}}, \qquad E_{II} = \frac{\left[\sum_{j=1}^{2} \left(K_{II,j} - K_{II,an}\right)^2\right]^{1/2}}{2K_{I,an}}, \tag{24}$$

with the j index running over the two fracture tips. The piecewise linear displacement representation of the MPSA discretisation does not capture the stress singularity at the fracture tips. Since the SIFs are computed from $[\![\boldsymbol{u}]\!]$ in these very tip cells, the method does not converge with mesh refinement. Rather, the results presented in Fig. 4 demonstrate robustness with respect to mesh size and the Poisson ratio ν. While we do not consider K_{II} in the subsequent simulations, we also present results demonstrating that the method indeed predicts tensile stresses (i.e. $K_{II} \ll K_I$) for this purely tensile problem.

The results of this test indicate that the MPSA solution can be used to estimate K_I in tensile problems, and thus form the basis of fracture growth evaluation.

4.1.2 Example 2: Propagation speed

We now consider a test case designed to evaluate the simulated propagation speed of a fracture in a tensile regime of stable propagation. The unit square domain contains two horizontal fractures Ω_2 and Ω_3 extending 1/4 from the left and right boundary, respectively, see Fig. 5. The boundary conditions for fluid and heat are no-flow in the matrix and Dirichlet for the fractures, with zero values on the right and $p = 5\,\text{MPa}$ and $T = -50\,\text{K}$ on the left. Thus, cold fluid flows from left to right, entering the matrix at the right end of Ω_2. The domain is mechanically fixed at the top and bottom and zero traction is imposed on

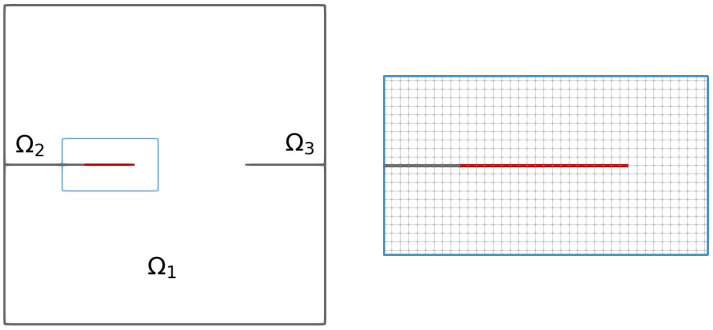

Figure 5: Left: Domain geometry used in Example 2. The grey lines indicate initial geometry, whereas the red line indicates the extension at the end of simulation. The blue box shows the location of the close-up to the right. Right: Close-up around the fracture showing the matrix mesh for refinement $h = 1/128$.

the left and right boundaries. The forces driving propagation are the elevated pressure inside Ω_2 and cooling of the surrounding matrix.

We use four temporal refinement levels and three spatial refinement levels in addition to a highly refined reference solution. The finest (non-reference) mesh and the final fracture geometry are illustrated in Fig. 5.

Figure 6 shows fracture size plotted against time for all refinement combinations. With one exception discussed below, the results group according to spatial resolution. While the propagation speed is fairly constant across all mesh sizes, propagation onset occurs earlier for the coarser meshes. We attribute this offset to the SIFs being evaluated on the basis of $[\![\boldsymbol{u}]\!]$ at the centre of the fracture tip cell. The location of this cell centre is closer to the boundary for the coarser meshes, implying shorter travel time for the cooling front. As expected, the plot indicates convergence with mesh refinement.

The outlier is the smallest mesh size combined with the largest time step, for which the propagation speed is notably lower. The propagation speed is simply not resolved by the spatio-temporal discretisation, i.e. the propagation speed exceeds h/dt. In other words: Given a spatial resolution, an upper bound on the time step must be honoured in the explicit type of propagation solution algorithm used herein.

4.2 Applications

We present two simulations that involve THM processes coupled with fracture propagation. The first case resembles geothermal energy production, with convection forced by fluid injection and production. The second case involves natural convection that takes place mainly inside fractures. In both cases, convection

Table 1: Parameters for the simulation examples. For Example 1, only mechanical parameters are relevant.

Parameter	Symbol	Examples	Value	Units
Biot coefficient	α	2-4	0.8	–
Friction coefficient	F	2-4	0.8	–
Dilation angle	ψ	2-4	3.0	$^\circ$
Fluid linear thermal expansion	β_f	2-4	4×10^{-4}	K^{-1}
Solid linear thermal expansion	β_s	2-4	5×10^{-5}	K^{-1}
Critical stress intensity factor	K_c	2-4	5×10^5	Pa
Fluid specific heat capacity	C_f	2-4	4.2×10^3	$\mathrm{J\,kg^{-1}\,K^{-1}}$
Solid specific heat capacity	C_s	2-4	7.9×10^2	$\mathrm{J\,kg^{-1}\,K^{-1}}$
Fluid thermal conductivity	κ_f	2-4	0.6	$\mathrm{W\,m^{-1}\,K^{-1}}$
Solid thermal conductivity	κ_s	2-4	2.0	$\mathrm{W\,m^{-1}\,K^{-1}}$
Reference fluid density	$\rho_{0,f}$	2-4	1×10^3	$\mathrm{kg\,m^{-3}}$
Reference solid density	$\rho_{0,s}$	2-4	2.7×10^3	$\mathrm{kg\,m^{-3}}$
Compressibility	c	2-4	4×10^{-10}	Pa^{-1}
Bulk modulus	K	1-4	2.2×10^{10}	Pa
Poisson ratio	ν	1-4	0.2	–
Matrix porosity	ϕ	2-4	0.05	–
Matrix permeability	$\mathcal{K}$	2-3	1×10^{-14}	m
Matrix permeability	$\mathcal{K}$	4	1×10^{-16}	m
Viscosity	μ	2-4	1×10^{-3}	Pa s
Residual aperture	a_{res}	2	1×10^{-3}	m
Residual aperture	a_{res}	3	3×10^{-4}	m
Residual aperture	a_{res}	4	2.0×10^{-3}	m

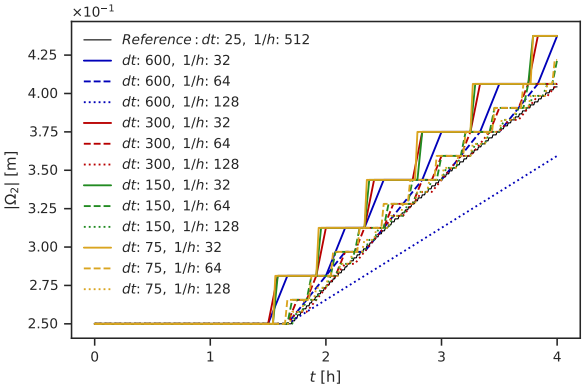

Figure 6: Example 2: Size of the propagating fracture Ω_2 vs. time for 13 refinement combinations. Line colours and styles correspond to temporal and spatial discretisation size, respectively.

acts to alter thermal stresses and thereby cause fracture propagation.

4.2.1 Example 3: Thermal fracturing and forced convection

We consider two immersed fractures in a cube shaped domain of side length 1000 m centred 1500 m below the surface. Each fracture contains one well, implemented as a source or sink term in a single cell, with injection in the leftmost fracture, Ω_2, and production in the rightmost fracture, Ω_3. The domain, fracture geometry and spatial mesh is shown in Fig. 7.

The flow rate is $5\,\mathrm{L\,s^{-1}}$ for both wells and the injection temperature is 30 K below the formation temperature. The anisotropic boundary tractions are based on lithostatic stress, with

$$\sigma_{xx} = 0.6\rho_s G z, \qquad \sigma_{yy} = 1.2\rho_s G z, \qquad \sigma_{zz} = \rho_s G z.$$

This background stress implies that Ω_3, with normal vector $\boldsymbol{n}_3 = [1, 0, 0]^T$, is initially more favourably oriented for propagation than is Ω_2.

The Fig. 9 fracture size plot shows that Ω_2 grows at a steady speed after an initial phase of limited propagation. The growth is driven by elevated pressure due to injection and matrix cooling, which is most pronounced on the side of Ω_2 facing Ω_3 due to the advective component of the heat flow, cf. Fig. 8. Assuming the thermal driving force to dominate, which is reasonable given the relative size of injection pressure and background stresses, the relatively constant speed could be linked to the constant rate and temperature of injection.

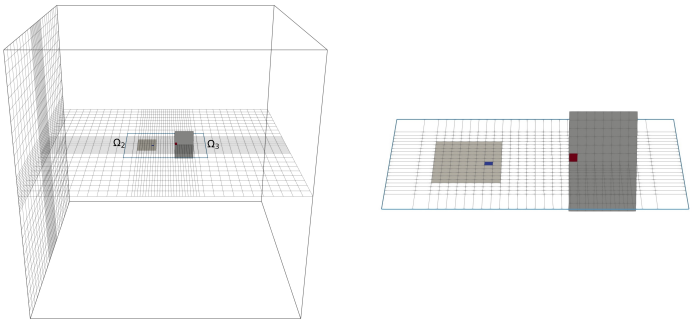

Figure 7: Example 3: Fracture network geometry, well locations and spatial mesh (left) and close-up of fractures with mesh and well cells (right). The blue fracture cell in Ω_2 marks injection, whereas the red cell in Ω_3 indicates production.

The fracture Ω_3, where fluid is produced, does not propagate at all. Towards the end of the 2.5 yr simulation, the magnitude of normal traction on Ω_3 has increased considerably relative to the initial value of approx. 1×10^7 Pa, see Fig. 9. We attribute this to the contraction ensuing from matrix cooling surrounding Ω_2, which leads to a larger proportion of the compressive forces being supported by the non-cooled surroundings, including Ω_3.

Figure 9 also shows temperature and pressure in the two wells throughout the simulation. Most notably, injection pressure gradually declines. This increased injectivity in Ω_2 is caused by the combination of an increased aperture in the pre-existing part of the fracture, and the increase in the geometric extension of the fracture. Thus, fracture deformation caused by thermal and hydraulic stimulation strongly affects the (flow) properties, providing a clear example of the two-way process-structure interaction characteristic of fractured porous media.

This simulation indicates that long-term cooling during geothermal energy production may alter the stress state to a stage where fractures propagate. It is thus important to develop simulation tools that can incorporate such changes to fracture geometry, in addition to handling multiphysics processes in the reservoir. Moreover, the injection pressure evolution shows the importance of also capturing deformation of existing fractures in the same model.

4.2.2 Example 4: Thermal fracturing and natural convection

As a final example, we consider fracture propagation driven by cooling that is mainly caused by convection cells inside vertical fractures. The process, known as convective downward migration, has been proposed as a mechanism for trans-

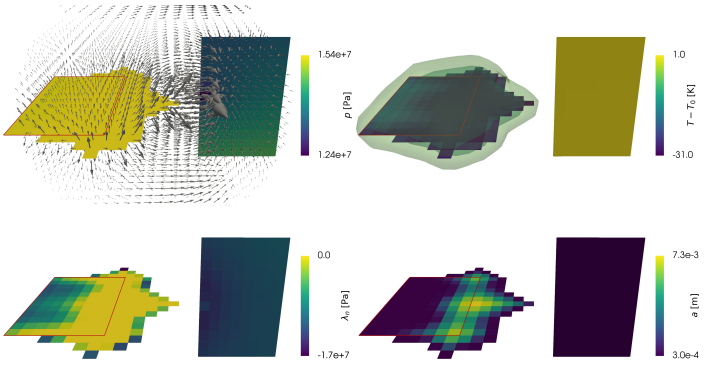

Figure 8: Example 3: Solution and fracture geometry at the end of the simulation. p, a and λ_n are shown on the fractures, while T is shown both on the fractures and as contour lines indicating where the matrix is significantly cooled (10 K and 20 K below initial formation temperature). The red rectangle in the bottom left figure indicates the initial shape of Ω_2.

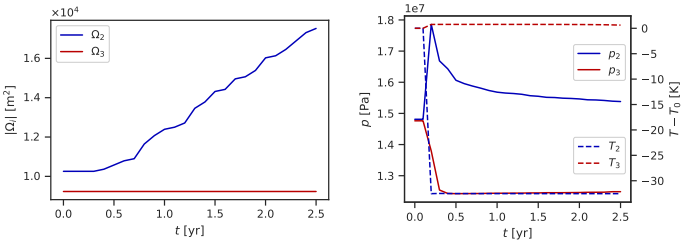

Figure 9: Example 3: Size of the two fractures vs. time (left) and pressure and temperature vs. time in the injection well cells (right). Only the injection fracture Ω_2 grows.

port of heat in the deep roots of volcanic geothermal systems [46, 13]. It is also predicted to have an important role in the source mechanism of hydrothermal activity in a more general perspective [13, 4].

We consider five vertical fractures evenly spaced along the x direction and extending from the top boundary half-way through the cube-shaped domain with side length 400 m, see Fig. 10. The domain is centred 2800 m below the surface to mimic conditions within the earth crust where natural heat convection is likely to take place. Boundary and initial conditions are hydrostatic pressure and temperature according to a vertical gradient of $-0.15\,\mathrm{K\,m^{-1}}$ and upper boundary temperature 500 K, considered to represent background temperature gradient close to the boundaries of geothermal areas. This value is estimated between -0.10 and $-0.15\,\mathrm{K\,m^{-1}}$ within Iceland's active zone of volcanism and rifting, where many high temperature systems exist [3]. The boundary traction is the same as in the previous example and the simulation time is 70 years. The results are displayed in Figures 10, 11 and 12.

The vertical temperature gradient leads to instabilities in fluid density, which triggers convection cells inside the fracture, see Fig. 12. As shown by the temperature contour surfaces in Fig. 11, the resulting energy transport cools the rock surrounding the fractures, to the point where propagation occurs at the lower end of the fractures. This change in fracture geometry, together with changes in aperture in the existing fracture due to contraction of the surrounding rock, again gives feedback to the fluid convection, as is evident from the difference in flow patterns between the solutions at the two different times reported in Fig. 12. As in Example 3, we see evidence of tight process-structure interaction, with the convection-induced cooling altering thermo-poro-mechanical stress sufficiently for the fractures to open and propagate.

Figure 10 displays size evolution for individual fractures. Propagation begins approximately half-way through the simulation, first for the fracture in the center of the domain. Even after all fractures have started propagating, the central fractures Ω_3, Ω_4 and Ω_5 propagate significantly faster than the two outermost. This should be understood in the context of the compressive boundary conditions: The normal tractions on Ω_2 and Ω_6, respectively, are not relieved by the cooling of any fractures lying between them and the left and right boundary.

After onset, propagation continues until the end of the simulation, but not at all time steps for all propagating fractures, and certainly not along the entire propagation front. This is because the matrix surrounding the new part of a fracture must be cooled before the fracture proceeds, and indicates that the fracture growth is stable as in Example 2 and that the propagation speed is resolved in the temporal discretisation. An approximate downward propagation speed for fractures 3-5 is obtained by dividing the estimated slopes from Fig. 10 by the initial lateral fracture length 200 m, yielding $\sim 2\,\mathrm{m\,yr^{-1}}$. The setup for this test case is based on average properties in high temperature settings, and the results are in agreement with previous assessments of $0.3\,\mathrm{m\,yr^{-1}}$ to $5\,\mathrm{m\,yr^{-1}}$ [13, 11], using a simple relation between the temperature difference sufficient for thermal stress to outweigh the hydrostatic force to keep the fracture closed, at approximatly 3 km depth in the crust with average properties of water and

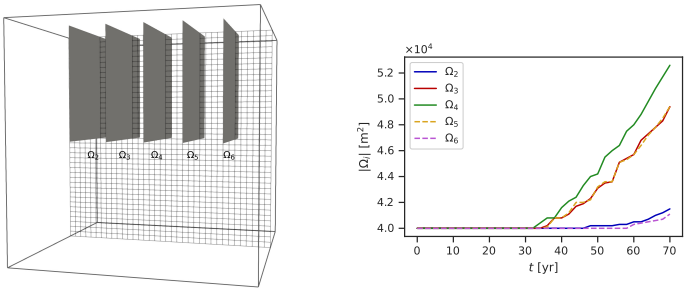

Figure 10: Example 4: Initial geometry (left) and size of the five fractures vs. time (right).

rock similar to the example.

5 Conclusion

While both numerical models considering flow and heat transfer in fractured media and models considering deformation of poroelastic media and fracture mechanics have separately been studied extensively, models which combine these fields are more recent. In the current work, we present a novel numerical model that couples fracture contact mechanics and propagation with deformation, flow and heat transfer in fractured thermo-poroelastic media. The methodology is built on a multi-point control-volume framework, combined with an active-set approach for fracture contact mechanics. The fracture propagation is based on stress intensity factors, and computed using a variant of the displacements correlation method. In the numerical model, fractures are restricted to propagate conforming to the existing grid. The numerical results show mesh convergence for computation of stress-intensity factors and fracture propagation speeds. Focusing on tensile fracture propagation, three-dimensional numerical test cases also show how the model can be used to investigate fracture propagation caused by forced and natural convection, exemplified by long-term thermal reservoir stimulation due to cooling and convective downward migration of fractures. The simulations demonstrate the need for coupled models accounting for both contact mechanics and fracture propagation as well as the coupled thermo-poroelasticity.

Acknowledgements Funding: This work was supported by the Research Council of Norway and Equinor ASA through grants number 267908 and 308733.

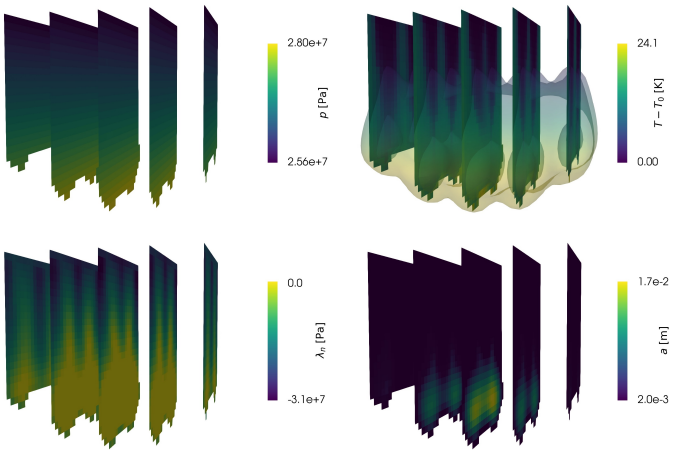

Figure 11: Example 4: Solution and fracture geometry at the end of the simulation. p, a and λ_n are shown on the fractures, while T is shown both on the fractures and as contour surfaces indicating where the matrix is significantly cooled (7.5 K and 15 K below initial formation temperature).

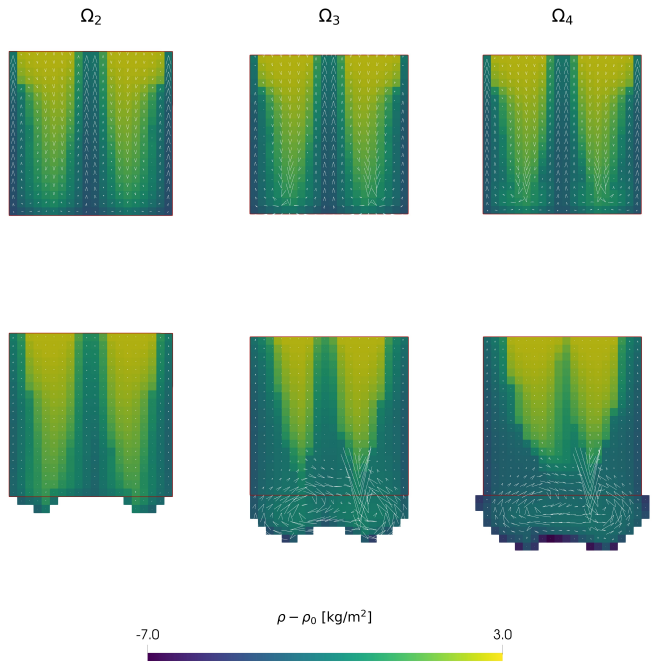

Figure 12: Example 4: Flux fields and density distribution for three fractures. The top and bottom row correspond to just before propagation onset ($t = 32\,\mathrm{yr}$) and the end of simulation ($t = 70\,\mathrm{yr}$), respectively. The scaling of the arrows indicating flux direction and magnitude is a factor five larger for the top row, when fluxes are smaller due to smaller apertures. The red rectangles indicate initial fracture geometry.

References

[1] Porepy v1.3.0 source code. DOI 10.5281/zenodo.4314343

[2] Aavatsmark, I.: An introduction to multipoint flux approximations for quadrilateral grids. Comput Geosci **6**, 405–432 (2002)

[3] Ágústsson, K., Flóvenz, Ó.G.: The thickness of the seismogenic crust in iceland and its implications for geothermal systems (2005). Proceedings World Geothermal Congress 2005, Antalya, Turkey, 24-29 April 2005

[4] Axelsson, G.: Hydrology and thermomechanics of liquid-dominated hydrothermal systems in iceland. (1985). PhD-Thesis. Oregon State University, USA, (1985)

[5] Baroth, J.: Uncertainty propagation through Thermo-Hydro-Mechanical modelling of concrete cracking and leakage – Application to containment buildings. In: Proceedings of the 10th International Conference on Fracture Mechanics of Concrete and Concrete Structures. IA-FraMCoS (2019)

[6] Barton, N.: The shear strength of rock and rock joints. In: Int J Rock Mech Min Sci Geomech Abstr, vol. 13, pp. 255–279 (1976)

[7] Berge, R.L., Berre, I., Keilegavlen, E., Nordbotten, J.M., Wohlmuth, B.: Finite volume discretization for poroelastic media with fractures modeled by contact mechanics. Int J Numer Methods Eng **121**(4), 644–663 (2020)

[8] Berre, I., Boon, W.M., Flemisch, B., Fumagalli, A., Gläser, D., Keilegavlen, E., Scotti, A., Stefansson, I., Tatomir, A., Brenner, K., et al.: Verification benchmarks for single-phase flow in three-dimensional fractured porous media. Adv Water Resour **147**, 103,759 (2020)

[9] Berre, I., Doster, F., Keilegavlen, E.: Flow in fractured porous media: A review of conceptual models and discretization approaches. Transp Porous Med **130**(1), 215–236 (2019)

[10] Biot, M.A.: General theory of three-dimensional consolidation. J Appl Phys **12**(2), 155–164 (1941)

[11] Björnsson, H., Björnsson, S., Sigurgeirsson, T.: Penetration of water into hot rock boundaries of magma at Grímsvötn. Nature **295**(5850), 580–581 (1982)

[12] Björnsson, S., Stefánsson, V.: Heat and mass transport in geothermal reservoirs. In: J. Bear, M.Y. Corapcioglu (eds.) Advances in Transport Phenomena in Porous Media, NATO ASI Series (Series E: Applied Sciences), vol. 128, pp. 143–183 (1987)

[13] Bodvarsson, G.: Terrestrial energy currents and transfer in iceland. Continental and oceanic rifts **8**, 271–282 (1982)

[14] Bois, A.P., Garnier, A., Galdiolo, G., Laudet, J.B., et al.: Use of a mechanistic model to forecast cement-sheath integrity. SPE Drill Completion **27**(02), 303–314 (2012)

[15] Boon, W.M., Nordbotten, J.M., Yotov, I.: Robust discretization of flow in fractured porous media. SIAM J Numer Anal **56**(4), 2203–2233 (2018)

[16] de Borst, R., Verhoosel, C.V.: Gradient damage vs phase-field approaches for fracture: Similarities and differences. Comput Method Appl M **312**, 78–94 (2016)

[17] Both, J.W., Kumar, K., Nordbotten, J.M., Radu, F.A.: The gradient flow structures of thermo-poro-visco-elastic processes in porous media. arXiv preprint arXiv:1907.03134 (2019)

[18] Bouhjiti, D.E.M., Baroth, J., Briffaut, M., Dufour, F., Masson, B.: Statistical modeling of cracking in large concrete structures under Thermo-Hydro-Mechanical loads: Application to Nuclear Containment Buildings. Part 1: Random field effects (reference analysis). Nucl Eng Des **333**, 196–223 (2018)

[19] Bouhjiti, D.E.M., Blasone, M.C., Baroth, J., Dufour, F., Masson, B., Michel-Ponnelle, S.: Statistical modelling of cracking in large concrete structures under Thermo-Hydro-Mechanical loads: Application to Nuclear Containment Buildings. Part 2: Sensitivity analysis. Nucl Eng Des **334**, 1–23 (2018)

[20] Brun, M.K., Berre, I., Nordbotten, J.M., Radu, F.A.: Upscaling of the coupling of hydromechanical and thermal processes in a quasi-static poroelastic medium. Transp Porous Med **124**(1), 137–158 (2018)

[21] Chan, S., Tuba, I., Wilson, W.: On the finite element method in linear fracture mechanics. Eng Frac Mech **2**(1), 1 – 17 (1970)

[22] Cheng, A.H.D.: Poroelasticity, vol. 27. Springer (2016)

[23] Coussy, O.: Poromechanics. Wiley (2004)

[24] Cusini, M., White, J.A., Castelletto, N., Settgast, R.R.: Simulation of coupled multiphase flow and geomechanics in porous media with embedded discrete fractures. arXiv preprint arXiv:2007.05069 (2020)

[25] Dang-Trung, H., Keilegavlen, E., Berre, I.: Numerical modeling of wing crack propagation accounting for fracture contact mechanics. Int J Solids Struct **204-205**, 233 – 247 (2020)

[26] Davis, T.A.: Algorithm 832: Umfpack v4.3—an unsymmetric-pattern multifrontal method. ACM Trans. Math. Softw. **30**(2), 196–199 (2004)

[27] Deb, R., Jenny, P.: An extended finite volume method and fixed-stress approach for modeling fluid injection–induced tensile opening in fractured reservoirs. Int J Numer Anal Methods Geomech **44**(8), 1128–1144 (2020)

[28] Flemisch, B., Berre, I., Boon, W., Fumagalli, A., Schwenck, N., Scotti, A., Stefansson, I., Tatomir, A.: Benchmarks for single-phase flow in fractured porous media. Adv. Water Resour. **111**, 239–258 (2018)

[29] Franceschini, A., Castelletto, N., Ferronato, M.: Block preconditioning for fault/fracture mechanics saddle-point problems. Comput Method Appl M **344**, 376–401 (2019)

[30] Franceschini, A., Castelletto, N., White, J.A., Tchelepi, H.A.: Algebraically stabilized lagrange multiplier method for frictional contact mechanics with hydraulically active fractures. Comput Method Appl M **368**, 113,161 (2020)

[31] Gallyamov, E., Garipov, T., Voskov, D., Van den Hoek, P.: Discrete fracture model for simulating waterflooding processes under fracturing conditions. Int J Numer Anal Methods Geomech **42**(13), 1445–1470 (2018)

[32] Gao, Q., Ghassemi, A.: Three-Dimensional Thermo-Poroelastic Modeling and Analysis of Flow, Heat Transport and Deformation in Fractured Rock with Applications to a Lab-Scale Geothermal System. Rock Mech Rock Eng **53**(4), 1565–1586 (2020)

[33] Garipov, T., Hui, M.: Discrete fracture modeling approach for simulating coupled thermo-hydro-mechanical effects in fractured reservoirs. Int J Rock Mech Min **122**, 104,075 (2019)

[34] Garipov, T., Karimi-Fard, M., Tchelepi, H.: Discrete fracture model for coupled flow and geomechanics. Comput Geosci **20**(1), 149–160 (2016)

[35] Giovanardi, B., Formaggia, L., Scotti, A., Zunino, P.: Unfitted fem for modelling the interaction of multiple fractures in a poroelastic medium. In: Geometrically Unfitted Finite Element Methods and Applications, pp. 331–352. Springer (2017)

[36] Griffith, A.A.: Vi. the phenomena of rupture and flow in solids. Phil T R Soc. A **221**(582-593), 163–198 (1921)

[37] Hüeber, S., Stadler, G., Wohlmuth, B.I.: A primal-dual active set algorithm for three-dimensional contact problems with coulomb friction. SIAM J Sci Comput **30**(2), 572–596 (2008)

[38] Jaffré, J., Mnejja, M., Roberts, J.: A discrete fracture model for two-phase flow with matrix-fracture interaction. Procedia Computer Science **4**, 967 – 973 (2011). Proceedings of the International Conference on Computational Science, ICCS 2011

[39] Karimi-Fard, M., Durlofsky, L.J., Aziz, K.: An Efficient Discrete-Fracture Model Applicable for General-Purpose Reservoir Simulators. SPE J **9**(2), 227–236 (2003)

[40] Keilegavlen, E., Berge, R., Fumagalli, A., Starnoni, M., Stefansson, I., Varela, J., Berre, I.: Porepy: An open-source software for simulation of multiphysics processes in fractured porous media. Comput Geosci (2020). DOI 10.1007/s10596-020-10002-5

[41] Keilegavlen, E., Nordbotten, J.M.: Finite volume methods for elasticity with weak symmetry. Int J Numer Methods Eng **112**(8), 939–962 (2017)

[42] Khoei, A.R., Vahab, M., Haghighat, E., Moallemi, S.: A mesh-independent finite element formulation for modeling crack growth in saturated porous media based on an enriched-fem technique. Int J Fracture **188**(1), 79–108 (2014)

[43] Király, L.: Large scale 3-d groundwater flow modelling in highly heterogeneous geologic medium. In: Groundwater flow and quality modelling, pp. 761–775. Springer (1988)

[44] Kogbara, R.B., Iyengar, S.R., Grasley, Z.C., Masad, E.A., Zollinger, D.G.: A review of concrete properties at cryogenic temperatures: Towards direct lng containment. Constr Build Mater **47**, 760–770 (2013)

[45] Lin, Y., Deng, K., Yi, H., Zeng, D., Tang, L., Wei, Q.: Integrity tests of cement sheath for shale gas wells under strong alternating thermal loads. Natural Gas Industry B (2020)

[46] Lister, C.: On the penetration of water into hot rock. Geophys J Int **39**(3), 465–509 (1974)

[47] Martin, V., Jaffré, J., Roberts, J.E.: Modeling Fractures and Barriers as Interfaces for Flow in Porous Media. SIAM J Sci Comput **26**(5), 1667–1691 (2005)

[48] Nejati, M., Paluszny, A., Zimmerman, R.W.: On the use of quarter-point tetrahedral finite elements in linear elastic fracture mechanics. Eng Frac Mech **144**, 194 – 221 (2015)

[49] Nordbotten, J.: Stable cell-centered finite volume discretization for biot equations. SIAM J Numer Anal **54**, 942–968 (2016)

[50] Nordbotten, J., Keilegavlen, E.: An introduction to multi-point flux (mpfa) and stress (mpsa) finite volume methods for thermo-poroelasticity. arXiv preprint arXiv:2001.01990 (2020)

[51] Paluszny, A., Zimmerman, R.W.: Numerical simulation of multiple 3d fracture propagation using arbitrary meshes. Comput Method Appl M **200**(9), 953 – 966 (2011)

[52] Ren, G., Jiang, J., Younis, R.M.: A fully coupled xfem-edfm model for multiphase flow and geomechanics in fractured tight gas reservoirs. Procedia Computer Science **80**, 1404–1415 (2016)

[53] Richard, H.A., Fulland, M., Sander, M.: Theoretical crack path prediction. Fatigue Fract Eng M **28**(1-2), 3–12 (2005)

[54] Salimzadeh, S., Paluszny, A., Nick, H.M., Zimmerman, R.W.: A three-dimensional coupled thermo-hydro-mechanical model for deformable fractured geothermal systems. Geothermics **71**, 212 – 224 (2018)

[55] Salimzadeh, S., Paluszny, A., Zimmerman, R.W.: Three-dimensional poroelastic effects during hydraulic fracturing in permeable rocks. Int J Solids Struct **108**, 153–163 (2017)

[56] Selvadurai, A.P., Suvorov, A.: Thermo-poroelasticity and geomechanics. Cambridge University Press (2017)

[57] Settgast, R.R., Fu, P., Walsh, S.D., White, J.A., Annavarapu, C., Ryerson, F.J.: A fully coupled method for massively parallel simulation of hydraulically driven fractures in 3-dimensions. Int J Numer Anal Method Geomech **41**(5), 627–653 (2017)

[58] Siratovich, P.A., Villeneuve, M.C., Cole, J.W., Kennedy, B.M., Bégué, F.: Saturated heating and quenching of three crustal rocks and implications for thermal stimulation of permeability in geothermal reservoirs. Int J Rock Mech Min **80**, 265–280 (2015)

[59] Sneddon, I.N.: The distribution of stress in the neighbourhood of a crack in an elastic solid. Philos T R Soc A **187**(1009), 229–260 (1946)

[60] Stefansson, I., Berre, I., Keilegavlen, E.: A fully coupled numerical model of thermo-hydro-mechanical processes and fracture contact mechanics in porous media. arXiv preprint arXiv:2008.06289 (2020)

[61] Stefansson, I., Keilegavlen, E.: Run scripts for PorePy simulations. DOI 10.5281/zenodo.4316328 (2020)

[62] Ucar, E., Keilegavlen, E., Berre, I., Nordbotten, J.M.: A finite-volume discretization for deformation of fractured media. Comput Geosci **22**(4), 993–1007 (2018)

[63] Wohlmuth, B.: Variationally consistent discretization schemes and numerical algorithms for contact problems. Acta Numer **20**, 569–734 (2011)

[64] Wu, Z., Zhou, Y., Weng, L., Liu, Q., Xiao, Y.: Investigation of thermal-induced damage in fractured rock mass by coupled FEM-DEM method. Comput Geosci (2020)

[65] Zimmerman, R.W., Bodvarsson, G.S.: Hydraulic conductivity of rock fractures. Transp Porous Med **23**(1), 1–30 (1996)

Paper H

Hydro-mechanical simulation and analysis of induced seismicity for a hydraulic stimulation test at the Reykjanes geothermal field, Iceland

Eirik Keilegavlen, Laure Duboeuf, Anna Maria Dichiarante, Sæunn Halldórsdóttir, Ivar Stefansson, Marcel Naumann, Egill Árni Guðnason, Kristján Ágústsson, Guðjón Helgi Eggertsson, Volker Oye, Inga Berre

Submitted to Journal of Geophysical Research - Solid Earth
Preprint: https://arxiv.org/abs/2011.03370

Hydro-mechanical simulation and analysis of induced seismicity for a hydraulic stimulation test at the Reykjanes geothermal field, Iceland

Eirik Keilegavlen[1], Laure Duboeuf[2], Anna Maria Dichiarante[2], Sæunn Halldórsdóttir[1], Ivar Stefansson[1], Marcel Naumann[3], Egill Árni Guðnason[4], Kristján Ágústsson[4], Guðjón Helgi Eggertsson[5], Volker Oye[2], Inga Berre[1]

[1]Department of Mathematics, University of Bergen, Norway

[2]Department of Applied Seismology, NORSAR, Norway

[3]Equinor ASA, Norway

[4]ÍSOR Iceland Geosurvey, Iceland

[5]HS Orka, Iceland

Corresponding author: Inga Berre, inga.berre@uib.no

Key Points:

- Framework for integrating different data types in development of a 3D faulted geothermal reservoir model
- Novel application of simulation tool for coupled hydro-mechanical processes in faulted geothermal reservoirs applied to injection-induced fault reactivation at Reykjanes, Iceland
- New insights through combined induced seismicity analysis and physics-based simulation of injection-induced fault reactivation

Abstract

The hydraulic stimulation of the well RN-34 at the Reykjanes geothermal field in Iceland caused increased seismic activity near the well. Here, we use this as a case study for investigation on how seismic analysis can be combined with physics-based simulation studies to further understand injection-induced fault reactivation. The work presents new analysis of the seismic data combined with application of a recent simulation software for modeling of coupled hydro-mechanical processes and fault deformation caused by fluid injection. The simulation model incorporates an explicit model of the fault network based on geological characterization combined with insights from seismic analysis. The 3D faulted reservoir model is then calibrated based on injection data. Despite limited data, the work shows how seismic interpretations can be used in developing simulation models and, reciprocally, how the modeling can add to the seismic interpretations in analysis of dynamics.

1 Introduction

Most of the Earth's accessible geothermal energy is stored in hard, competent rock. In such rock types, fractures and faults are the main conduits for fluid flow, which is essential for production of geothermal fluid to the surface. To enhance permeability in such formations, fluids at elevated pressures can be injected to cause slip and dilation of existing fractures or faults. This stimulation mechanism, called hydroshearing, has proved successful for permeability enhancement for several geothermal reservoirs (Chabora et al., 2012; Genter et al., 2010; Schindler et al., 2010; Zimmermann & Reinicke, 2010). This stimulated slip and dilation is often realized as microseismic events, or microearthquakes, emitting seismic waves. These waves of small elastic deformations can be recorded by local seismic networks; hence, the process of hydroshearing can be continuously detected, located, and analyzed in real time. In general, the stimulation aims to induce only small seismic events of magnitudes $M_w < 2$ (Ellsworth, 2013), but larger events have also been linked to hydraulic stimulation of fractured geothermal reservoirs. The most prominent are the 2017 M_w 5.4 Pohang earthquake in South-Korea (Ellsworth et al., 2019; Grigoli et al., 2018; Kim et al., 2018) and the 2006 ML 3.4 earthquake related to the Basel EGS project (Bachmann et al., 2011; Deichmann & Giardini, 2009). In Iceland, the most prominent induced seismicity has been two magnitude 4 events that were observed related to geothermal wastewater reinjection in Húsmúli at the Hellisheidi geothermal area, with flow rates reaching 500 kg/s (Juncu et al., 2020).

Hydroshearing of fractures occurs in an interplay between coupled hydraulic, thermal, mechanical, and chemical reservoir processes and the fractured structure of the formation. To design hydraulic stimulation operations while mitigating induced seismicity, understanding of these coupled, nonlinear dynamics is crucial. In this, physics-based numerical models can provide valuable insights: either as a tool to forecast outcomes of a stimulation or to complement dynamic data in understanding the governing mechanisms and structural features at depth.

Several physics-based numerical modeling studies have considered how an increase in pore pressure reduces effective stress on preexisting fractures or faults, thus causing slip (Bruel, 2007; Gischig & Wiemer, 2013; Goertz-Allmann et al., 2011; Hakimhashemi et al., 2014; Kohl & Mégel, 2007; Rothert & Shapiro, 2003; Shapiro, 2015). To incorporate the important effect of stress redistribution due to hydroshearing is challenging; even the more advanced numerical models are typically based on strong simplifications of the physics governing flow, mechanics,

or coupled hydromechanics related to the fractures and/or the domain surrounding them (McClure & Horne, 2011; Norbeck et al., 2016; Ucar et al., 2017; 2018a). Recently, however, numerical modeling tools which consider networks of fractures or faults in 3D domains have been developed that consistently account for fully coupled hydro-mechanical processes as well as fracture-contact mechanics (Berge et al., 2020; Gallyamov et al., 2018; Garipov et al., 2016; Garipov & Hui, 2019; Keilegavlen et al., 2019). In this paper, we investigate how simulations based on such numerical models can complement dynamic data in an investigation of hydroshearing, considering a specific case study for a stimulation test at the Reykjanes geothermal field in SW Iceland on 29 March 2015.

The large-scale exploitation of the Reykjanes field for geothermal energy started when Hitaveita Suðurnesja (Reykjanes District Heating), now HS Orka, acquired the development concession rights for the geothermal field and drilled its first well for electrical generation in 1998. In 2006, production started at the 100 MWe Reykjanes power plant. As of 2019, a total of 37 wells have been drilled in Reykjanes for exploration, production, and re-injection. The conceptual model of the geothermal system is described by Khodayar et al. (2018), Weisenberger et al. (2019), and Nielsson et al. (2020).

In 2014 and 2015, the wells RN-33 and RN-34 were drilled from a well pad northwest of Sýrfell, about 2 km northeast of the center of the main production area (Figure 1c). The wells were intended for re-injection of separated brine from the Reykjanes Power Plant. Well RN-33 is directionally drilled to the SW and connected to the production field through a NE-SW trending fissure zone. Well RN-34 is directionally drilled to the NW and results of tracer tests indicate that the well is not hydraulically connected to the production field. For RN-34 a fall-off test followed by 10 hours of cyclic stimulation was conducted on 29 March 2015 (see Supporting Information, Texts S3 and S4). Seismic events related to the injection were observed near the injection point.

During the period of interest, this seismicity at Reykjanes was recorded by both a permanent and a temporary seismic network (Figure 1b). The permanent network (PS) was run until 2018 by the Iceland Geosurvey (ISOR) on behalf of HS-Orka and was composed of eight short-period sensors mostly located above the geothermal reservoir on the SW part of the Reykjanes Peninsula (Weemstra et al., 2016). A temporary network (TS) with 20 broadband and 10 short–period sensors covering the entire Reykjanes Peninsula was installed as part of the European Project IMAGE and took recordings from March 2014 to August 2015 (Blanck et al., 2020; Jousset et al., 2016). The variety of sensor types and the short (0.8 km) and long (35 km) interstation distances increase network resolution and the capability of recording close and far events. Induced events have been observed at Reykjanes since the start of the geothermal activity (Blanck et al., 2020; Flovenz et al., 2015; Guðnason, 2014).

In this paper, we present an investigation of the hydraulic stimulation of RN-34 based on new analysis of the seismic data combined with an unprecedented simulation study of the reservoir dynamics. Based on all available data relevant to the study of the hydraulic stimulation test, we develop a novel hydro-mechanical model of the faulted reservoir to simulate the subsurface dynamics that occur as a response to hydraulic stimulation. For the simulation, we employ a simulator constructed for fully coupled flow, poroelasticity, and fracture deformation

(Keilegavlen et al., 2019). The simulation model accounts for flow in both explicitly represented faults and the low-permeable surrounding porous medium, slip of faults based on a Coulomb friction law, and coupled poroelastic response of the porous medium to fluid pressure and fault slip. To our knowledge this represents the first application of a simulator constructed for fully coupled poroelasticity and fracture deformation to model stimulation of an actual geothermal reservoir.

The paper is structured as follows: In section 2, we present the regional context of the 29 March 2015 RN-34 stimulation test, including regional information for the stress state and a model of the dominating fault geometry near RN-34. Section 3 presents dynamic observations related to the RN-34 stimulation, including dynamic well data and analysis of induced seismicity. In section 4, we present the mathematical model and the simulation model, including parameter identification based on well data. Section 5 presents the numerical model and simulation results. A discussion of the combined results from seismic analysis and physics-based simulations is given in section 6, followed by a summary and concluding remarks in section 7.

2 From regional geological context to local fault model geometry

To model the coupled dynamics of a geothermal reservoir and analyze microseismic data, consideration of the target area's geological setting is important, including how the setting dictates today's local stress field conditions. In this section, we first introduce the regional geological setting: the larger structures and stresses that surround our target area. Then, we bring these into context with existing local-scale geological interpretations and recent seismological observations, which are integrated to understand the stresses that acted at a given time on certain faults involved in the local model.

The fault and fracture orientation reading convention used in this paper is strike (0°–360°)/dip (0°–90°) and rake (hanging-wall slip vector is measured on the plane of the fault) for recording fault planes/focal planes and their relative kinematics and trend (0°–360°)/plunge (0°–90°) for stress axes. Both conventions follow the right-hand rule, and both stereonets and focal mechanisms are projected on the lower hemisphere.

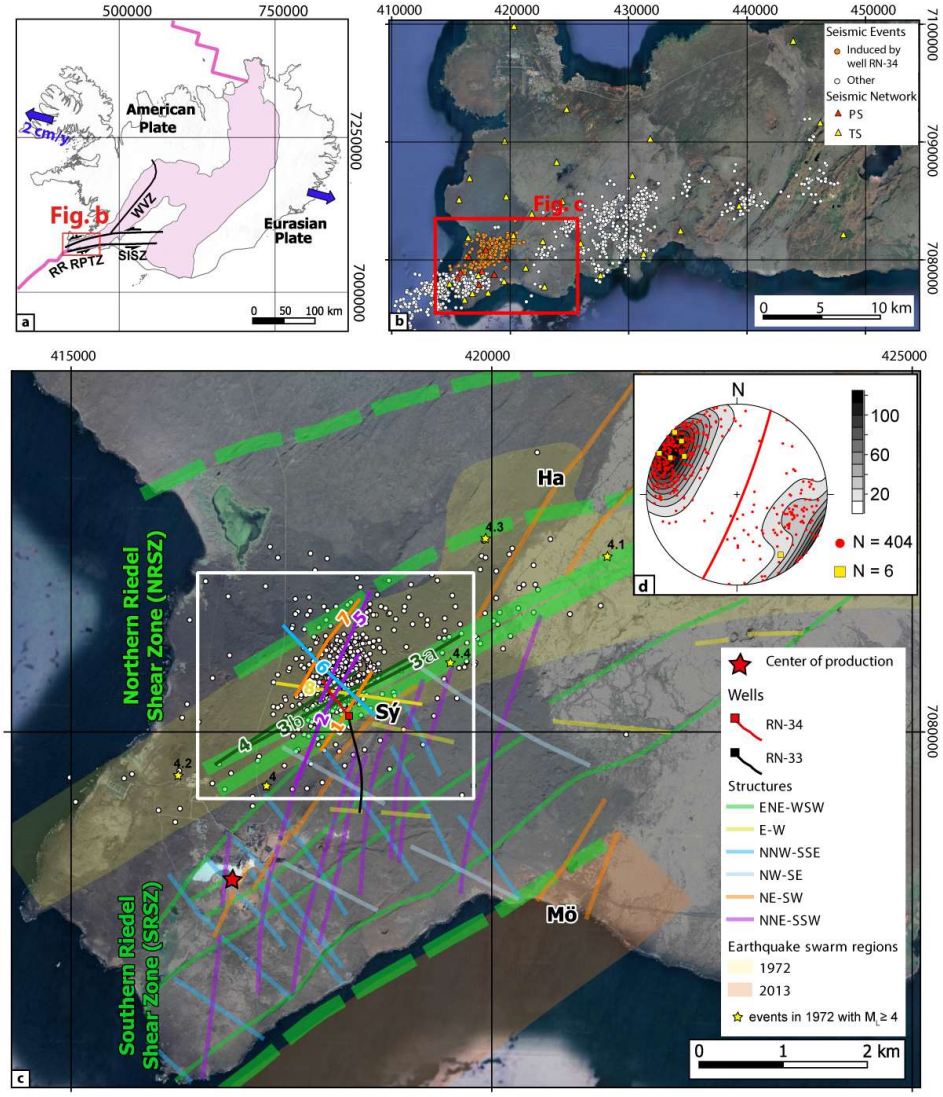
500000
750000
7250000
7000000
American Plate
2 cm/y
Fig. b
WVZ
Eurasian Plate
RR
RPTZ
SISZ
0 50 100 km
a
410000
420000
430000
440000
450000
7100000
7090000
7080000
Seismic Events
Induced by well RN-34
Other
Seismic Network
PS
TS
Fig. c
0 5 10 km
b
415000
420000
425000
7080000
Ha
Sý
Mö
4.1
4.2
4.3
4.4
1
3a
3b
4
5
6
7
N
100
60
20
N = 404
N = 6
d
Center of production
Wells
RN-34
RN-33
Structures
ENE-WSW
E-W
NNW-SSE
NW-SE
NE-SW
NNE-SSW
Earthquake swarm regions
1972
2013
events in 1972 with M_L ≥ 4
0 1 2 km
Northern Riedel Shear Zone (NRSZ)
Southern Riedel Shear Zone (SRSZ)
c

Figure 1. (a) Plate boundary across Iceland showing the study location (red box); the Reykjanes Peninsula Transtensional Zone (RPTZ) is located in the region where the Reykjanes Ridge (RR), South Iceland Seismic Zone (SISZ), and the Western Volcanic Zone (WVZ) meet. The plate boundary (line) and rocks of age less than 0.8 Ma (adapted from Khodayar et al., 2018) are shown in pink. **(b)** The Reykjanes Peninsula showing the two networks (yellow and red triangles, respectively) for the temporary seismic (TS) network and the permanent seismic (PS) network as well as the re-located seismic events (shown by white and orange dots). The events analyzed in this study are those shown by yellow dots. **(c)** Simplified structural map of the Reykjanes geothermal field adapted from Khodayar et al. (2018) showing boundaries of the two major Riedel shear zones: the Northern Riedel Shear Zone (NRSZ) and the Southern Riedel Shear Zone (SRSZ). Also shown are the outlines of the 1972 (yellow) and 2013 (orange) earthquake swarms as well as events from the 1972 swarm (Klein et al. 1977, Björnsson et al., 2020) with $M_L \geq 4$ (yellow stars). Structures are shown as transparent lines in the SRSZ and elsewhere and the initial considered fault model is shown using non-transparent lines in the studied area. For both, the color scheme is based on orientation. Induced seismic events are shown in white. The locations Sýrfell (Sý), Mölvík (Mö), and Haugur (Ha) are shown. The wellhead location of wells RN-34 and RN-33 is marked with a square and the well paths with lines. The approximate location of the center of production is indicated by a red star and the study area by a white rectangle. **(d)** Equal area stereonet plot and density contour of the fractures interpreted from well RN-34 by Árnadóttir et al. (unpublished report, Supporting Information, Text S1). Fractures are represented as pole to planes (red dots), and fractures with a mechanical aperture >19 mm as yellow squares (Supporting Information, Table S2). Mean orientation of fractures interpreted with high confidence is represented by a large red circle (Supporting Information, Table S1).

2.1 Regional geological setting

Iceland is located at a complex mid-ocean ridge plate boundary between the Eurasian and American plates (Figure 1a), coinciding with a relatively large amount of hot, upwelling mantle material, which explains its volcanic activity. The Reykjanes geothermal field is located on the southwest tip of the Reykjanes Peninsula Transtensional Zone (RPTZ) in SW Iceland, where the Reykjanes Ridge (RR) comes onshore and the plate boundary changes direction. Rifting becomes oblique on the RPTZ and the rift segments split into a series of NE-SW trending eruptive fissures, which can be grouped into four en echelon volcanic fissure swarms (Sæmundsson, 1978). The fissure swarms, from east to west, Hengill, Brennisteinsfjöll, Krýsuvík and Reykjanes-Eldvörp-Svartsengi (for location see Fig. 1 in Keiding et al., 2009), consist of normal faults and tension fractures in addition to the eruptive fissures. They are intersected by a series of near vertical N-S trending right-lateral strike slip faults (Keiding et al., 2009). The regional extension direction of this oblique rift (extension is not orthogonal to plate boundary) is N101-103°E with an extension rate of 19–20 mm/yr along both active rift and transform segments (e.g., Keiding et al., 2009).

The patterns of natural seismicity are valuable in understanding the complex geological structures of the Reykjanes Peninsula (see, e.g., Björnsson et al., 2020, and Keiding et al., 2009). Based on GPS measurements taken during the 1993 and 1998 seismic swarm events, which showed almost exclusively strike-slip deformation, Clifton and Kattenhorn (2006) interpreted the geological structural complexity in Reykjanes, concluding that, to accommodate oblique spreading, episodes of tectono-magmatic activity (during extension) and episodes of left-lateral strike-slip motion alternate with different periodicity and in different structural blocks. However,

fault plane solutions computed from two of many earthquake swarms on the Reykjanes Peninsula (in 1972 and 2013) showed that both normal, strike–slip, and oblique motions occurred during both earthquakes in a magmatic phase (Björnsson et al., 2020; Khodayar et al., 2018), supporting the idea that deformation might occur simultaneously on differently oriented structures. Furthermore, these two earthquake swarms helped to delineate two sinistral Riedel shear zones (ENE-striking boundary structures represented in green in Figure 1c). The largest seismic events in 1972 ($M_L > 4$) were located at the boundary (up to 2.6 km wide) between these Riedel shear zones (Figure 1c).

A comprehensive paper by Khodayar et al. (2018)—which integrated remote sensing, field geology, and seismicity—showed that both the NRSZ and the SRSZ, located within the Reykjanes geothermal field, are populated by a series of minor and differently oriented structures and that the SRSZ block is more intensely fractured than the NRSZ block. The authors categorized these structures in terms of their orientation and kinematics (Figure 1c): ENE-striking structures, which are subparallel to the NRSZ boundary, display sinistral sense of shear; N-striking to NNE-striking structures, which are mainly dextral strike-slip; NNE-striking to NE-striking structures, that bound for example two grabens at Haugur (Ha) and Mölvík (Mö), are mainly extensional faults and dikes intruding along NE-oriented fissures and faults; E-W structures, which, with significant uncertainty, are inferred to be dextral; and NW-striking to NNW-striking and WNW-striking structures, which are dextral (Figure 1c; Khodayar et al., 2018). Dextral N-striking to NNE-striking structures in the SRSZ are difficult to observe at surface; hence, they are mainly mapped from earthquakes (Keiding et al., 2009). These are interpreted to represent a conjugate fault system together with the ENE-striking structures (Khodayar et al., 2018) and are observed to cut across NE-striking volcanic fissures and normal faults. Both these volcanic fissures and normal faults accommodate extension while N-S faults accommodate the transform component (Sæmundsson et al., 2020).

2.2 Preliminary fault model

In this section, we extract a local fault model for our case study in which we incorporate measurements from wells and local geological studies. The study area is located at Sýrfell (Sý in Figure 1c), approximately 2 km NE of the center of production (Figure 1c), mainly in the NRSZ and partially across the boundary between the two shear zones (Figure 1c). Structural information on this region relies on fault traces interpreted by Khodayar et al. (2018) and well data and televiewer interpretation from well RN-34 (see Supporting Information, Text S1). Although a detailed outcrop study of the area is missing, movements along the faults (or kinematics) are believed to mirror the overall structural pattern of Reykjanes. Furthermore, televiewer images from well RN-34 provide valuable information on orientation, infill, (mechanical) aperture, and kinematics of fractures intercepted by the well. A total of 404 N-striking and NE-striking fractures were interpreted in an unpublished report by Árnadóttir et al. (unpublished report, Supporting Information, Text S1). The dominating fractures (interpreted with high confidence) are subvertical (83°) and strike NNE (022°) on average. An apparent mechanical aperture larger than 19 mm was measured for a series of NNE-striking to NE-striking fractures.

Due to the opening of the NNE-striking to NE-striking fractures and their vicinity to feed points, Árnadóttir et al. (unpublished report, see Supporting Information, Text S1) assume that four of these fractures act as fluid pathways.

In an unpublished report, Khodayar et al. (Supporting Information, Text S2) suggested five preliminary fault models consisting of nine structures (labelled 1 to 8 and 3b in the white rectangle in Figure 1c), representing the starting point of our local fault model for the case study. Two of these faults have known dips (75° to NW) from the outcrop study; they did not intersect the well and are far from the seismic cloud. These faults were therefore excluded from the fault model. In the models, the remaining faults are believed to have constant dip, as do all of the faults in each model (70°, 75°, or 90°). The NW-oriented fault trace (no. 6 in Figure 1c), together with a similarly oriented lineament to the east (not shown in Figure 1c), is, according to Khodayar et al. (2018), likely bounding the seismic cloud of the 2015 swarm (including events occurring on 12 December 2014). This structure is unfavorably oriented to slip since it is orthogonal to the σ_1 axis (as discussed in sections 2.3 and 2.4). We assume that it has limited impact on flow. Therefore, it has also been excluded from the fault model.

2.3 Revised fault model based on the analysis of induced seismicity

In this section we incorporate observations from seismicity clouds and focal mechanisms to generate the local fault model geometry. Using locations of induced and naturally occurring seismicity is a well-suited alternative for the identification of faults where a lack of clear reflectors and large impedance contrasts impair the value of conventional active seismic methods. One benefit of analyzing induced seismicity is that only active faults will be identified; active faults are likely to have relatively large aperture and permeability and are thus suitable for geothermal exploration. Since seismicity will also be induced during fluid injection, the respective locations of seismic events can be utilized to further constrain the geometry of the local fault model.

2.3.1 Brief overview of the methods used to interpret seismicity

Together, individual earthquakes and clouds of smaller seismic events contain two main pieces of information that can be used to construct and improve fault models: i) The relative location of a seismic cloud reveals the general fracture orientation (strike and dip), a.k.a. seismic lineation. Statistical analysis of the cloud (e.g., through the collapsing method [Fehler, 2000]) can further provide uncertainty estimates of the fracture orientation. ii) Focal mechanisms can be determined from larger individual events to constrain the orientation and kinematics of causative slipping fractures.

We employ the collapsing method to interpret fracture orientation from the cloud of seismic events. Introduced by Jones and Stewart (1997), this statistical method entails moving event locations iteratively within their relative uncertainty until the desired accuracy is obtained. Each event is represented by a point with a confidence ellipsoid. This ellipsoid will generally contain a cloud of other events, and an event is moved toward the centroid of the point cloud by a fraction of the event-centroid distance. By repeating this procedure, all the events are “collapsed” within their uncertainty ellipsoids, with the exception of very isolated events. Then, we apply a plane fitting method based on the computation of the covariance matrix of the collapsed events’ point cloud to extract strike and dip and compare this geometry to the fault plane geometry already in the model.

To determine fault plane slipping during a seismic event, focal mechanisms are computed. These graphical representations provide two orthogonal fault plane solutions, of which only one is the correct, active or causative fault. Discriminating between the two solutions often relies on other information (e.g., distribution in space of the focal mechanisms, fault mapped at surface, etc.). Constraining focal mechanisms of small events can be more challenging when the amplitudes of first arrivals are small and the noise levels are high, as is often the case when investigating microseismic events with surface networks.

2.3.2 Interpretation of seismicity

Here, we focus on the seismic events occurring from 20 May 2015 to the end of the TS network recording, i.e., 13 August 2015 (the yellow region in Figure 2a). Automatic detection was applied on continuously recorded seismic data and led to ~6500 seismic events. About 3000 of these events were automatically picked based on pattern matching identification (Duboeuf, Oye, Berre, Keilegavlen, and Dando, 2019) and were quality controlled visually. The entire set of picked events was located using the Icelandic 1-D layer velocity model South Iceland Lowland (SIL, Bjarnason et al., 1993) and a differential evolution algorithm (Storn & Price, 1997; Wuestefeld et al., 2018).The location accuracy was increased using a Double-Difference relative location method (Waldhauser, 2000) (Figure 1b). A detailed analysis of seismic processing methods can be found in Duboeuf, Oye, Berre and Keilegavlen. (2019). Seismic events were grouped into several families based on waveform similarities and event locations. One group of 687 events was likely related to a fluid injection in injection well RN-34 (Figure 1b). The moment magnitudes (M_w) of these events range from about 0.8 to 3 and were determined by fitting a Brune model (Brune, 1970) to the observed seismic spectra. The resulting frequency-magnitude distribution follows the Gutenberg-Richter law, characterized by a high b-value (1.47), as often observed in fluid injection areas (Eaton et al., 2014; Shapiro et al., 2013).

Furthermore, seven time periods display a distinct increase in the seismic activity that surpasses the daily average (> 10 events/day); these are numbered 1 to 7 in Figure 2a. We refer to this spatially and temporarily limited increase in seismic activity as “bursts.” Bursts occur within short time intervals (from a few hours to one week) and are concentrated in relatively small spatial regions, supporting the idea that they might be caused by slip on the same structure.

The collapsing method was applied to all the bursts (1 to 7 in Figure 2a), with the result indicating that six out of seven fitting planes are ENE-striking (ellipses in Figure 2b). Strike and dip of the planes are reported in Figure 2b, showing larger variability in the dip than the strike. This is likely attributable to greater uncertainty in the depth of these events due to the lack of sensors at depth, resulting in poorly constrained dip of the faults. Bursts with a larger number of events (numbers 1 and 4 with 95 and 313 events, respectively) suggest steep (81° to 88°) fault planes. The closest similarly oriented structure to these fitting planes is Fault 4 (Figure 1c). However, because of the proximity (approx. 200 m) of the two other, similarly oriented structures (Faults 3a and 3b, Figure 1c), we cannot rule out that the causative structure could also be one of those.

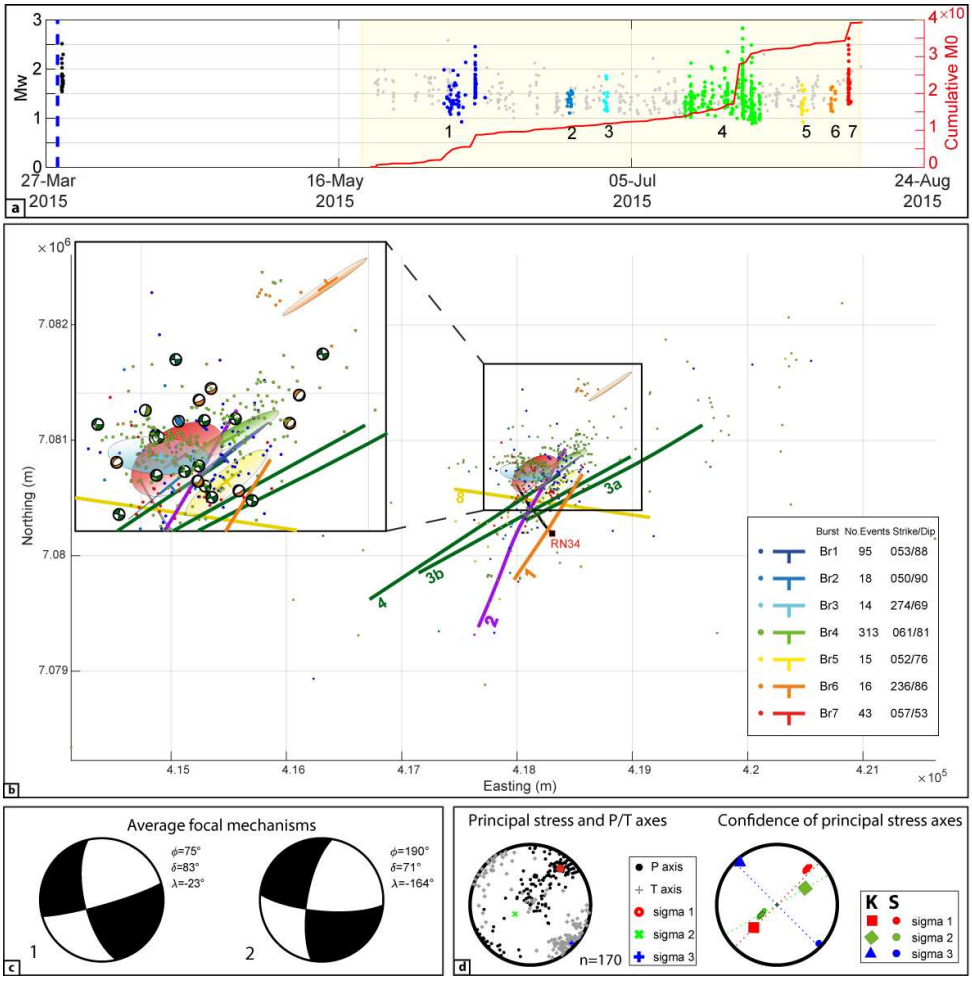

Figure 2. (a) Time vs. moment magnitude (Mw) plot showing post-stimulation seismicity at well RN-34. White regions represent periods where no data are available. Seven periods of increased seismicity for the period between 20 May and 13 August 2015 are shown as colored dots, numbered from 1 to 7. Cumulative seismic moment (M0) during the same period is also shown (red curve). **(b)** Collapsed bursts of seismicity (dots in the same color scheme as used in Figure 2a), fitted planes (ellipse and strike/dip symbol), and well-resolved focal mechanisms occurring in the same region. Focal mechanisms are colored by fault type: orange for normal, blue for reverse, and green for strike-slip. Well RN-34 is also shown (grey). **(c)** Average of 170 focal mechanisms showing strike–slip kinematics, with Φ denoting strike, δ dip, and λ rake. **(d)** Left: principal stress and P/T (Pressure or compression/Tension) axes; Right: confidence of principal stress axes inverted from 170 focal mechanisms (S) and stress orientation from Keiding et al. (2009). Note that P/T axes correspond to σ_1 (sigma 1) and σ_3 (sigma 3) axes.

170 focal mechanisms were computed from P-wave first motion polarities. The focal mechanism solutions indicate that the prevailing faulting types are strike-slip (52%) with near-vertical focal planes, normal (19%), and normal oblique (15%). Purely thrust (5%) and strike-slip with thrust component (2%) fault motions have also been identified. Finally, 7% of the determined focal mechanisms present a non-double-couple component, which might be expected in an injection area (Julian et al., 1998; Zhao et al., 2014). In the inset in Figure 2b, a selected number of focal mechanisms of high quality are superimposed on the collapsed planes. The quality of these focal mechanisms is normalized and based on the number of solutions, observations, and misfits. However, the locations of these focal mechanisms do not clearly align along one specific structure. The two most recurrent focal mechanisms indicate two possible fault plane solutions: (1) sinistral 075°/83° or dextral 165°/72° and (2) dextral 190°/71° or sinistral 100°/80° (Figure 2c). Although the strike variation between the fault plane solutions of the two average focal mechanisms is only 25°, we analyze these results separately and compare them with fitted fault planes and fault traces. The ENE-striking focal plane (075°/83°) of the first average focal mechanism has a similar orientation to the fitted planes of the collapsed events. It is also consistent in terms of both orientation and kinematics (sinistral strike-slip) with fault numbers 3a, 3b, and 4 of the fault model. Associating the second average focal mechanism to a causative structure in the fault model is more complicated and not unique. The N-striking dextral strike-slip focal plane (190°/71°) is, to a certain extent, similar to Fault 2 (Figure 1c); similarly oriented faults are recognized as responsible for earthquakes on the Reykjanes Peninsula (see, e.g., Keiding et al., 2009). Although the other focal plane (100°/80°) of this focal mechanism has the same orientation as structure number 8, this fault is likely to be dextral (Khodayar et al., unpublished report, Supporting Information, Table S3) and therefore does not fit with the focal mechanism solution. N-striking and ENE-striking planes could represent conjugate fault planes that have been observed elsewhere in Iceland (Khodayar et al., 2018). Based on fractures intercepted by the well and on computed focal mechanisms, the faults in the model are interpreted to be vertical.

2.3.3 Final revised fault model

Based on the analysis presented in the previous section, the final fault model consists of six vertical faults: one N-striking to NNE-striking structure (028°), Fault 2; one NNE-striking to NE-striking structure (034°), Fault 1; three ENE-striking structures (between 058° and 063°), Faults 3a, 3b, and 4; and one E-striking structure (strike of 100°), Fault 8 (Figure 3, left). ENE-oriented fault traces (Faults 3a, 3b, and 4 in Figure 1c) coincide with this interpreted surface expression of the boundary between the northern and the southern Riedel Shear Zones. They show a right-stepping en échelon arrangement similar to what has been observed elsewhere on the Reykjanes peninsula, typical of sinistral strike-slip kinematics (see Figure 1c). Uncertainties exist on the cross-cutting relationships (e.g., terminations or abutments) between the different fault sets (e.g., ENE-striking and NNE-striking to NE-striking), and interpretation in Khodayar et al. (2018) (section 2.1) did not match what was previously presented in a fault model scenario by Khodayar et al. (unpublished report, Supporting Information, Text S2). For example, in the former, ENE-striking faults are believed to cut NNE-striking to NE-striking volcanic fissure and normal faults, while in the latter, Fault 3b (ENE-striking) terminates on Fault 2 (NNE-striking to NE-striking). For this reason, cross-cutting relationships are not included in our fault model.

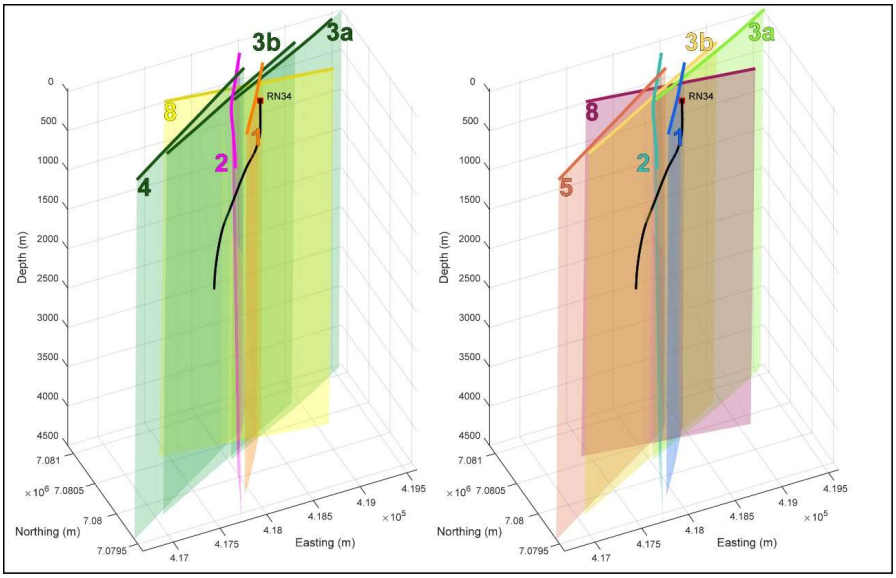

Figure 3. Fault model consisting of six faults. Left: Color scheme based on orientation and kinematics following unpublished work by Khodayar et al. (unpublished report, Supporting Information, Text S2). Right: Color scheme used for visualization of simulation results (see section 5), with different colors for each fault. Well location (square) and path (black line) are also shown.

2.4 Stress state

Focal mechanisms can also be used to infer the orientation of the stress state (see Figure 2d). The direction of the stress as derived from focal mechanism inversion is compared to strain rates from GPS data in Keiding et al. (2009) for different regions in Iceland and to the maximum horizontal stress derived from 15 orientation breakouts in RN-34 (Ziegler et al., 2016). The orientation for the western Reykjanes peninsula (extrapolated from Keiding et al., 2009, Figure 7) is approximately 220°/50° for the maximum principal stress axis σ_1, 064°/40° for the intermediate principal stress axis, and 323°/10° for the minimum stress axis σ_3. However, eastwards, the stress orientation changes toward the strike-slip regime of the SISZ. A model that advocated the permutation of two of the principal stress axes, σ_1 and σ_2, was initially used to explain oblique rifting, supported by the alternation of extension and strike-slip episodes and tectono-magmatic activity. However, the observed coexistence of normal, strike-slip, and oblique fault ruptures during both the swarm in 1972 and in 2013 (Khodayar et al., 2018; Klein et al., 1977) suggests a transtensional regime (intermediate case between normal and strike-slip regimes) in which differently oriented structures accommodate deformation.

For the 170 focal mechanisms derived in this study, we conducted a stress field inversion based on the method of Vavryčuk (2014); our resulting principal stress orientations are σ_1 (040° ± 5°)/23°, σ_2 (230± 10°)/66°, and σ_3 (140° ± 10°)/7°). The orientation of σ_1 is consistent with the strike of the maximum horizontal stress (034°) derived from breakouts in RN-34 (Ziegler et al., 2016). Note that the orientation of σ_3 is almost identical to that predicted by Keiding et al. (2009)

(Figure 2c, right), while σ_1 and σ_2 show the same trends but plunge on opposite quadrants. In addition, a series of stress inversion tests with varying friction coefficient shows that the most robust stress state is obtained for a friction coefficient of 0.4. This value is quite low compared to the 0.6–0.8 usually used (Byerlee, 1978). However, such a value has previously been observed when faults are partially filled with clays or low-friction minerals (Janecke & Evans, 1988; Kanji, 1974). In high temperatures, such as those present in the study region and relevant faults, decreased friction coefficients with temperature have been observed (e.g., by Di Toro et al., 2011).

Although information on stress orientation exists for the Reykjanes peninsula, direct measurements or estimates of stress intensity are lacking. Scenarios of four stress cases (corresponding to Andersonian's stress orientation plus a transtensional case) were accounted for by Peter-Borie et al. (2018) in their modeling of drilling effects and fracture initiation caused by stimulation of well RN-15/IDDP2 (circa 1.5 km SW of the study area). In their study, vertical stress intensity was estimated according to gravitational loading (134 MPa at a depth of 4560 m); and horizontal stress magnitudes were extrapolated from the stress state modelled by Batir et al. (2012) and Peter-Borie et al. (2018). The numerical model of stress was then compared to observations from well images suggesting that the strike-slip fault scenario and, to a lesser extent, the transtensional regime scenario predicted the breakouts more accurate.

3. The 29 March 2015 RN-34 fall-off test and cyclic well stimulation

This section describes available static measurements from well RN-34 as well as data from the 29 March 2015 testing and stimulation of the well. The operation consisted of two stages: a fall-off test followed by cyclic stimulation. For both stages, pressure and volume data are available, as is information from seismic monitoring.

3.1 Static and dynamic well data

RN-34 had been drilled to a depth of 2667 m on 27 March 2015 (Supporting Information, Text S3)[1]. Following rinsing of the well, a televiewer survey was conducted. Televiewer imaging indicated several possible feed points along the wellbore, with the main feed points most likely in the depth interval 2300–2600 m (Supporting Information, Text S1).

Testing of the well commenced on 29 March 2015 with a fall-off test followed by hydraulic stimulation. The fall-off test consisted of constant injection at a rate of 43 L/s from 07:15 to 09:50, followed by an abrupt shut-in. The pressure was monitored in the well at a depth of 1400 meters, that is, about 1000 m above the assumed leakage points from the well into the rock. Recording of data (shown in Figure 4b; see also Supporting Information, Text S4) started about 30 minutes before the shut-in and continued until 1.5 hours after shut-in (recording period 09:20–11:15). As can be seen from Figure 4b, the pressure was stable toward the end of the injection period and then decreased significantly after shut-in. The pressure drop between plateaus during and after injection was about 28 bar.

The following well stimulation was performed from 12:00 to 22:00 with a cyclic injection pattern with injection rates of 100 L/s applied for 1h, followed by rates of 20 L/s for periods of

[1] Drilling was completed at the final depth of 2695 m 2 April 2015 (Supporting Information, Text S3).

20–30 min (Supporting Information, Text S3). In the stimulations reported in Section 5, the durations of low injection rates were set to 30 min (see also the illustration in Figure 4c).

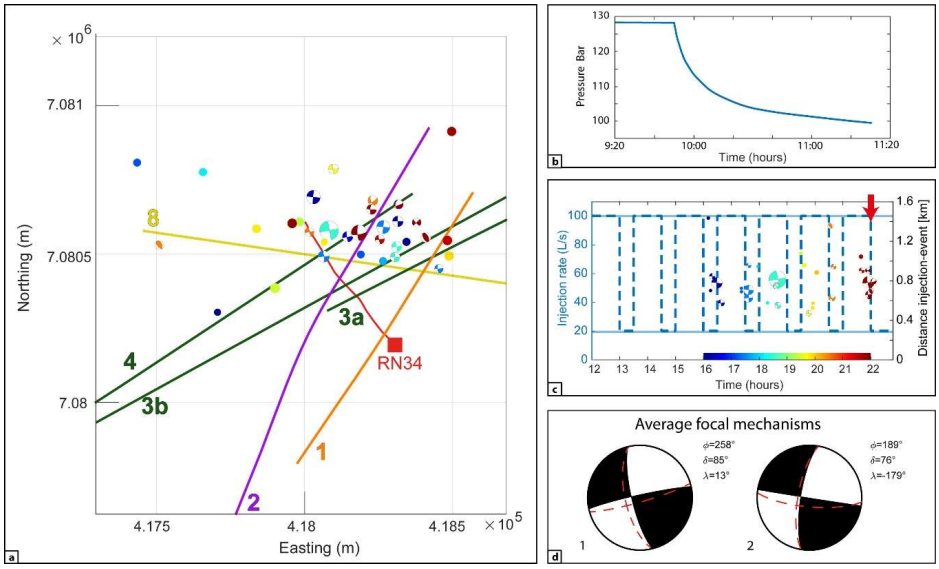

Figure 4. RN-34 injection test on 29 March 2015, seismic event occurrence, magnitude, and focal mechanisms. **(a)** Seismic event locations in map view, fault traces, and RN-34 well location. Colored dots represent seismic events; focal mechanisms are shown where determinable. The color scale applied to seismic events range in time from 16:00 (blue) to 22:00 (red); see subfigure (c). **(b)** Pressure evolution at the monitoring point during the fall-off test. **(c)** Injection rate and seismicity vs time, including the distance of a seismic event to the injection point. The applied injection rate was between 20 and 100 L/s, with periodic oscillations of 20–30 min intervals (Note: Detailed injection data not available). Dot and beach ball sizes are scaled by moment magnitude Mw 1.51 to 2.51. Red arrow corresponds to stimulation end. **(d)** Average of 19 focal mechanisms showing strike-slip kinematics. Red dashes show average focal planes from the three months of injection.

3.2 Induced seismic events

No seismicity was observed during the fall-off test. A sequence of 33 seismic events was observed in the period from 16:00 to 22:00, four hours after the stimulation characterized by the highest injection rate (100 L/s) started. The events are mainly located east of the injection point and north of Fault 8 (Figure 4a), consistent with observations during the three months of injection (Figure 1c). As the pressure and injection flux were not recorded at the well during the stimulation (Figure 4c), we could not link the triggered seismicity to any potential change in well pressure. However, the injection rates were higher than during the fall-off test. The proximity of the seismic events to the injection point (Figures 4a and 4c) and the fact that the events occurred during the stimulation phase suggest that they were induced by the fluid injection. The moment magnitudes vary from 1.5 to 2.5, which is within the range of the magnitudes estimated for the three months of seismic analysis (M_w 0.8 to 3). However, the seismicity shows neither clear

pattern (for example in terms of the spatial, temporal and magnitude distribution of events) nor correlation between locations and event occurrence time (Figure 4a). Moreover, the sequence of individual events does not show any clear increase in the distance to the injection point with time (Figure 4c) and does, hence, not follow a radial diffusion law (Shapiro et al., 2002).

The two principal focal mechanisms computed for 29 March 2015 (Figure 4d) show similar orientation and motion as the two principal focal mechanisms identified through the three-month period (20 May to 13 Aug 2015) of seismic analysis shown in section 2 (Figure 2b). With regard to the first principal focal mechanisms for both periods (29 March 2015 and the three-month period), one of the fault plane solutions is an ENE-striking plane with similar strike (258° vs. 75°) and dip (83° vs. 85°) but opposite dip-direction (north vs. south). The other fault plane solution is a N-striking plane with similar strike (165° vs. 168°) and dip-direction, but slightly different dip (85° vs. 72°). With regard to the second principal focal mechanisms for both periods, the N-striking plane solutions have a similar strike (190° vs. 189°), dip (76° vs. 71°), and dip-direction. These differences are not significant with respect to the relatively small number of events analyzed here. Thus, the reactivated structures during the stimulation on 29 March 2015 are likely the same as the structures reactivated during the latter three months of continuous injection.

To summarize, the sequence of 33 seismic events 29 March appears to be representative for the period from 20 May to 13 August in terms of spatial location and temporal occurrence, magnitude, focal mechanisms, and reactivated structures. This justifies our choice of the local fault model for this particular day as representative for a longer injection period. In addition, it also reinforces the hypothesis of vertical fractures used for the modeling.

4 Hydro-mechanical simulation tool

In this section we introduce a hydro-mechanical reservoir model to conceptualize the observations presented in sections 2 and 3 and to simulate fluid injection into a fault network as well as the mechanical response of the faults and the host rock to the fluid injection.

One main challenge in the numerical modeling of processes in faulted rocks is the large aspect ratio of faults and heterogeneity between faults and host rock. As the dominant physical processes in the faults are either different from those in the host rock or have substantially different characteristics, an upscaled representation that integrates host rock and faults into a continuous medium leads to models with poor accuracy. In particular, modeling of fracture reactivation and slip requires accounting for the deformation of the faults and the host rock and the coupling between them. How to incorporate this into a simulation model depends on whether the faults are resolved by the computational grid or not. Several studies have avoided resolving the fractures by applying subgrid-scale models to represent fracture-matrix interactions (Izadi & Elsworth, 2014; Norbeck et al., 2016; Rutqvist et al., 2015). Herein, we pursue a different approach, based on Discrete Fracture Matrix (DFM) principles (Berre et al., 2019), with the major faults explicitly represented in the computational grid. To avoid resolving the domain across the relatively thin faults , the faults are represented as lower-dimensional objects. The explicit representation gives transparent couplings of processes in host rock, fault network, and on the fault walls and, moreover, allows for high resolution of the sliding process. The effect of small-scale fractures, which are not explicitly represented, may be approximated by upscaling into matrix parameters.

While variants of DFM models have previously been applied to study shear stimulation of fault networks in geothermal reservoirs (Kolditz & Clauser, 1998; Sun et al., 2017; Ucar et al., 2017; Ucar et al., 2018a), this, to the best of our knowledge, is the first attempt at applying DFM models to simulation of coupled flow, mechanics, and fracture reactivation and slip for a case study from an actual geothermal reservoir.

The processes included in our simulation model are summarized as follows: The host rock is considered a poroelastic medium with a linear isotropic relation between stress and displacement. Fluid flow in the rock matrix and the fault network is modeled by Darcy's law. The deformation of the fault is modeled as a frictional contact problem between the fault walls: the fault can be open, in contact but sticking, or in contact and sliding. The latter is characterized by a jump in the tangential displacement of two opposing fault walls. This model is similar to previous models for poroelastic media with fractures modeled by contact mechanics considered recently (Berge et al., 2020; Gallyamov et al., 2018; Garipov et al., 2016; Garipov & Hui, 2019; Keilegavlen et al., 2019; Stefansson et al., 2020). Due to the limited data available to parameterize the model, the model applies only a constant friction coefficient and does not account for permeability enhancement due to shear dilation, although this could have been included (e.g., as by Stefansson et al., 2020). The full set of governing equations can be found in Supporting Information, Text S5.

The computational grid is constructed to conform to the explicitly represented faults. Faces on a fault surfaces are split, and lower-dimensional cells are inserted between the split faces (see Figure 5). The degrees of freedom in the simulation model are specified as illustrated in Figure 5: In the matrix grid, displacement and pressure are represented as cell-centered variables. Additional displacement degrees of freedom are placed on the faces on the fault surfaces. Finally, in the fault grid, fluid pressure and contact force (both normal and tangential) are represented by cell center values.

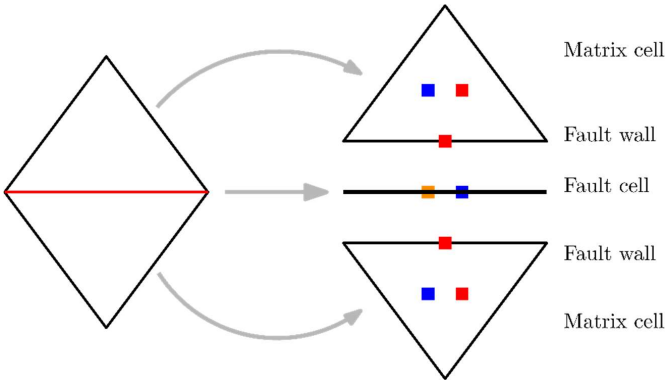

Figure 5. Illustration of conceptual model and degrees of freedom, shown in 2D for simplicity. Left: A DFM conceptual model, where the fault (red line) is represented as a lower-dimensional object. Right: Degrees of freedom: The deformation (red) is represented in matrix cells and on fault walls, fluid pressure (blue) in matrix and fault, and contact force (orange) in the fault.

The simulations are performed using the open-source simulator PorePy, described in Keilegavlen et al. (2019), and applying the following combination of discretization schemes: Poroelastic

deformation of the matrix is discretized by the Multipoint Stress Approximation (Nordbotten, 2016; Nordbotten & Keilegavlen, 2020; Ucar et al., 2018b). Flow in matrix and faults is discretized by a Multipoint Flux Approximation (Aavatsmark, 2002), with the fluid flow between matrix and faults considered within the framework presented by Nordbotten et al. (2019). The simulation framework does not include a well-model but represents injection in a simplified manner by point sources in cells. The contact mechanics formulation for fault deformation uses a semi-smooth Newton approach, as described by Berge et al. (2020) and Hüeber et al. (2008).

5 Simulation results: Cyclic stimulation 29 March 2015 of RN-34

Our goal in this section is to present simulations of the stimulation event on 29 March 2015 and to compare the results with the analysis of seismic events as described in Section 5. To that end, a simulation model is constructed based on the geological information above.

5.1 Construction of simulation model

The geometry of the fault network is taken as described in section 2, and the full simulation domain is specified by a bounding box with a horizontal extent of 10x10 km. In the vertical direction, the simulation domain is set to 4 km. The faults are represented as being linear in the horizontal direction and assumed to be vertical and extending to the top and bottom boundaries of the domain (Figure 6). The simulation grid is created by first meshing the 2D horizontal domain with 1702 cells and then vertically extruding the grid with nine layers of non-uniform thickness, so that the zone near the injection has the highest grid resolution. The simulation grid for the matrix is illustrated in Figure 6.

The elastic moduli of the rock matrix are defined according to the seismic velocities of the rock, accounting for vertical variations of the rock properties; the assigned values are based on those reported by Bodvarsson et al. (1996) and given in the Supporting Information, Table S8. In accordance with section 2.4, the stress is assumed to be in a strike-slip regime, with the maximum and minimum principal stress directions both in the horizontal plane. Their magnitudes are taken as 1.5 times and 0.45 times the lithostatic stress, respectively, in accordance with Peter-Borie et al. (2018), with the maximum principal stress oriented in a NE-SW direction (see Figure 2d). These values are boundary conditions for the momentum conservation in the simulation model. The static friction coefficient on fracture surfaces was set to 0.4 in accordance with the analysis presented in section 2.4. The Biot coefficient was set to 0.8 and rock density to 3000 kg/m^3.

The parameters used in the flow model are fault and matrix permeability, matrix porosity, and the location of the feed points from the injection well into the formation. All of these parameters are both critical for the simulated formation response to the stimulation and highly uncertain.

As the feed points are assumed to be toward the bottom of the well (section 3.1) and associated with faults, the simulation model implements the feed point in the fault cell closest to the well at a depth of 2500 m. In practice, this places the feed point in Fault 4.

Table 1

Hydraulic rock parameters for the three different cases.

	Case A	**Case B**	**Case C**
Matrix permeability K_M [m^2]	1e-12	2e-12	1e-11
Hydraulic aperture a [m]	1e-2	1e-2	1e-2
Tangential conductivity fault 1-4	$a^3/12$	$a^3/12$	$a^3/12$
Normal conductivity fault 1-4	$a/6$	$a/6$	$a/6$
Tangential conductivity fault 8	$a^3/12$	$a \cdot K_M$	1e-2 $\cdot K_M \cdot a$
Normal conductivity fault 8	$a/6$	$K_M/(a/2)$	1e-2 $\cdot K_M/(a/2)$

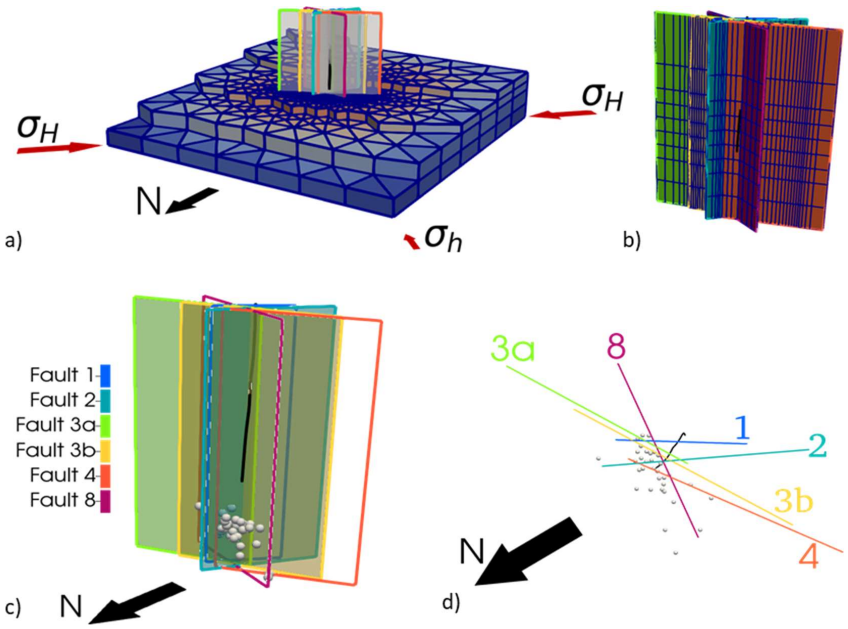

Figure 6. (a) The 3D simulation grid, split to expose the fractures. The coloring of the matrix cells shows the perturbation in pressure from the initial state for Case C. **(b)** The simulation grid in the fault network. **(c)** The fracture network with the color coding used for all visualization of simulation results, the well path (black), and the seismic observations (spheres). The orientation is chosen for optimal readability of the simulation results (Figures 7-9). **(d)** The fracture network, well path, and seismic observations seen from above.

The permeability values for the faults and matrix are reported in Table 1 The values are homogeneous in the matrix and for each of the faults and were held constant during the simulations. High permeabilities are assumed for Faults 1 to 4. The permeability of Fault 8 is considered as unknown prior to the simulation study, as its orientation relative to the regional stress field indicates it may have very low permeability and therefore practically sealing. Based on this, three scenarios were defined, with Fault 8 defined as permeable (Case A), as having permeability equal to that of the matrix (Case B), and as sealing (Case C). For each of these scenarios, the matrix permeabilities were tuned to reproduce the pressure drop measured in the leak-off test run on the morning of 29 March 2015. In this calibration, mechanical effects were ignored. While we acknowledge the simplicity of this approach, a richer parametrization and more elaborate calibration is not warranted due to the scarcity of data. Fluid properties are given in the Supplementary Information, Section 5. The flow simulation model is complemented by hydrostatic conditions at the lateral and upper boundaries and no-flow conditions at the bottom.

The hydro-mechanical simulation model is initialized by simulating a scenario with no injection until steady state is reached. As we have no information on the stress history of the reservoir, the stress boundary conditions in this initialization are taken as the current background stress field. Hence, the initial stress state of the faults in the simulation model may deviate from that of the reservoir, and fractures are critically stressed where slip has occurred. In the initialization, Faults 2 to 5 all undergo slip with a magnitude of order centimeters. Thereafter, the cyclic injection pattern described in section 3 is simulated with a time step of 15 minutes. In the discussion that follows, we mainly focus on the fault network; however, Figure 6 also shows the pressure perturbation in the matrix for Case C.

5.2 Simulation results

We first consider the initial slip tendency, defined as the ratio of tangential to normal forces on the fault surfaces (see Supporting Information, Text S5). As can be seen in Figure 7, the slip tendencies at the start of the stimulation for significant parts of Faults 2, 3a, and 3b attain the maximum possible value (equal to a fault friction coefficient of 0.4) and are thus critically stressed. Except for the tip of Fault 4, Faults 1, 4, and 8 have lower values. The slip tendencies along the faults undergo only minor changes during the stimulation. Hence, faults 1, 4, and 8 remain primarily uncritically stressed, and we report pressure profiles and tangential sliding for Faults 2, 3a, and 3b only. Of these, Fault 2 is connected to the injection point through the fault network without going through the potentially blocking Fault 8, while Faults 3a and 3b are favorably oriented with respect to the background stress field.

Figure 8 depicts pressure perturbations from the steady state at the end of the stimulation period (red arrows in Figure 4c). For Case A, the pressure perturbation is relatively high due to its lower matrix permeability, and pressure is diffused throughout the fracture network. In contrast, for Case C, the pressure perturbation is much lower and, to a large degree, localized in the part of Fault 2 that is on the same side of the sealing fault as the injection point. For the intermediate Case B, there is substantial pressure diffusion in the fault network due to the lack of a seal.

The slip along Faults 2, 3a, and 3b is shown in Figure 9. The slip profile is remarkably similar for the three cases, although the magnitudes of slip differ between them; the largest magnitudes were observed for Case A, which also has the most pronounced pressure diffusion in the fault

network. The slip along Fault 2 for Case C is divided into a region close to the injection point and a region on the far (south) side of Fault 8. A similar division is not present in Cases A and B. Thus, for Case C it seems reasonable that the slip on the north side of Fault 8 is directly caused by fluid injection, while slip on the south side can be attributed to changes in the poroelastic stress in the surrounding rock matrix.

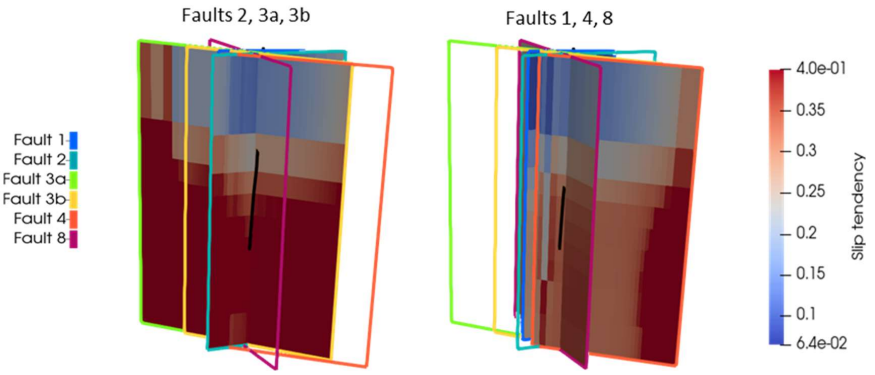

Figure 7. Slip tendency for Faults 2, 3a and 3b and Faults 1, 4 and 8 at the start of stimulation, computed for Case A.

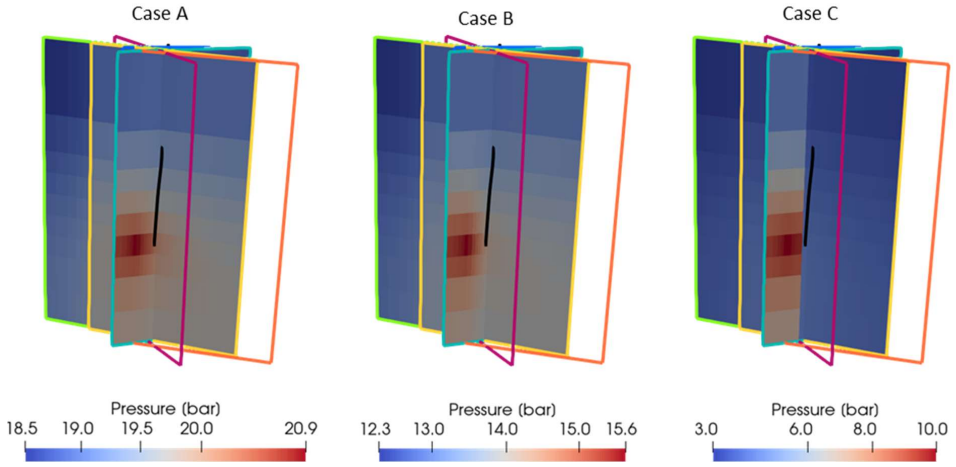

Figure 8. Difference in fault pressure between the end of the cyclic stimulation and the initial state for Case A, Case B and Case C. Note that the scale of the pressure color bar is different for each of the three cases.

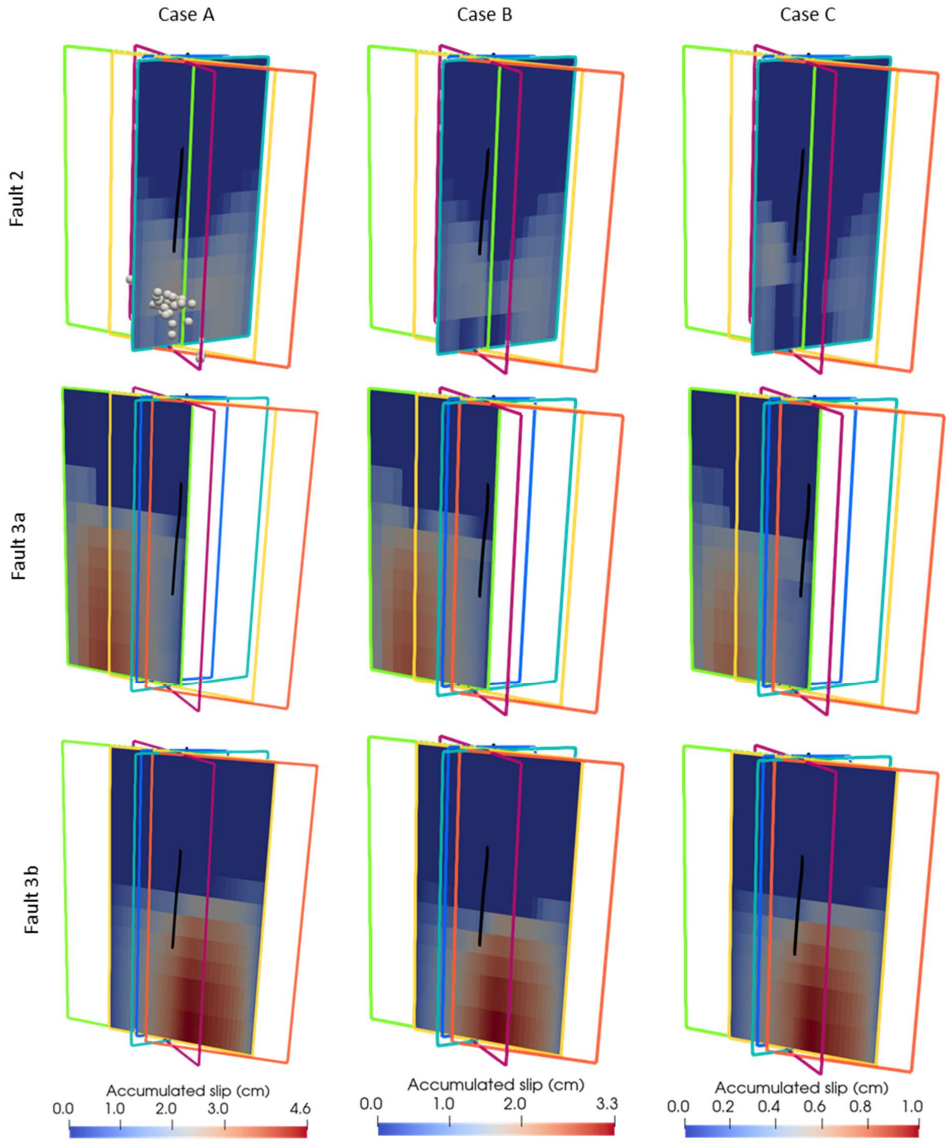

Figure 9. Accumulated slips at the end of the stimulation with Cases A, B, and C in the first, second, and third column respectively, and Faults 2, 3a, and 3b in the first, second and third row, respectively. The color bars (bottom) apply column-wise. Note that the scale of the color bar is different for each of the three cases. The upper left figure also shows the observed seismic events, as discussed in section 3.2. For the legend for fault numbers and orientation of north, see Figure 6.

6 Discussion

During the cyclic stimulation of RN34 on 29 March 2015, 33 seismic events were observed. The events were mainly located east of the injection point, north of Fault 8, and below the bottom of the well. For the given simulation model, the main active faults are Faults 2, 3a, and 3b, showcasing how modeling is able to discriminate slip on close-by and similarly oriented faults (e.g., 3a, 3b, and 4), where seismicity fails because location uncertainties are larger than stepover width. Regions of main simulated slip along these faults are consistent with observed seismicity during stimulation of RN-34. At the same time, the faults also have simulated slip in regions farther from the seismic cloud. However, simulated slip in regions where little seismic activity is observed is not a clear proof of model deficiency, as slip in this region could be aseismic. Evidence of aseismic slip is, e.g., observed in the Brawley (Wei et al., 2015) or Soultz-Sous-Forêts (Cornet et al., 1997) geothermal fields; and in decameter-scale experiments (De Barros et al., 2019; Duboeuf et al., 2017; Guglielmi et al., 2015). Seismic analysis (section 2.3) of the data from the latter three-month injection period, 20 May to 13 August 2015, identifies the ENE-striking faults (Faults 3a, 3b, and 4) as most likely being the active faults. Simulation results show that while Faults 3a and 3b are active, Fault 4, located in the shadow of the nearby active faults, is mainly inactive. However, Fault 4 has some slip and a high slip tendency, in particular near the tip. Shadow effects can also be seen on Fault 2, which has less slip in the region close to where it is intersected by Faults 3a and 3b. Hence, when the location of seismicity is uncertain in regions of nearby and similarly oriented faults, modeling allows us to discriminate on which fault slip occurs.

The discussion above shows that the simulation model can contribute to the understanding of coupled hydromechanical processes interacting with deformation along preexisting faults. At the same time, the current model has severe limitations. While a friction model incorporating stable and unstable slip could be introduced in the simulation model to investigate this issue further, the available data is insufficient to parametrize such a refined model. While the local stress field before stimulation has strong influence on the extent to which faults are reactivated during the stimulation, the initialization process for the simulations is based on strong approximations, which are in turn based on fixed stress boundary conditions and a simple friction model. These aspects, along with the high uncertainty in model parameters, indicate significant model error.

Among these uncertainties, fault network geometry plays an important role as it can strongly affect connectivity. For example, our model representation of faults as linear in the horizontal direction has Faults 2 and 3a as crossing; this may not be the case based on fault traces mapped at surface. Furthermore, a cross-cutting relationship between different fault sets at depth largely affects connectivity. However, modeling allows testing of different geometries, comparing the outcomes, and linking them with observations. As the seismic cloud during stimulation is located mainly to the north of Fault 8, on the same side of the fault as the fluid injection, a simple scenario-based study was designed to investigate the effect of varying the relative permeability of Fault 8 compared to the other faults and the matrix. For Case A, Fault 8 had a high permeability equal to that of the other faults; in Case B, it had a permeability equal to that of the matrix; and in Case C, it had a permeability significantly lower than the matrix. There is significant difference in maximum accumulated slip along the active faults in the different cases, with longest slip in Case A and shortest in Case C. In Cases A and B, the regions of the faults that have slipped are similar and have similar slip profiles. The reason is likely that the faults are

already critically stressed when injection starts, so that only small change in fluid pressure or poroelastic stress state will induce additional slip, which will redistribute poroelastic stress and further affect slip tendencies. For Case C, the effect of Fault 8 as a barrier to flow and the higher matrix permeability relative to Cases A and B can clearly be seen on Fault 2. The higher matrix permeability results in pressure migrating more easily into the matrix and lower pressures in all faults, including Fault 2 as compared in Cases A and B. At the same time, considering the large difference in results when changing the permeability of structures in the formation, slip distances along the active faults are clearly sensitive to the permeabilities of the faults and the matrix. Due to limitations in available data, the permeability of all faults (except Fault 8 in Cases B and C) was set as equal. Given that the NNE-striking to NE-striking structures (including Fault 1) display an aperture in the televiewer and that Fault 1 was deduced as open from the outcrop study (Khodayar et al., unpublished report, Supporting Information, Text S2), an alternative scenario could differentiate these fault sets from those that are ENE-striking (Faults 3a, 3b, and 4). This scenario is further supported by considering the normal load on the two sets of structures. Furthermore, the model is set up considering explicit representation of only six planar faults, while the actual fault geometry of the formation is richer, with larger-scale structures that are not resolved with the current model. Finally, the choice of a static friction and ignoring dilation of fractures with slip is also a simplification of the real situation.

7 Conclusion

Combining analysis of seismicity observed during well stimulation with simulation of injection-induced reservoir dynamics has the potential to improve our understanding of injection-induced fault reactivation as well as interpretations of data. Considering a case study from Reykjanes, Iceland, we have presented a workflow where we first used new analysis of seismic data to establish a revised fault model before this model was used in simulation experiments. Reciprocally, the simulation results show how modeling can be used as a tool to improve interpretations from seismic analysis, e.g., in discriminating slip along close-by and similarly oriented faults. The test cases investigated also show how sensitive fault slip is to the initial stress state as well as the permeability of the faults and their surrounding formation.

Limitations of the current work are related to uncertainty in geological characterization and seismic analysis and model error. While the model framework allows for the introduction of more complex physics, this would lead to over-parameterization as the data are insufficient for identification of the additional parameters. For the seismic analysis, downhole monitoring instrumentation would allow for more precise event locations that could be used to inform the fault model. Furthermore, additional data from pressure transient testing with downhole pressure measurements would improve calibration of permeabilities for the different structural components of the model.

Acknowledgements and Data

HS Orka is acknowledged for allowing information from their reports produced by ÍSOR to be published in the Supporting Information (Texts S1-4 and Tables S1-7) to this paper.

Source code and run scripts for the simulations in this paper are openly available under Version 3 of the GPL license (Keilegavlen & Stefansson 2020).

Seismic data will be made available upon publication of the manuscript.

References

Aavatsmark, I. (2002). An introduction to multipoint flux approximations for quadrilateral grids. *Computational Geosciences* 6(3–4), 405–32. https://doi.org/10.1023/A:1021291114475

Bachmann, C. E., Wiemer, S., Woessner, J., & Hainzl, S. (2011). Statistical analysis of the induced Basel 2006 earthquake sequence: introducing a probability-based monitoring approach for Enhanced Geothermal Systems. *Geophysical Journal International* 186(2), 793–807. https://doi.org/10.1111/j.1365-246X.2011.05068.x

Batir, J., Davatzes, N. C., & Asmundsson, R. (2012). Preliminary model of fracture and stress state in the Hellisheidi Geothermal Field, Hengill Volcanic System, Iceland. In *Proceedings of the 37th Workshop on Geothermal Engineering, Stanford*.

Berge, R. L., Berre, I., Keilegavlen, E., Nordbotten, J. M., & Wohlmuth, B. (2020). Finite volume discretization for poroelastic media with fractures modeled by contact mechanics. *International Journal for Numerical Methods in Engineering* 121(4), 644–63. https://doi.org/10.1002/nme.6238

Berre, I., Doster F., & Keilegavlen, E. (2019). Flow in fractured porous media: A review of conceptual models and discretization approaches. *Transport in Porous Media* 130(1), 215–36. https://doi.org/10.1007/s11242-018-1171-6

Bjarnason, I. T., Menke, W., Flóvenz, Ó. G., & Caress, D. (1993). Tomographic image of the mid-Atlantic plate boundary in southwestern Iceland. *Journal of Geophysical Research: Solid Earth* 98(B4), 6607-6622. https://doi.org/10.1029/92JB02412

Björnsson, S., Einarsson, G. P., Tulinius, H., & Hjartardóttir, Á. R. (2020). Seismicity of the Reykjanes Peninsula 1971–1976. *Journal of Volcanology and Geothermal Research* 391: 106369. https://doi.org/10.1016/j.jvolgeores.2018.04.026

Blanck, H., Jousset, P., Hersir, G. P., Ágústsson, K., & Flóvenz, Ó. G. (2020). Analysis of 2014–2015 on- and off-shore passive seismic data on the Reykjanes Peninsula, SW Iceland. *Journal of Volcanology and Geothermal Research* 391: 106548. https://doi.org/10.1016/j.jvolgeores.2019.02.001

Bodvarsson, R., Rognvaldsson, S. T., Jakobsdottir, S. S., Slunga, R., & Stefansson, R. (1996). The SIL data acquisition and monitoring system. *Seismological Research Letters* 67(5), 35–46. https://doi.org/10.1785/gssrl.67.5.35

Bruel, D. (2007). Using the migration of induced seismicity as a constraint for fractured hot dry rock reservoir modelling. *International Journal of Rock Mechanics and Mining Sciences* 44(8), 1106–1117. https://doi.org/10.1016/j.ijrmms.2007.07.001

Brune, J. N. (1970). Tectonic stress and the spectra of seismic shear waves from earthquakes. *Journal of Geophysical Research* 75(26), 4997–5009. https://doi.org/10.1029/JB075i026p04997

Byerlee, J. (1978). Friction of rocks. *Pure and Applied Geophysics* 116, 615–626. https://doi.org/10.1007/BF00876528

Chabora, E., Zemach, E., Spielman, P., Drakos, P., Hickman, S., & Lutz, S. (2012). Hydraulic stimulation of Well 27-15, Desert Peak Geothermal Field, Nevada, USA. In *Proceedings of the 37th Workshop on Geothermal Engineering, Stanford*.

Clifton, A. E., & Kattenhorn, S. A. (2006). Structural architecture of a highly oblique divergent plate boundary segment. *Tectonophysics* 419(1–4), 27–40. https://doi.org/10.1016/j.tecto.2006.03.016

Cornet, F. H., Helm, J., Poitrenaud, H., & Etchecopar, A. (1997). Seismic and aseismic slips induced by large-scale fluid injections. In S. Talebi (Ed.), *Seismicity Associated with Mines, Reservoirs and Fluid Injections*, 563–583. Basel: Birkhäuser Basel. https://doi.org/10.1007/978-3-0348-8814-1_12

De Barros, L., Cappa, F., Guglielmi, Y., Duboeuf, L., & Grasso, J.-R. (2019). Energy of injection-induced seismicity predicted from in-situ experiments. *Scientific Reports* 9(1), 4999. https://doi.org/10.1038/s41598-019-41306-x

Deichmann, N., & Giardini, D. (2009). Earthquakes induced by the stimulation of an enhanced geothermal system below Basel (Switzerland). *Seismological Research Letters* 80(5), 784–798. https://doi.org/10.1785/gssrl.80.5.784

Di Toro, G., Han, R., Hirose, T., De Paola, N., Nielsen, S., Mizoguchi, K., et al. (2011). Fault lubrication during earthquakes. *Nature* 471(7339), 494–498. https://doi.org/10.1038/nature09838

Duboeuf, L., De Barros, L., Cappa, F., Guglielmi, Y., Deschamps, A., & Seguy, S. (2017). Aseismic motions drive a sparse seismicity during fluid injections into a fractured zone in a carbonate reservoir: injection-induced (a)seismic motions. *Journal of Geophysical Research: Solid Earth* 122(10), 8285–8304. https://doi.org/10.1002/2017JB014535

Duboeuf, L., Oye, V., Berre, I., & Keilegavlen, E. (2019). Induced seismicity in the Reykjanes Geothermal Reservoir, Iceland: seismic event monitoring, characterization and clustering. In *Proceedings of the European Geothermal Congress*.

Duboeuf, L., Oye, V., Berre, I., Keilegavlen, E., & Dando, B. (2019). *Automatic picking for induced seismicity in Iceland using an EAT (Empirically Aggregated Template) methodology*. Poster presented at Third Schatzalp Workshop on Induced Seismicity, Davos, Switzerland. https://doi.org/10.13140/RG.2.2.17248.51206

Eaton, D. W., Davidsen, J., Pedersen, P. K., & Boroumand, N. (2014). Breakdown of the Gutenberg-Richter Relation for microearthquakes induced by hydraulic fracturing: influence of stratabound fractures. *Geophysical Prospecting* 62(4), 806–818. https://doi.org/10.1111/1365-2478.12128

Ellsworth, W. L. (2013). Injection-induced earthquakes. *Science* 341(6142), 1225942–1225942. https://doi.org/10.1126/science.1225942

Ellsworth, W. L., Giardini, D., Townend, J., Ge, S., & Shimamoto, T. (2019). Triggering of the Pohang, Korea, earthquake (Mw 5.5) by enhanced geothermal system stimulation. *Seismological Research Letters* 90(5), 1844–1858. https://doi.org/10.1785/0220190102

Fehler, M. (2000). Improved relative locations of clustered earthquakes using constrained multiple event location. *Bulletin of the Seismological Society of America* 90(3), 775–780. https://doi.org/10.1785/0119990095

Flovenz, O., Augustsson, K., Guðnason, E. Á., & Kristjansdottir, S. (2015). Reinjection and induced seismicity in geothermal fields in Iceland. In *Proceedings of the World Geothermal Congress*.

Gallyamov, E., Garipov, T., Voskov, D., & van den Hoek, P. (2018). Discrete fracture model for simulating waterflooding processes under fracturing conditions. *International Journal for Numerical and Analytical Methods in Geomechanics* 42(13), 1445–1470. https://doi.org/10.1002/nag.2797

Garipov, T. T., & Hui, M. H. (2019). Discrete fracture modeling approach for simulating coupled thermo-hydro-mechanical effects in fractured reservoirs. *International Journal of Rock Mechanics and Mining Sciences* 122, 104075. https://doi.org/10.1016/j.ijrmms.2019.104075

Garipov, T. T., Karimi-Fard, M., & Tchelepi, H. A. (2016). Discrete fracture model for coupled flow and geomechanics. *Computational Geosciences* 20(1), 149–160. https://doi.org/10.1007/s10596-015-9554-z

Genter, A., Evans, K., Cuenot, N., Fritsch, D., & Sanjuan, B. (2010). Contribution of the exploration of deep crystalline fractured reservoir of Soultz to the knowledge of Enhanced Geothermal Systems (EGS). *Comptes Rendus Geoscience* 342(7–8), 502–516. https://doi.org/10.1016/j.crte.2010.01.006

Gischig, V. S., & Wiemer, S. (2013). A stochastic model for induced seismicity based on non-linear pressure diffusion and irreversible permeability enhancement. *Geophysical Journal International* 194(2), 1229–1249. https://doi.org/10.1093/gji/ggt164

Goertz-Allmann, B. P., Goertz, A., & Wiemer, S. (2011). Stress drop variations of induced earthquakes at the Basel geothermal site. *Geophysical Research Letters* 38 L09308, https://doi.org/10.1029/2011GL047498

Grigoli, F, Cesca, S., Rinaldi, A. P., Manconi, A., López-Comino, J. A. Clinton, J. F., et al. (2018). The November 2017 Mw 5.5 Pohang Earthquake: a possible case of induced seismicity in South Korea. *Science* 360(6392), 1003–1006. https://doi.org/10.1126/science.aat2010

Guðnason, E. Á. (2014). Analysis of seismic activity on the western part of the Reykjanes Peninsula, SW Iceland, December 2008–May 2009 (Master's thesis). University of Iceland.

Guglielmi, Y., Cappa, F., Avouac, J.-P., Henry, P., & Elsworth, D. (2015). Seismicity triggered by fluid injection-induced aseismic slip. *Science* 348(6240), 1224–1226. https://doi.org/10.1126/science.aab0476

Hakimhashemi, A. H., Schoenball, M., Heidbach, O., Zang, A., & Grünthal, G. (2014). Forward modelling of seismicity rate changes in georeservoirs with a hybrid geomechanical–statistical prototype model. *Geothermics* 52, 185–194. https://doi.org/10.1016/j.geothermics.2014.01.001

Hüeber, S., Stadler, G., & Wohlmuth, B. (2008). A primal-dual active set algorithm for three-dimensional contact problems with Coulomb Friction. *SIAM Journal on Scientific Computing* 30(2), 572–596. https://doi.org/10.1137/060671061

Izadi, G., & Elsworth, D. (2014). Reservoir stimulation and induced seismicity: Roles of fluid pressure and thermal transients on reactivated fractured networks. *Geothermics* 51, 368–379. https://doi.org/10.1016/j.geothermics.2014.01.014

Janecke, S. U., & Evans J. P., (1988). Feldspar-influenced rock rheologies. *Geology* 16(12), 1064–1067. https://doi.org/10.1130/0091-7613(1988)016<1064:FIRR>2.3.CO;2

Jones, R. H., & Stewart, R. C. (1997). A method for determining significant structures in a cloud of earthquakes. *Journal of Geophysical Research: Solid Earth* 102(B4), 8245–8254. https://doi.org/10.1029/96JB03739

Jousset, P., Blanck H., Franke S., Metz, M., Augustsson, K., Verdel, A., et al. (2016). Seismic tomography in Reykjanes, SW Iceland. In *Proceedings of the European Geothermal Congress*.

Julian, B. R., Miller, A. D., & Foulger, G. R. (1998). Non-double-couple earthquakes 1. Theory. *Reviews of Geophysics* 36(4), 525–549. https://doi.org/10.1029/98RG00716

Juncu, D., Árnadóttir, T., Geirsson, H., Guðmundsson, G. B., Lund, B., Gunnarsson, G., et al. (2020). Injection-induced surface deformation and seismicity at the Hellisheidi geothermal field, Iceland. *Journal of Volcanology and Geothermal Research* 391(1), 106337. https://doi.org/10.1016/j.jvolgeores.2018.03.019

Kanji, M. A. (1974). The relationship between drained friction angles and Atterberg limits of natural soils. *Géotechnique* 24(4), 671–674. https://doi.org/10.1680/geot.1974.24.4.671

Keiding, M., Lund, B., & Árnadóttir, T. (2009). Earthquakes, stress, and strain along an obliquely divergent plate boundary: Reykjanes Peninsula, Southwest Iceland. *Journal of Geophysical Research* 114(B9): B09306. https://doi.org/10.1029/2008JB006253

Keilegavlen, E., Berge, R., Fumagalli, A., Starnoni, M., Stefansson, I., Varela, J., & Berre, I. (2019). PorePy: An open-source software for simulation of multiphysics processes in fractured porous media. ArXiv: 1908.09869.

Keilegavlen, E., & Stefansson, I. (2020). *Keileg/RN-34-Stimulation: Simulation of Hydraulic Stimulation* (version v1.0). Zenodo. https://doi.org/10.5281/ZENODO.4005633

Khodayar, M., Björnsson, S., Guðnason, E. Á., Níelsson, S., Axelsson, G., & Hickson, C. (2018). Tectonic control of the Reykjanes geothermal field in the oblique rift of SW Iceland: from regional to reservoir scales. *Open Journal of Geology* 08(03), 333–382. https://doi.org/10.4236/ojg.2018.83021

Kim, K.-H., Ree, J.-H., Kim, Y. H., Kim, S., Kang, S. Y., & Seo W. (2018). Assessing whether the 2017 Mw 5.4 Pohang Earthquake in South Korea was an induced event. *Science* eaat6081. https://doi.org/10.1126/science.aat6081

Klein, F. W., Einarsson, P., & Wyss, M. (1977). The Reykjanes Peninsula, Iceland, earthquake swarm of September 1972 and its tectonic significance. *Journal of Geophysical Research* 82(5), 865–888. https://doi.org/10.1029/JB082i005p00865

Kohl, T., & Mégel, T. (2007). Predictive modeling of reservoir response to hydraulic stimulations at the European EGS site Soultz-Sous-Forêts. *International Journal of Rock Mechanics and Mining Sciences* 44(8), 1118–1131. https://doi.org/10.1016/j.ijrmms.2007.07.022

Kolditz, O., & Clauser, C. (1998). Numerical simulation of flow and heat transfer in fractured crystalline rocks: application to the hot dry rock site in Rosemanowes (U.K.). *Geothermics* 27(1), 1–23. https://doi.org/10.1016/S0375-6505(97)00021-7

McClure, M. W., & Horne, R. N. (2011). Investigation of injection-induced seismicity using a coupled fluid flow and rate/state friction model. *GEOPHYSICS* 76(6), WC181–98. https://doi.org/10.1190/geo2011-0064.1

Nielsson, S., Eggertson, G., Weisenberger, T.B., Tulinius, H., Gudnason, E.Á., & Friedleifson, G. (2020). The Reykjanes geothermal system—an extended conceptual model. In *Proceedings of the World Geothermal Congress*.

Norbeck, J. H., McClure, M. W., Lo, J. W., & Horne, R. N. (2016). An embedded fracture modeling framework for simulation of hydraulic fracturing and shear stimulation. *Computational Geosciences* 20(1), 1–18. https://doi.org/10.1007/s10596-015-9543-2

Nordbotten, J. M. (2016). Stable cell-centered finite volume discretization for Biot Equations. *SIAM Journal on Numerical Analysis* 54(2), 942–968. https://doi.org/10.1137/15M1014280

Nordbotten, J. M., & Keilegavlen, E. (2020). An introduction to multi-point flux (MPFA) and stress (MPSA) finite volume methods for thermo-poroelasticity. *ArXiv:2001.01990*. http://arxiv.org/abs/2001.01990.

Nordbotten, J. M., Boon, W. M., Fumagalli. A., & Keilegavlen, E. (2019). Unified approach to discretization of flow in fractured porous media. *Computational Geosciences* 23(2), 225–237. https://doi.org/10.1007/s10596-018-9778-9

Peter-Borie, M., Loschetter, A., Merciu, I. A., Kampfer, G., & Sigurdsson, O. (2018). Borehole damaging under thermo-mechanical loading in the RN-15/IDDP-2 Deep Well: towards validation of numerical modeling using logging images. *Geothermal Energy* 6, 17. https://doi.org/10.1186/s40517-018-0102-7

Rothert, E., & Shapiro, S. (2003). Microseismic monitoring of borehole fluid injections: data modeling and inversion for hydraulic properties of rocks. *Geophysics* 68(2), 685–689. https://doi.org/10.1190/1.1567239

Rutqvist, J., Dobson P. F., Garcia J., Hartline, C., Jeanne, P., Oldenburg, C. M., Vasco, D. W., & Walters, M. (2015). The northwest geysers EGS demonstration project, California: pre-stimulation modeling and interpretation of the stimulation. *Mathematical Geosciences* 47(1), 3–29. https://doi.org/10.1007/s11004-013-9493-y

Sæmundsson, K., Sigurgeirsson, M. Á., & Friðleifsson, G. Ó. (2020). Geology and structure of the Reykjanes volcanic system, Iceland. *Journal of Volcanology and Geothermal Research* 391, 106501. https://doi.org/10.1016/j.jvolgeores.2018.11.022

Schindler, M., Baumgärtner, J., Gandy, T., Hauffe, P., Hettkamp, T., Menzel, H., et al. (2010). Successful hydraulic stimulation techniques for electric power production in the Upper Rhine Graben, Central Europe. In *Proceedings of the World Geothermal Congress*.

Shapiro, S. A. (2015). *Fluid-Induced Seismicity*. Cambridge. https://doi.org/10.1017/CBO9781139051132

Shapiro, S. A., Krüger, O. S., & Dinske, C. (2013). Probability of inducing given-magnitude earthquakes by perturbing finite volumes of rocks. *Journal of Geophysical Research: Solid Earth* 118(7), 3557–3575. https://doi.org/10.1002/jgrb.50264

Shapiro, S. A., Rothert, E., Rath, V., & Rindschwentner, J. (2002). Characterization of fluid transport properties of reservoirs using induced microseismicity. *Geophysics*, 67(1), 212-220. doi.org/10.1190/1.1451597

Stefansson, I., Berre, I., & Keilegavlen, E. (2020). A fully coupled numerical model of thermo-hydro-mechanical processes and fracture contact mechanics in porous media. *ArXiv:2008.06289*. http://arxiv.org/abs/2008.06289.

Storn, R., & Price, K. (1997). Differential evolution—a simple and efficient heuristic for global optimization over continuous spaces. *Journal of Global Optimization* 11(4), 341–359. https://doi.org/10.1023/A:1008202821328

Sun, Z.-X., Zhang, X., Xu, Y., Yao, J., Wang, H.-X., Lv, S., et al. (2017). Numerical simulation of the heat extraction in EGS with thermal-hydraulic-mechanical coupling method based on discrete fractures model. *Energy* 120, 20–33. https://doi.org/10.1016/j.energy.2016.10.046

Sæmundsson, K. (1978). Fissure swarms and central volcanoes of the neovolcanic zones of Iceland in Crustal evolution in northern Britain and adjacent regions. *Geological journal Liverpool* 10, 415-432.

Ucar, E., Berre, I., & Keilegavlen, E. (2017). Postinjection normal closure of fractures as a mechanism for induced seismicity: postinjection fracture closure. *Geophysical Research Letters* 44(19), 9598–9606. https://doi.org/10.1002/2017GL074282

Ucar, E., Berre, I., & Keilegavlen, E. (2018a). Three-dimensional numerical modeling of shear stimulation of fractured reservoirs. *Journal of Geophysical Research: Solid Earth* 123(5), 3891–3908. https://doi.org/10.1029/2017JB015241

Ucar, E., Keilegavlen, E., Berre, I., & Nordbotten, J. M. (2018b). A finite-volume discretization for deformation of fractured media. *Computational Geosciences* 22(4), 993–1007. https://doi.org/10.1007/s10596-018-9734-8

Vavryčuk, V. (2014). Iterative joint inversion for stress and fault orientations from focal mechanisms. *Geophysical Journal International* 199(1), 69–77. https://doi.org/10.1093/gji/ggu224

Waldhauser, F. (2000). A Double-Difference earthquake location algorithm: method and application to the Northern Hayward Fault, California. *Bulletin of the Seismological Society of America* 90(6), 1353–1368. https://doi.org/10.1785/0120000006

Weemstra, C., Obermann, A., Verdel, A., Paap, B., Blanck, H., Guðnason E. Á, et al. (2016). Time-lapse seismic imaging of the Reykjanes Geothermal Reservoir. In *Proceedings of the European Geothermal Congress*. Strasbourg, France.

Wei, S., Avouac, J.-P., Hudnut, K. W., Donnellan, A., Parker, J. W., Graves, R. W., et al. (2015). The 2012 Brawley swarm triggered by injection-induced aseismic slip. *Earth and Planetary Science Letters* 422, 115–125. https://doi.org/10.1016/j.epsl.2015.03.054

Weisenberger T.B., Harðarson B.S, Mesfin K.G., Einarsson G.M., Níelsson S., Zierenberg R.A., & Friðleifsson G.Ó. (2019). The Iceland Deep Drilling Project at Reykjanes - 4.5 km Deep Drilling into Supercritical Conditions. In *Proceedings of the 44th Workshop on Geothermal Reservoir Engineering*, Stanford University, Stanford, California, February 11-13, 2019, SGP-TR-214

Wuestefeld, A., Greve, S. M., Näsholm, S. P., & Oye, V. (2018). Benchmarking earthquake location algorithms: a synthetic comparison. *GEOPHYSICS* 83(4), KS35–47. https://doi.org/10.1190/geo2017-0317.1

Zhao, P., Kühn, D., Oye, V., & Cesca, S. (2014). Evidence for tensile faulting deduced from full waveform moment tensor inversion during the stimulation of the Basel enhanced geothermal system. *Geothermics* 52, 74–83. https://doi.org/10.1016/j.geothermics.2014.01.003

Ziegler, M., Rajabi, M., Heidbach, O., Hersir, G. P., Ágústsson, K., Árnadóttir, S., & Zang, A. (2016). The stress pattern of Iceland. *Tectonophysics* 674, 101–113. https://doi.org/10.1016/j.tecto.2016.02.008

Zimmermann, G., & Reinicke, A. (2010). Hydraulic stimulation of a deep sandstone reservoir to develop an enhanced geothermal system: laboratory and field experiments. *Geothermics* 39(1), 70–77. https://doi.org/10.1016/j.geothermics.2009.12.003

Graphic design: Communication Division, UiB / Print: Skipnes Kommunikasjon AS

uib.no